Cyclic Lateral Loading of Monopile Foundations in Cohesionless Soils

Christelle Nadine Abadie

Cyclic Lateral Loading of Monopile Foundations in Cohesionless Soils

Christelle N. Abadie

St Catherine's College

University of Oxford

A thesis submitted for the degree of
Doctor of Philosophy

Michaelmas Term 2015

Abstract

Cyclic Lateral Loading of Monopile Foundations in Cohesionless Soils

Christelle N. Abadie

The monopile is the dominant foundation type for offshore wind turbines, with current design guidance based on knowledge transferred from the oil and gas industry. Whilst there are some similarities between wind turbine and oil and gas pile design, there are also a number of key differences. Notably, offshore wind turbine monopiles are subjected to many cycles of large horizontal loads during their lifetime, whereas such loading conditions are not as prevalent in oil and gas design. As a result, the pile response due to this cyclic loading is poorly accounted for in current practice.

This thesis presents experimental and theoretical research, aimed at improving the understanding of the behaviour of rigid monopiles in cohesionless soils, when subjected to lateral cyclic loading. The experimental work involves laboratory floor model tests, scaled to represent a full-scale wind-turbine monopile. The test programme is designed to identify the key mechanisms driving pile response. It is divided into four main parts, investigating loading rate effect, hysteretic behaviour during unloading and reloading, as well as pile response to long-term single and multi-amplitude cyclic loads. In particular, the results show that the pile response conforms to the extended Masing rules, with permanent deformation accumulated during non-symmetric continuous cyclic loads. This ratcheting behaviour is characterised by two features: first, the ratcheting rate decreases with cycle number and depends on the cyclic load magnitude and secondly, the shape of the hysteresis loop tightens progressively, involving increased secant stiffness and decreased loop area. Tests investigating multi-amplitude loading scenarios prove that the interaction between these mechanisms describes the pile response. Finally, the continuous cyclic test results are interpreted using the p-y method combined with the Degradation Stiffness Model, and this shows a good fit to the observed pile deformation.

The key experimental findings are used for the development of a constitutive model that captures ratcheting while conforming to the observed Masing behaviour. The model, called HARM, is rigorous yet simple, and is framed within the hyperplasticity approach presented by Houlsby and Puzrin (2006). The model is tuned to capture the macro response of the pile under monotonic and cyclic loading, and is calibrated using the experimental data. The results demonstrate that HARM can successfully reproduce the main elements of the pile response with high accuracy. The method could easily be within common design approaches, such as the p-y method.

Résumé

Chargement Latéral Cyclique des Fondations Monopieu dans des Sols Sans Cohésion

Christelle N. Abadie

Le monopieu est le type de fondation le plus utilisé pour l'installation des éoliennes offshore. De nos jours, leur dimensionnement est basé sur un transfert de connaissances de l'industrie pétrolière et gazière. Si des similitudes existent entre le dimensionnement des pieux pour l'éolien offshore et celui des plateformes pétrolières, plusieurs différences significatives subsistent également. En particulier, au cours de leur durée de vie, les fondations monopieux utilisées en éolien offshore sont soumis à de nombreux cycles de larges chargements horizontaux. A l'inverse, ce type de chargement n'est pas dimensionnant dans le cas des plateformes pétrolières. C'est pourquoi, les méthodes de dimensionnement actuelles ne permettent pas de prendre correctement en compte la réponse des pieux soumis à ces chargements cycliques.

Ce manuscrit présente un travail de recherche expérimental et théorique ayant pour objectif d'approfondir la compréhension du comportement des monopieux rigides soumis à des chargements cycliques latéraux dans des sols sans cohésion. Le travail expérimental est effectué au moyen d'un banc d'essai en laboratoire sur un modèle à échelle réduite, dimensionné afin de représenter des pieux de tailles réelles pour l'éolien offshore. Le programme d'essais est conçu afin d'identifier les mécanismes clés dirigeant la réponse du pieu. Il est divisé en quatre parties permettant l'étude de la dépendance en fréquence de chargement, du comportement hystérétique lors de la charge et de la décharge ainsi que de la réponse à un chargement cyclique continu à grand nombre de cycles et multi-amplitude. Les résultats montrent notamment que la réponse du pieu obéit aux règles de Masing généralisées et emmagasine des déformations permanentes sous chargement cyclique non-symétrique. Cet effet rochet est alors caractérisé par deux phénomènes : tout d'abord, le taux de rochet diminue avec le nombre de cycles et dépend de l'intensité de chargement cyclique, ensuite, la forme de la boucle d'hystérèse se resserre progressivement et induit une augmentation de la rigidité sécante et une diminution de l'aire de la boucle. Les tests étudiant des scenarios de chargement multi-amplitude démontrent que l'interaction entre ces mécanismes caractérise la réponse du pieu. Pour finir, les résultats des tests cycliques continus sont interprétés au moyen de la méthode *p-y*, en association avec le «Degradation Stiffness Model» (Modèle impliquant une dégradation de la rigidité), et les résultats sont en adéquation avec la déformation du pieu observée expérimentalement.

Les résultats clés de l'étude expérimentale sont utilisés pour le développement d'un modèle constitutif modélisant l'effet rochet tout en se conformant au comportement de Masing observé. Le modèle, appelé HARM, est rigoureux tout en restant simple, et est formulé dans le cadre de l'approche hyper-plastique présentée par Houlsby et Puzrin (2006). Le modèle est ensuite adapté afin de reproduire la réponse macroscopique du pieu sous chargement monotonique et cyclique, et calibré au moyen des résultats expérimentaux. Les résultats obtenus démontrent que HARM peut reproduire les éléments principaux de la réponse du pieu avec succès et grande précision. Cette méthode pourrait facilement être intégrée aux techniques de dimensionnement actuelles, telles que la méthode *p-y*.

To my parents, my grand-parents

and Ginette

Acknowledgements

First and foremost, I would like to thank my supervisors, Prof. Byron Byrne and Dr. Sarah Levy-Paing. Throughout the course of this DPhil, Byron has provided invaluable input for the research and comments to improve my writing skills, encouraging me to always stretch my personal capabilities. When visiting EDF, or during our frequent meetings over the phone, Sarah has been of extremely valuable support, guidance and enthusiasm and has helped me overcome the difficulties faced during the early stages of the project. I have also been very privileged to work with Prof. Guy Houlsby, whose guidance, motivation and knowledge have been a driving force for this thesis developments. I will never thank him enough for the long meetings and fascinating discussions we had. I would also like to thank Dr. Nicolas Relun, for his time and advice at the end of the project. Finally, I am very thankful to my examiners, Prof. Martin Achmus and Prof. Harvey Burd, for reviewing my thesis and providing the final sense of achievement to this project.

I am also grateful for the generous support of EDF Energies Nouvelles and for their interest in this project and its application for engineering design.

I would like to thank Alison May, for her assistance and support, Sylvie Gaudin and Armelle Leprat, for their help with the administration at EDF, and the technicians at Oxford, Bob Sawala and Clive Baker, for their guidance in the laboratory.

Such a project is only possible when working in a stimulating and cheerful environment. My very deep gratitude goes to my friends and colleagues in the Jenkin building, whose help, enthusiasm and support have helped me at every stages of this DPhil. Firstly, to Ross McAdams, Brian Sheil, Chris Vogel, Susannah Cooke and Dan Claff for their valuable feedbacks, when reviewing my thesis, but also for checking on my experiments when running for days, helping me with the photos of the rig, discussing technical methods for design, or simply for the nice (and sometimes animated) chats over a cup of tea. Also, to the geotechnical group, and in particular, Elisabeth Williams and Laith Tapper, for their technical advice. And finally, to my friends, YiLing He and Coco Wing Nam Yiu, for the rare, but necessary relaxing time during the final push. Finally, at EDF, I am particularly thankful for the encouragements and technical advice of Pierre Bousseau.

Part-time work at EDF would never have been possible without the help of my brother Pierre at the time of my moving to Paris; and the warm welcomes of my friends, Florence, Guillaume and Mélanie, during my frequent visits to EDF. Finally, I would like to thank my parents, my grand-parents and my family for their support and love, and for always encouraging me during these doctorate studies.

Table of Contents

Nomenclature

1. Common variables

Greek alphabet

α	[-]	Internal kinematic variables (hyperplasticity theory)
α_r	[-]	Ratcheting strain (HARM)
α_h	[-]	Accumulation of ratcheting strain (HARM)
α_{h0}	[-]	Initial value of hardening parameter (HARM+)
γ'	$[FL^{-3}]$	Effective unit weight
δ	[-]	Degradation coefficient (DSM)
ϵ	[-]	Strain (plasticity theory)
ϵ^p	[-]	Plastic strain (plasticity theory)
ϵ_{pU}	[-]	Ultimate monotonic plastic strain defining shape of loading curve (HARM+)
ζ_b	[-]	Maximum load magnitude during cyclic loading $\zeta_b = M_{max}/M_R$
ζ_c	[-]	Cyclic load amplitude $\zeta_c = M_{min}/M_{max}$
η	[-]	Internal coordinate (hyperplasticity theory)
θ	[deg./rad.]	Pile rotation
θ_{max}	[deg./rad.]	Pile rotation at maximum cyclic load
θ_{lim}	[deg./rad.]	Maximum tolerated pile rotation
θ_0	[deg./rad.]	Pile rotation at initial maximum cyclic load
θ_S	[deg./rad.]	Rotation that would occur in a static test when the applied load is equal to the maximum cyclic load
θ_R	[deg./rad.]	Pile rotation at ultimate capacity
$\Delta\theta$	[deg./rad.]	Pile accumulated rotation
μ	$[FL^{-2}T]$	Viscosity
σ	$[FL^{-2}]$	Stress (plasticity theory)
σ_{max}	$[FL^{-2}]$	Maximum cyclic stress (HARM)
σ_v	$[FL^{-2}]$	Vertical effective stress
υ	$[L]$	Pile displacement at ground level
υ_R	$[L]$	Pile displacement at ground level at ultimate capacity
ϕ'	[deg./rad.]	Peak angle of friction of shearing resistance
ϕ_{cr}	[deg./rad.]	Critical angle of friction of shearing resistance
$\chi, \overline{\chi}, \chi_r,$ $\overline{\chi}_r, \chi_h, \overline{\chi}_h$	$[FL^{-2}]$	Generalised stresses (hyperplasticity theory)
ψ'	[deg./rad.]	Peak angle of dilation

Latin alphabet

A	(1)	[-]	Empirical dimensionless coefficient (p-y method)
	(2)	$[FL \cdot rad/FL^2]$	Hysteresis loop area (experimental results, 1-way loading)
A_{hys}		$[FL \cdot rad]$	Hysteresis loop area
A_{el}		$[FL \cdot rad]$	Area corresponding to elastic energy stored in system
C		[NA]	Generic empirical constant
C_1, C_2, C_3		[-]	Empirical factors (p-y method)
D		$[L]$	Pile diameter
D_a		[-]	Damping ratio
D_{1a}		[-]	Measure of damping for 1-way loading tests
E		$[FL^{-2}]$	Elastic modulus (hyperplasticity theory)
E_pI_p		$[FL^2]$	Bending Stiffness
E_S		$[FL^{-2}]$	Soil modulus (dimensional analysis)
E_{S0}		$[FL \cdot rad^{-1}]$	Initial modulus (experimental results, moment-rotation curve)
E_{SL}		$[FL^{-2}]$	Soil modulus at pile tip (dimensional analysis)
E_t		$[FL^{-2}]$	Tangent modulus (hyperplasticity theory)
E_{t0}		$[FL \cdot rad^{-1}]$	Tangent modulus to monotonic curve (experimental results, moment-rotation curve)
G_0		$[FL^{-2}]$	Shear modulus at small strain
H	(1)	$[F]$	Lateral force load on top of the pile
	(2)	$[FL^{-2}]$	Kinematic hardening modulus (conventional plasticity and hyperplasticity theories)
K_p		[-]	Rankine's passive earth pressure
K_R		[-]	Pile relative stiffness (Poulos and Hull, 1989)
K_S		$[FL \cdot rad^{-1}]$	Absolute stiffness
L		$[L]$	Pile embedded depth
M		$[FL]$	Moment load at mud-line
M_R		$[FL]$	Static moment capacity
M_{ult}		$[FL]$	Theoretical lateral pile resistance
M_{y0}		$[FL]$	Initial elastic threshold (experimental results)
N		[-]	Number of cycles
N_{py}		[-]	Number of elements down the pile (p-y method)
N_S		[-]	Number of surfaces (hyperplasticity model)
Q		[-]	Base shear (p-y method)
R	(1)	$[FL^{-2}]$	Isotropic hardening parameter (conventional plasticity theory)
	(2)	[-]	Ratcheting parameter (HARM)
R_0		[-]	Initial ratcheting rate (HARM)
R_d		[%]	Relative density
R_{fac}		[-]	Acceleration factor (HARM)

R_m		$[FL^2]$	Discretised bending stiffness (p-y method)
T_b, T_c		[-]	Dimensionless empirical functions (experimental results, accumulated rotation)
V		$[F]$	Axial force load on top of the pile
X		$[FL^{-2}]$	Kinematic hardening parameter (conventional plasticity theory)
c, c_1, c_2		[-]	Dimensionless constants
c_r		$[T^{-1}]$	Constraint defining ratcheting strain (HARM)
c_h		$[T^{-1}]$	Constraint defining accumulation of ratcheting strain (HARM)
d	(1)	$[L]$	Pile pivot point depth (experimental results)
	(2)	$[FL^{-2}T^{-1}]$	Dissipation potential (hyperplasticity theory)
d_{50}		$[L]$	Mean particle size
f	(1)	$[FL^{-2}]$	Yield surface (conventional plasticity theory)
	(2)	$[FL^{-2}]$	Specific Helmholtz free energy (hyperplasticity theory)
f_r		$[T^{-1}]$	Loading frequency
g		$[FL^{-2}]$	Specific Gibbs free energy
h	(1)	$[L]$	Pile element length (p-y method)
	(2)	$[FL^{-2}]$	Isotropic hardening modulus (conventional plasticity theory)
h_e		$[L]$	Load eccentricity
k	(1)	$[FL \cdot rad^{-1}]$	Secant stiffness (experimental results)
	(2)	$[FL^{-2}]$	Kinematic hardening surface strengths (hyperplasticity theory)
k_0		$[FL \cdot rad^{-1}]$	Initial secant stiffness
k_b, k_c		$[FL \cdot rad^{-1}]$	Empirical functions (experimental results, secant stiffness)
k_{U0}, k_{L0}		$[FL^{-2}]$	Upper and Lower limit stress (HARM)
k_y		$[FL^{-3}]$	Initial modulus of subgrade reaction (p-y method)
l_1, l_2, l_a		$[L]$	Set-up length (loading rig)
$m_1, m_2,\ m_3$		$[M]$	Rotating and suspended masses (loading rig)
m_α, m_θ, m_A		[-]	Empirical exponents (experimental results)
m_h		[-]	Monotonic exponent defining shape of loading curve (HARM+)
m_k		[-]	Exponent defining rate at which the hysteresis loop closes with hardening parameter (HARM+)
m_p		[-]	Empirical exponent (p-y method)
m_s		[-]	Exponent defining dependence of rate of ratcheting on stress (HARM+)
m_r		[-]	Exponent defining dependence of rate of ratcheting on hardening parameter (HARM+)

p	(1)	$[FL^{-1}]$	Soil reaction distributed load
	(2)	[-]	Accumulation of plastic strain (conventional plasticity theory)
p_a		$[FL^{-2}]$	Atmospheric pressure
p_u		$[FL^{-1}]$	Ultimate soil resistance
t	(1)	$[L]$	Pile wall thickness (experimental equipment)
	(2)	$[T]$	Time (hyperplasticity theory)
w		$[FL^{-2}T^{-1}]$	Flow potential (hyperplasticity theory)
x		$[L]$	Depth down the pile
y		$[L]$	Pile displacement (p-y method)
$\overline{y}$		[-]	Canonical yield surface (hyperplasticity theory)
y_c		[-]	$y_u = 8y_c$ = lateral displacement required to mobilise ultimate response (p-y method)
z		$[FL^{-2}T^{-1}]$	Force potential (hyperplasticity theory)

2) Common subscripts and diacritics

X_0	Initial value of X / Value of X during initial cycle
X_1, X_2	Value of X in the principal direction 1 (respectively 2) (HARM 2-D)
X_e	Value of X at pile end
X_h	Accumulated ratcheting variables (HARM)
X_m	(1) Pile element index (p-y method)
X_m, X_{min}	(2) Value of X at minimum cyclic load (experimental results, hyperplasticity model)
X_N	Value of X at cycle N
X_n	Surface index (hyperplasticity model)
X_p, X_{max}	Value of X at peak load (experimental results, hyperplasticity model)
X_R	Reference value of X, related to ultimate capacity
X_r	(1) Reference value of X
	(2) Variables and functions describing ratcheting (HARM)
X_t	Value of X at pile top
$\tilde{X}$	Normalised parameter X
$\dot{X}$	Rate of X with time
$\hat{X}$	Function of the internal variable η, $\hat{X} \equiv X(\eta)$

3) Functions

$S(.)$	Modified/Generalised signum function:	$\begin{cases} S(x) = 1, & x > 0 \\ S(x) = -1, & x < 0 \\ S(x) \in [-1, 1], & x = 0 \end{cases}$
$< . >$	Macaulay brackets:	$\begin{cases} < x >= 0, & x < 0 \\ < x >= x, & x \geq 0 \end{cases}$

4) Abbreviations

Test name acronyms (Table 2.6, p. 65)

M	**Monotonic (loading)**
MCr	Monotonic Creep
MCo	Monotonic Continuous
MD	Monotonic, Diameter (effect)
MRH	Monotonic RH110
MLB	Monotonic LBDA30
H	**Hysteresis (testing)**
HIM	Hysteresis, Increasing Magnitude
HC	Hysteresis, Cyclic
HA	Hysteresis, Alternated (1-way/2-way)
H1IM	Hysteresis, 1-way (loading), Increasing Magnitude
C	**Continuous (cyclic loading)**
CMC	Continuous cyclic-Monotonic, Cycle (number effect)
CMLT	Continuous cyclic-Monotonic, Long-Term ($\geq 100,000$ cycles)
CMM	Continuous cyclic-Monotonic, (load) Magnitude (effect)
CMA	Continuous cyclic-Monotonic, (load) Amplitude (effect)
CC	Continuous Cyclic
CCLB	Continuous Cyclic Leighton Buzzard (DA30)
MA	**Multi-Amplitude (cyclic loading)**
MALL	Multi-Amplitude, Large Load (series)
MASL	Multi-Amplitude, Small Load (series alternated with large load series)

Other common acronyms

OWF	Offshore Wind Farm
ULS	Ultimate Limit State
ALS	Accidental Limit State
SLS	Serviceability Limit State
FLS	Fatigue Limit State
LVDT	Linear Variable Displacement Transducer
LBDA30	Leighton Buzzard DA30
RH110	Red Hill 110
YLB	Yellow Leighton Buzzard
DSM	Degradation Stiffness Model
HARM	Houlsby Abadie Ratcheting Model (Fundamental model)
HARM+	Tuned HARM capturing ratcheting behaviour aspects

Chapter 1

Overview, Motivation and Background

1.1 Introduction

Reducing greenhouse gas emissions and reliance on fossil fuels is of primary concern for governments and industries worldwide. This has recently been reaffirmed in a historic international conference, attended by delegates from 195 countries, that aimed to discuss and adopt the first-ever universal agreement on climate change (COP 21, 2015, *Paris climate agreement*). The European Union initiated its energy transition plan in 2010, with a binding agreement of producing 20% of its total energy needs from renewable energy sources by 2020 (European Commission, 2010). This involves significant subsidy support schemes, industrial projects and research campaigns.

In the current renewable energy mix, wind power has developed rapidly and is now vital for reaching the 2020 European low-carbon target (Figure 1.1). This includes both onshore and offshore wind energy sources. Even though onshore wind presently contributes slightly more than offshore wind in the total production share (e.g. electricity generation of 4.85 TWh against 3.57 TWh in the UK for the second quarter 2015; DECC, 2015), offshore wind has an immense potential and the number of projects constructed and planned across the North Sea, Baltic Sea, Atlantic Ocean

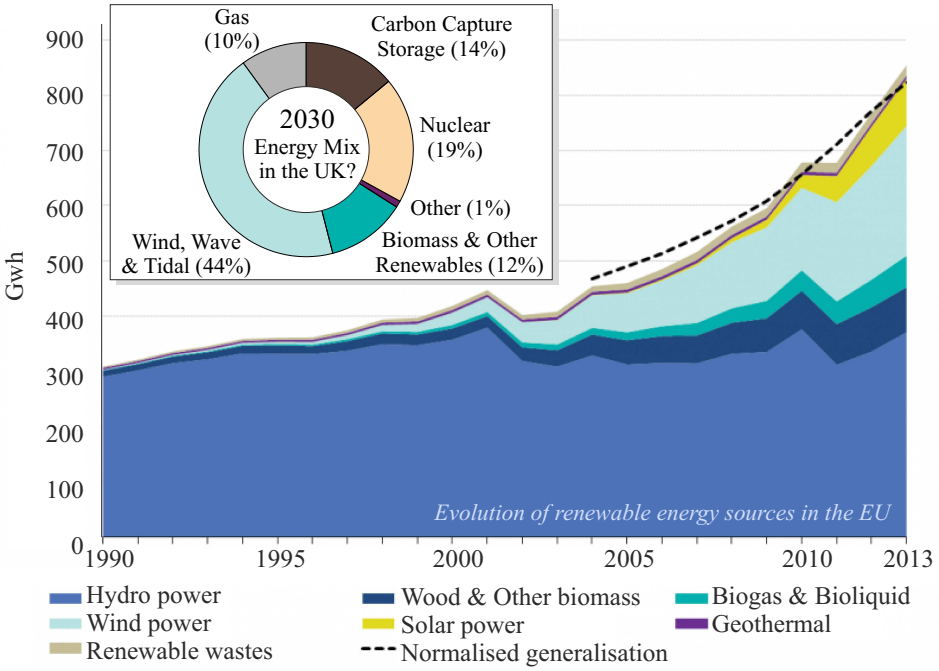

Figure 1.1: Importance of wind power in the European low-carbon transition plan *Stacked area chart*: Evolution of the gross electricity generation from renewable sources in European Union from 1990 to 2013 (from Eurostat, 2015); *Pie diagram*: Possible 2030 low-carbon energy mix target in the UK (from RenewableUK, 2014)

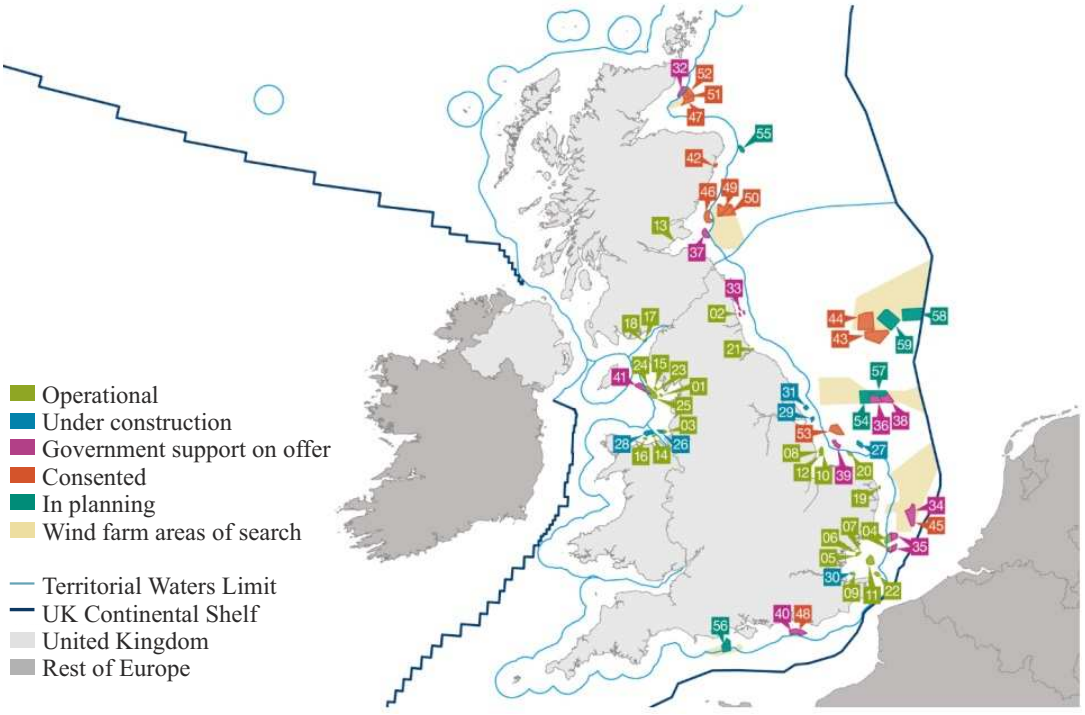

Figure 1.2: Location of UK's offshore wind resource as of May 2015 (from The Crown Estate, 2014)

and Mediterranean Sea has recently multiplied. Since 2012, the grid connected capacity of the European waters has more than doubled from 5 GW to 10.4 GW (EWEA, 2013, 2015*a*), targeting 40 GW by 2020. As an illustration, the map from Figure 1.2 highlights the scale of the design challenges in the United Kingdom and the number of new wind farm projects planned across the country.

Even though offshore wind infrastructure and turbine technology have improved significantly in a very short time, the construction and maintenance costs can still be prohibitive. In the UK, the estimated cost of offshore wind projects started in 2013 was £120/MWh, which compares with £80/MWh for Combined-Cycle Gas Turbines (CCGT), £90/MWh for nuclear energy and £101/MWh for onshore wind (DECC, 2013). Consequently, the place of offshore wind within the energy mix and its future beyond 2020 relies upon reducing its cost.

This implies firstly, that significant technology changes need to be developed in order to optimise the designs. Also, wind farms have to move further offshore, where stronger and steadier winds are available (e.g. locations of the "areas of search" on Figure 1.2). So far, wind turbines have been anchored at depths of 10 to 40 meters and up to 110 km from shore but research and development projects are currently studying substructure designs adapted for water depth greater than 50 m. Moving to deeper waters also comes with the aim of operating much larger turbines. This enables the design, build and installation of smaller numbers of support structures per wind farm for the same power output, leading to substantial economies. In 2011, the average turbine power was 3.6 MW. This has progressed to an average of 4.2 MW (EWEA, 2015*a*) with full-scale grid-connected turbines of 6 MW being presently installed (e.g. Schroeder *et al.*, 2015) and projects of 10 MW turbines being considered (e.g. SWAY project, EWEA, 2013).

Reducing offshore wind farm costs while targeting installations of larger turbines in deeper water is therefore the primary challenge of the wind industry. One of the steps to reach this goal is to develop and optimise the designs of the support structure

and foundation (The Crown Estate, 2012). The foundation accounts for 35% of the total installed cost of a wind turbine (Byrne and Houlsby, 2003; Bhattacharya and Adhikari, 2011) and prohibitive costs to anchor a structure at a particular site can make a project infeasible. The major developers of the offshore wind sector are therefore investing in significant technology development in order to provide adapted and optimised substructure designs.

A range of foundation types are currently considered for anchoring wind turbines (Figure 1.3(a)). The choice of foundation depends mostly on soil conditions, turbine size and water depth (e.g. Figure 1.3(b)). The final design must also be suited for a large range of site conditions as any turbine array is spread across a large area, with turbines usually installed more than 500 m apart (Byrne, 2011). The simplest foundation type is a single large diameter pile driven 20 to 35 m into the soil, called a monopile. This foundation is adapted for a wide range of site conditions and is presently used in water depths up to 35 m. In January 2015, the monopile represented 78.8% of the foundations installed in Europe (EWEA, 2015*b*). The gravity base foundation (GBF) is an alternative to the monopile for near-shore shallow water. It consists of a concrete, flat-base structure that is anchored using ballast and is presently used in 10.4% of the European commercial projects (EWEA, 2015*b*). Wind farms in deeper waters are also supported using multi-footing substructures such as jackets (4.7%), tripods (4.1%) or tripiles (1.9%) (Figure 1.3(a)). These offer improved resistance to overturning and can therefore support larger turbines (Figure 1.3(b)). When moving further offshore ($>$ 60m), buoyant structures are seen as a cost-effective substitute to bottom-fixed foundations. However, the development of this group of technologies is still at a very early stage and to date, only two full-scale grid-connected floating prototypes have been built in Norway (Hywind) and Portugal (WindFloat). Finally, suction caissons are considered as a possible alternative to piled foundations (either monopiles or multi-footing; e.g. Byrne and Houlsby, 2003; Tjelta, 2014). When mature, it is believed that this technology will offer a relatively

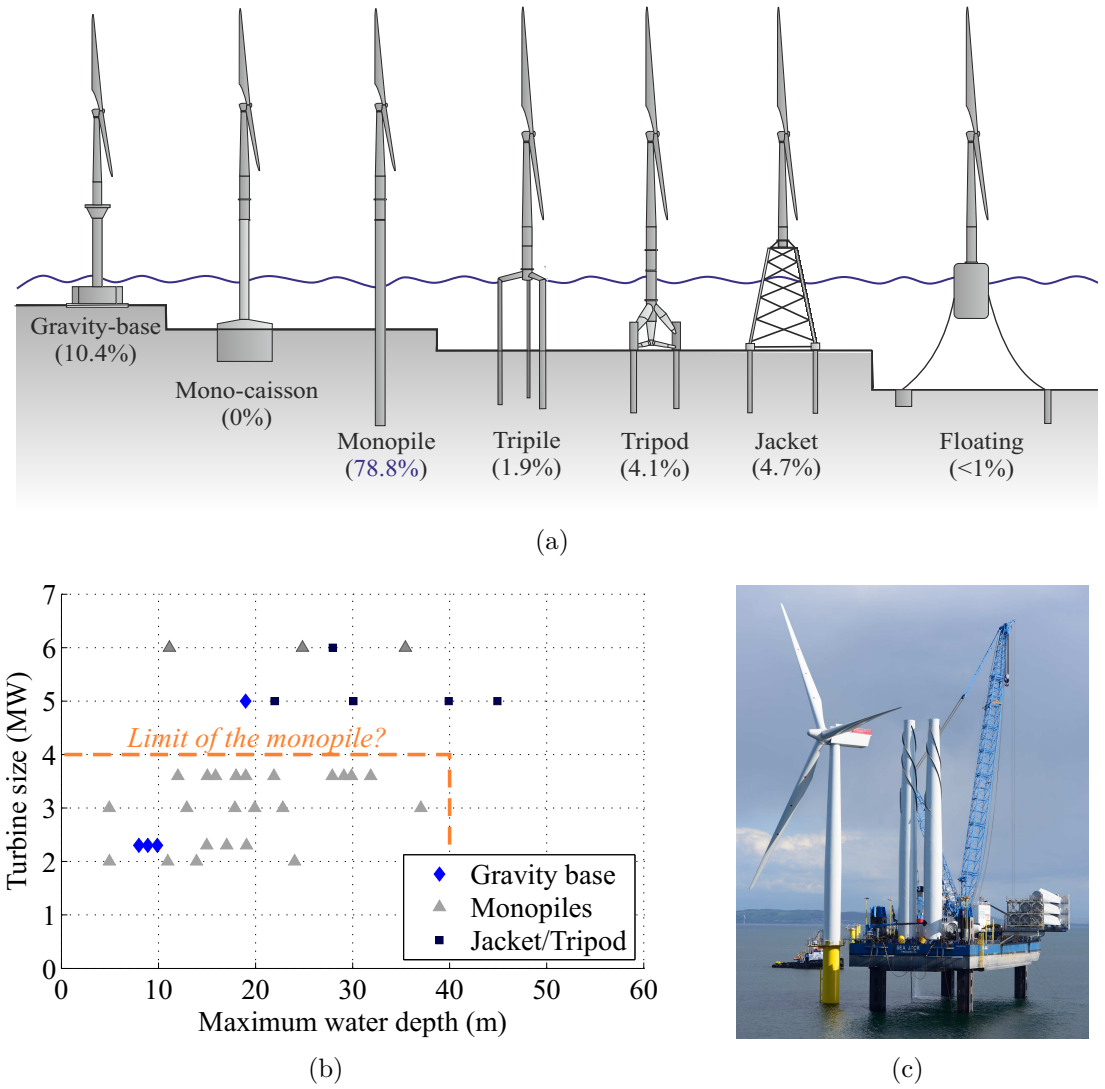

Figure 1.3: (a) Range of substructure concepts presently in use or considered for offshore wind turbines. Shares in European commercial projects as of January 2015 after EWEA (2015*b*) (b) Offshore wind turbine foundation types with regards to water depth and turbine size used in commercial projects in the North Sea as of April 2014 (Muir Wood, 2014) (c) Gwynt y Môr offshore wind farm (credit: www.siemens.co.uk)

light structure that is adapted to a wide range of soil conditions, does not require expensive or noisy driving force and provides a greater resistance to lateral loads.

Despite the continuous increase of turbine capacities, the monopile is, and is likely to remain, the dominant foundation for the future. This is mainly because it is a simple, cost-effective and robust design that is well suited to many current and future European projects (e.g. soil conditions, water depth of 30-40 m). In addition, the knowledge and track record in drivability and mechanical behaviour

gives great confidence in this foundation, and its supply chain is very well developed (e.g. Kallehave *et al.*, 2015a). In comparison, multi-piled foundations need to be specifically adapted to local water depth and ground conditions and include a number of welded joints that make the support-structure more expensive and complicated to design, mass-produce, transport and install and also reduce its service life. Radical change in offshore design is rare and transition to new approaches such as caissons or floating structures will take years before becoming fully mature. Consequently, there is a great interest in further understanding and optimising the design of monopiles in order to (i) reduce their weight and the amount of steel used, (ii) allows them to be used further offshore to replace jackets and (iii) extend their service life.

This introductory chapter presents the relevant considerations and prevailing techniques for the design of offshore wind turbine monopiles under lateral loading. The perceived problematic areas of the methodologies are then discussed before presenting an overview of the recent research efforts to improve current practice. Finally, the latest sections detail the objectives and outline of this thesis.

As suggested by the thesis title, the following chapters will be focused on lateral loading of piles in sands, and more specifically on cyclic loading, i.e. repeated loads of small amplitude (defined as a small fraction of pile ultimate capacity) and low frequencies ($< 1Hz$). The literature review presented in this chapter will therefore be oriented in this direction and the relevance of this scope of work will be justified in later sections, when presenting general loading and soil conditions (Sections 1.2.1, p. 7 and 1.2.2, p. 9).

1.2 Design considerations for offshore wind turbine monopile foundations

1.2.1 Design loads

Offshore wind turbine structures are subjected to operational and environmental loads. Operational loads arise from the rotor while environmental loads refer to the action of the winds, waves, currents and in some cases, ice. These loads are responsible for large lateral loads acting on the turbine foundation that can represent up to 60% of the net vertical load (Figure 1.4; Byrne and Houlsby, 2015). In this thesis, the focus is exclusively on the design to lateral loads, which mostly result from winds and waves forces (80 to 90% contribution; Peralta, 2010).

The wind loads applied on the turbine and tower include (i) steady aerodynamic forces generated by the mean wind speed and (ii) stochastic aerodynamic forces due to turbulent wind structures (e.g. gusts). The latter are the most difficult to predict. The hydrodynamic forces from the waves consist of drag, inertia and cross-flow forces and depend on the water depth, wave height and period. An example of relevant environmental parameters for the calculation of loads in the North Sea is given in Table 1.1. The calculation of the aerodynamic and hydrodynamic forces on the structure is normally performed using specialised design packages, such as Bladed, HAWC, FAST or FLEX5. The description of the models behind the calculations though, falls beyond the scope of this thesis.

The aerodynamic and hydrodynamic forces result in a combined shear force and over turning moment at foundation level. Wind and wave loading are acting at different heights above ground level, resulting in different contributions to horizontal force and moment components. Aerodynamic forces are applied at a high level on the turbine hub and typically account for 25% of the horizontal load and 75% of the overturning moment (Byrne and Houlsby, 2003). For information, examples of

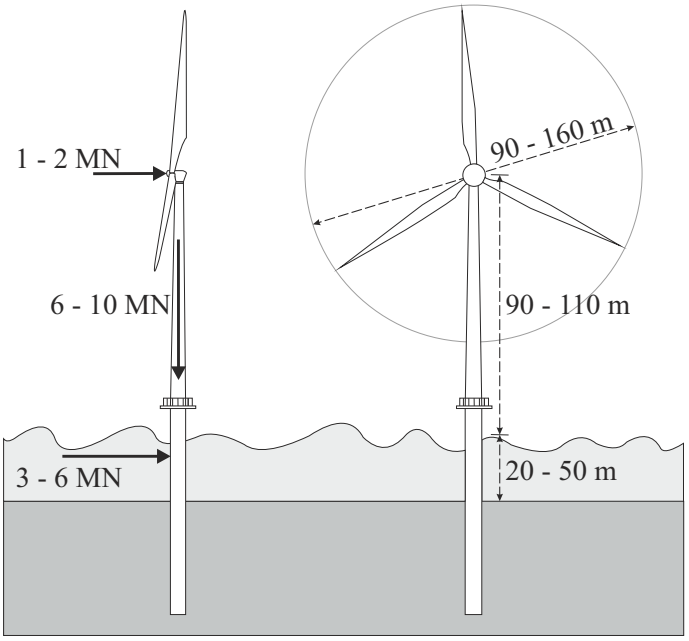

Figure 1.4: Typical dimensions and loads on a 3.5 - 5 MW offshore wind turbine in water depth from 20 to 50 m (from Byrne and Houlsby, 2015)

Table 1.1: Environmental conditions in the southern of the North Sea (after Lesny and Wiemann, 2005)

Wind:	
Hub-height 50-year extreme 10min mean wind	50.0m/s
Hub-height 50-year extreme 5s gust	60.0m/s
Water Depth:	
Mean water depth	35m
50-year extreme water depth	41m
Wave and currents:	
50-year maximum wave height Hmax	22.3m
Related wave period T	14.5s
50-year tidal current surface velocity	1.71m/s
50-year storm surge current surface velocity	0.43m/s

Table 1.2: Typical loading on a 2 MW and 5 MW wind turbine (after LeBlanc *et al.* (2010a) and Lesny and Wiemann (2005) respectively)

Load type	2 MW	5 MW
Vertical load V (MN)	5	35
Horizontal load H (MN)	4.6	16
Bending moment M (MNm)	95	562

Table 1.3: Definition of the design limit states (after LeBlanc *et al.*, 2010a)

	N	H/H_{ULS} (%)
ULS	1	100%
ALS	1	73%
SLS	10^2	47%
FLS	10^7	29%

load magnitudes on the foundation for a 2 MW and a 5 MW turbines are provided in Table 1.2. Of course, the values of the horizontal loads vary depending on the environmental conditions and the water depths (see for example Lesny and Wiemann, 2005).

Due to the nature of the wind and waves, the lateral load scenarios include cyclic loads of variable amplitudes and magnitudes. The design of the foundation must address four load conditions (API, 2010; DNV, 2014). First, the Ultimate Limit State (ULS) relates to extreme load cases, such as the worst case storm event or a turbine emergency stop. The worst expected load, or Accidental Limit State (ALS) accounts for rare accidental loads such as a ship impact on the turbine. The Serviceability Limit State (SLS) refers to repeated routine loading over the lifetime of the design that could result in excessive deformation. Finally, the Fatigue Limit State (FLS) relates to repeated loading of small amplitude over a large period of time that could possibly lead to failure. Table 1.3 summarises the values of the load amplitude in terms of percentage of the ULS (H/H_{ULS}) as well as the relevant number of cycles N for each limit state.

1.2.2 Soil response

Offshore wind turbines are installed in a wide range of soil conditions, ranging from dense sands to stiff clays to rock to layered soils. An example of typical marine strata in the North Sea and Baltic Sea is provided in Figure 1.5. This thesis focuses on the response of piles in cohesionless soils, such as encountered in the North Sea.

The response of cohesionless soil to the range of stress amplitude and loading frequencies during operation (SLS and FLS, frequency range below $1Hz$, see later Figure 1.7) is sufficiently low so that no pore-pressure is expected to develop within the soil (Peralta, 2010) and dynamic and inertia effects are negligible (Table 1.4). Under rare extreme events, wave or impulse loads can develop rapidly and induce rate-dependent effects and partial drainage of the soil. In this thesis though, the loading

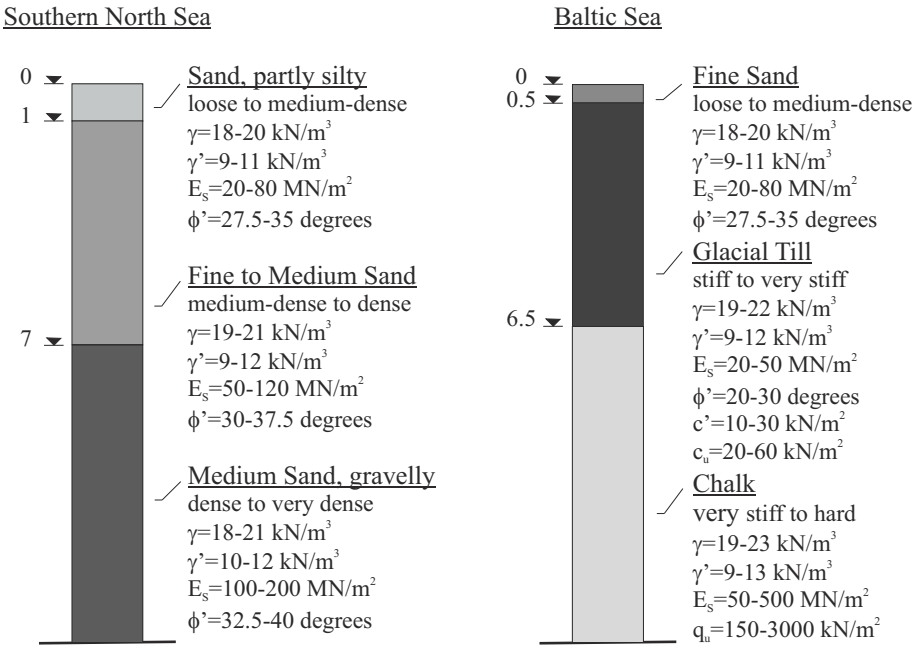

Figure 1.5: Typical marine strata in the southern of the North Sea and Baltic Sea (from Lesny and Wiemann, 2005)

Table 1.4: Approximate classification of repeated loading of soils (classification by Gotschol (2002), reported by Peralta (2010))

Repeated loading of soils:	Cyclic	Cyclic-Dynamic	Dynamic
Frequency	0 to 1 Hz	1 to 10 Hz	>10Hz
Inertia	Negligible	Relevant	Relevant

regime is limited to quasi-static cyclic loads that relate to operational conditions.

The determination of the pile reaction below the ground is a difficult task for the geotechnical engineer. The normal and shear stress components oppose the pile movement and follow the distribution displayed at the top of Figure 1.6(a) (Smith, 1987). In a number of analytical methods, this distribution is simplified to a single uniform frontal soil reaction p spread across the projected width of the pile (bottom part of Figure 1.6(a)). For 1-dimensional models, such as the p-y method (c.f. Section 1.3, p. 14), where the width of the pile is not considered, the soil reaction is then simplified further to the average value of the frontal soil reaction.

The estimation of the soil reaction distribution with depth is a key element of the foundation design process. At ultimate limit state, a first approximation can be

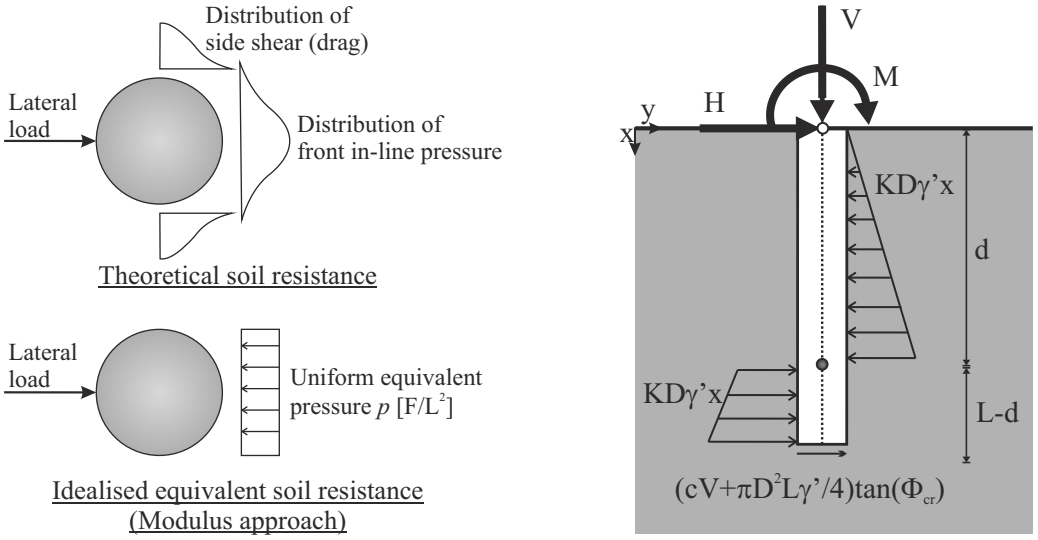

Figure 1.6: (a) Theoretical (top) and simplified equivalent (bottom) distribution of passive net pressure distribution in a cross section of the soil after lateral loading of the pile (after Smith, 1987); (b) Idealised horizontal stress distribution in ultimate limit state for laterally loaded stiff pile in sand (e.g. Broms, 1964)

obtained using the idealised stress distribution displayed in Figure 1.6(b). The soil reaction is divided into a large passive normal stress below the pivot point, a small above and a shear resistance at the bottom of the pile. The net distributed load along the pile is a linear function of the depth, which depends on the pile diameter D, the effective unit weight γ' and the angle of friction ϕ' through the empirical factor K. In a very simplified analysis, K can typically be taken as three times the passive earth pressure coefficient $K = 3K_p$ with $K_p = tan^2\left(\frac{\pi}{4} + \frac{\phi'}{2}\right) = \frac{1 + sin\phi'}{1 - sin\phi'}$ (Broms, 1964). The pile toe will theoretically shear at the critical angle of friction ϕ_{cr}, so that the resulting shearing force is a combination of the shear resistance at the bottom of the pile and a contribution of the vertical effective force cV, where c is a dimensionless constant between 0 and 1. Finally, the pile embedded length is noted L and the pivot point depth d.

The static resistance of a monopile is equal to the horizontal stress distribution along the pile when reaching the ultimate lateral limit state. According to the above,

the equilibrium equations for the horizontal H and moment M loads at ULS are:

$$M = (cV + \frac{\pi}{4}D^2L\gamma')L \cdot sin(\phi_{cr}) + \frac{1}{3}(L^3 - \frac{2d^3}{3})KD\gamma' \tag{1.1}$$

$$H = (cV + \frac{\pi}{4}D^2L\gamma')sin(\phi_{cr}) + (d^2 - \frac{L^2}{2})KD\gamma' \tag{1.2}$$

These two Equations will be referred to later in Chapter 2.

1.2.3 Structural response and design requirements

The technical lifetime of an offshore wind turbine is nominally 20 to 25 years (EWEA, 2009) after which, an overhaul project is usually conducted to extend the lifetime of the wind farm. Consequently, the long-term loading is one of the key design drivers. The structural integrity and fatigue lifetime of an offshore wind turbine strongly depends on its fundamental mode of vibration f_0, also called the first tower bending mode, and how this is excited by environmental and operational loads. The operational excitation of a 3-bladed wind turbine consists of the rotational frequency of the rotor f_{1P} and the blade passing frequency as the blades pass the tower f_{3P} (see Figure 1.7). Offshore wind turbines are commonly designed so that the 1^{st} natural frequency is within the soft-stiff region, that is to say between the f_{1P} and f_{3P} excitation domains. The reasons for such design is that the soft-soft region is close to wave and wind loading frequencies (see Figure 1.7) while designs in the stiff-stiff domain are cost prohibitive. As a result, the estimation of the natural frequency, and its evolution over time, is critical for the structural engineer. A faulty assessment could indeed lead to an early decommission of the turbine, while a more accurate determination might extend the lifetime of the structure.

The fundamental mode of vibration of the structure highly depends on the soil stiffness. Consequently, assessment of the soil stiffness is high priority for the geotechnical engineer, in addition to capacity.

The dynamic response, and in particular, the amplitude of the structural vibrations

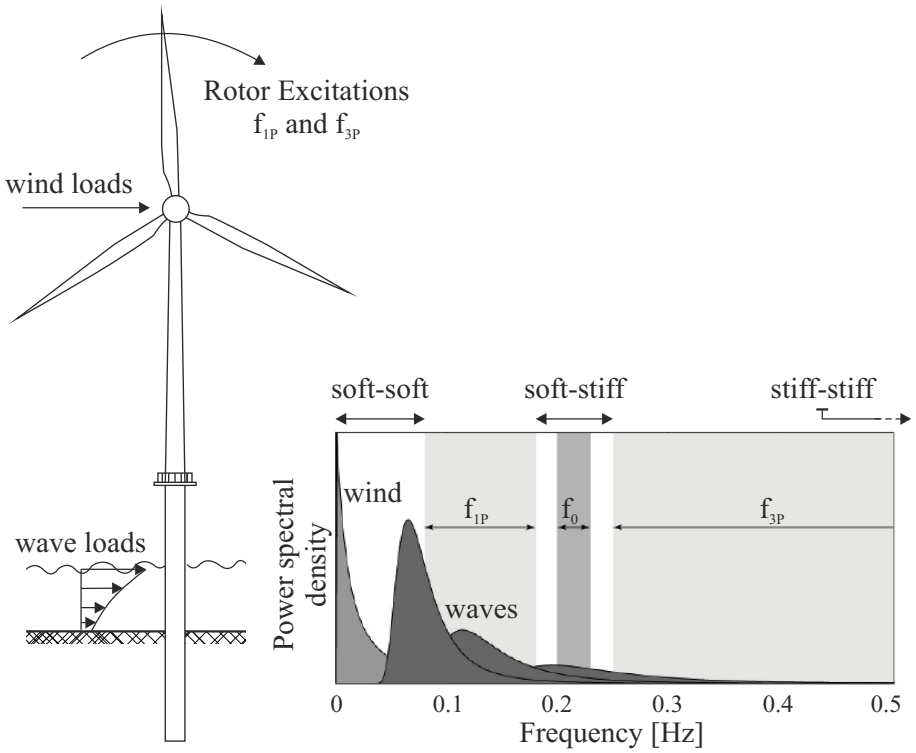

Figure 1.7: Typical loads and excitation ranges of a modern offshore wind turbine for a range of different wind speeds; not to scale (from Kallehave *et al.*, 2015a)

are then governed by the damping of the structure. The overall damping of an offshore wind turbine structure is a combination of aerodynamic damping, hydrodynamic damping, structural damping, tower oscillation dampers and soil damping (e.g. Germanischer Lloyd, 2005; Tarp-Johansen *et al.*, 2009; Devriendt *et al.*, 2013; Cook and Vandiver, 1982). The highest damping contribution arises from soil damping (Germanischer Lloyd, 2005) but is unfortunately difficult to estimate. Soil damping can be divided in three types: (i) radiation damping is generated by the propagation of elastic waves within the soil mass when loading at high frequency ($f > 1Hz$), (ii) material damping is derived from the hysteretic response of the soil and corresponds to dissipation of energy by the soil when being loaded and squashed by the pile and (iii) pore-pressure dissipation occurs only when the pile is installed in very permeable sand and gravels (Cook and Vandiver, 1982; LeBlanc Thilsted and Tarp-Johansen, 2011). According to Cook and Vandiver (1982) and Tarp-Johansen *et al.* (2009), non-linear hysteretic damping is the dominant damping phenomenon that needs to

be addressed in design.

Finally, serviceability and fatigue design must also ensure limited displacement of the infrastructure over time. The maximum tilt rotation of the support structure is generally specified by the turbine manufacturer to guarantee good operation of the turbine (Golightly, 2014; DNV, 2014, Section 10.3.2.6, p. 173). Typically, the maximum tolerance for the foundation tilt over its lifetime (including installation tolerance) is 0.5° (e.g. Achmus *et al.*, 2009; Malhotra, 2011; Lombardi *et al.*, 2013; DNV, 2014, Section 10.3.2.6, p. 173), with a maximum requirement of 0.25° rotation induced by SLS (DONG Energy, 2013; DNV, 2014).

In conclusion, the fatigue design of the foundation is driven by:

(a) An accurate estimation of the **foundation stiffness** both during extreme events and operational conditions

(b) Determination of the foundation **hysteretic damping**

(c) Accurate prediction of the **accumulation of permanent deformations** of the foundation

1.3 Current design practice

Modelling the interaction of the pile with the ground is a key task for the geotechnical engineer. Three possible design approaches can be used and developed in order to model the monopiles response to lateral loading (Figure 1.8):

(1) Complete 3-D Finite Element analysis allows the entire soil continuum to be modelled and can predict the detailed and realistic response of the foundation, providing an appropriate constitutive model and input soil parameters are used. When this is the case, it is then the most accurate numerical modelling method, and probably the most appropriate when it comes to modelling complex soil stratigraphies and foundation geometries. However, it is not currently possible to model the response of piles to cyclic loading in a rigorous and sensible manner

using this method, as no robust constitutive model is yet capable of modelling cyclic loading accurately for this purpose. Also, if such a model existed, difficulties would arise regarding the computation time as a cycle by cycle method would probably become prohibitive for use in long-term cyclic loading analysis. Finally, with the technology currently available, it would be unrealistic performing the design of all the monopiles across a wind farm site using 3-D FE analysis and therefore, a more simplistic method is required.

(2) The Winkler-type approach is a 1-D model where the pile acts as a beam and the soil-pile interaction response is represented by a series of independent springs down the pile length. Soil layers can be considered but, the model cannot capture the interaction between the strata. It is computationally fast and is therefore a satisfactory compromise between accuracy and time.

(3) Finally, the simplest technique consists of a surface spring model where the entire behaviour of the foundation is reduced to representative springs at the soil

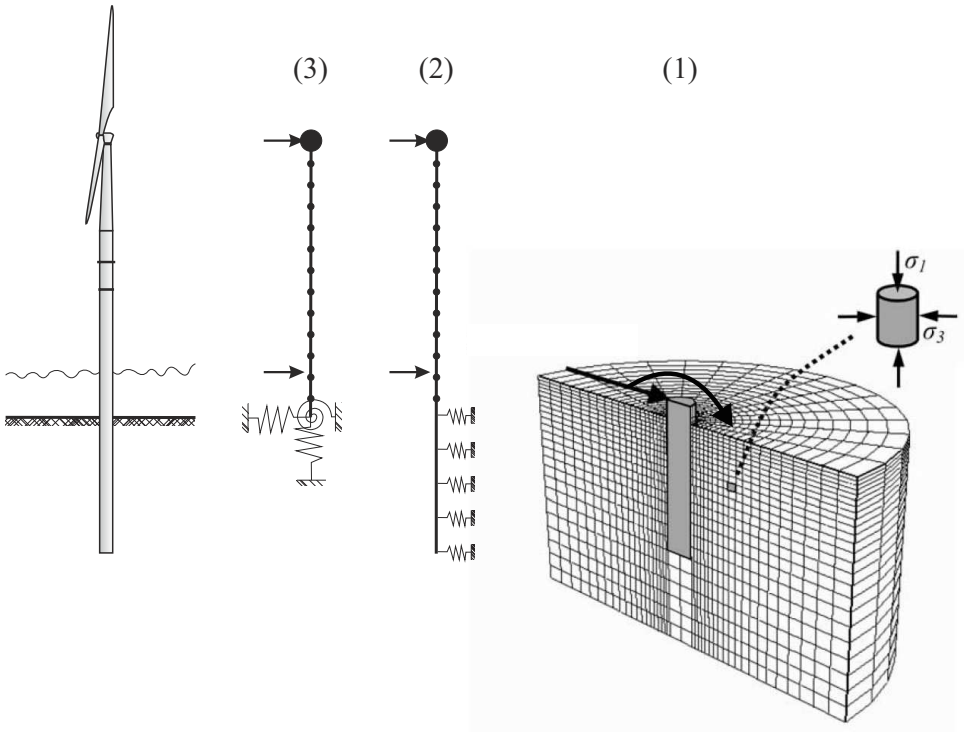

Figure 1.8: Schematic representation of the possible pile design methodologies (3D-FE mesh from Achmus *et al.*, 2009)

surface, also called a macro-element model. This type of model is very simplistic and is consequently the least accurate. It is also very difficult to calibrate when considering layered soil profiles. However, it is computationally fast and efficient in modelling the foundation within structural analysis packages.

In current practice, the design of offshore piles to resist lateral loading is addressed using the nonlinear Winkler modelling approach (Winkler, 1867), commonly known as the *p-y* method (e.g. DNV, 2014; DONG Energy, 2013; Kallehave *et al.*, 2012). This framework was originally derived from large-scale field tests on long flexible piles relevant to the oil and gas industry for the design of pile-supported platforms. The accuracy of the methodology relies on the correct definition of the local soil reaction at each point down the pile, i.e., the governing law of each uncoupled spring. This is generally described by a non-linear law $p(x, y)$ that empirically embodies the properties of the soil and pile geometry. $p(x, y)$ depends on both the depth x and the pile displacement y and is determined based on field test data. For piles in sand, the tests were performed by Cox *et al.* (1974) on a long flexible pile of 0.61 m diameter and 21 m length. The methodology was described by Reese *et al.* (1974), refined by O'Neill and Murchison (1983) and adopted in design practices to address ultimate capacity of long flexible piles (e.g. API, 2010).

In 2004, these design methodologies were extrapolated to monopiles for applications in offshore wind (DNV, 2004, first edition) and are the recommended design practice since (e.g. DNV, 2014). This section details the design procedure as described in Reese *et al.* (1974) and Reese and Van-Impe (2011) and the limitations when applied to offshore wind monopiles. As the focus of this thesis is on cohesionless soils, the following section only presents the methodologies for piles in sand, though, similar approaches also exist for clay.

1.3.1 Principles (following Reese and Van-Impe, 2011)

The pile is generally modelled using an Euler-Bernoulli beam on elastic foundations subjected to horizontal H and moment M loading on top and to a compressive force V acting at the center of gravity of the end cross-section of the pile as shown in Figure 1.9. In most cases though, the action of V is negligible (Reese and Van-Impe, 2011). In the following analysis, the pile length axis is noted x and the axis of loading direction y (see Figure 1.9).

Considering the equilibrium of an infinitely small unloaded beam element of length dx, located at a depth x, the equilibrium of forces and moments at element base gives:

$$\begin{cases} T_y - (T_y + \mathrm{d}T_y) - p\mathrm{d}x = 0 \\ (M_z + \mathrm{d}M_z) - M_z + V_x dy - T_y \mathrm{d}x = 0 \end{cases} \tag{1.3}$$

And therefore:

$$\begin{cases} \dfrac{\mathrm{d}T_y}{\mathrm{d}x} + p = 0 \\ \dfrac{\mathrm{d}M_z}{\mathrm{d}x} + V_x \dfrac{\mathrm{d}y}{\mathrm{d}x} - T_y = 0 \end{cases} \tag{1.4}$$

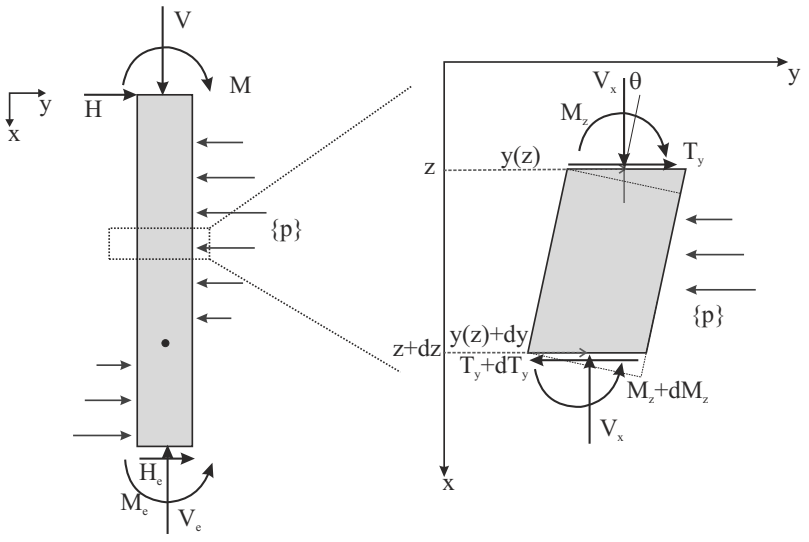

Figure 1.9: Schematic representation of the forces acting on a pile element

The Euler-Bernoulli beam assumption enforces that perpendicular sections remain perpendicular to the beam deformed main fibre, and therefore:

$$\frac{\mathrm{d}^2 M_z}{\mathrm{d}x^2} = E_p I_p \frac{\mathrm{d}^4 y}{\mathrm{d}x^4} \tag{1.5}$$

where $E_p I_p$ is the bending stiffness of the pile. Now, p is expressed according to:

$$p = E_{py} \cdot y \tag{1.6}$$

where E_{py} is the modulus of soil reaction. It depends on the depth and the pile deflection and its expression will be discussed in more detail in Section 1.3.4 (p. 21). Assuming that V is constant with depth and eliminating T_y from the system of Equations 1.4, it can then be shown that:

$$E_p I_p \frac{\mathrm{d}^4 y}{\mathrm{d}x^4} + V \frac{\mathrm{d}^2 y}{\mathrm{d}x^2} + E_{py} y = 0 \tag{1.7}$$

Solving Equation 1.7 gives the pile deflection y as a function of depth x and leads to the expression of the soil reaction (Equation 1.6), the bending moment (Equation 1.5) and the shearing force (Equation 1.4) along the pile. The pile curvature angle S can also be deduced from the pile deflection (Equation 1.8). When the pile is perfectly rigid and thus, is not bending, S is equal to the rotation of the pile, also called θ. Hence, the solution of Equation 1.7 provides an analytical expression for all the parameters used in the analysis of a laterally loaded pile.

$$S = \frac{dy}{dx} \tag{1.8}$$

1.3.2 Solution by finite difference

The analytical solution of Equation 1.7 is generally not possible because E_{py} is usually a non-linear function of y (see Figure 1.10(b) for example). Consequently, a

numerical approximation of the derivatives is required. This can be achieved using either finite difference or finite element approaches. It is common practice to use the finite difference approach (e.g. Reese and Van-Impe, 2011), which is the methodology detailed below. Of course, the results obtained using one or the other method will be the same.

The pile is divided into N_{py} elements of length h (i.e. $N_{py}+1$ nodes, see Figure 1.10(a)) and Equation 1.7 is discretised at each pile node according to Equation 1.9.

$$\begin{aligned}
&\forall m \in [0, N_{py}+1] \\
&y_{m-2}R_{m-1} \\
&+y_{m-1}(-2R_{m-1} - 2R_m + V_x h^2) \\
&+y_m(R_{m-1} + 4R_m + R_{m+1} - 2V_x + E_{pym}h^4) \\
&+y_{m+1}(-2R_m - 2R_{m+1} + V_x h^2) \\
&+y_{m+2}R_{m+1} = 0
\end{aligned} \tag{1.9}$$

In most calculation codes, N_{py} ranges from 50 to 200 (Reese and Wang, 2006). The pile bending stiffness $R_m = (E_p I_p)_m$ can vary along the pile and the modulus of soil

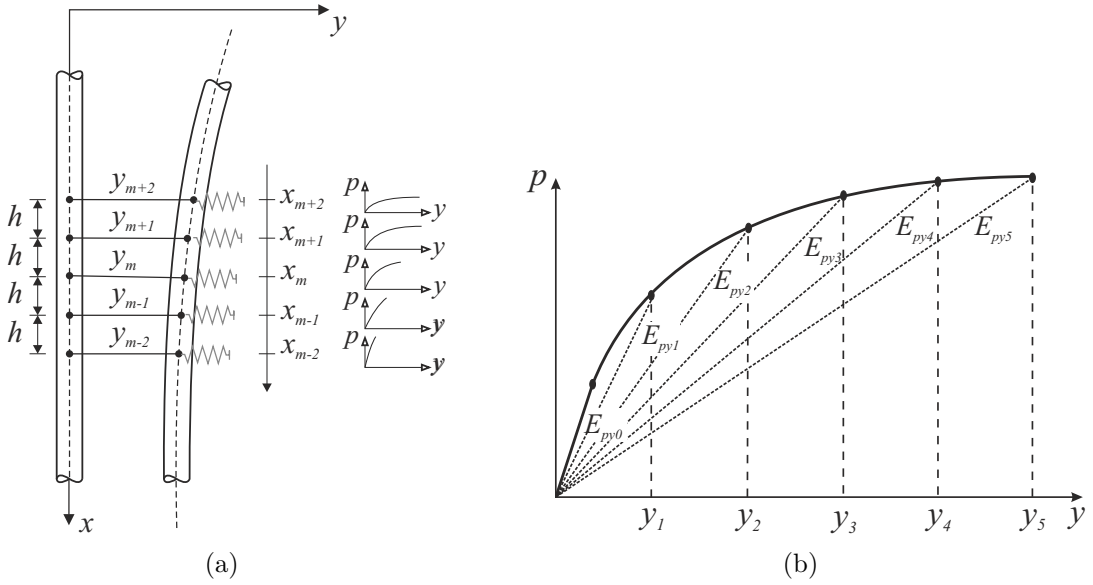

Figure 1.10: (a) Schematic of the pile finite difference discretisation (after Reese and Van-Impe, 2011); (b) Definition of the soil reaction modulus E_{py}

reaction E_{pym} can vary with both depth x and pile deflection y (Figures 1.10(a) and 1.10(b)). Accurate estimation of E_{pym} can be obtained via an iterative process using the fixed-point theorem.

1.3.3 Boundary conditions

The expression of Equation 1.9 at nodes $m = 0$ and $m = N_{py} + 1$ requires the addition of 2 fictional nodes at each pile extremity. This brings the total number of nodes to $N_{py} + 5$. The number of equations derived from Expression 1.9 is equal to $N_{py} + 1$ and therefore, 4 boundary conditions, 2 at each pile end, are required to solve the problem. A number of combinations can be considered such as: shear and rotation fixity at the pile head, moment and deflection fixity at the pile head, moment and shear fixity at the pile tip or moment and deflection fixity at the pile tip. In the case of offshore wind turbine monopiles, the most relevant is to express the moment and force at the pile head and tip. This gives:

$$\begin{aligned}
\frac{R_t}{2h^3}(y_{t-2} - 2y_{t-1} + 2y_{t+1} - y_{t+2}) + \frac{V_x}{2h}(y_{t-1} - y_{t+1}) &= H \\
\frac{R_t}{h^2}(y_{t-1} - 2y_t + y_{t+1}) &= M \\
\frac{R_e}{2h^3}(y_{e-2} - 2y_{e-1} + 2y_{e+1} - y_{e+2}) + \frac{V_x}{2h}(y_{e-1} - y_{e+1}) &= H_e \\
y_{e-1} - 2y_e + y_{e+1} &= M_e
\end{aligned} \tag{1.10}$$

where subscripts t and e refer to the pile top and tip respectively. A non-zero moment at the pile tip occurs when the pile is loaded with an eccentric axial load (i.e. when short rigid pile carry their load in end bearing), or in the case of rather large pile base area, when the soil plug is acting rigidly with the pile. In most calculations though, the moment at pile tip is taken equal to zero, regardless of the pile stiffness or diameter.

Finally, soil resistance due to shearing can develop at the pile tip, depending on the relative flexibility of the pile and soil. For flexible piles, the base is clamped in

the soil and H_e is equal to zero. For rigid piles though, the base moves and the soil below generates a resistance force opposite to its movement. In this case, H_e is likely to be a function of the pile deflection at the tip. Unfortunately, there are presently no guidelines regarding the appropriate expression for H_e (Reese and Van-Impe, 2011) and an estimate of H_e can only be derived from experimental results when available. This point will be developed in more detail later in Chapter 2, Section 2.6 (p. 78).

1.3.4 *p-y* curve expressions

It is fairly clear now that a correct design using the above method relies heavily on the choice for the expression of the soil reaction p as a function of y, or more precisely, the modulus of soil reaction E_{py} that is derived from the p-y curve (see Figure 1.10(b)). The very first expression for p-y curves for piles in sand was proposed by Reese *et al.* (1974). It was developed based on experimental results at Mustang Island on long slender piles in saturated sand (Cox *et al.*, 1974, test properties reported in Table 1.5). The formulation was a piece-wise function made of 2 linear sections, an hyperbola and a constant upper limit. The parameters involved in the expression are largely empirical and based on the results from Mustang Island (Cox *et al.*, 1974). An example of these p-y curves is given in Figure 1.11(a).

The expressions for the p-y curves have been refined by O'Neill and Murchison (1983) and adopted in the API and DNV design guidelines (API, 2010; DNV, 2014). The objective was to fit the original p-y curves while selecting a continuous function

Property	Value
Pile length (m)	21
Pile diameter (m)	0.61
Pile bending stiffness (kNm^2)	163,000
Submerged unit weight (kNm^{-3})	10.4
Relative density	0.9

Table 1.5: Mustang Island test case data (Cox *et al.*, 1974)

that would provide (i) a smooth transition between the initial slope and the ultimate limit asymptote and (ii) a continuous derivable function. Consequently, an hyperbolic function has been selected for cohesionless soils:

$$\begin{cases} p(x,y) = Ap_u \cdot tanh\left(\dfrac{k_y.x}{Ap_u}y\right) \\ A = max\left(0.9, \left(3 - 0.8\dfrac{x}{D}\right)\right) \\ p_u = \begin{cases} (C_1 x + C_2 D)\gamma' x & for\ 0 < x \leq x_R \\ C_3 D \gamma' x & for\ x > x_R \end{cases} \end{cases} \tag{1.11}$$

In this Equation k_y is the initial modulus of subgrade reaction, also called the soil spring constant, and is a function of the angle of friction ϕ' (Figure 1.12(a)). C_1, C_2 and C_3 are three empirical factors given by Figure 1.12(b). When considering cyclic loading, the value of A is fixed to 0.9, regardless of the number of cycles.

Figure 1.11(a) displays a comparison of the original p-y curves proposed by Reese *et al.* (1974) with the current DNV-API formulation (API, 2010; DNV, 2014) at relevant depth. This plot relates to the Mustang-Island test case. Figure 1.11(b) then shows the prediction of the pile head displacement obtained with the models

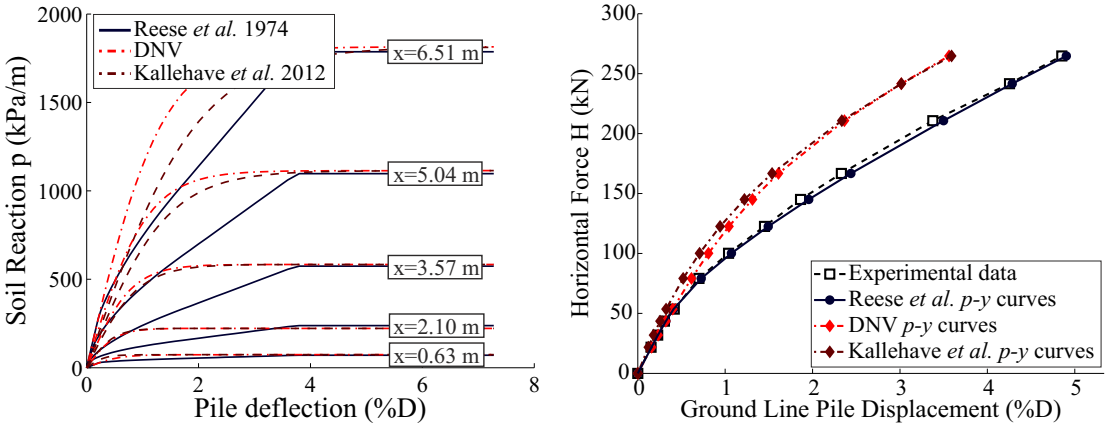

(a) (b)

Figure 1.11: (a) Reese *et al.* (1974), DNV (2014) and Kallehave *et al.* (2012) p-y curves plotted at relevant selected depth (towards the top of the pile) for the test case of Mustang Island (Cox *et al.*, 1974) (b) Mustang Island pile deflection at Mudline: numerical simulations compared with experimental results

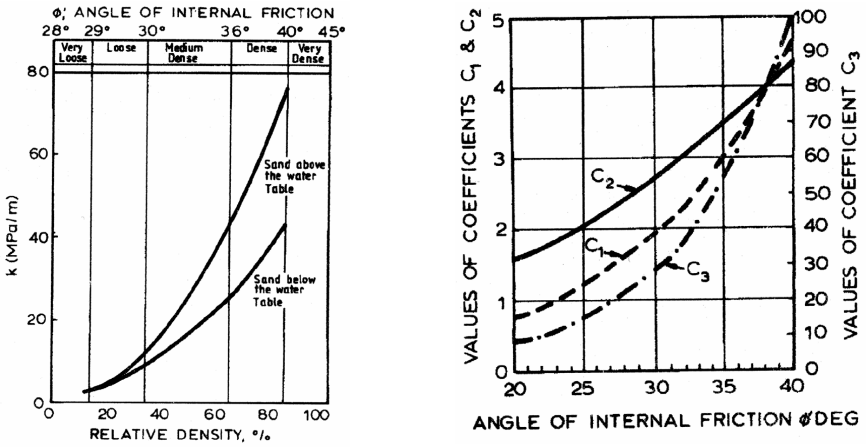

(a) (b)

Figure 1.12: (a) Modulus of subgrade reaction and (b) Empirical coefficients in DNV as a function of friction angle (Figures from DNV, 2014)

presented above and compared with results from full-scale testing. As Reese *et al.*'s *p-y* curves have been calibrated based on this particular test case, it is expected that the corresponding prediction is accurate. The API-based model by comparison, proposes a more rigid global response of the pile.

1.3.5 Limitations for offshore wind applications

The methodologies described above have barely been modified when standardised for offshore wind applications and are now routinely used in design. However, there are a number of key differences when compared with oil and gas platform piles that weaken the confidence in these design techniques.

First of all, the pile dimensions are noticeably distinct. Offshore wind monopiles are substantially larger diameter and stiffer than oil and gas piles, with an outer diameter commonly between 5.5 - 7.5 m and an embedded depth of 20 - 35 m (Schroeder *et al.*, 2015). Therefore, their aspect ratio (length over diameter) is usually between 4 - 8, compared with 30 - 50 or more for oil and gas jacket piles (e.g. Byrne, 2011). Consequently, offshore wind monopiles are more likely to rotate when long slender piles are expected to bend under lateral loading (Figure 1.13(a)).

Because the *p-y* method mostly relies on field tests with long slender piles, it is unsure whether this approach accurately predicts rigid pile response. This major limitation has recently been underlined in the design guidelines (see DNV, 2014, last edition, statement F.2.4.1, p. 213), advising for complementary FE calculations for rigorous design.

In addition, recent data from full-scale monitored turbines at Walney offshore wind farm (Kallehave *et al.*, 2012) demonstrate that the API *p-y* curves appear to under-predict the foundation stiffness. For most foundation designs, under-estimation of the stiffness is conservative. However, Figure 1.7 (Section 1.2.3, p. 13) clearly showed that in the case of offshore wind, prediction of the stiffness must be accurate. Also, under-estimation of the soil stiffness involves stiffer and larger support structure design and is therefore one of the primary reasons for increased use of steel, higher costs of the foundation and restriction of the use of monopiles to shallow water depths

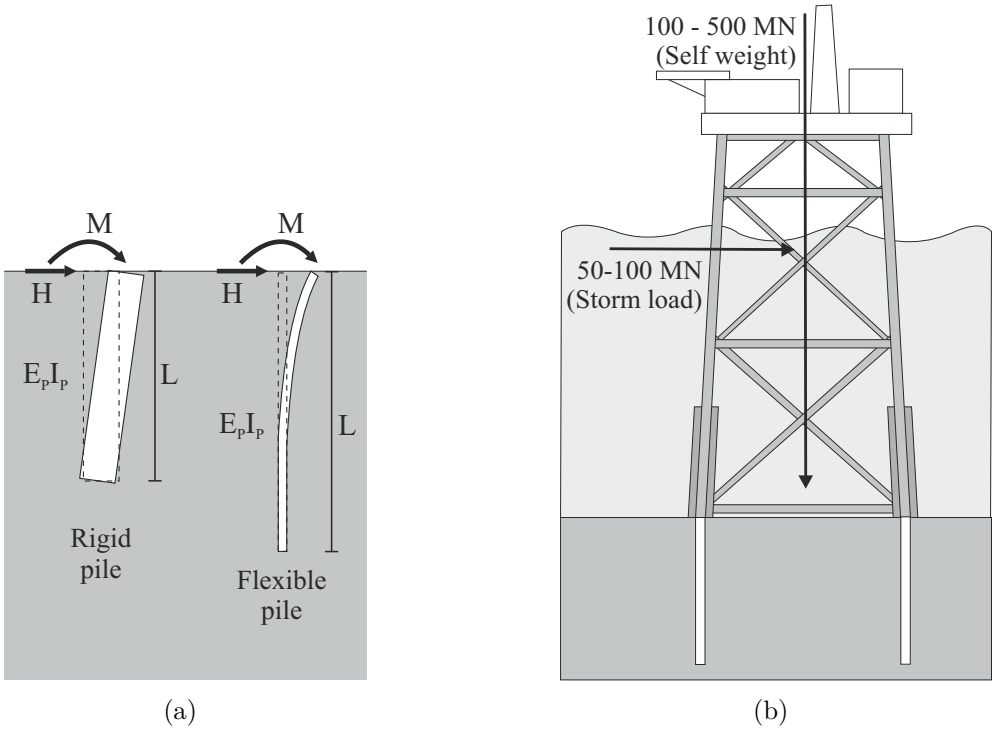

Figure 1.13: (a) Difference in pile response to lateral loading for a rigid and flexible pile; (b) Example of typical loads on an Oil and Gas platform in water depth up to 60 m (from Schneider and Senders, 2010)

(LeBlanc Thilsted and Tarp-Johansen, 2011).

Also, the approach described in the previous section does not account for the hysteretic behaviour of the soil, and therefore, poorly accounts for soil damping.

Finally, the loading on oil and gas support-structures and wind turbines is very different (see Figure 1.13(b) for comparison with Figure 1.4, p. 8). In particular, horizontal loads on an oil and gas jacket pile are a small fraction of the vertical load and therefore, lateral cyclic loading is not a determining condition for design. Consequently, the effects of cyclic loading are virtually ignored in API/DNV though not completely. In the *p-y* curve expressions proposed in Section 1.3.4, a load reduction factor is suggested for cyclic loading and the value of A is then changed to 0.9 in Equation 1.11. Figures 1.14(a)-(b) display the difference observed in soil reaction curves and pile head displacement between static and cyclic loading. Unfortunately, even then, the resulting displacement is the same whether the number of cycles is 10 or 1,000,000. Obviously, this framework does not address the change in soil stiffness with cycle number either. As highlighted in Section 1.2.3, p. 12, the cyclic evolution of the pile response is a key fatigue design condition that needs to be accounted for in design (see also DNV, 2014, paragraph 10.3.2.4, p. 172).

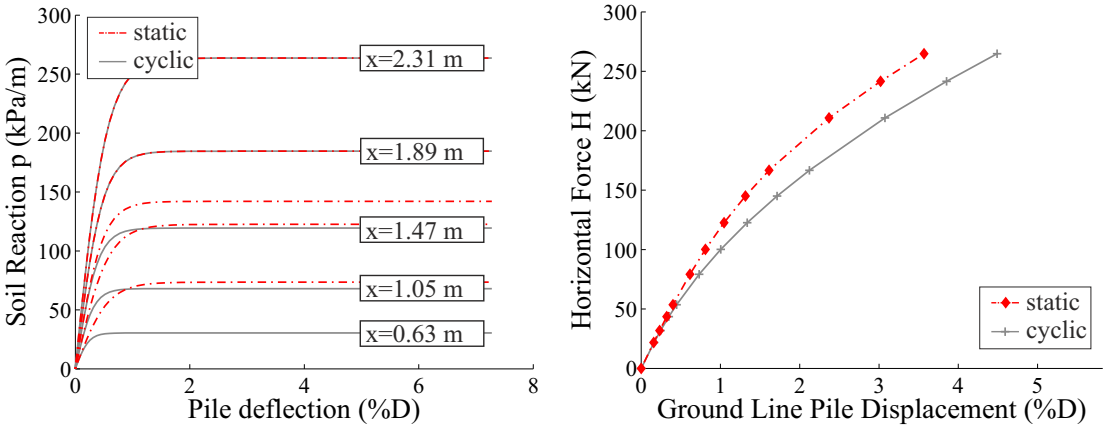

(a) (b)

Figure 1.14: (a) Comparison of static and cyclic DNV *p-y* curves at relevant selected depth for the Mustang Island test case (Cox *et al.*, 1974) (b) Mustang Island pile deflection at Mudline: comparison between static and cyclic DNV *p-y* methods

As a consequence of the above limitations, offshore wind developers are seriously concerned about whether current design approaches are robust and adapted for their industry. For example, DONG Energy, leading offshore wind energy company in Northern Europe, thoroughly enumerated the major technical issues of the p-y method in a document defining a research scope of work to improve guidelines, called the PISA project (DONG Energy, 2013). This list is reported in Table 1.6. The first row summarizes the issues concerning the design to ULS, but this aspect is not the primary objective of this thesis. The last two rows outline the lack of knowledge on the response to cyclic loads and support the need for an accurate prediction of the permanent deformations, soil stiffness and damping due to both long-term operational and short-term storm events. This problem is the key driver behind this research project.

Table 1.6: Specific limitations of the *p-y* approach and consequences in design, as described in the PISA scope of work documentation (table extracted from DONG Energy (2013))

Limitations of existing *p-y* approach	**Consequences**
The pile testing forming the basis for the development of the current *p-y* approach is only partly representative for piled structures in the offshore wind turbine industry – The *p-y* curves were developed for flexible pile failure and not the rigid failure associated with monopiles – The *p-y* curves were developed for high L/D ratios – The *p-y* stiffness was derived on basis of soil strength parameters rather than soil stiffness parameters – Dominating moment loads were not explicitly considered when deriving the *p-y* guidelines – Very dense and strong soils are not accurately modelled	The ultimate lateral pile capacity predicted using the existing *p-y* approach is uncertain and may be under - or overestimated
Effects of cyclic loading are poorly addressed through degraded pseudo-static *p-y* curves – Permanent deformations due to cyclic loading are not addressed – The characteristics of the cyclic loading are not taken into account – The cyclic soil properties are not taken into account	Empirically derived cyclic degradation factors are most likely over - or underestimated depending on site-specific conditions. Large uncertainties exist in predicting permanent deformations over the lifetime of the turbine potentially leading to an over-conservative design
The soil response under operational conditions is poorly addressed – The original *p-y* formulations do not focus on the small-strain response experienced during operational conditions – Long term effects on the stiffness are not considered – No guideline is provided on estimating soil-pile damping – The impact of pile diameter on stiffness is not well investigated	Stiffness and damping are likely to be underestimated which leads to an uneconomical design due to over-conservatism. Existing support structures may have shorter or longer life-times than currently anticipated

1.4 Recent research contributions

In this context, significant research and technology development efforts have been initiated worldwide and strongly supported by the offshore wind industry (e.g. the PISA project, DONG Energy, 2013; Byrne *et al.*, 2015a) in order to contribute to the understanding of the response of large diameter monopiles and develop optimised and tailored design guidelines. This section outlines the prevailing contributions currently available in published literature, with a focus on cyclic loading.

The investigation of laterally loaded piles can be achieved using (a) controlled experiments (laboratory or large scale in the field), (b) instrumented full-scale turbines or (c) numerical or theoretical analyses. Each technique provides different insights and examples of each are presently available in literature.

1.4.1 Response to monotonic loading

In recent years, a number of wind turbine prototypes have been instrumented in order to better understand the response of the foundation and assess the lifetime of the structure. Some of the results are available in published literature and provide a very important insight for future designs. Hald *et al.* (2009) and Kallehave *et al.* (2012) recently reported results from full-scale wind turbine measurements at Horns Rev and Walney offshore wind farm respectively. These trials demonstrate that the API *p-y* curves under-estimate the foundation stiffness. Following this observation, Kallehave *et al.* (2012) proposed to modify the current API *p-y* curves in order to account for a greater initial stiffness for large diameter monopiles. The proposed expression for the modulus of soil reaction is:

$$E_{py}^{Kall} = k_{DNV} \cdot x_r \cdot \left(\frac{x}{x_r}\right)^m \left(\frac{D}{D_r}\right)^{0.5} \tag{1.12}$$

where $D_r = 0.61m$ and $x_r = 2.5m$ are reference diameter and depth respectively. They aim to ensure that the formulation is consistent with the Mustang Island test case (see Figure 1.11(b)). The exponent m is a site-specific parameter and is expected to be in the range $0.4 - 0.7$. A comparison of Kallehave *et al.*'s *p-y* curves with Reese *et al.*'s and DNV's is provided in Figure 1.11(a).

Observations from full-scale monitored turbines have indicated that savings could be achieved by optimising the design of the foundation and better understanding the response of stiff monopiles. This motivated a joint industry project, PISA (Pile Soil Analysis), that aims to develop improved design methods for large diameter monopiles under lateral loading. This project involves a number of leading offshore wind developers, as well as a technical review panel and an academic work group and is structured around three main tasks: (i) large-scale field testing in clay and sand and (ii) 3D advanced finite element analyses leading to (iii) development of a new design method to supersede the current *p-y* method. The results are not yet available in the public domain but the structure of the project and key objectives have been presented in three conference papers so far (see Byrne *et al.*, 2015a,b; Zdravković *et al.*, 2015). The project is directed towards better estimation of monotonic response. Some aspects of the project also address cyclic loading and damping, but this is not the primary objective. Initial published work from the project indicate that some substantial improvements on the monotonic design of monopiles will be possible.

Finally, it is noteworthy to mention the work of Suryasentana and Lehane (2014) which addresses an aspect of the *p-y* curves that is not studied in the projects referenced above. This paper proposes a methodology for directly deriving the sand response adjacent to the pile, and therefore, the *p-y* curve expressions, from CPT end resistance. The proposed methodology is supported by theoretical developments based on 3D finite element analyses and introduces an interesting and accessible way of accommodating design methodologies to a given site.

1.4.2 Pile response to continuous cyclic loading

With regards to the *p-y* curves currently used in design (Equation 1.11), one major concern is the lack of specification when it comes to operational loads. When considering cyclic loads, as opposed to ultimate limit state, the only change in the *p-y* expression comes from A which is fixed to a constant value ($A_{cyclic} = 0.9$). This means that the methodology provides a lowerbound on the response, which is independent of cycle number. Recent research on pile response to cyclic lateral loading demonstrate that repeated periodic loading of constant amplitude can cause significant increases in pile deflection and rotation over time, as well as changing the secant stiffness (e.g. LeBlanc *et al.*, 2010a; Peralta and Achmus, 2010; Klinkvort, 2012; Cuéllar, 2011; Abadie and Byrne, 2014). However, none of these phenomena are currently captured in design.

This major gap in the design practice has motivated a number of research studies in order to derive an empirical framework for capturing the pile response to continuous cyclic loading and integrate them within numerical tools. The following paragraphs detail some of the progress published on this topic.

1.4.2.1 Laboratory model testing

A few laboratory test campaigns have been reported in the literature that address the accumulation of pile displacement and rotation for large cycle numbers (e.g. LeBlanc *et al.*, 2010a; Peralta and Achmus, 2010; Klinkvort, 2012; Cuéllar, 2011; Abadie and Byrne, 2014). Empirical expressions have been derived by fitting recorded measurements using both power and logarithmic laws by the various authors. It was found that the use of a power-law matches the experimental results presented in this thesis (see Chapter 3) and simplifies the subsequent theoretical developments (Chapter 5), and therefore, the framework predominantly used during the research presented here is that of LeBlanc *et al.* (2010a). Hence, this paper is presented in

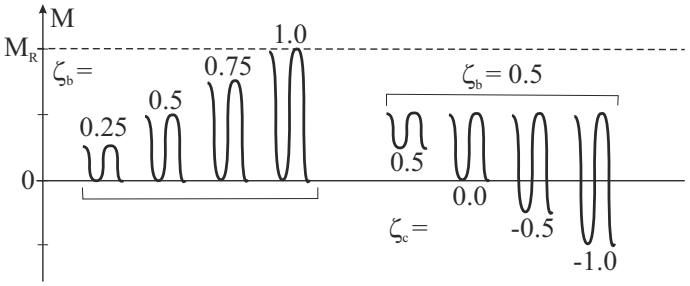

Figure 1.15: Characteristics of cyclic loading defined in terms of ζ_b and ζ_c (from LeBlanc *et al.*, 2010a)

more details below. However, it is noted that whether power law or logarithmic law descriptions are used, both account for an increase in deformation with cycle number in a reasonable similar manner.

The framework introduced by LeBlanc *et al.* (2010a) is based on a comprehensive laboratory testing program, which involves cyclic loading series of 7,000 to 65,000 cycles. The loading is characterized in terms of two normalised parameters: the magnitude ζ_b and amplitude ζ_c (see Figure 1.15):

$$\zeta_b = \frac{M_{max}}{M_R} \tag{1.13}$$

$$\zeta_c = \frac{M_{min}}{M_{max}} \tag{1.14}$$

where M_{min} and M_{max} are the minimum and maximum moment over a load cycle and M_R is the static moment capacity of the pile. ζ_b ranges between 0 and 1. ζ_c characterises the cyclic load, with $\zeta_c = 1$ for a static test, 0 for a one-way loading test and -1 for a two way loading test. LeBlanc (2009) reports that realistic loading most commonly involves load cycles where $\zeta_c \in [-0.5, 1]$. However, for completeness, LeBlanc *et al.* (2010a) tested values of ζ_c between -1 and 1.

LeBlanc *et al.* (2010a) evaluated the displacement of the pile via the magnitude of rotation $\Delta\theta = \theta_{N,max} - \theta_{0,max}$ caused by cyclic loading. They related $\Delta\theta$ to the rotation θ_S that would occur in a static test when the applied load is equal to the maximum cyclic load (see Figure 1.16). Their test results show that the accumulated

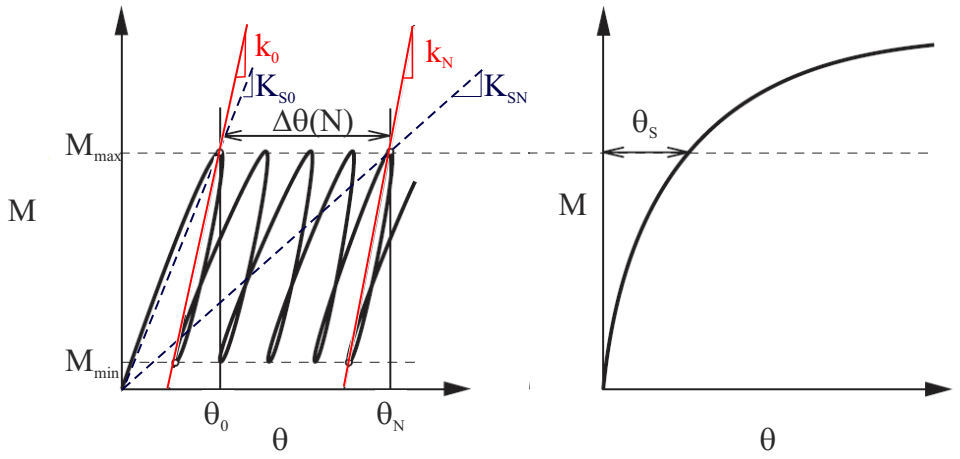

Figure 1.16: Definition of accumulated rotation (Equation 1.15), cyclic secant stiffness (small k_N, Equation 1.16) and absolute stiffness (capital K_{SN}, Degradation stiffness model, Section 3.3.2, p.109) (after LeBlanc *et al.*, 2010a)

rotation follows a power law relationship with the number of cycles:

$$\frac{\Delta\theta}{\theta_S} = T_b(\zeta_b, R_d)T_c(\zeta_c)N^{m_\alpha} \tag{1.15}$$

where T_b and T_c are dimensionless empirical functions depending on the soil relative density R_d and the load characteristics, whilst m_α is an empirical evolution parameter equal to 0.31.

Their test results also highlight a logarithmic evolution of the cyclic secant stiffness (small k_N in Figure 1.16) with the number of cycles according to:

$$\tilde{k}_N = \tilde{k}_b(\zeta_b)\tilde{k}_c(\zeta_c) + Cln(N) \tag{1.16}$$

In this equation, $\tilde{k}_N = k_N \Big/ L^{5/2}D\sqrt{p_a\gamma'}$ is the non-dimensional stiffness (see Chapter 2, Section 2.2 for details on dimensional analysis), $\tilde{k}_b$ and $\tilde{k}_c$ are empirical functions that depend on the load characteristics. C is a dimensionless empirical constant equal to 8.02.

It is noteworthy that in their experimental program, LeBlanc *et al.* (2010a) have highlighted that the most severe loading condition on a pile is generated by cycling

at $\zeta_c \simeq -0.6$.

The above study only covers a limited range of testing conditions and further work at different institutions have addressed the influence of a range of pile geometries and soil properties. In particular, following on earlier work from Dietrich (1982), Peralta (2010) demonstrates that the pile aspect ratio (embedded length L over diameter D) and pile relative stiffness are two key design parameters for laterally loaded rigid piles.

1.4.2.2 Numerical modelling

The effect of cyclic loading on the lateral response of piles has been acknowledged from the very beginning of the development of the *p-y* curves. Reese *et al.* (1974) indeed suggest that the soil resistance should be reduced by a constant factor when considering cyclic loads. In the same vein, O'Neill and Murchison (1983) proposed to reduce the monotonic value of the soil resistance for repeated periodic loading. However, in both papers and also in the current design standards the number of cycles is not accounted for.

The effect of repeated cyclic loads was originally addressed by Poulos (1982) and Little and Briaud (1988) who introduced the idea of degradation factors with cycle number. The model then developed was based upon experimental observation that the soil absolute stiffness (capital K_{SN} in Figure 1.16) degrades with the cycle number. This led to the following expressions for the soil resistance p and the soil reaction modulus E_{py}:

$$p_N = p_0 \cdot N^{-\delta} \tag{1.17}$$

$$R_n = \frac{E_{pyN}}{E_{py0}} = N^{-\delta} \tag{1.18}$$

In these equations, p_0 and E_{py0} are the soil resistance and soil reaction modulus during initial loading and p_N and E_{pyN} at cycle N. δ is the degradation coefficient

that represents the relative effect of cyclic loading on the degradation of p and E_{py}. In the following, this framework will be referred to as the "*Degradation Stiffness Model (DSM)*".

Following this work, Long and Vanneste (1994) applied this framework to 34 full-scale tests gathered from 15 papers and refined the value of δ. The collection addresses the pile response for a wide range of soil densities, load conditions, pile types and materials. They estimated δ to be between 0.52 and 0.00 for virgin cyclically loaded piles with an average of 0.22. They also showed that δ ranges between 0.00 and 0.35 for pre-cycled piles with an average of 0.18. The models proposed by Long and Vanneste (1994) is based upon tests that mostly involve 50 cycles or less on long slender piles. Consequently, the above framework needs to be validated and extended through experiments for short rigid piles and large number of cycles.

As an alternative to the *p-y* approach, the response of the pile can also be modelled using advanced 3-D finite element analyses. However, capturing cyclic loading behaviour using this technique is a very complicated exercise. Firstly, the pile response is usually computed incrementally cycle by cycle and is therefore computationally extremely time consuming, or even prohibitive when modelling large cycle numbers (see for example Bourgeois *et al.* (2010)). Besides, the identification or development of a suitable constitutive model for sand that would also capture the change in behaviour induced by cyclic loading, is an extremely complex task.

An alternative to the cycle-by-cycle approach is to adapt the degradation stiffness model to 3-D FE analyses. This approach is developed for example by Achmus *et al.* (2009) based on experimental results from cyclic triaxial tests on sand. In this paper, the soil behaviour is modelled using an elasto-plastic material and a Mohr-Coulomb failure criterion. The effect of cycle number is then accounted for by degrading the oedometric stiffness modulus in a similar way as achieved for the soil reaction modulus in Equation 1.18. The results from the FE analyses obtained by Achmus *et al.* (2009) compare favourably with experimental test results on model piles and

in particular, with the results from LeBlanc *et al.* (2010a) (see Achmus *et al.*, 2011). This demonstrates that this approach can be used as a compromise between time and accuracy in the later stage of the design process.

1.4.3 Extension to multi-amplitude loading

Real loading on offshore structures is not constant amplitude but consists of a range of loading amplitudes, and is referred to as multi-amplitude cyclic loading. The investigation of the effect of multi-amplitude loading, and in particular during storm event, is still at an early stage. Kallehave *et al.* (2015b) report the response of a full-scale instrumented turbine at Horns Reef II during operational conditions and an extreme storm event. Reduction of the foundation stiffness is observed during the storm event, but no significant change in stiffness due to long-term cyclic loads following the event was recorded. Possible explanations of these observations are discussed in the paper, but much further work is needed to fully understand the behaviour observed.

The investigation of the relationship between spectrum loading and fatigue lifetime is important to accurately predict the evolution of pile deflection through random cyclic loading. First, the random loading history is decomposed into an equivalent set of uniform load reversals. This is a common procedure in fatigue life assessment and can be performed with extended rain-flow counting (Rychlik, 1987). The decomposition of the load series enables a damage rule to be applied for predicting the fatigue life-time. A common method is the linear cumulative damage rule, initially proposed by Palmgren (1924), and then popularised by Miner (1945). This concept was applied to laterally loaded piles by Lin and Liao (1999), following the work of Stewart (1986). They demonstrated a good fit to their experimental results; however, their experiments only involved 50 cycles maximum. Extending this, published work by LeBlanc *et al.* (2010b); Peralta (2010) and Abadie *et al.* (2015) investigated the influence of ascending and descending load combinations

on pile response for larger cycle numbers (up to 45,000 for Peralta (2010), 10,100 for LeBlanc *et al.* (2010b) and 12,000 for Abadie *et al.* (2015)). These studies demonstrate that the loading history has an influence on the pile response whilst LeBlanc *et al.* (2010b) and Abadie *et al.* (2015) found that Miner's rule provides a reasonable approximation for the sequences investigated. The superposition method adopted in LeBlanc *et al.* (2010b) has been used in Abadie *et al.* (2015) and differs slightly from that in Peralta (2010). This procedure is described briefly below.

If there are two load sequences subscripted a and b, in the order N_a then N_b, then firstly the accumulated rotation caused by N_a cycles of lateral load a is determined using Equation 1.15:

$$\Delta\theta_a = \left(T_b T_c \theta_s\right)_a N_a^{0.31} \tag{1.19}$$

This can be made equivalent to N_{ab}^{eq} cycles of load type b using the calculation:

$$N_{ab}^{eq} = \left(\frac{\Delta\theta_a}{(T_b T_c \theta_s)_b}\right)^{0.31} \tag{1.20}$$

If N_b cycles of load b are then applied to the pile, the overall accumulated rotation is given by:

$$\Delta\theta_{tot} = (T_b T_c \theta_s)_b \left(N_b + N_{ab}eq\right)^{0.31} \tag{1.21}$$

The total pile rotation is then calculated as:

$$\theta_b = \Delta\theta_{tot} + max\{\theta_{0,a}, \theta_{0,b}\} \tag{1.22}$$

1.4.4 Other relevant research efforts

1.4.4.1 Multi-directional loading

The research on cyclic loading described above only considers uni-directional loading. However, the loading caused by wind and wave will comprise of a range of varying directions. This is illustrated in Figures 1.17(a) and 1.17(b) where the wind and wave directions at Hornsea wind farm, in the North Sea, are displayed. The figures show that both wind and wave loading include a wide range of directions, and also, that the principal direction of each load type is probably not co-linear.

Very little research has currently been reported on the impact of multi-directional loading on the foundation response. Test results at both 1-g and n-g have been published in Rudolph *et al.* (2014) and another set of tests has been separately presented by Peralta (2010). Rudolph *et al.* (2014) demonstrate that multi-directional loading induces significant increase in pile accumulated displacement while Peralta (2010) suggests that loading at varying directions might actually be beneficial in terms of pile deflection. It is noteworthy that the testing programmes, and in particular the series of loading directions selected in these two studies, are very different. The

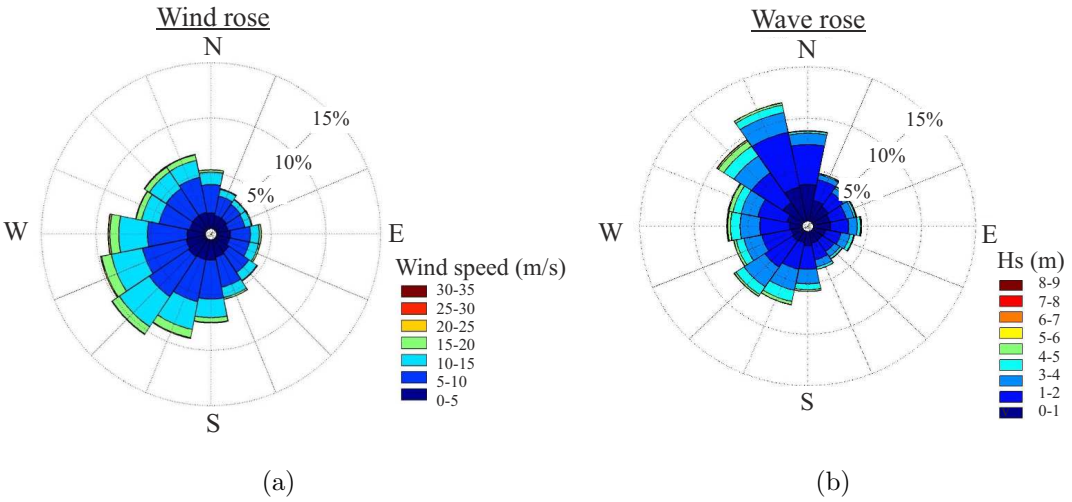

Figure 1.17: (a) Wind speed and (b) significant wave height roses at Hornsea wind farm (from Smart Wind Limited, 2013)

principal difference between the two is that Rudolph *et al.* (2014) constrained all loading within a single quadrant while Peralta (2010) completed the whole rose circle (360°) by changing the direction quadrant by quadrant. This illustrates that multi-directional loading is an area of large uncertainty and that it needs to be addressed in more detail in future research.

1.4.4.2 Convective displacement of soil particles

Cuéllar *et al.* (2009) propose an interesting study of the movement of grains in the soil during cyclic loading. They carried out a series of 1g lateral cyclic loading tests during which the sand particles surrounding the pile were coloured and tracked. The results show a progressive densification of the sand due to a long-term convective granular flow near the pile. They also outline the existence of two domains in the soil near the pile: a *convected* and a *static* soil domain. The convective domain is where the convective flow has been observed, whereas the static domain covers the rest of the soil. This does not mean that the soil in the static domain does not actually move but that it remains undisturbed at the end of the cyclic loading. These domains are separated by a direct shear surface that is clearly identified following testing. It is noteworthy that this study and the full set of results reported in Cuéllar (2011) is the only published work available in the literature that relates the pile response to over 1,000,000 cycles.

1.5 Research objectives

1.5.1 Targeted technical challenges

The previous paragraphs have outlined the methodologies presently used in design, their limitations and the progress of current research to improve guidance. This section cross-examines the limitations listed in Table 1.6 (p. 27) with the research improvements presented in Section 1.4 and identifies the technical challenges for the

design of laterally loaded piles in sand. Design to the ULS (first row of Table 1.6) is here left aside as this is not the primary objective of this thesis.

The second row of Table 1.6, relates to permanent deformation and plastic behaviour of the pile due to cyclic loading, both continuous and multi-amplitude. Empirical laws exist that describe the evolution of the foundation response (e.g. rotation, stiffness) with the number of cycles during both loading conditions (e.g. LeBlanc *et al.*, 2010a; Peralta, 2010; Klinkvort, 2012; Cuéllar, 2011). They can be integrated within Winkler type or 3D-FE design approaches using the Degradation Stiffness Model, providing further validation for large cycle number. However, these procedures are highly empirical and based on small-scale model tests. There is first the issue of whether the full-scale behaviour compares to these results. Also, there is a need for more rigorous approaches which describe the plastic behaviour and mechanisms of the soil response due to cyclic loading and are validated through specific experiments.

The last row of Table 1.6 refers to two main issues: (a) evolution of the stiffness and (b) damping. There is presently very little understanding of the evolution of the stiffness during the lifetime of the wind turbine, and especially, during load series of variable amplitude. There is first the issue that, despite the data currently available on the cyclic development of the stiffness for small-scale model piles, no numerical or theoretical model is capable of accurately capture the observed evolution. Besides, very few experimental data, if hardly any, address the hysteretic behaviour of the pile response, and therefore, it is presently difficult to develop or calibrate numerical models capable of capturing the plastic response of the foundation. Both mechanisms are probably linked and are essential for the service life assessment of the structure.

Finally, the development of numerical methods, such as cycle-by-cycle p-y curves or complete 3D FE, adapted for the prediction of the pile response to large cycle number is still at a very early stage. One of the difficulties is devising a model that accurately captures the response to large number of cycles while being computationally

efficient and relatively fast. The latest numerical models can be investigated using constitutive modelling, with the aim of accurately capturing the targeted behaviour while adapting the model to fast computation of large numbers of cycles.

This thesis describes work that contributes to the development and understanding of the above limitations and features (a) an experimental programme, directed towards the analysis of the plastic response of the pile during cyclic loading and (b) the development of a theoretical model that accurately and efficiently captures the key experimental findings. The primary objectives of each part are detailed in the paragraphs below and a summary of the key objectives of the project is provided in Table 1.7.

1.5.2 Experimental investigations

The investigation, presented in this thesis, of the key mechanisms driving the pile response to cyclic lateral loading is achieved through laboratory scale testing of a rigid pile embedded in a cohesionless soil (dry sand). The objective of the test programme is twofold: (a) analysing the plastic behaviour of the pile-soil interaction and its evolution with cyclic loading as input into the development of a constitutive model and (b) deriving and validating empirical frameworks for use in the p-y (or other similar design) method for cyclic loading. The scope of the experimental work is specified below.

The test campaign starts with analysing rate effects on pile response in order to assess whether the load frequency would influence the pile behaviour. It is followed by a series of tests that aim at identifying the hysteretic response of the pile, to determine the primary response mechanism for constitutive modelling. This framework is then extended to long-term continuous cyclic loading. In line with the conclusions from Section 1.2.3, the targeted parameters of the experimental study are: (a) the accumulated deformation of the pile (b) the secant stiffness and (c) the hysteretic damping which directly relates to the hysteresis loop area (see detailed

relationship in Chapter 3, Section 3.2, p. 93). The data collected on the permanent displacement during long-term cyclic tests are also used for further validation of the *Degradation Stiffness Model*. This could enable a first approximation of the pile response to cyclic loading in the early stage of the design process.

This phase of work is followed by a series of tests that investigate the evolution of the static loading response following cyclic loads of given cycle number and load amplitude/magnitude. This provides insight into the evolution of the pile capacity with cyclic loading. Finally, this is extended further with a test campaign specifically directed towards the analysis of the pile response to multi-amplitude loading, and in particular, the effect of alternating storm-type event with continuous operational loads. This analysis is of great importance for designs with respect to serviceability and fatigue limit states.

1.5.3 Theoretical and numerical development

The key experimental findings are then used to develop numerical and theoretical models. This thesis presents the theoretical development of a novel constitutive model (HARM) that is capable of capturing accumulation of irreversible deformation under constant cyclic loading at non-zero mean load (ratcheting). The model is framed within the hyperplasticity framework presented by Houlsby and Puzrin (2006) which enables rigorous yet simple modelling of ratcheting. The strength of the model is that it can easily be accelerated to simulate large cycle numbers through the computation of only few cycles, offering considerable computational benefits.

This framework is then developed further in order to capture specific aspects of the cyclic behaviour, and in particular, the evolution of the secant stiffness and loop area, and also, the response to multi-amplitude cyclic loading. The final model is then calibrated based on experimental test results and applied to series of relevant tests selected from the experimental programme.

Table 1.7: Key objectives of research work

Topic	Thesis objective	Motivation
Part 1 - Experimental work (model pile tests in dry sand)		
1) Rate effects	Does the pile response exhibit rate-dependent behaviour?	Important for design of piles to quasi-static operational conditions and impact of loads at faster rate
2) Hysteretic response	What is the hysteretic response of the foundation?	Decay of vibrations in the structure depends on soil damping which depends on the hysteretic response of the foundation. Determination of the plastic behaviour is required for development of theoretical modelling of pile response
3) Accumulated displacement	Does the pile accumulate deformation with cycle number and does it eventually reach a plateau? How can this be simply predicted in design?	Important for adhering to the maximum design tolerances specified by turbine manufacturer
4) Secant stiffness at ground level	How does the secant stiffness develop with cycle number?	Both fatigue and ultimate limit state designs need to address the natural frequency of the structure, which is a function of the secant stiffness
5) Hysteresis loop area	How does the hysteresis loop area develop over time?	Important for assessing the evolution of soil damping due to cyclic loading
6) Multi-amplitude loading	What is the static response of the pile after a series of cyclic loads? How does accumulated deformation develop during random cyclic loading? How does the application of random cyclic loading affects the secant stiffness and hysteresis loop area?	Important for the design to service limit states and assessment of pile tilting during and after extreme storm events

Continued on next page

Topic		Thesis objective	Motivation
Part 2 - Theoretical and numerical developments			
7)	Constitutive modelling of ratcheting	How to accurately and rigorously capture accumulation of deformation with cycle number (ratcheting)?	Important for development of rigorous base model for capturing cyclic response
8)	Accelerated modelling	How to accurately model very large cycle numbers in a reasonable time frame?	Important for applications of developed method to engineering design
9)	Accumulated rotation	How to accurately capture the change in accumulated deformation with cycle number and load magnitude/amplitude?	Important for accurate design prediction of pile displacement with time and loading
10)	Secant stiffness and damping	How to model the change in hysteretic response?	Important for accurate estimation of the evolution of natural frequency and damping
11)	Multi-amplitude loading	How to capture the response to series of loads of variable amplitude?	Compulsory for fatigue and serviceability limit state design
12)	Calibration	How do the model parameters relate to experimental data?	Important for future calibration in design codes

1.6 Thesis outline

The outline of the thesis is structured around the two key tasks described above.

Chapter 1 *(Overview, Motivation and Background)* described the state of the art for the design of offshore wind monopiles and identified the key limitations of the current methodologies. It proposed an overview of recent improvements published in the Literature before presenting this thesis statement.

Chapter 2 *(Experimental Pile Testing: Set-up and Monotonic Loading)* presents the experimental methods used during this research project and details the test programme carried out. It also describes the results of a short monotonic test campaign that aims to validate the testing procedures and derive parameters required for the following analyses.

Chapter 3 *(Experimental Pile Testing: Cyclic Loading)* presents the experimental test results and analyses with regards to the objectives outlined in Table 1.7, part 1.

Chapter 4 *(Constitutive Modelling for Ratcheting (HARM))* discusses the theoretical developments of the HARM model that enables it to capture ratcheting. It also explains how the model can be accelerated and extended to multi-directional loading.

Chapter 5 *(Calibration against Experimental Data)* presents how the fundamentals of the HARM model can be extended to accommodate specific aspects of the ratcheting behaviour, and ultimately, capture the key experimental findings identified in Chapter 4. It also presents a short calibration procedure based on the data of selected continuous cyclic tests and an application for the prediction of a wider selection of test results.

Chapter 6 *(Conclusions)* summarises the key findings of the thesis and proposes future directions of research.

Chapter 2

Experimental Pile Testing: Set-up and Monotonic Loading

2.1 Introduction

Physical modelling (large or laboratory scale) is an important step in geotechnic research. In the case of pile design, it provides fundamental insights on the foundation behaviour (e.g. hysteresis, ratcheting etc.) that determine how to take the development of theoretical and numerical models forward. Also, experimental data are required when validating and calibrating new numerical tools. Large scale field tests enable to accurately estimate a specific behaviour and provide realistic geotechnical parameters for design. However, they are also extremely expensive and are only carried out when their incurred costs are justified by a significant gain of knowledge, leading to substantial savings on future projects. When this is not the case, small-scale model testing is then a cost-effective way to understand the key aspects of a full-scale prototype and to provide a database for calibration of numerical models. Two small-scale laboratory model test techniques are common for investigating soil-structure interaction: (i) unit gravity (1-g) and (ii) geotechnical centrifuge (n-g).

The main advantage for model testing on the centrifuge is that the soil stresses are correctly scaled, which means that similitude relationships are more straightforward

than for 1-g testing. However, testing apparatus must be designed to work at increased accelerations and in confined spaces. Instrumentation systems are therefore complex and are required to work at greater resolutions. Also, long-term cyclic tests with very large cycle number require advanced control system and consequently, costs can quickly build up. Finally, the size of the centrifuge container is restricted and therefore, so is the size of the pile. Hence, the scaling of the sample particle size compared with the pile dimensions has to be carefully considered.

An alternative to centrifuge testing is to conduct experiments at small scale in the laboratory. Providing a safe design of the loading equipment, it is possible to explore the pile response to very large cycle numbers. A key advantage is that high resolution instrumentation capable of measuring very small displacements can be used, which might not be possible on the centrifuge (e.g. measurement of microns). Also, tests can involve larger model piles and the costs for running overnight are much less than for say a centrifuge. Because stress-strain behaviour of soil does not scale linearly with stress, scaling of model tests and results must be addressed adequately. This approach is the one followed in this thesis. However, the key response captured with either n-g or 1-g equipment should compare, between them and also to the large-scale prototype.

This chapter introduces the experimental work carried out during this research project. First, the dimensional analysis framework employed for the design of the experiments is introduced. Then, details on the testing equipment (i.e. rig, data acquisition system, samples and piles) are provided, followed by the experimental method and detailed testing programme. Finally, in the last two sections, the first set of experimental test results is presented, predominantly of monotonic loading tests, and interpreted using the p-y method.

2.2 Scaling considerations

Physical modelling using laboratory floor tests requires careful consideration of the scaling to ensure that the experimental outcome gives appropriate insight into full-scale behaviour. However, formulating a rigorous and unique similitude framework is a difficult task that can only be confirmed by comparing test results at different scales. Such database is not yet available for laterally loaded piles and therefore, aspects of scaling are still discussed within the geotechnical community. Nonetheless, normalisation frameworks that pertain to 1-g model tests have been proposed in the published literature and give a reasonable approximation of how loads, stresses and dimensions should scale up. This section presents the dimensional framework proposed by LeBlanc *et al.* (2010a) and an example of application for the design of laboratory model piles.

2.2.1 Methodology

In applied mathematics, the Buckingham Pi theorem (Buckingham, 1914) provides the basics of dimensional analysis of physical systems. This theorem states that, if a problem involves m physical variables that are expressed in terms of l independent quantities, then the problem can be reduced to an equation involving only $m - l$ dimensionless parameters. The dimensionless group of parameters that results from this analysis is sufficient to completely describe the problem and is independent of the fundamental units of measurements.

A common approach for the determination of this similitude group is called the *Buckingham Pi method* (Buckingham, 1914), which is a formalization of the Rayleigh's method (Rayleigh, 1877). It consists in listing all the variables involved in the problem, defining the "repeating variables" (i.e. dimensionally-independent scaling variables, also called "governing variables", which number corresponds to the number of reference dimensions involved in the list of variables) and then non-

dimensionalising the remaining variables by the repeating variables. There are rules relating to the selection of the repeating variables, in that they cannot themselves make a dimensionless group. However, when the number of variables m in the problem is much greater than the number of repeating variables l, there are also $m - l$ possible dimensionless group and it may become difficult to determine the most relevant functional form using this methodology.

An alternative is to start from one of the governing equations, and progressively re-arrange the terms until the equation is normalised. Of course, this approach is less methodical and does not enable to normalise all the variables of the system, but relevant normalised form of the parameters then appear naturally. This is the technique that LeBlanc *et al.* (2010a) adopted, following from the work published by Kelly *et al.* (2006) for suction caissons. The procedure is briefly summarized below and the relevant parameters are identified in Figure 2.1. The resulting framework is the one employed in this thesis for the design of the experiments and for presenting the test results.

First, the pile is assumed to be sufficiently stiff that bending can be neglected

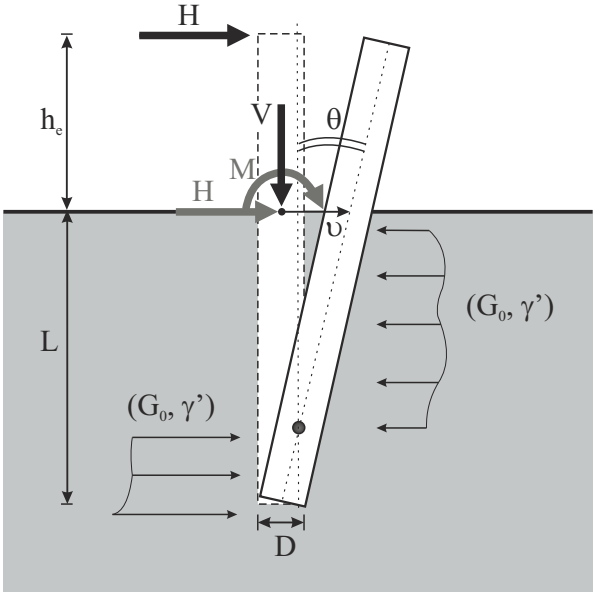

Figure 2.1: Parameters considered in the dimensional framework proposed by LeBlanc *et al.* (2010a)

and the response is dominated by ground deformation. The sand properties are then characterised by the shear modulus at small strain G_0. Kelly *et al.* (2006) suggest to account for the influence of isotropic stress level by considering the relationship:

$$\frac{G_0}{p_a} = c_1 \left(\frac{\sigma'_v}{p_a} \right)^n \tag{2.1}$$

In this equation, p_a is the atmospheric pressure, c_1 is a dimensionless coefficient and σ'_v is the effective vertical stress expressed according to:

$$\sigma'_v = c_2 L \gamma' \tag{2.2}$$

where c_2 is another dimensionless constant and γ' is the effective unit weight. Finally, in Equation 2.1, n is the pressure coefficient and LeBlanc *et al.* (2010a) recommend to take $n = 0.5$, following earlier work from Wroth and Houlsby (1985), Schanz and Vermeer (1998) and Kelly *et al.* (2006). Now, six of the key dimensionless parameters ($\tilde{M}$, $\tilde{k}$, $\tilde{\theta}$, $\tilde{H}$, $\tilde{v}$ and $\tilde{h}_e$) fall out from the elastic stiffness relationship:

$$\begin{bmatrix} \frac{M}{L} \\ H \end{bmatrix} = DG_0 \begin{bmatrix} k_1 & k_2 \\ k_2 & k_3 \end{bmatrix} \begin{bmatrix} L\theta \\ \upsilon \end{bmatrix} \tag{2.3}$$

where k_1, k_2 and k_3 are dimensionless constants and υ is the pile displacement at ground level. Combining these two equations, it comes:

$$M = \left(\frac{G_0 L^2 D \left(k_1 k_3 - k_2^2 \right)}{k_3 - k_2 (HL/M)} \right) \theta \tag{2.4}$$

Combining the above with Equations 2.1 and 2.2, it then follows:

$$\underbrace{\frac{M}{DL^3\gamma'}}_{\tilde{M}} = \underbrace{\left(\frac{c_1 \sqrt{c_2} \left(k_1 k_3 - k_2^2 \right)}{k_3 - k_2 (HL/M)} \right)}_{\tilde{k}} \underbrace{\sqrt{\frac{p_a}{L\gamma'}} \theta}_{\tilde{\theta}} \tag{2.5}$$

This gives the dimensionless form of the moment $\tilde{M}$, rotation $\tilde{\theta}$ and secant stiffness $\tilde{k}$. The expression of $\tilde{k}$ also gives the dimensional expression of the load eccentricity $\tilde{h}_e = M/HL$. The Expression of the dimensionless stiffness can be re-arranged according to:

$$\tilde{k} = \frac{k}{L^{5/2} D \sqrt{p_a \gamma'}} \tag{2.6}$$

Similarly, the dimensionless expressions for $\tilde{H}$ and $\tilde{v}$ arise from Equation 2.3:

$$\tilde{H} = \frac{H}{L^2 D \gamma'} \tag{2.7}$$

$$\tilde{v} = \frac{v}{D} \sqrt{\frac{p_a}{L \gamma'}} \tag{2.8}$$

Finally, using Equation 1.1 (or 1.2, Chapter 1, p. 12), LeBlanc *et al.* (2010a) demonstrate that the dimensionless form of the vertical load is:

$$\tilde{V} = \frac{V}{D L^2 \gamma'} \tag{2.9}$$

The above framework highlights a set of dimensional parameters that characterise the pile response. These have been summarised in Table 2.1. This procedure does not unlock all the parameters though, and in particular, those related to the soil conditions. However, (a) the behaviour of the foundation in sand is dominated by the frictional behaviour, and therefore, further consideration is needed regarding the peak friction angle and (b) as the stress level in the laboratory is much smaller than at full scale, careful understanding of the sample dilation compared as that in the field is required. This is thoroughly explained by Bolton (1986) and the reasoning is outlined in the section below.

Table 2.1: Non-dimensional framework for scaling laterally loaded model pile tests LeBlanc *et al.* (2010a)

Moment loading	$\tilde{M} = \dfrac{M}{L^3 D\gamma'}$
Horizontal force	$\tilde{H} = \dfrac{H}{L^2 D\gamma'}$
Vertical force	$\tilde{V} = \dfrac{V}{L^2 D\gamma'}$
Rotation	$\tilde{\theta} = \theta \cdot \sqrt{\dfrac{p_a}{L\gamma'}}$
Displacement	$\tilde{\upsilon} = \dfrac{\upsilon}{D}\sqrt{\dfrac{p_a}{L\gamma'}}$
Secant stiffness	$\tilde{k} = \dfrac{k}{L^{5/2} D\sqrt{p_a\gamma'}}$
Load eccentricity	$\tilde{h}_e = \dfrac{M}{HL}$

2.2.2 Consideration of sample dilatancy (Bolton, 1986)

In his paper, *The stress and dilatancy of sands*, Bolton clarifies the relationship between the peak angle of friction of shearing resistance ϕ', the peak angle of dilatancy ψ', the relative density and the mean effective stress at failure. First, the friction and dilation angles are proportional. From Rowe's stress-dilatancy relationship (Rowe, 1962), Bolton (1986) indeed infers that:

$$\phi' - \phi'_{cr} = 0.8\psi' \tag{2.10}$$

where ϕ'_{cr} is the critical angle of friction. Additionally, it is clear that the soil dilation depends on its relative density. In addition, for a given relative density, increase of the confining pressure induces particles deformations, and therefore, a decrease of ϕ' (Bishop, 1972). Similarly, because of the crushing of the particles, the maximum angles of friction and dilation ϕ'_{max} and ψ'_{max} decrease with confining pressure increase

(Vesic and Clough, 1968; Billiam, 1972; Bishop, 1972). Based on these observations, Bolton (1986) formulates empirical relationships between the maximum angles of friction and dilation, the mean effective stress at failure p' and the relative density. For the dilation angle, he suggests:

$$\psi'_{max} = AR_d \ln\left(\frac{p'_{cr}}{p'}\right) \tag{2.11}$$

where p'_{cr} is the stress threshold to eliminate dilation by crushing and A is an empirical constant. For the angle of friction, the relationship is expressed through the dilatancy index I_R according to:

$$I_R = R_d\,(10 - \ln(p')) - 1 \quad ; \quad \begin{cases} I_R = \dfrac{(\phi'_{max} - \phi'_{cr})}{3} & for\ plane\ strain \\ I_R = \dfrac{(\phi'_{max} - \phi'_{cr})}{5} & for\ triaxial\ strain \end{cases} \tag{2.12}$$

The above therefore demonstrates that the angles of friction and dilation are proportional to the relative density and inversely proportional to the stress level. For 1-g model test design, this means that, as the stress level in the laboratory is much smaller than that in the field, the sample relative density must be accordingly smaller to reproduce the rate of dilatancy at full scale. This justifies why 1-g model test samples should always be prepared at low relative densities.

Following this framework, Schnaid (1990) inferred a relationship between the angle of friction, the relative density and mean stress level for Yellow Leighton Buzzard 14/25 sand, which enables to correlate laboratory test samples to full-scale conditions. This was later used by LeBlanc *et al.* (2010a) in order to scale their laboratory test (Figure 2.2), which also corresponds to most of the samples prepared during this research project (c.f. Section 2.3.3, p. 58).

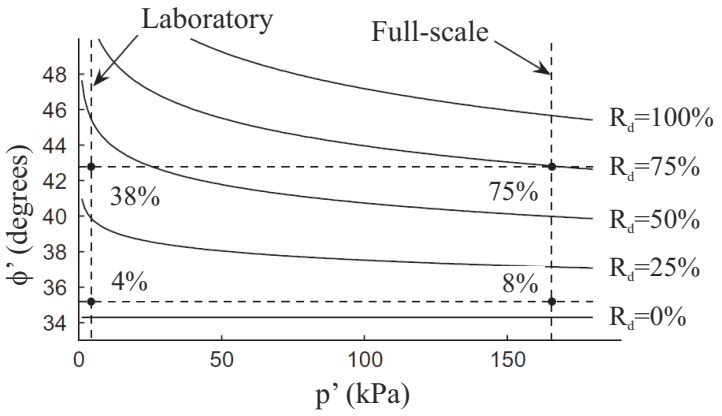

Figure 2.2: Friction angles of yellow Leighton Buzzard Sand as function of effective isotropic stress p' and relative density R_d (from LeBlanc *et al.*, 2010a)

2.2.3 Analysis of pile flexibility

In order to complete the above framework, further consideration is given to the pile aspect ratio (embedded length L over diameter D) and pile relative stiffness. Dietrich (1982) and Peralta (2010) suggest that a perfectly rigid pile response strongly depends on the L/D ratio while a perfectly flexible pile response depends more on the bending stiffness. For this reason, these two parameters are likely to be key design and scaling variables for model test piles.

Figure 2.3 shows a plot of aspect ratio against pile relative stiffness, K_R, for a range of designs relevant to UK offshore wind farms (OWF). The pile relative stiffness is calculated according to Poulos and Hull (1989):

$$K_R = \frac{E_p I_p}{E_{SL} \cdot L^4} \quad \begin{cases} > 0.208 & \text{Rigid pile behaviour} \\ < 0.0025 & \text{Slender pile behaviour} \end{cases} \tag{2.13}$$

$E_p I_p$ is the pile bending stiffness and E_{SL} is the soil Young's modulus at the pile tip, estimated from the small strain shear modulus ($E_{SL} = 2(1+\nu) \times G_0$). An order of magnitude of E_{SL} for the different soil types is given in Table 2.2 and the boundaries for rigid and flexible piles defined by Poulos and Hull (1989) have been reported on Figure 2.3. Highlighted on this figure are three sets of data: (i) current wind farm

monopiles in sand, (ii) current wind farm monopiles in clay and (iii) piles that were used in the 1960s and 1970s for the development of the *p-y* methods. The selected wind farm sites are those of Barrow, Walney, London Array, Gunfleet Sands, Kentish Flats, Lynn and Inner Dowsing, Robin Rigg, Scroby Sands, Sheringham Shoal, North Hoyle, Burbo Bank and Rhyl Flat. The *p-y* method test results reported here are those of Cox *et al.* (1974) and Mansur and Hunter (1970) for piles in sand and Maltock (1970); Reese and Welch (1975) and Meyer (1979) for piles in clay. A summary of all the test results can be found in Reese and Van-Impe (2011). Figure 2.3 identifies the region where model piles should be located to capture field conditions, towards the top left corner. This is where the piles for the work described in this thesis are positioned. The graph also indicates the location of some of the laboratory model piles referenced in published literature and frequently cited in this thesis.

Table 2.2: Estimation of the soil modulus for different soil conditions

Soil Conditions	E_{SL} (MPa)
Dense Sand	50
Soft to medium clay	3
Stiff Clay	30
Hard Clay	300

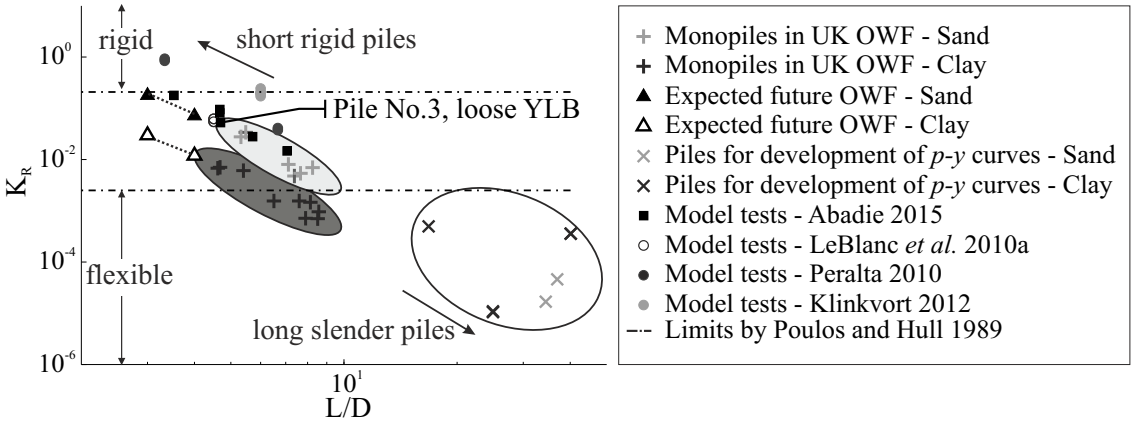

Figure 2.3: Dimensionless pile flexibility factor vs. L/D ratio for full-scale Offshore Wind Farm (OWF) monopiles in the UK as well as piles used for the design of the p-y curves

2.3 Experimental equipment

2.3.1 Loading rig

The model experiments described in this thesis were conducted using equipment developed by Rovere (2004), and used by LeBlanc *et al.* (2010a) and LeBlanc *et al.* (2010b). The system consists of a combination of rotating and suspended masses, a motor, a steel structure and a sand container (Figures 2.4(a) and 2.4(b)). The mass m_3 balances the weight of the main beam and the motor. Then, m_1 and m_2 are selected according to:

$$\begin{cases} m_1 = (\frac{l_2}{l_a} \cdot H_a - H_0) \cdot \frac{1}{g} \\ m_2 = \frac{l_c}{l_a} \cdot \frac{H_a}{g} \end{cases} \tag{2.14}$$

where $H(t) = H_0 + H_a \cdot sin(\omega t)$ is the sinusoidal force that is to be applied on top of the pile. l_2, l_a and l_c are relevant set-up lengths (cf. Figure 2.4(a)). When running, the motor carries m_1 along a circular path that makes the gravity centre of the main beam change sinusoidally. The wire located in-between the main beam and the pile directly applies the lateral cyclic load at a representative height above the soil surface. The motor frequency is 0.106 Hz. This corresponds to the peak frequency of offshore waves and is sufficiently low for avoiding dynamic effects in the soil response. This rig offers the possibility of applying thousands of repeatable cycles in a reasonably short timeframe. As an estimate, the required time for performing 1,000 cycles is 2 hours 40 minutes, 10,000 cycles corresponds to 26 hours and 100,000 to 11 days.

All the tests were performed with the vertical load held constant and equal to the total foundation weight (pile below the ground) plus the weight above the ground (For pile No.3 in Table 2.4, the additional vertical weight above the ground is $m_{top} = 1.8kg$). This mimics the structural dead weight of the super-structure and

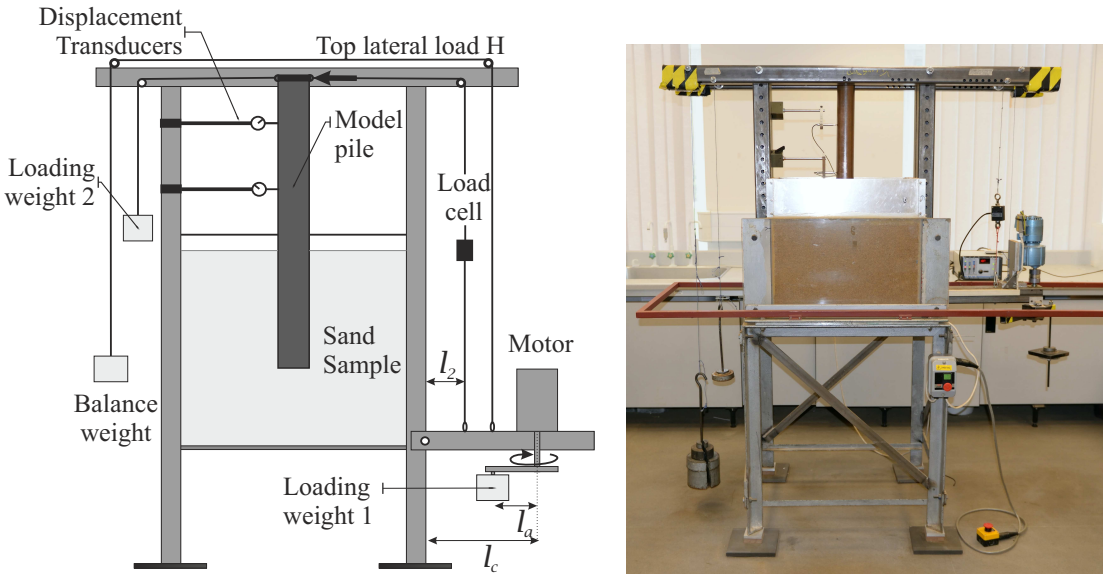

Figure 2.4: (a) Schematic and (b) Photo of the loading rig

turbine, though it is not expected that axial loading would have an effect of primary order on the pile lateral response.

2.3.2 Data acquisition

High-quality measurement of the pile deflection was determined using two Linear Variable Differential Transformers (LVDTs), from which the pile rotation was also calculated (Figure 2.5(b),(d)). The selected transducers are DC RDP electronic LVDTs D5/200 AG and have a range of ±5 mm. They were usually set up opposite to the main load direction at a minimum distance of 180 mm from each other. For long-term cyclic tests (multiple days), Dial Gauges were used for verification of the LVDTs logging in order to correct for any electrical drift (Figure 2.5(b)).

The load applied to the pile head was monitored using a Tokyo Sokki Kenkyujo Co. TCLZ - 100KA load-cell. The transducer excitation voltage was supplied, regulated and amplified using a RDP Modular 600 amplifier module and then transmitted to the computer via a 14-bit analogue-digital converter (see Figure 2.5(d)). The data acquisition was controlled and logged using *NI LabVIEW Signal Express*.

Finally, it is important to underline that the data presented in this Chapter and the next one have not been filtered during post-processing. The sampling frequency was selected depending on the type of test carried out and in order to log enough data to obtain continuous plots and enable detailed analysis. Typical sampling frequencies for the test presented in Section 2.6 are 106 Hz for monotonic tests, 5.3 Hz for short-term cyclic tests (less than 2 days - 50 samples per cycle) and 3.18 Hz for long-term cyclic loading tests (30 samples per cycle).

The instrumentation used during this research programme enabled capturing very accurately the macro-behaviour of the pile, that is to say, the horizontal force applied

(a) (b) (c)

(d) (e)

Figure 2.5: (a) Driving motor (b) LVDT and Dial Gauge (c) Pile during installation (d) Data acquisition system (e) Pictures of the piles used for testing

on top versus the displacement at ground level, the rotation, and the parameters that can be derived from these macro variables (moment at ground level, tangent and secant stiffness in particular). Early in the research programme, consideration was given to instrumenting one pile with strain gauges in order to derive experimental soil reaction curves. However, the required size and relative stiffness of the pile (see Figure 2.3, p. 54) would not lead to sufficient resolution of strain measurement, so this option was not pursued any further. The soil reaction curves have been derived from the pile macro-behaviour (see Section 2.6,p. 78).

2.3.3 Samples properties

The samples were prepared in a 600 mm x 600 mm x 527 mm tank. These dimensions ensured clearance between the pile and the container wall in the loading direction to avoid any significant boundary effects. The sand was poured from a low drop height in order to achieve a very low relative density for all samples. Sand dilates more at low stress levels (laboratory model tests) than at higher stress levels (full-scale prototype) (Bolton, 1986) and therefore preparing samples at lower relative densities compensates for such differences (Section 2.2.2, p. 51; Byrne and Houlsby (2004)). Furthermore, this allows for very repeatable and reliable sample preparation. All samples were prepared dry in order to mimic drained conditions.

Three different sands were used during the test campaigns (Figure 2.6(a)) but most of the tests were performed using Yellow D14/25 Leighton Buzzard (YLB). Relevant parameters for each of the three sands are listed in Table 2.3 and grading curves are shown in Figure 2.6(b). Unless otherwise indicated, the values for Redhill 110 are obtained from Schupp (2009), the properties for LB DA30 are given by Sandford (2012) and those for YLB by LeBlanc *et al.* (2010a). The grading curve for YLB proposed in Figure 2.6(b) has been obtained by dry sieving relevant samples of the sand used for the experiments presented in this thesis.

The relative densities of the samples have been deduced by weighing the sand

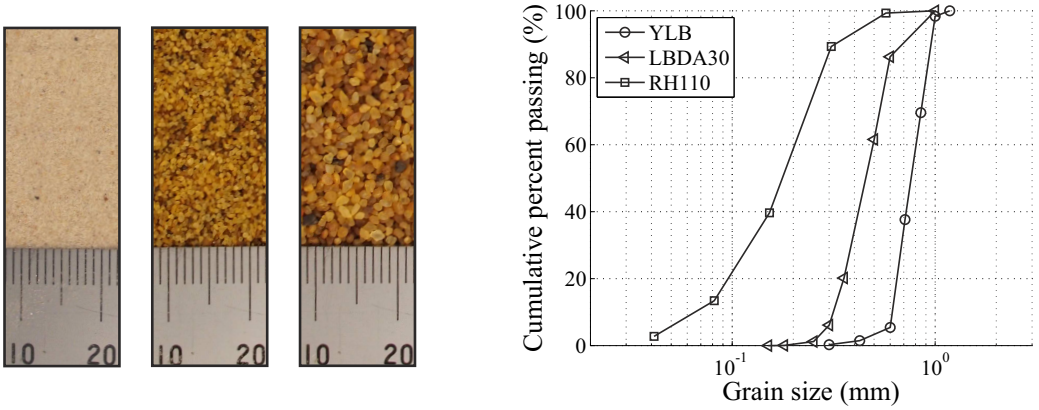

(a) (b)

Figure 2.6: (a) Pictures of the sand used for testing. From left to right: Red Hill 110, Leighton Buzzard DA 30 and Yellow Leighton Buzzard (Table 2.3) . (b) Grading curve for RH 110 sand (Schupp, 2009), LB DA30 (Sandford, 2012) and YLB (measured data)

Table 2.3: Properties of RedHill 110, Leighton Buzzard DA30 and Yellow Leigthon Buzzard

Property	Description	RH110	LBDA30	YLB
	Sand properties			
γ_{max} (kN/m^3)	Maximum dry unit weight	12.64	14.7	14.65
γ_{min} (kN/m^3)	Minimum dry unit weight	15.72	16.0	17.58
G_s (-)	Specific gravity	2.63	2.65	2.65
ϕ'_{cr} (degrees)	Critical angle of friction	36	34.3	34.3
d_{50} (mm)	Mean particle size	0.137	0.46	0.80
	Test sample properties			
R_d (%)	Relative Density	20	5	2

introduced into the tank and assuming that the sand placement procedure produced a homogeneous deposit. The average sample weights are: 254 $\pm$ 2 kg for Red Hill 110 , 285 $\pm$ 2 kg for Leighton Buzzard DA 30 and 284 $\pm$ 2 kg for Yellow Leighton Buzzard; leading to sample average relative densities of 20%, 5% and 2% respectively.

2.3.4 Test piles and installation

Four piles of the same length but different diameters were used during this research campaign (Table 2.4, Figure 2.5(e)). Most of the tests were performed using

Table 2.4: Model piles properties

Property	Description	Pile 1	Pile 2	Pile 3	Pile 4
L (m)	Pile embedded length	0.36	0.36	0.36	0.36
h_e (m)	Load eccentricity	0.43	0.43	0.43	0.43
D (mm)	Pile diameter	51	63	77	102
t (mm)	Wall thickness	1	1	2	1.5
E_p (MPa)	Modulus of elasticity	210	210	120	210

Table 2.5: Sand plug height inside the pile (as a percent of the embedded depth) for each sample and pile combinations (NA means that no test corresponding to this combination has been performed)

Pile No. / Sand	1	2	3	4
RH110	NA	NA	80% ± 1.5%	NA
LBDA 30	NA	NA	77% ± 2.5%	NA
YLB	82% ± 0.5%	85% ± 0.5%	69% ± 3%	91%

the copper pile No.3. The outer dimensions of this pile are scaled to 1:80 of a typical 3.6 MW turbine monopile (see Figure 2.3, p. 54), although it is geometrically similar to larger or smaller wind turbine piles.

During installation, the pile was fixed horizontally and gently driven into the sand sample using a rubber hammer (Figure 2.5(c)). When reaching the final penetration depth, the number of hammer strokes and the sand plug depth inside the pile was compared with similar tests for consistency. The sand plug height observed for each sample-pile combination is provided in Table 2.5.

2.4 Testing method

2.4.1 Typical procedures

The testing proposed in this thesis comprises four different categories: (1) monotonic loading, (2) single load reversal loading (hysteresis), (3) continuous cyclic and (4) multi-amplitude cyclic. Each category relates to specific testing procedure that are detailed below.

1) Monotonic loading: Preliminary monotonic tests are presented at the end of this chapter and involve either continuous or incremental loading. Continuous loading is achieved using the set-up described above with a large value of m_1. However, here, m_2 only balances the weight of the load-cell and m_3 now balances the weight of the main beam, rotor and m_1 when in minimum position. Accordingly, the main beam is horizontal when m_1 is in minimum position and this set-up enables for better control of 1-way loading and monotonic tests starting from zero. Incremental loading, or creep tests, are performed by simply hanging masses successively on the relevant side of the pile and the motor is therefore unused. For all the tests, the load step is 0.5 kg and the time step varies from 1 min to 15 min depending on the test.

2) Hysteresis loading: These tests correspond to perfectly symmetric two-way loading tests (where M_{min} exactly equals $-M_{max}$). Unfortunately, performing this type of tests using the "continuous set-up" is particularly difficult due to slight variations in set-up equilibrium during the first loading phase of the cyclic test (e.g. length of the wire, position of the main beam). Therefore, hysteresis tests have been carried out manually using the "incremental set-up", i.e. by adding and suppressing masses on the relevant side of the pile. Based on the monotonic loading tests, an appropriate time step was chosen, while the load step was kept at 0.5 kg.

3) Continuous cyclic loading: A subsequent part of the testing involved continuous cyclic loading. These tests were performed using the loading rig as described previously in Section 2.3, p.55, or using the same set-up as for continuous monotonic tests with smaller values of m_1 for one-way loading tests. It is noted that it is quite difficult performing exact one-way loading because of the accumulation of minute changes in set-up during the test. In the following, tests with $\zeta_c \in [-0.1, 0.1]$ will be considered as one-way. Some of the continuous cyclic tests were immediately followed by a monotonic test, employing the same experimental technique as for multi-amplitude cyclic tests.

4) Multi-amplitude cyclic loading: The last phase of testing involved cyclic

loading at different amplitudes. For these tests, the change of loads is a critical time where the pile must not be disturbed despite the changes in set-up. At this stage, the motor is first stopped when the main beam passes to minimum position and a removable screw is set for maintaining the main beam in this position. Some tests then involve re-calibration and re-positioning of the LVDTs to maximize the stroke range of the transducers (this is the case of all the cyclic tests that are followed by a monotonic test for example). When doing this, the other LVDT is used in order to double-check that the pile remains undisturbed. Then, the loading weights are carefully changed while the LVDTs output is monitored and verified. Finally, the screw is removed for the test to go on.

2.4.2 Relevant parameters for cyclic response

Cyclic loading is described in terms of ζ_b and ζ_c as defined in Chapter 1, Section 1.4 (p. 31). The amplitude and magnitude values and relevant cycle number of each continuous and multi-amplitude cyclic tests have been chosen according to the design limit states specified in Table 1.3 (p. 8). The initial loading-unloading cycle is denoted 0 (Figure 2.7(a)) and refers to the initial monotonic loading and hysteresis behaviour (c.f. Chapter 3, Section 3.2.1, p. 91).

In published literature, the results of cyclic loading tests are expressed either in terms of moment-rotation or load-displacement curves. Designers and turbine manufacturers usually express the pile deformation in terms of rotation, and therefore, it is easier to identify design tolerance values for the foundation tilt angle (see Chapter 1, Section 1.2, p. 14). Consequently, unless stated otherwise, the experimental results are usually presented in the moment-rotation parameter space. Also, in order to quantify the deformation due to cyclic loading only, the results will sometimes be expressed in terms of accumulated rotation $\Delta\theta = \theta_N - \theta_0$, such as originally defined by LeBlanc *et al.* (2010a) (see Chapter 1, Section 1.4, p. 32).

In addition to pile deformation, the relevant parameters used in this thesis to

describe the pile response to cyclic loading are the **secant stiffness** and the **loop area**. The definition of the secant stiffness used in this thesis departs slightly from that used by LeBlanc *et al.* (2010a) (Chapter 1, Figure 1.16, p.1.16), and is illustrated in Figure 2.7(a). Comparison of these two figures show that LeBlanc *et al.* (2010a) chose to characterise the cyclic stiffness from the maximum peak to the following minimum peak, while the definition selected in this thesis is from minimum to maximum. This definition was chosen in order to be coherent with the developments and notations then adopted in Chapter 5, and also, in order to be consistent between the definition of a cycle (see Figure 2.7(a)) and the corresponding definition of the stiffness for this given cycle. However, the author believes that the difference in definitions is sufficiently small that results from this experimental campaign can still be compared with those from LeBlanc *et al.* (2010a). Also, Figure 2.7(a) represents the definition of the loop area. While determination of the secant stiffness from experimental results is fairly straightforward, estimation of the loop area for cyclic loading tests is a more intricate task. One efficient and accurate way to do so is the "triangle method" and Figure 2.7(b) explains the procedure used for calculation. First, the closest downwards X_D and upwards X_U points to the loop intersection are identified, together with a reference point X_0. Then, the triangle area between the

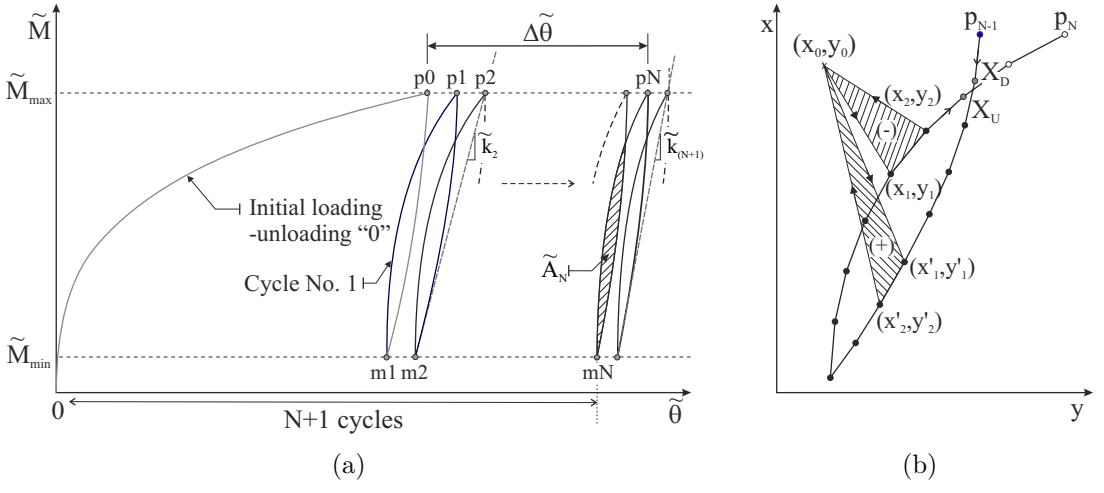

Figure 2.7: (a) Definition of cycle numbering, accumulated rotation, stiffness and loop area (b) Method for calculation of experimental loop area

reference point and two consecutive points between X_D and X_U (in this order) is calculated and the cycle loop area is simply deduced by summing all the triangle areas, accounting for their sign. The area exterior to the loop area naturally cancels, leaving the area enclosed by the unloading-reloading curve only. In the results presented in this thesis, the reference point X_0 was taken as p_{N-1} (Figure 2.7(a)).

Finally, it is worth mentioning that, as cycle "0" corresponds to initial - or monotonic - loading, the cyclic secant stiffness and loop area are only relevant for cycle number 1 and above.

2.4.3 Test programme

As highlighted in Section 2.4.1, the test programme performed during this research project can be divided in four parts: (1) monotonic loading, (2) hysteresis loading, (3) continuous cyclic and (4) multi-amplitude cyclic. Detail on each test campaign is provided in Tables 2.6 (Parts 1 and 2), 2.7 (Part 3) and 2.8 (Part 4) and meaning of the test name acronyms is provided in the Nomenclature (p. xiii). The tables indicate the testing procedure, the loading sequence, the sample conditions and pile geometry. For all creep tests (Parts 1 and 2, Table 2.6), the incremental time step is indicated within the brackets. Note that $(3/1min)$ means that 3 minute time-steps where performed during the loading phases while 1 minute time steps where selected for the unloading phases in order to achieve the experiments in a reasonable time frame. In Table 2.7, continuous cyclic tests followed by a monotonic test have been marked "-M" in the *Test method* cell. Finally, the load cases used for the multi-amplitude cyclic tests (Table 2.8) are listed in Table 2.9.

Each test campaign contributes to address the objectives previously listed in Table 1.7 (Chapter 1, Section 1.5, p. 42). The results of the test campaigns are displayed and analysed in the last section of this chapter (Part 1) and in corresponding sections of Chapter 3.

Table 2.6: Test Programme Parts 1 and 2: Monotonic loading and hysteresis tests

Test No.	**Test method**	**Pile No.**	**Sample**	**Loading description**
Part 1 - Monotonic tests				
MCr1	Creep (15min)	3	YLB	$M_{max} = 30Nm$
MCr2	Creep (3min)	3	YLB	$M_{max} = 30Nm$
MCr3	Creep (1min)	3	YLB	$M_{max} = 27Nm$
MCo1	Continuous	3	YLB	$M_{max} = 30Nm$
MCo2	Continuous	3	YLB	$M_{max} = 29.4Nm$
MCo3	Continuous	3	YLB	$M_{max} = 28.5Nm$
MCo4	Continuous	3	YLB	$M_{max} = 29Nm$
MD51	Creep	1	YLB	$M_{max} = 14.8Nm$
MD63	Creep	2	YLB	$M_{max} = 14.8Nm$
MD102	Continuous	4	YLB	$M_{max} = 29Nm$
MRH	Creep	3	RH110	$M_{max} = 25.3Nm$
MLB	Creep	3	LBDA30	$M_{max} = 27.4Nm$
Part 2 - Hysteresis behaviour				
H0	Creep (3/1min)	3	YLB	Symmetric reversed loading 1 cycle, ($M_{max} = 23.1Nm$)
HIM	Creep (3/1min)	3	YLB	Symmetric reversed loading increasing magnitudes 4 cycles, ($M_{max,cycles} = 10.7Nm$, $14.8Nm,\ 19.1Nm,\ 23.2Nm$)
HC	Creep (3/1min)	3	YLB	Symmetric reversed loading 3 cycles, ($M_{max} = 21.2Nm$)
HA1	Creep (3/1min)	3	YLB	Alternated 2-way/1-way same maximum load 8 cycles, ($M_{max} = 21.1Nm$)
HA2	Creep (1min)	3	YLB	Alternated 2-way/1-way same maximum load 4 cycles, ($M_{max} = 23.1Nm$)
H1IM1	Continuous	3	YLB	1-way loading increasing magnitudes 7 cycles, ($M_{max,cycles} = 8.2Nm$, $11.3Nm,\ 12.9Nm,\ 16.7Nm,$ $19.8Nm,\ 23.2Nm,\ 28.8Nm$)
H1IM2	Creep (3/1min)	3	YLB	1-way loading increasing magnitudes 5 cycles ($M_{max,cycles} = 10.7Nm$, $14.8Nm,\ 19Nm,\ 23.2Nm,$ $29.6Nm$)

Table 2.7: Test Programme Part 3: Continuous cyclic tests

Test No.	**Test method**	**Pile No.**	**Sample**	**Loading description**		
				ζ_b	ζ_c	N
Cyclic loading tests followed by Monotonic loading						
CMC1	Continuous-M	3	YLB	0.42	0.18	1
CMC2	Continuous-M	3	YLB	0.42	0.18	10
CMC3	Continuous-M	3	YLB	0.42	0.18	100
CMC4	Continuous-M	3	YLB	0.42	0.18	1000
CMC5	Continuous-M	3	YLB	0.42	0.18	10000
CMC6	Continuous-M	3	YLB	0.47	0.13	1000
CMC7	Continuous-M	3	YLB	0.47	0.13	10,000
CMLT1	Continuous-M	3	YLB	0.31	0.24	100,000
CMLT2	Continuous-M	3	YLB	0.42	0.18	100,000
CMLT3	Continuous-M	3	YLB	0.47	0.13	100,000
CMM1	Continuous-M	3	YLB	0.34	0.07	10
CMM2	Continuous-M	3	YLB	0.42	0.02	10
CMM3	Continuous-M	3	YLB	0.49	0.01	10
CMM4	Continuous-M	3	YLB	0.59	0.00	10
CMA1	Continuous-M	3	YLB	0.45	−0.21	1000
CMA2	Continuous-M	3	YLB	0.38	−0.55	1000
Complementary continuous cyclic loading tests						
CC1	Continuous	3	YLB	0.19	0.16	5500
CC2	Continuous	3	YLB	0.25	0.06	5300
CC3	Continuous	3	YLB	0.27	0.14	3300
CC4	Continuous	3	YLB	0.31	0.01	155,100
CC5	Continuous	3	YLB	0.35	0.27	7600
CC6	Continuous	3	YLB	0.45	0.46	17,000
CC7	Continuous	3	YLB	0.68	0.13	50
CCLB1	Continuous	3	LBDA30	0.23	0.25	7500
CCLB2	Continuous	3	LBDA30	0.26	0.18	7000
CCLB3	Continuous	3	LBDA30	0.19	0.32	8000
CCLB4	Continuous	3	LBDA30	0.24	0.14	21,800

Table 2.8: Test Programme Part 4: Multi-amplitude cyclic tests

Test No.	**Test method**	**Pile No.**	**Sample**	**Loading description**
Series of large load events				
MALL1	Continuous	3	YLB	$100 \times C - 10 \times D - 1 \times E$
MALL2	Continuous	3	YLB	$1 \times E - 100 \times C - 10 \times D$
MALL3	Continuous	3	YLB	$10 \times D - 1 \times E - 100 \times C$
MALL4	Continuous	3	YLB	$10 \times E - 100 \times C$
MALL5	Continuous	3	YLB	$100 \times E - 100 \times C$
MALL6	Continuous	3	YLB	$10 \times F - 100 \times C$
Combination of long-term small and short-term large load events				
MASL1	Continuous	3	YLB	$1000 \times A - 100 \times C - 1^{+} \times E$
MASL2	Continuous	3	YLB	$100 \times C - 1 \times E - 1000 \times A$
MASL3	Continuous	3	YLB	$1 \times E - 100 \times C - 1000 \times A$
MASL4	Continuous	3	YLB	$10,000 \times A - 100 \times C - 1^{+} \times E$
MASL5	Continuous	3	YLB	$1000 \times B - 100 \times C - 1^{+} \times E$
MASL6	Continuous	3	YLB	$900 \times A2 - 100 \times C2 - 1 \times E2 - 100 \times C2 - 900 \times A2 - 100 \times C2 - 1 \times E2 - 100 \times C2 - 9,500 \times A2$
MASL7	Continuous	3	YLB	$1,000 \times A2 - 1 \times (0.41, 0.26) - 500 \times A2 - 1 \times (0.45, 0.24) - 500 \times A2 - 1 \times (0.49, 0.09) - 500 \times A2 - 1 \times (0.54, 0.15) - 500 \times A2 - 1 \times (0.6, 0.11) - 500 \times A2 - 1 \times (0.62, 0.1) - 500 \times A2 - 1 \times (0.66, 0.1) - 6,500 \times A2$

Table 2.9: Load cases for multi-amplitude cyclic tests

Load case	ζ_b	ζ_c	Test Nos.
A	0.30	0.11	MASL1,2,3,6
B	0.38	0.08	MASL4
C	0.49	0.00	MALL1,2,3,4,5,6; MASL1,2,3,4,5
D	0.59	0.03	MALL1,2,3
E	0.69	0.00	MALL1,2,3,4,5; MASL1,2,3,4,5
F	0.83	0.00	MALL6
A2	0.31	0.29	MASL6,7
C2	0.51	0.15	MASL6
E2	0.72	0.10	MASL6

2.5 Monotonic test results

This section presents the test results, predominantly from the monotonic test campaign (Part 1, Table 2.6), that are used for (i) validation of the testing procedures, (ii) determination of relevant parameter values required for future analysis of the test results presented in Chapter 3, (iii) calibration of the numerical model parameters describing the monotonic curve in Chapter 5. Unless otherwise indicated, the test results are presented in their normalised form (denoted by a tilde) according to Table 2.1 (p. 51).

2.5.1 Parameters deduced from load-displacement curve

2.5.1.1 Ultimate capacity

Prior to the hysteresis and the cyclic tests, a static test was carried out to determine the ultimate capacity of the pile M_R. This parameter is used as a reference for the choice of the load magnitude in the cyclic loading tests (Definition of ζ_b, Equation 1.13, p. 31). An example of monotonic test results and determination of ultimate capacity for pile No. 3 in Yellow Leighton Buzzard sand is given in Figure 2.8 and the procedure is detailed below.

There is little information in the public domain concerning the appropriate definition of the pile failure criteria. This is because no clear failure behaviour appears on the moment-rotation curve and the pile, especially short rigid ones, accumulates displacement with load increase. The combined lateral and moment loading at ultimate limit state are commonly estimated by (i) calculating the theoretical design total lateral pile resistance and (ii) estimating "the lateral displacement at the pile head [and ensuring that it does] not exceed some specified limit" (DNV, 2014, p.172).

The theoretical total lateral pile resistance is assessed by vectorial integration of the lateral resistance over the length of the pile. Using the idealised stress distribution

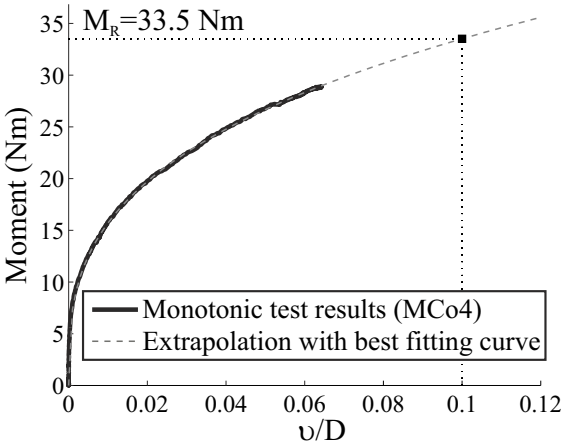

Figure 2.8: Determination of the ultimate capacity for test Mco4

Pile No.	1	2	3	4
RH110	-	-	23.9	-
LBDA 30	-	-	35.1	-
YLB	13.5	15.7	33.5	32.7

Table 2.10: Ultimate capacity values (Nm) for the the tests stated in Table 2.6

displayed in Figure 1.6(b) (p. 11), this gives for pile No.3 in Yellow Leighton Buzzard sand $M_{ult} = 64.8Nm$. Extrapolating the laboratory test results (cf. Figure 2.8), this would lead to a pile displacement at mud-line of $\upsilon_{ult} = 74\% \times D$, which is not acceptable in design.

Unfortunately, the design requirements in terms of ultimate displacement for large-scale turbine are usually confidential and are rarely divulged in published literature. Byrne *et al.* (2015b) (PISA project) propose an ultimate criteria defined by the minimum momentum resulting from a ground level displacement of $\upsilon_R = 10\% \times D$ and a ground level rotation of $\theta_R = 2\ degrees$.

This criteria was applied to the test results proposed in Table 2.6 and the results for test MCo4 are displayed in Figure 2.8. The stroke range for the LVDTs hardly never enables to reach the displacement or rotation limits. Consequently, for each loading curve, the initial portion was fitted and extrapolated to the requested pile displacement/rotation. Fortunately, all the test results match perfectly with a power law (see Figure 2.8 and later, Section 2.5.2.2, Figure 2.11). For all the monotonic tests performed during this experimental programme, the limiting criteria was the pile displacement and the results for each tested pile-sample combinations are provided in Table 2.10.

2.5.1.2 Initial moduli and elastic threshold

The initial elastic modulus E_{S0} is a key parameter for the research work described in this thesis. First, it is often used in design for the calculation of the structure eigenmodes and natural frequency. As a result, experimental work presented in Chapter 3 proposes to track its evolution with cyclic loading. This value is also one of the input values of the constitutive model developed in Chapters 4 and 5. The following also identifies the values of the tangent modulus E_{t0} and the elastic threshold M_{y0}, which will also be referred to in Chapter 3.

The initial modulus is established by fitting a linear law over the first few points of the loading curve (Figure 2.9). The tangent modulus is determined through the same process over the last few points. While these two moduli are usually straightforward to assess, determination of the elastic threshold is less clear. Since yield is a gradual process, the transition between elasticity and yield is usually smooth. There are a number of conventions available in published literature for the definition of the elastic threshold and one of the most widely used is the "0.2% definition" (Lemaitre and Chaboche, 2010). This states that the elastic limit is artificially picked so that the limit strain, when the loading curve departs from the initial elastic line, is equal

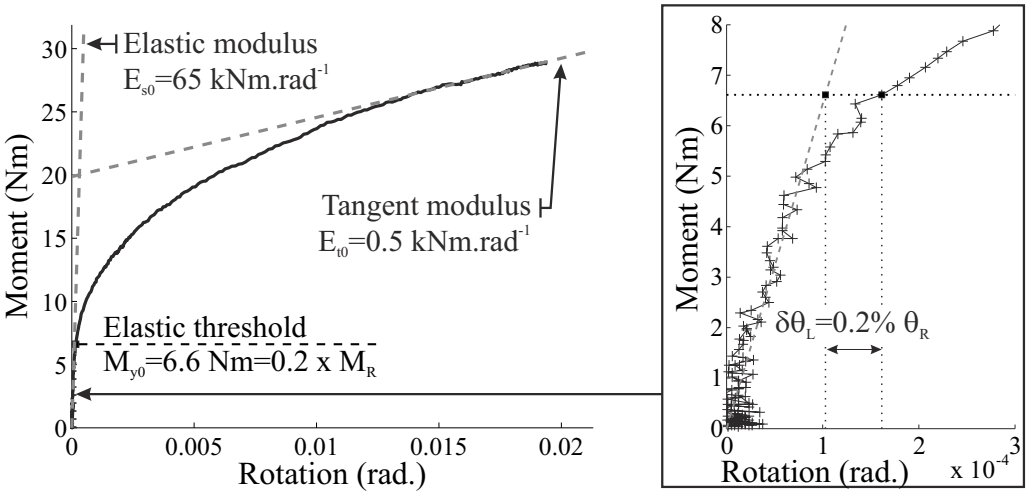

Figure 2.9: Elastic and tangent initial moduli plus elastic threshold for Pile No. 3 (Copper, D=77mm) in Yellow Leighton Buzzard (Test MCo4)

to 0.2% of the total strain at ultimate capacity.

In the following, the determination of these three parameters is only needed for pile number 3 in Yellow Leighton Buzzard (test MCo4, Table 2.6). The results are displayed in Figure 2.9 where the initial portion of the curve is also provided. The initial modulus is equal to $E_{S0} = 65kNm.rad^{-1}$, the tangent modulus to $E_{t0} = 0.5kNm.rad^{-1}$ and the elastic threshold to $M_{y0} = 6.6Nm$ corresponding to 20% of the pile ultimate capacity.

2.5.2 Repeatability and consistency

2.5.2.1 Reliability of testing procedures

A small number of tests were specifically performed to verify the repeatability and accuracy of the testing procedures. In the following, some of the hysteresis test results (initial loading only) are used to corroborate reliability of the incremental testing method. The results are displayed in Figures 2.10(a) and 2.10(b) and show very high consistency. To better present the step-wise plots, particularly when several results are superimposed, the inner curve is often used. This is justified later in Section 2.5.5 (p. 77).

Plotted on Figure 2.10(c) are the results of the four continuous monotonic tests. The graph shows that a very high accuracy is achieved during testing. Finally, Figure 2.10(d) relates to the continuous cyclic testing method. The accumulated displacement induced between two cycles of a cyclic test is very small. For example, for a cyclic test of load magnitude $M_{max} = 50\%\ M_R$, the accumulated rotation between cycle 1 and 2 is 60 times smaller than the rotation observed during a monotonic test. Consequently, minute differences in experimental set-up will have a larger impact on the cyclic test results than on the monotonic. However, Figure 2.10(d) shows that high quality results were obtained for the cyclic experiments.

Finally, it is noteworthy that, as mentioned in Section 2.3.2, the selected sampling

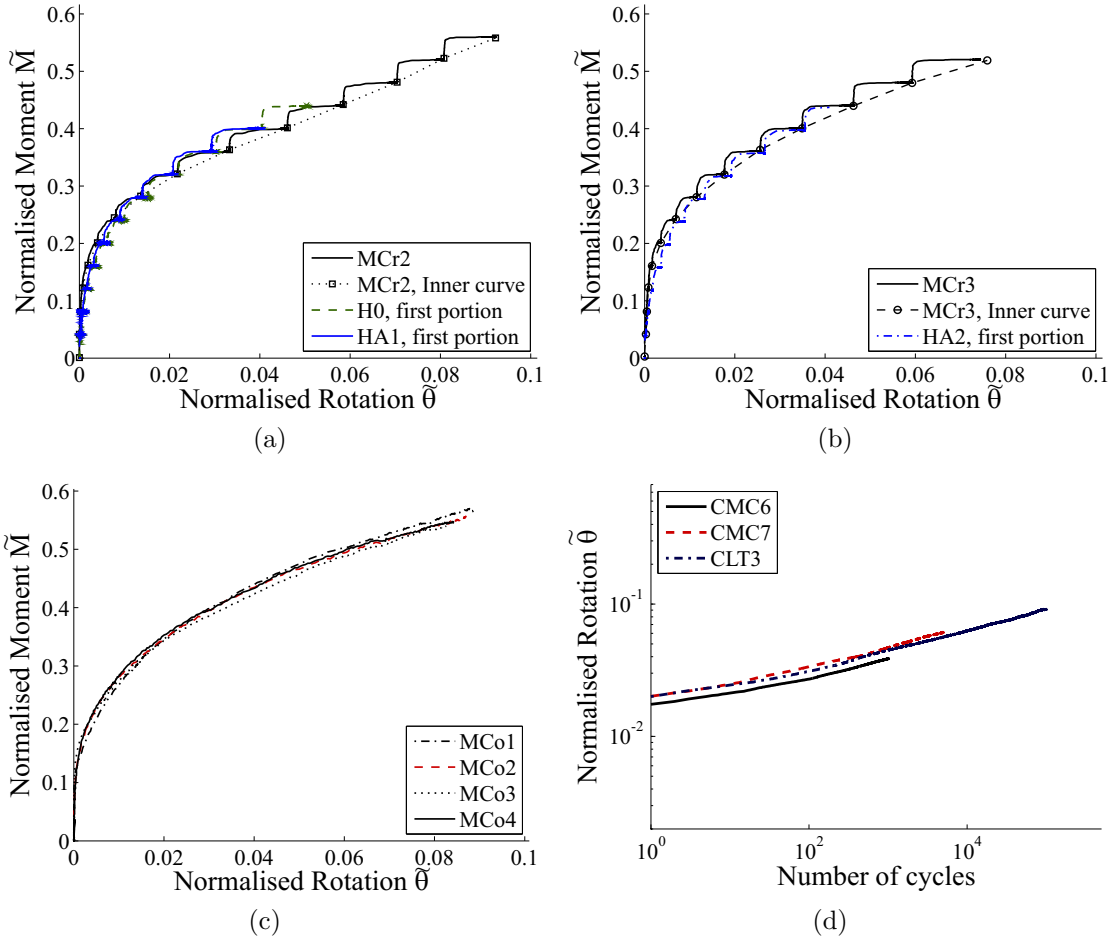

Figure 2.10: Illustration of the repeatability of the testing procedures for incremental tests with a (a) 3 min and (b) 1 min time step, (c) continuous monotonic tests and (d) continuous cyclic tests

rates are chosen so that maximum information can be extracted and continuous plots are obtained. For example, curve MCr3 on Figure 2.10(a) and curve MCo4 on Figure 2.10(c) consist of about 277,000 and 700 data points respectively.

2.5.2.2 Comparison with test results from literature

In addition to the repeatability of the testing procedure, it is also important to verify that the results are consistent with other experimental data available in literature. The selected published data were carefully chosen so that the final set of tests involved different load eccentricities (7 different h_e/L ratio), pile geometries (5 different L/D ratio), sample conditions (4 different relative densities and angle of

friction) and testing procedure (1-g and n-g). The properties of the selected tests are listed in Table 2.11. Given the published data, it was easier here to compare the pile displacement at the soil surface rather than the rotation. The results are compared in a normalised form, and in this case, normalisation of the moment load was achieved using the ultimate load capacity (M/M_R). This was found to neutralise the effects of different aspect ratio, load eccentricities and sample conditions, leading the test results to super-impose.

Figure 2.11 displays the results of the comparative study. The graph shows that the test results obtained from this test campaign compare favourably with results from the literature. It also shows that the monotonic test results can be captured with a power law according to:

$$\frac{M}{M_R} = 2.04 \cdot \left(\frac{\upsilon}{D}\right)^{0.31} \tag{2.15}$$

In this Equation, 2.04 and 0.31 are empirical parameters that have been estimated by calculating the average of the power law coefficients over the whole range of test

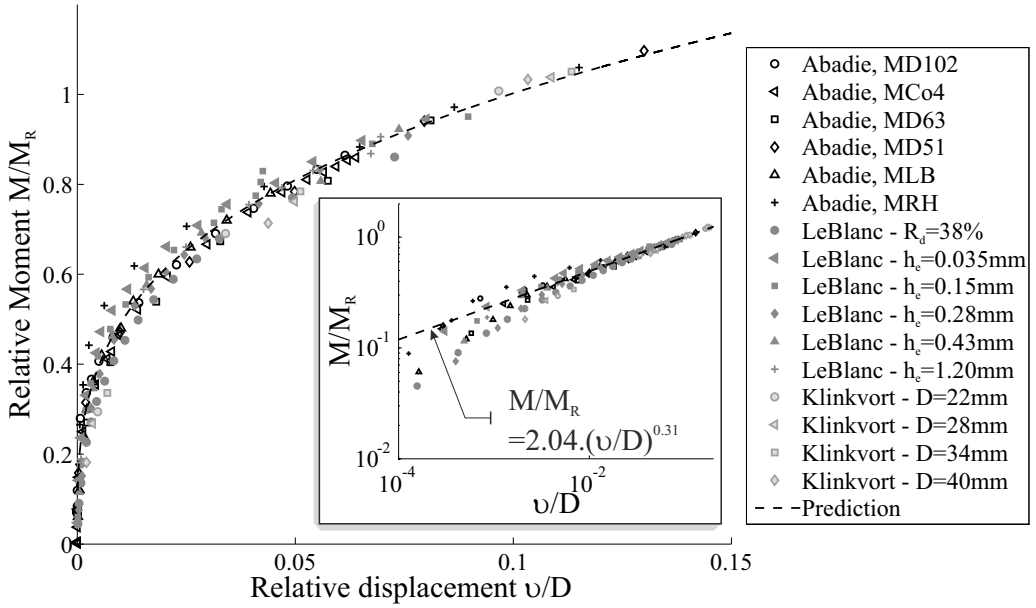

Figure 2.11: Comparative study of the monotonic test results with other published results from LeBlanc *et al.* (2010a) and Klinkvort (2012)

Test No.	Pile length (m)	Pile diameter (m)	L/D	Load eccentricity (m)	Submerged unit weight (kNm^2)	Relative density (%)
LeBlanc et al. *(2010a)*						
1	0.36	0.08	4.5	0.035	14.7	4
2	0.36	0.08	4.5	0.15	14.7	4
3	0.36	0.08	4.5	0.28	14.7	4
4	0.36	0.08	4.5	0.43	14.7	4
5	0.36	0.08	4.5	1.2	14.7	4
15	0.36	0.08	4.5	0.43	15.6	38
Klinkvort (2012)						
22	0.132	0.022	6	0.33	16.4	90
23	0.168	0.028	6	0.42	16.6	90
24	0.204	0.034	6	0.51	16.6	90
25	0.240	0.040	6	0.60	16.4	84

Table 2.11: Relevant properties of the monotonic tests selected from LeBlanc *et al.* (2010a) and Klinkvort (2012)

results. This expression will be used in the next section, as well as in Chapter 5.

2.5.3 Grain size effect

The model and prototype sands are assumed to have similar particle size, and therefore, the ratio between the pile diameter and grain size might be an issue. Studies on the effect of particle size on lateral response have been reported in published literature for long slender piles. Hoadley *et al.* (1981) state that a minimum pile diameter to mean grain size ratio of 50 must be adopted to suppress particle size scaling effects, Remaud *et al.* (1998) recommend a minimum ratio of 60. Klinkvort (2012) recently updated this framework for short rigid piles and found that this ratio should be at least 88. However, all of these studies involved centrifuge testing. Consequently, it was judged useful to conduct a short series of tests to verify that the grain size has no effect on the results for 1-g testing, in particular, in the case of Yellow Leighton Buzzard (YLB) which has a high mean particle size.

Most of the tests conducted during this test campaign were indeed performed

with YLB and pile number 3. The ratio between pile diameter and average grain size diameter in this case is 96. In order to address the issue of grain size effect, a monotonic test with a sand of very similar properties and twice smaller particle size (Leighton Buzzard DA30, LBDA30) has been performed (Table 2.3, Figure 2.6(b), p. 59). This sand comes from the same quarry as YLB and the sample preparation with this sand leads to a similar relative density and angle of friction. In addition, a third test involving a much finer sand with different properties (Red Hill 110, RH110) has been performed to complete this framework. The sample obtained with this sand is still loose but of higher relative density and angle of friction (see Table 2.3, p. 59).

The results of the tests are displayed in Figure 2.12(a). First, the results obtained with YLB and LBDA30 are comparable and the small difference observed can be attributed to experimental error. This shows that grain size does not have an effect on the experimental results presented herein. In addition, results obtained with RH110 depart from the two other plots, proving that the relative density and angle of friction have a significant impact on the pile response, even at low relative densities. This had already been reported by LeBlanc *et al.* (2010a) and Peralta (2010) but no specific test campaign has been reported yet to investigate this phenomenon in more detail.

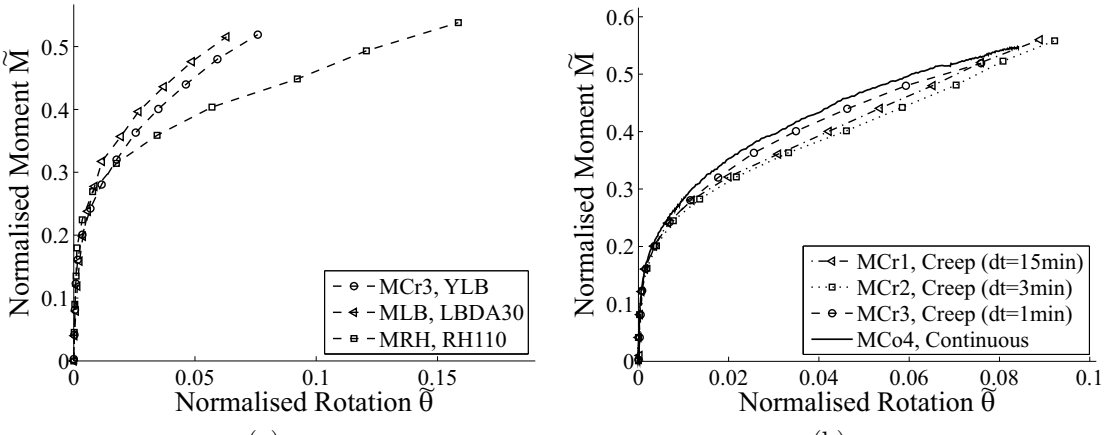

(a) (b)

Figure 2.12: (a) Results of the static tests with different sand samples (Table 2.6: MCo4, MLB, MRH). (b) Influence of creep on model pile response

Finally, tests using the three sands in dry loose/very loose conditions are all found to exhibit a similar trend that matches a power law. This is also illustrated in Figure 2.11, showing that the general behaviour of the foundation is not affected by sample conditions. It would be useful in the future to extend this conclusion to partially drained and undrained conditions and to layered soil samples.

2.5.4 Pivot point depth

Assuming that the pile does not translate, the relationship between pile displacement and rotation therefore relies on the pivot point depth. Its value can be deduced from the LVDT measurements and results for the monotonic tests listed in Table 2.6 are given in Figure 2.13(a). They are compared with the original data used for LeBlanc *et al.*'s paper (2010a). A repartition function of the pile pivot point depth among the test results is provided and shows that the piles pivot at about 70% of the pile embedded depths. Interestingly, the test results plotted here involve a range of pile geometries and eccentricities and also various sample properties. This proves that the pile pivot point depth is likely to be independent of these parameters.

Finally, Figure 2.13(b) displays the evolution of the pivot point depth during three long-term cyclic tests. The graph shows that it slightly increases during the

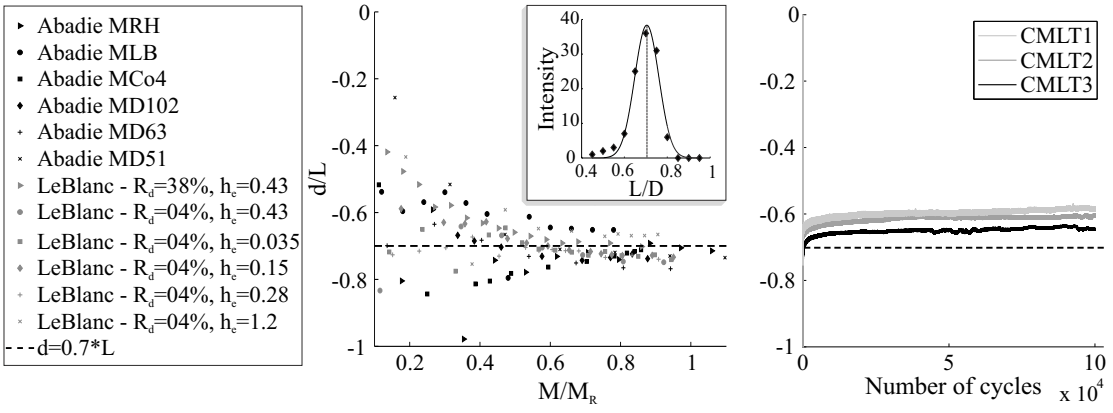

(a) (b)

Figure 2.13: Pivot point depth for a range of (a) monotonic tests listed in Table 2.6 and tests from LeBlanc *et al.* (2010a) (b) relevant cyclic tests in Table 2.7

first few cycles of the loading history and then stabilises.

2.5.5 Loading rate effect

The response of the soil to shearing can possibly involve rate-dependency effects. Creep is indeed expected when the pile is subjected to steady wind loads while instantaneous response might be observed when a large impulse load is generated by a large wave. This effect is often discarded in design and very few data are presently available in published literature to address this phenomenon.

For correlation of the data from the continuous and incremental tests, it is important to better understand this phenomenon and verify that rate-dependency will not affect the results for the selected load frequency and that the trends are comparable. For this purpose, incremental tests involving a range of different time steps have been performed and plotted against continuous test data. The results are displayed in Figure 2.12(b). While the plots do not exactly superimpose, there is no significant differences between the test results and the small disparity between curves is within experimental error (less than 10%). This shows that tests with the creep phases do mimic a continuous load of 0.1 Hz. This means that for this particular pile geometry, sample conditions and load frequency, rate-dependency effects are not relevant and can be discarded. This also justifies the fact that the inner curve is the most pertinent simplification of the incremental test results.

This phenomenon can also be studied directly from the step-wise plots of Figures 2.10(b) and 2.10(a). The initial portion of each load step corresponds to transition in load application whereas the horizontal portion, corresponds to creep (see Figure 2.14). At the end of the load step, and after a certain time, the points finally all superimpose and the pile is not moving any more. For clarity, Figure 2.14 also displays the applied moment as a function of time and reports the transition and creep phases of the loading curve. According to monitored results from test MCr3, for each load step, the load transition (jump portions of the curve) takes place in about

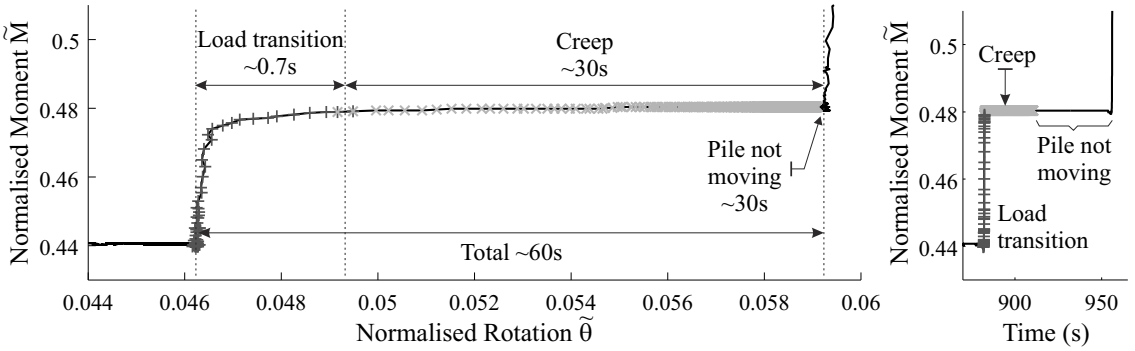

Figure 2.14: Analysis of a load step (Test MCr3; sampling frequency = 106Hz)

0.7 seconds while the complete creep response takes about 30 seconds. Therefore, rate-dependency effects would only be significant in this case when loading at a much faster rate in the order of 1 Hz. This also illustrates that rate-dependency effects might actually be relevant for large-scale prototypes and impact loads at much faster rate might induce less deformation and a stiffer response. Also, different soil conditions will probably involve different rate effects, especially with the presence of water and the possibility of getting partially drained or un-drained response of the soil. Design of the loading rig should be modified in future in order to investigate rate effect in more detail.

2.6 Implications for *p-y* method

This final section discusses the application of conventional design methodologies presented in Chapter 1, Section 1.3 (p. 14) for modelling the monotonic response observed in the laboratory. The three p-y curves expressions presented in Chapter 1, Section 1.3.4. (p. 21) (Reese *et al.*, 1974; DNV, 2014; Kallehave *et al.*, 2012) have been applied to model the monotonic response of the copper model pile in loose yellow Leighton Buzzard sand and compared to the experimental data from test MCr3 (Table 2.6, p. 65). Since there is presently no guidelines regarding the shearing force at pile tip, this component has been fixed to zero initially. The results are displayed in Figure 2.15 and plotted in the horizontal force-displacement space

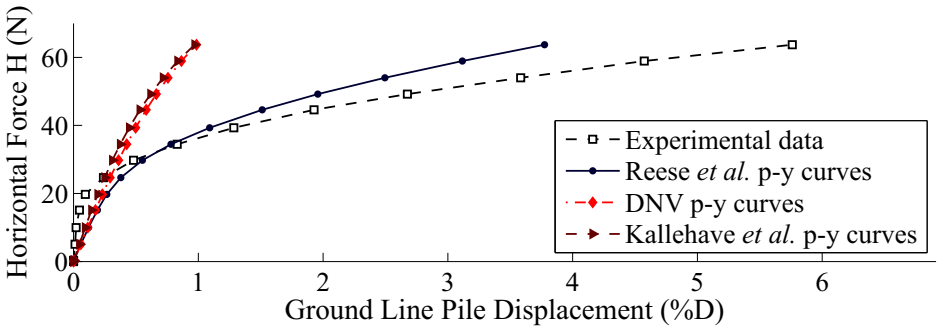

Figure 2.15: Experimental results compared with predictions from classical p-y curves for test MCr3

for consistency with other results on the p-y method published in literature. The graph shows that none of the current p-y curves expression closely predicts the macro-response of the model pile. In particular, while Reese et al.'s curve is not too far from the test results, the DNV expression is much stiffer than the actual response, proving that the p-y curve expression probably needs to be revised for this case.

Additionally, when considering the rigid pile equilibrium, the fact that the base shear is currently ignored infers that the sum of the forces are unbalanced. This is obviously unacceptable and therefore an expression for the shearing force at pile tip is required in order to equal the sum of the forces to zero. This is investigated later in this Section.

This section therefore proposes a very short study, aiming at re-working the expression of the p-y curves in order to match the experimental results from the monotonic test MCr3, while accounting for the base shear force at pile tip. Note that the corresponding conclusions and results do not pretend to derive a suitable framework for prediction of pile response to static loading and the objective here is not to discuss the methodology employed. The aim is solely to find a decent p-y approach that provides a close match of the backbone curve as this is a precondition for the following work on cyclic loading. Hence, the results from this section will then be used as a modelling base for the developments of the Degradation Stiffness Model to predict cyclic loading test results (Chapter 3, Section 3.3.2, p. 109).

2.6.1 Case of rigid piles

In the case where the pile is perfectly rigid (i.e. does not bend), it is possible to deduce a suitable expression of the soil reaction curves based on experimental data and equilibrium equations.

2.6.1.1 General equilibrium equation

In the following, the action of the vertical loads on the pile is discarded and the moment at pile tip is taken equal to zero. The external forces acting on the pile are the horizontal force and moment loading at the top, the shearing force at pile tip and the distributed soil reaction on pile shaft (Figure 2.16). The moment and force equilibrium therefore give:

$$H_t + H_e - \int_0^L p_y(x,y)\,\mathrm{d}x = 0 \tag{2.16}$$

$$-M_t + H_e L - \int_0^L p_y(x,y)x\,\mathrm{d}x = 0 \tag{2.17}$$

Combining Equations 2.16 and 2.17 to suppress H_e, it then comes:

$$\int_0^L p_y(x,y)(x-L)\,\mathrm{d}x = M_t + H_t L \tag{2.18}$$

The above equations are valid for both rigid and flexible piles.

2.6.1.2 Rigid pile hypotheses

In the case of perfectly rigid piles, the deflection is a linear function of the depth (Figure 2.16) according to:

$$y(x) = tan(\theta)(\alpha L - x) \simeq \theta(\alpha L - x) \tag{2.19}$$

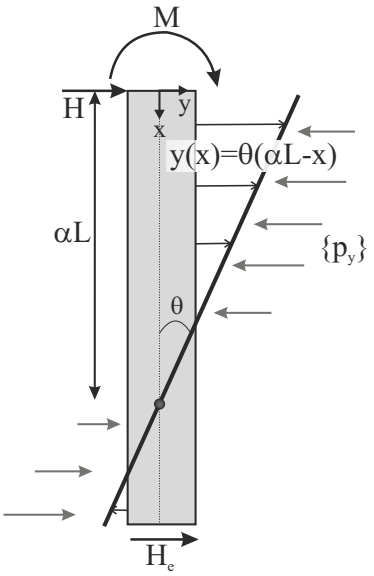

Figure 2.16: Global equilibrium equation of a laterally loaded rigid pile

where θ is the pile rotation and is constant with depth and $d = \alpha L$ is the pivot point depth. Equation 2.19 is valid only for small displacements of the pile where θ remains small (i.e. $\theta \ll 1$). This is the case for all test results considered in this thesis, and should also be the case of full-scale offshore wind monopiles.

Figure 2.13(a) (Section 2.5, p. 76) demonstrated that the location of the pivot point depth was constant and equal to about 70% of the pile length, irrespective of the soil conditions, load eccentricity or pile diameter. It is therefore assumed that $\alpha = 0.7$. Substituting Equation 2.19 within Equation 2.18, θ is now expressed as a function of $p(x, \theta)$.

2.6.1.3 Expression of the soil response $p(x, y)$

For a given expression of $p(x, y)$, it is then possible to deduce an analytical expression for θ from Equation 2.18. Through comparisons to the experimental data, a range of p-y curve expressions can be evaluated until a match with the experimental results is obtained. This requires that the expressions of p selected are integrable within $[0, L]$ and, preferably, simple enough so that they can directly be integrated using classical solver (or analytically).

Figure 2.11 (Section 2.5.2.2, p. 73) showed that the pile response to monotonic loading could, in a wide range of small scale model test cases, be accurately captured using a power-law. Accordingly, in order to account for the ultimate pressure of the soil response and conform with the DNV guidelines, $p(x, y)$ is expressed as:

$$\begin{cases} p(x) = k_y x, & y \leq y_e \\ p(x) = sign\left(\dfrac{y}{y_c}\right)\dfrac{Ap_u}{2}\left(\dfrac{|y|}{y_c}\right)^{m_p}, & y_e < y \leq 8y_c \\ p(x) = Ap_u, & y > 8y_c \end{cases} \tag{2.20}$$

where Ap_u is given by the DNV guidelines for sand (see Chapter 1, Equation 1.11, p. 22), k_y is the modulus of subgrade reaction (Chapter 1, Figure 1.12(a), p. (a)), and $y_u = 8y_c$ is the lateral displacement required to mobilise ultimate soil response. The initial linear portion of the curve is required to ensure that the initial modulus of soil reaction is not equal to infinity. y_e is then the elastic limit and is given by continuity of the p_y function. m_p is an empirical exponent.

Substituting Equation 2.19 within the above for $y_e < y < 8y_c$ then yields:

$$p(x) = sign\left(\frac{\alpha L - x}{y_c}\right)\frac{Ap_u}{2}\theta^{m_p}\left(\frac{|\alpha L - x|}{y_c}\right)^{m_p} \quad ; \quad for \;\; y_e < y \leq 8y_c \tag{2.21}$$

Now, integrating p between 0 and L and replacing within Equation 2.18 gives:

$$\begin{cases} \theta = \left(\dfrac{M_t + H_t L}{F}\right)^{\frac{1}{m_p}} \\ F = \displaystyle\int_0^L \frac{Ap_u}{2} sign(\alpha L - x)(x - L)\left(\frac{|\alpha L - x|}{y_c}\right)^{m_p} \mathrm{d}x \end{cases} \tag{2.22}$$

where F is a non-zero constant and $M_t = h_e \times H_t$. The results from Figure 2.11 and Equation 2.15 (Section 2.5.2.2, p. 73) give $m_p \simeq 1/3$. The value of y_c is more difficult to assess but can be optimised to match experimental results for each test. Reese *et al.* (1974) suggest that the soil reaches ultimate failure for $y_R = 3D/80$ and therefore, at the end of each optimisation process, the value of $8y_c$ is compared with

the corresponding value of y_R for validation of the order of magnitude.

Finally, it is interesting that the expression obtained in the end for $p(x, y)$ is very similar to that used for clay in current practice, with the same value for the power-law exponent (see DNV, 2014).

2.6.1.4 Consideration of base shear

As identified, there is no recommended expression for the shearing force at pile tip. However, it is an important loading component for laterally loaded rigid piles. Considering Equations 2.16 and 2.17, the value of H_e can now be deduced from the selected expression for $p(x, y)$:

$$H_e = \int_0^L p_y(x, y)\,\mathrm{d}x - H_t \tag{2.23}$$

The above expression holds true for both rigid and flexible piles and can easily be calculated using a standard solver. Therefore, one possible option for calculating the shear force at the pile base is to directly implement Equation 2.23, thus ensuring that the equations are balanced. When applied to flexible piles, e.g. the Mustang Island test case, it is logically found that Equation 2.23 gives $H_e = 0$.

Another intuitive option would be to consider that the soil response at the pile tip is very similar to that around the pile shaft; therefore, the expression for the shear force at the pile base, also called Q-y curve, is that of the p-y curves. The pressure term $Ap_u/2$ is then replaced by the shear force at the tip multiplied by the area enclosed by the end of the pile, accounting for direction of loading. However, to apply this method, further investigation of the lateral and moment loads acting on the pile, and their expressions, are needed in order to balance the sum of the forces. For this reason, this approach was not followed any further, and Equation 2.23 was used instead.

2.6.2 Application and validation

The finite difference framework outlined in Chapter 1, Section 1.3, p. 19 is now used in combination with the new p-y curve expression (Equation 2.20) for the prediction of a range of experimental data. For each set of experimental data, the value of y_c is optimised to obtain the closest match to experimental results.

First, the procedure has been benchmarked against the Mustang Island test case (Table 1.5, p. 1.5). Figure 2.17(a) shows a comparison between the power law p-y expression as proposed in Equation 2.20 with the conventional p-y curves presented previously in Chapter 1, Section 1.3 (p. 22). The outcome of the optimisation routine gives $8y_c = 0.053 \times D$ which compares with $y_R = 3/80 \times D = 0.037 \times D$. Figure 2.17(b) demonstrates that Equation 2.20 can be adapted for capturing flexible pile response and enables a close prediction of the Mustang Island test results.

Similarly, the above has been applied to the laboratory test MCr3 (Table 2.6, p. 65). The results are displayed in Figures 2.18(a) - (d) and have been obtained with $8y_c = 0.069D$. First, the curves on Figure 2.18(a) display the various forms of the p-y curves mentioned previously in the case of the laboratory rigid pile. Finally,

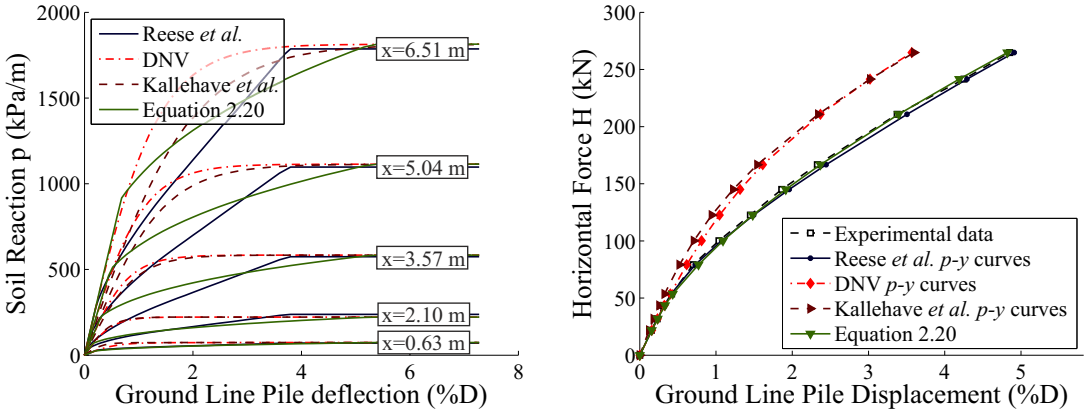

(a) (b)

Figure 2.17: (a) Reese *et al.* (1974), DNV (2014), Kallehave *et al.* (2012) and Equation 2.20 p-y curves plotted at relevant selected depth (towards the top of the pile) for the test case of Mustang Island (Cox *et al.*, 1974) (b) Mustang Island pile deflection at Mudline: numerical simulations compared with experimental results

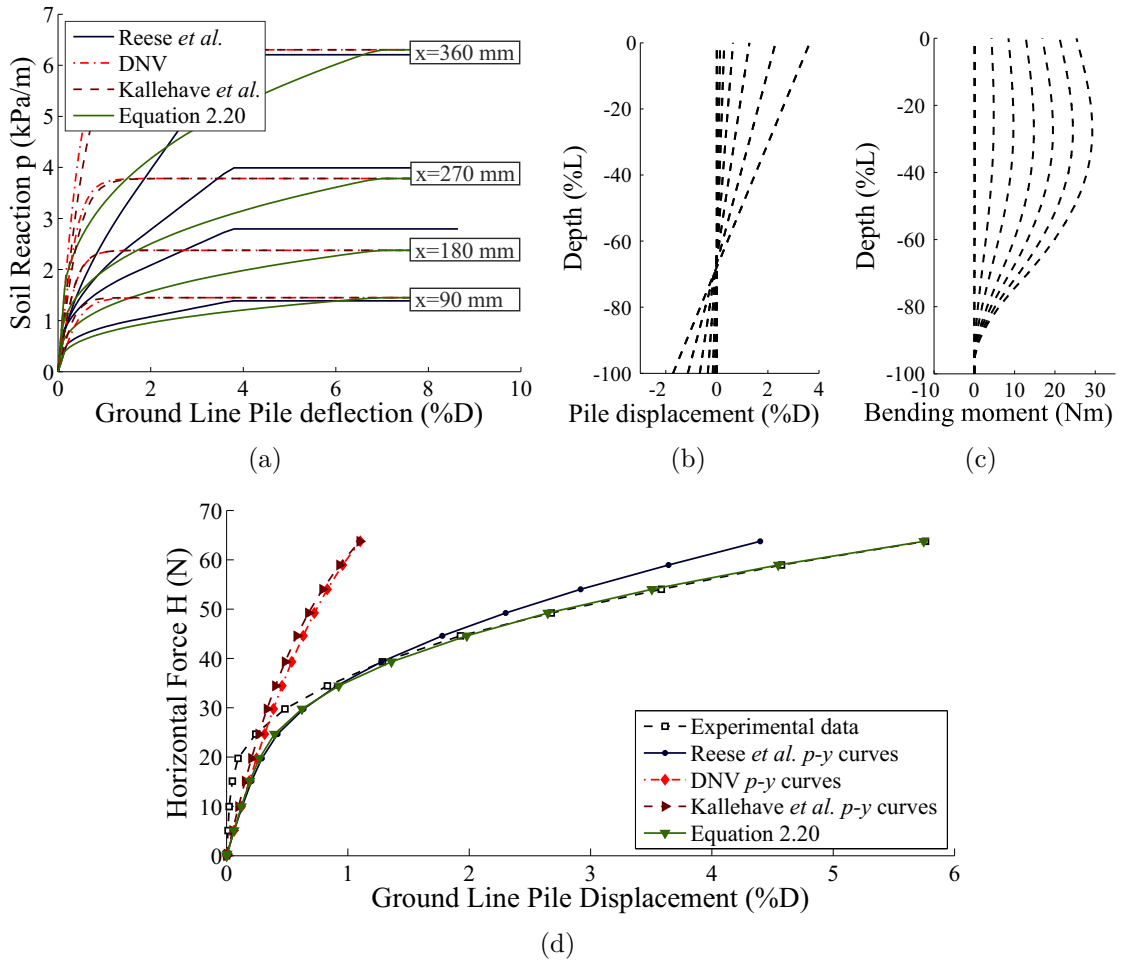

Figure 2.18: Laboratory test case MCr3: (a) Comparison between different expressions of *p-y* curves. Distribution of (b) Pile displacement and (c) bending moment down the pile. (d) Prediction of pile head displacement using the different methods

Figure 2.18(d) shows the compared prediction from Equation 2.20 with the other *p-y* methods, demonstrating that Equation 2.20 enables a close match to experimental results. For all these computations, the shear base at pile tip was deduced from Equation 2.23. Finally, Figures 2.18(b) and 2.18(c) display the pile displacement and bending moment distribution down the pile at different stages of loading obtained with the power-law method and show that the obtained response is perfectly rigid.

In conclusion, Figures 2.19(a) - (d) display experimental data and predictions using Equation 2.20 for a range of experimental test results from this research programme (Table 2.6) and from the literature. The published test results are those of LeBlanc *et al.* (2010a) and Klinkvort (2012) previously detailed in Section 2.5,

Table 2.11 (p. 74), plus one test on a flexible pile from Verdure *et al.* (2003) (Table 2.12). The range of tests chosen covers different testing procedures (1-g (LeBlanc *et al.*, 2010a), n-g (Klinkvort, 2012; Verdure *et al.*, 2003)), pile dimensions and flexibilities (rigid (LeBlanc *et al.*, 2010a; Klinkvort, 2012), flexible (Verdure *et al.*, 2003)) and soil conditions. The optimised value of $8y_c$ for rigid piles (LeBlanc *et al.* (2010a); Klinkvort (2012) and tests from Table 2.6) is between $0.019D$ and $0.411D$ with an average and median values equal to $0.19D$ and $0.15D$ respectively. The selected results unfortunately are not adapted for investigating the expression of y_c

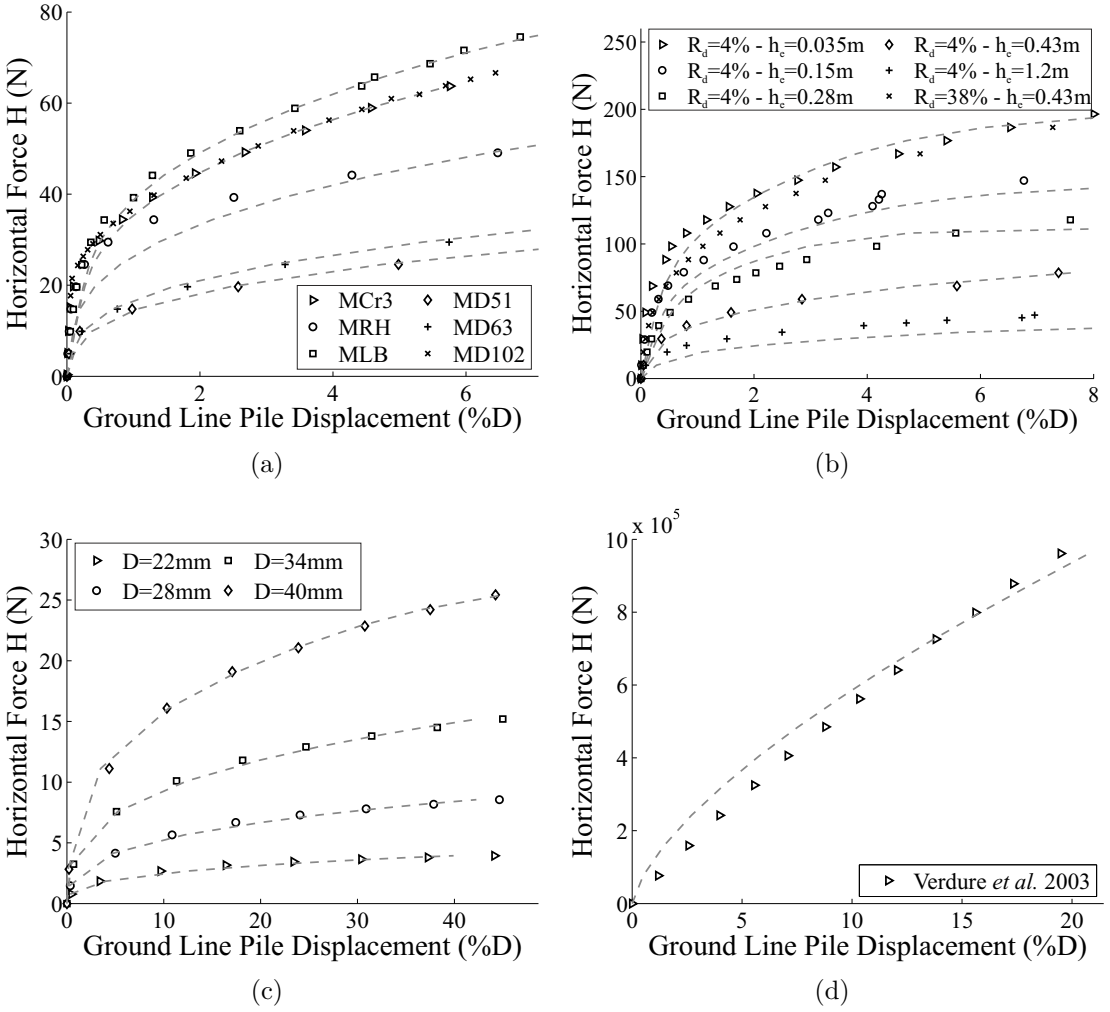

Figure 2.19: Comparison between experimental results (scattered points) and predictions using Equations 2.20 and 2.23 (dashed lines) for a range of relevant tests from (a) Table 2.6, (b) LeBlanc *et al.* (2010a), (c) Klinkvort (2012) and (d) Verdure *et al.* (2003) (Monotonic portion of Figure 6)

Test No.	Pile length (m)	Pile diameter (m)	L/D	Load eccentricity (m)	Submerged unit weight (kNm^2)	Relative density (%)
C1-40	12	0.72	16.7	1.6	16.3	95

Table 2.12: Relevant properties of the tests selected from Verdure *et al.* (2003)

any further and more work would be required to replace the optimisation procedure by a more rigorous approach. Nevertheless, the graphs show that satisfactory predictions can be obtained using Equation 2.20 and therefore, this formulation was retained for the following development of the Degradation Stiffness Model. As stated at the beginning of the section, the *p-y* curves expression proposed should not strictly be applied to ranges outside of that considered herein and the methodology for static loading probably needs much further investigation in future. Suggestions for future research directions will be detailed in Chapter 6.

2.7 Conclusions

This chapter described the testing equipment and methodologies employed during this research programme. Aspects of scaling for the design of laboratory 1-g model tests were also discussed and a summary of the normalised parameters can be found in Table 2.1 (p. 51). A comprehensive and detailed test programme has been provided in Table 2.6 (p. 65) and will be frequently referred to in the following chapters of this thesis. The test campaigns are divided into four phases: (1) monotonic loading, (2) hysteresis loading, (3) continuous cyclic and (4) multi-amplitude cyclic, and the test programme table is organised accordingly.

In addition, preliminary test results were presented, involving predominantly results from the monotonic test campaign. The key outcome from the research work presented in this chapter relates to rate-dependency effects and creep. It was found that the pile response to the range of loading frequencies investigated here is not

affected by rate effects and this conclusion will be used later in Chapter 5. Also, the monotonic test results were used for the development of a *p-y* curve expression, adapted for capturing both flexible and rigid pile response. A summary of the experimental findings outlined in Section 2.5 is provided in Table 2.13.

Table 2.13: Summary of preliminary test conclusions

Conclusions	**Tests No.**	**Figures No.**
1) Testing procedures are reliable and repeatable	MCr2-3, HA1-2, H0, MCo1-4, CMC6-7, CLT3	2.10(b) - (d)
2) Monotonic test results compare with experimental data extracted from literature and match a power law: $M/M_R = 2.04 \cdot (v/D)^{0.31}$	MD102, MD63, MD51, MRH, MLB, Mco4	2.11
3) Grain size has no effect on experimental results presented in this thesis	MCr3, MLB, MRH	2.12(a)
4) Creep has no effect on pile responses presented in this thesis but might become significant for faster loading rates and different sample conditions	MCr1-3, MCo4	2.12(b), 2.14
5) Laterally loaded piles pivot at about 70% of embedded depth, independently of loading conditions, pile geometry and sample properties. This tends to develop with cycle number.	MD102, MD63, MD51, MRH, MLB, MCo4, CMLT1-3	2.13(a),(b)
6) A power law expression for the *p-y* curves with a power exponent of 1/3 enables to closely predict flexible and rigid pile response to monotonic loading (Equation 2.20, p. 82)	MCr3 + range of tests from Table 2.6 and published literature	2.17(b); 2.18(d); 2.19(a)-(d)

Chapter 3

Experimental Pile Testing: Cyclic Loading

3.1 Introduction

The description of the non-linear cyclic behaviour of the foundation using theoretical and numerical models requires an understanding of the key mechanisms driving the pile response. As described in Chapter 2, this is achievable using 1-g model testing with the experiments listed in Tables 2.6, 2.7 and 2.8 (p. 65-67) specifically focused towards this objective. This chapter presents both the results and an analysis of the hysteresis tests, along with the continuous and multi-amplitude cyclic tests (Parts 2 to 4 of Tables 2.6, 2.7 and 2.8). The aim is to use the key findings as a basis for the constitutive model development in Chapters 4 and 5.

As described in Chapter 1, the data currently available in published literature focus on empirical descriptions of the accumulated rotation and change of secant stiffness with cycle number. Very little information is available on the detailed elasto-plastic behaviour of the soil-pile interaction during the cyclic loading. In particular, the development of a constitutive model that adapts with cycle number requires knowledge of the hysteretic response, evolution of the elastic modulus, plastic limit and monotonic response with increasing load and cycle number, as well as detailed analysis of the ratcheting behaviour. Beyond constitutive modelling, these provide

important inputs that determine the evolution of the fundamental mode of vibration, the soil hysteresis damping and the deformation of the foundation and hence, are essential for the development of future fatigue design guidance.

The outline of this chapter follows that of Tables 2.6-2.8. First, the hysteretic behaviour of the pile is investigated through experiments that involve targeted load cases, with very few load cycles. This section provides fundamental material on the pile response that can then be developed further for long-term cyclic loading. Experimental results on continuous cyclic loading are then split into two sections. The first focuses on the cyclic loading response and gives additional details on the evolution of the pile deformation, secant stiffness and hysteresis loop area. It also proposes an interpretation of the results using the p-y method supplemented with the Degradation Stiffness Model. The second section then presents an analysis of the results of monotonic tests performed immediately after the continuous cyclic tests. Finally, the findings from the earlier sections are extended to multi-amplitude cyclic loading, with load cases relevant for alternating operational-storm type loading. The final section discusses the implications of the recent findings for the design of offshore wind turbine monopiles. The test name acronym meanings are listed in the Nomenclature (p. xiii).

Unless otherwise indicated, the experimental data are presented in their normalised form according to the framework presented in Chapter 2, section 2.2 (see summary in Table 2.1, p. 51). The only exception is the normalised moment which is presented in this chapter as a fraction of the static capacity M/M_R.

3.2 Hysteretic behaviour

As demonstrated in Chapter 1, soil hysteresis damping can significantly influence the fatigue response of the offshore wind turbine structure. This is an area that has been poorly investigated so far. In the following section, experiments involving

symmetric 2-way loading are presented, with the aim of identifying the plastic and hysteretic response of the rigid pile. The test campaign presented here is described in the second part of Table 2.6 (p. 65). Test H0 involves a single 2-way loop and is used as a reference response. The subsequent test results investigate the effect of load increase (test HIM), cycle number (test HC), and cyclic loads at non-zero mean loads (tests HA1,2 and H1IM1,2). The fundamental hysteretic behaviour, which determined the starting point for the development of the theoretical model presented in Chapter 4, is derived from the test results displayed in this section.

3.2.1 Masing rules

The plastic behaviour of non-degrading materials is commonly modelled under the principles of kinematic and isotropic hardening (separately or combined). Kinematic hardening describes a translation of the yield surface with load increase while isotropic hardening accounts for a change in shape and size of this surface. The typical response and differences between the two mechanisms is illustrated in Figure 3.1. While conceptually recognisable, the experimental method to demonstrate how active the two mechanisms are, is not always obvious. Yet, it is legitimate to start exploring kinematic hardening first. When kinematic hardening is dominant, simple rules and testing procedures may quickly establish whether this mechanism

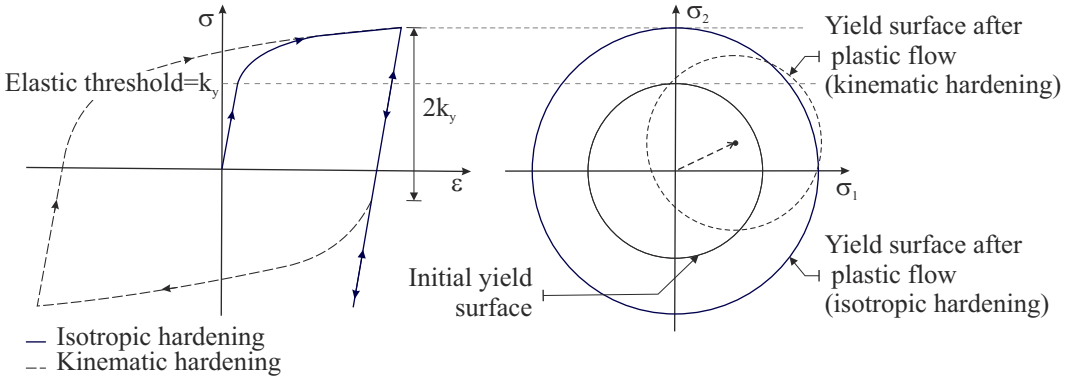

Figure 3.1: Representation of kinematic and isotropic hardening in the stress-strain plane and the bi-dimensional stress plane

predicts the response. Additionally, soil behaviour has been modelled extensively with kinematic hardening based approaches (e.g. Prevost, 1977; Pyke, 1979; Vucetic, 1990).

Masing (1926) established that pure kinematic hardening could be identified from a perfectly symmetric loading test providing that the two following rules are respected:

(i) The unloading and reloading curves are defined based on the initial loading curve, called the *backbone curve*, enlarged by a factor of 2

(ii) After any load reversal, the tangent shear modulus is the same as the initial shear modulus of the backbone curve

Actually, the first rule encompasses the second. A powerful outcome of the Masing rules, is that the response to any subsequent load reversal can be deduced based on the backbone curve.

Test H0 (Table 2.6) aims at identifying whether the above framework applies to the laboratory pile response as described in these experiments. The results are displayed in Figures 3.2(a) and 3.2(b). On Figure 3.2(a), the red dotted line results from the reversed loading data (unload path), scaled down by a factor of two and plotted from the origin. On Figure 3.2(b), this same unload portion has been flipped

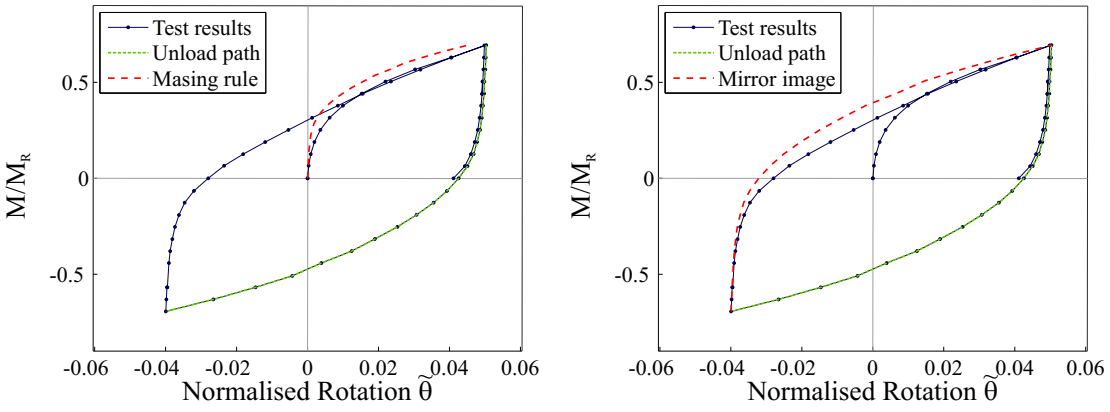

Figure 3.2: Test H0, application of Masing rules: (a) comparison of unloading path with initial loading curve (b) comparison of unloading path with reloading curve

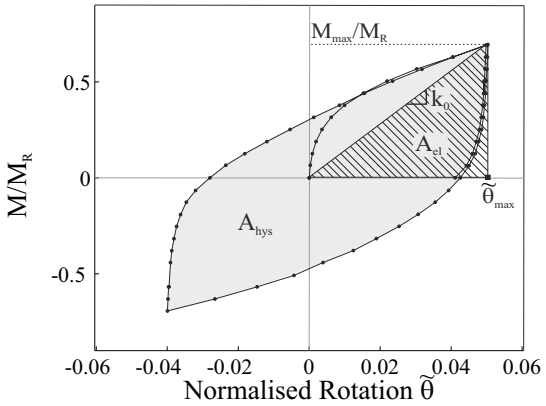

Figure 3.3: Test H0: Definition of the parameters used for calculation of the damping ratio (Equation 3.1; Shaded area = A_{el} and Solid area = A_{hys})

and plotted from the origin of the reloading portion (red dotted line). Both graphs show that the scaled unload curve gives a close approximation of the original loading and reloading paths and therefore that the response conforms to the above Masing rules. At this stage, it is difficult to assess whether the differences observed can be interpreted using another mechanism (such as isotropic hardening) or ascribed to experimental errors. However, from the results displayed here, it is clear that a very good first approximation of the pile response to symmetric cyclic loading can be obtained using kinematic hardening.

Figures 3.2(a) and 3.2(b) also provide information on the hysteretic damping of the foundation when loading at high magnitude and at a frequency of 0.106 Hz. The damping ratio is the dimensionless parameter commonly used to measure how vibrations decay due to energy dissipation. In the case of soil hysteresis damping, it is defined as the ratio between the dissipated energy during a cycle over the stored elastic energy (Vucetic and Dobry, 1991). Using the notations from Figure 3.3, it is expressed according to:

$$D_a = \frac{1}{4\pi}\frac{A_{hys}}{A_{el}} = \frac{A_{hys}}{2\pi k_0 \theta_{max}^2} \tag{3.1}$$

For test H0, the above gives $D_{a0} = 0.28$. This is significantly higher than the few values reported in published literature for similar, but larger pile geometries

(e.g. Tarp-Johansen *et al.*, 2009, estimation of soil damping ratio between 0.035 and 0.05). However, this compares favourably with similar laboratory tests performed on suction caissons in dense sand where comparable hysteresis loop shapes and a damping ratio of 0.2 were observed (Byrne, 2000, Chapter 5). This was then

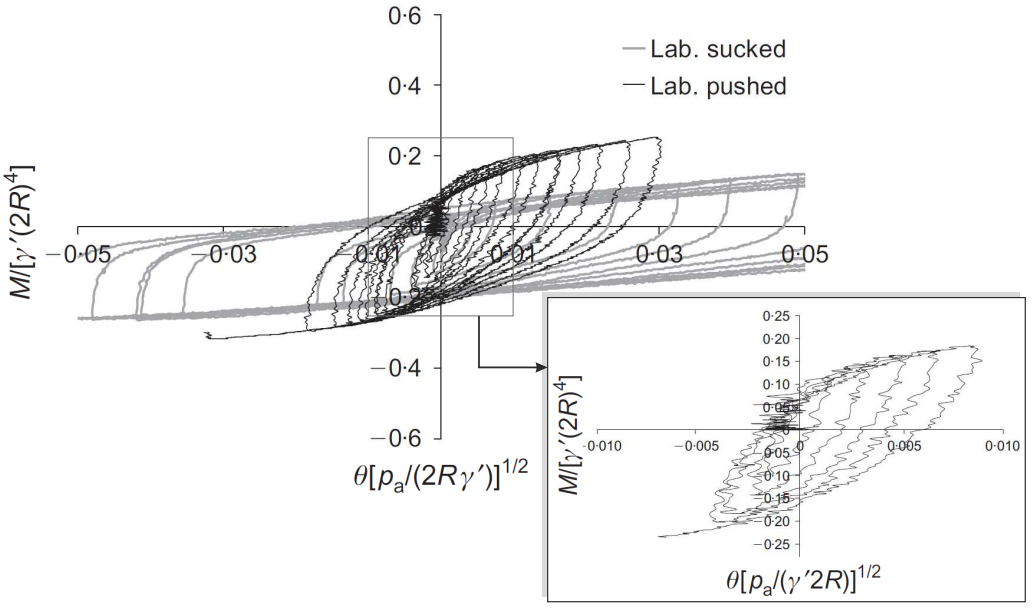

(a)

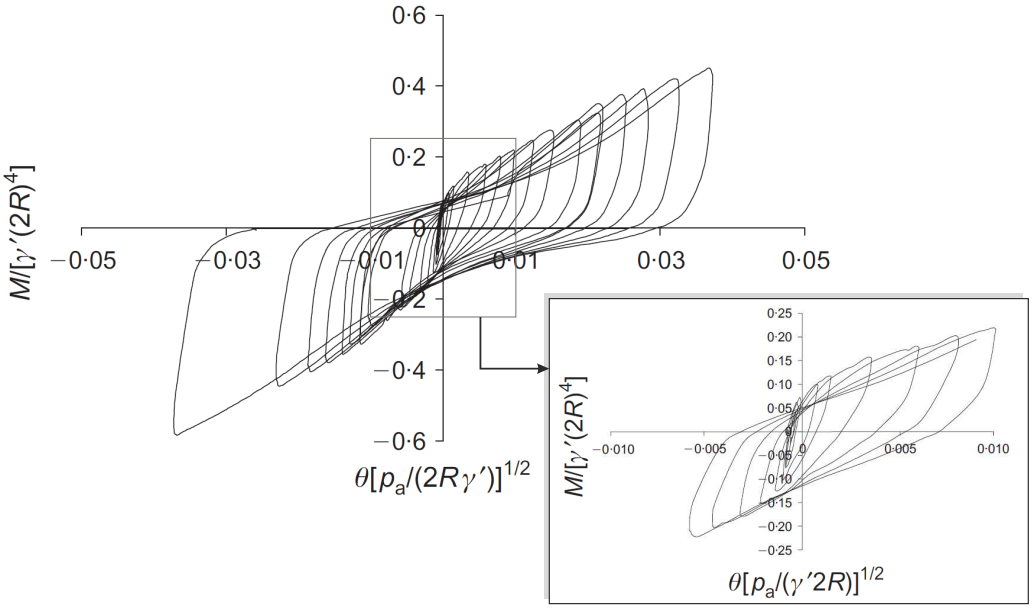

(b)

Figure 3.4: Moment loading caisson response from Kelly *et al.* (2006): (a) laboratory test data, 0.2 m diameter caisson (b) field test data, 3.0 m diameter caisson

completed by a comparative study between laboratory-scale and large-scale field tests (Kelly *et al.*, 2006). The results, reported here in Figure 3.4(a) and (b), show that the hysteretic response at small loads is comparable, but differs for larger loads. The differences between the two plots are explained by the formation of a gap between the sand and the caisson, occuring during field tests and not captured by laboratory tests.

Even though operational loads are expected to be quite small, this phenomenon could also apply to the laboratory test results presented in this thesis. Furthermore, as the plastic volume change under shearing is a function of the dilation angle (Vermeer and de Borst, 1984), the hysteretic behaviour observed for full-scale monopiles might differ slightly from that displayed here, especially with regards to the damping ratio value (i.e. hysteresis loop openness). Finally, since the sample is relatively loose compared to that expected in the field, the rate of dilatancy is also smaller (cf. Chapter 2, Section 2.2.2, p. 51). Large-scale field tests would therefore be of great contribution in order to relate the laboratory model scale pile behaviour to that of real offshore wind monopiles.

3.2.2 Effect of peak load increase

The two Masing rules formulated above describe the response to regular cyclic loading of constant amplitude only. For general loading, Pyke (1979) contributed to the above framework with two additional statements:

(iii) When exceeding the maximum shear stress, the unloading or reloading curve follow that of the backbone curve until the next load reversal

(iv) In general, each time an unloading or reloading path intersects a curve from a previous cycle, the stress-stain curve then follows that curve

The four rules enumerated above are referred to as *extended Masing rules*. They imply that the symmetric cyclic stress-strain behaviour can be entirely defined provided the backbone curve is chosen properly. To investigate whether the soil

response conforms to these extended rules, a 2-way cyclic test at increasing load magnitude was performed (Test HIM, Table 2.6, Figure 3.5(a)). The test results are displayed in Figure 3.5(b) and superimposed with the results of test H0.

The graph shows that, on passing extreme load levels from previous cycles, the reloading path follows that of the backbone curve. This indicates that the pile response complies with the extended Masing rules. Also, it is clear that the secant stiffness $\tilde{k}_0$ reduces with load increase (Figure 3.5(c)).

Finally, Figure 3.5(d) displays the damping ratio of each load reversal and shows that, for cyclic load magnitudes above 30% of static capacity, the damping ratio is

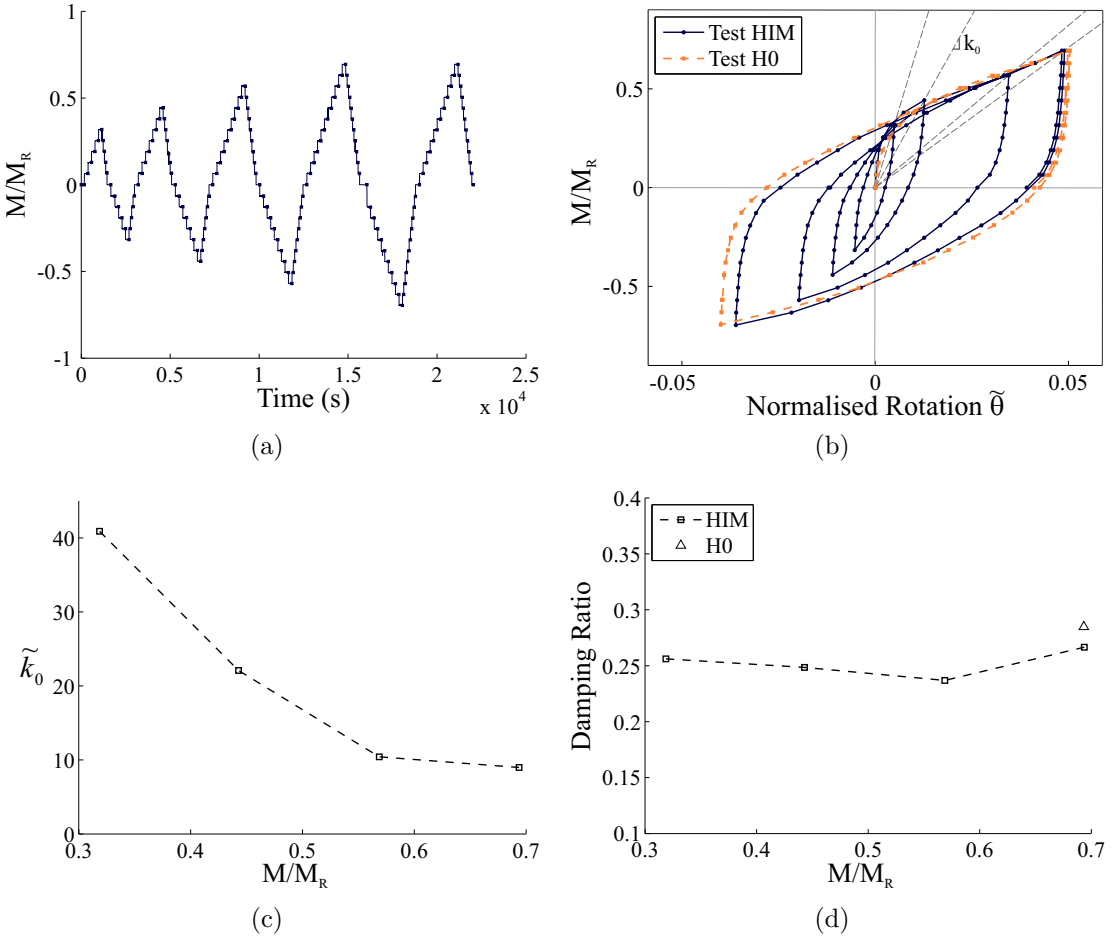

Figure 3.5: Test HIM: (a) Load applied on the pile (b) Identification of extended Masing rules (Pyke, 1979), comparison with test H0 (c) Evolution of secant stiffness with load magnitude (d) Damping ratio as a function of the maximum applied load (tests H0 and HIM)

independent of the load magnitude. A similar conclusion was also obtained by Byrne (2000) for increasing peak moment loads on suction caissons in dense sand.

3.2.3 Effect of cycle number

As shown in Section 3.2.1, there is a small discrepancy between the prediction using Masing rules and the experimental results. One possible explanation is that the results cannot be interpreted using solely kinematic hardening. If the response was indeed pure kinematic hardening, then, according to the Masing rules, the response of the pile to subsequent 2-way loading cycles would be exactly identical to the initial external cycle loop (see load case no. 1, Figure 3.6(a)). In order to verify this statement, 3 consecutive full load reversals were applied to the top of the pile (test HC, Table 2.6, Figure 3.7(a)). The results are displayed in Figure 3.7(b).

The graph shows that the response to the three loops do not perfectly superimpose upon each-other. At this stage, it is quite difficult to identify whether this should be interpreted as (a) experimental errors or (b) combined isotropic hardening. The response indeed approximately corresponds to typical combined isotropic hardening, displayed in Figure 3.6(b). This theoretical stress-strain curve was obtained using a Mroz multi-surface linear kinematic hardening model, combined with non-linear isotropic hardening (see Chapters 4 and 5 for further details). The non-linear relationship used for the non-linear evolution of the yield surfaces centres (isotropic hardening) is that of Ramberg-Osgood, which is commonly used in solid mechanics of standard materials (Lemaitre and Chaboche, 2010).

However, the loading rig is unlikely to apply a perfectly symmetric load and the small differences observed in Figure 3.7(b) may be due to errors generated by the loading system itself. This means that further investigation, possibly using asymmetric loading, is needed. This is developed in the following sections.

From Figure 3.7(b) though, it is reasonable to say that the differences in cycle loops are not dominating and that pure kinematic hardening is sufficient for a first

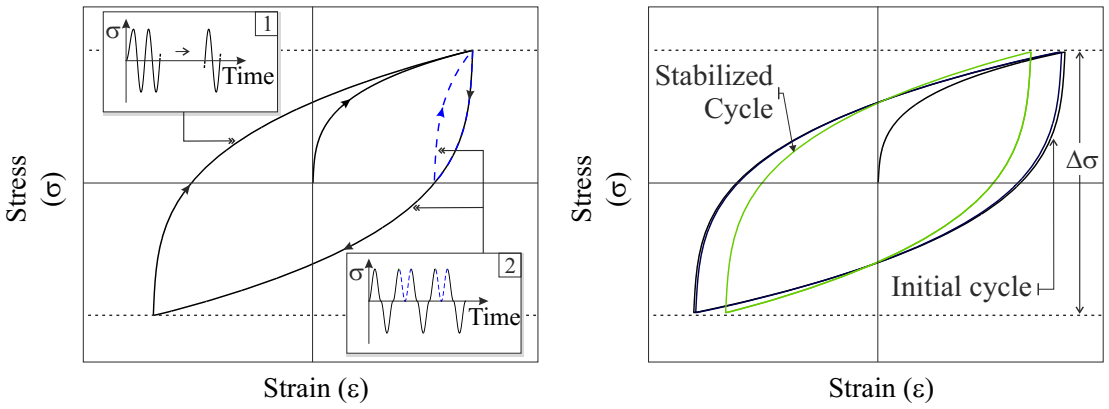

(a) (b)

Figure 3.6: (a) Typical kinematic hardening response; (b) Typical response from combined kinematic and isotropic hardening. Isotropic hardening: Ramberg Osgood law; $R = Q_y p^{m_y}$, with typical value of $m_y = 1/3$ (e.g. Lemaitre and Chaboche, 2010)

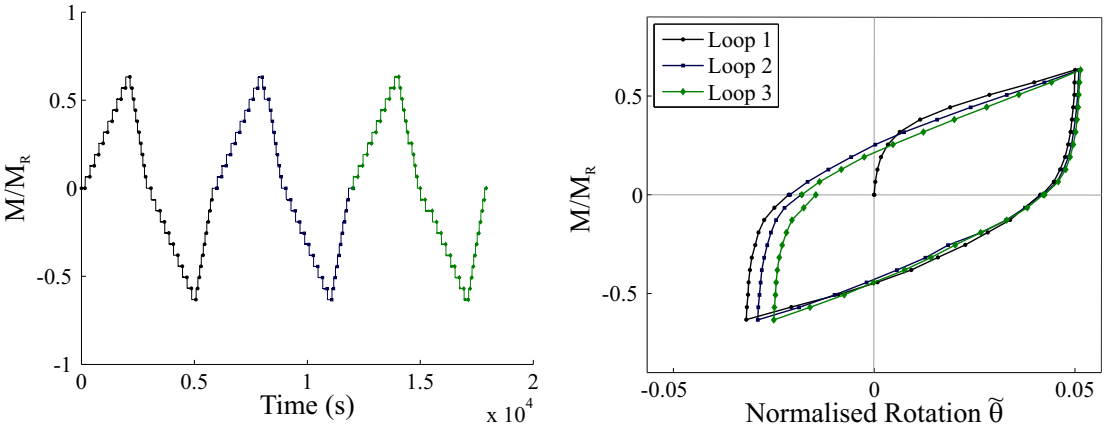

(a) (b)

Figure 3.7: Test HC: (a) Load applied on the pile (b) Moment-rotation curve

approximation of the pile response to symmetric loading. In particular, the response to maximum load remains unchanged after the series of loops and no maximum cyclic accumulated rotation is observed. This emphasizes the fact that kinematic hardening is the dominant mechanism for modelling of the pile response.

3.2.4 Effect of non-symmetric loading

The tests presented above all involve perfectly symmetric loading. The next step was to consider non-symmetric load cases. This was performed through alternating

2-way / 1-way loading tests (HA1 and HA2, Table 2.6, Figures 3.8(a) and 3.8(c)) and the results are displayed in Figures 3.8(b) and 3.8(d).

The plots exhibit almost similar trends as that observed in Figure 3.7(b). The only variation occurs when performing the 1-way cycle loop that then generates an additional hysteresis loop, during which accumulated rotation is experienced. This phenomenon cannot be explained with pure kinematic hardening as the 1-way loading loop would theoretically tend towards the same displacement as that of 2-way loading (see load case no.2, Figure 3.6(a)).

According to the previously published results (e.g. LeBlanc *et al.*, 2010a; Klinkvort, 2012; Peralta and Achmus, 2010), it is expected that the pile response will keep experiencing accumulation of rotation when subjected to non-symmetrical load cycles, even at large cycle number (Cuéllar, 2011). Therefore, even combined isotropic and kinematic hardening would be insufficient for describing such behaviour, as this type of models always converges to a stabilized loop after few cycles. This means that the accumulation of deformation due to cyclic loading at non-zero mean load, also called ratcheting, probably needs to be captured using a different type of mechanism and therefore needs specific and detailed experimental investigation in order to develop appropriate modelling tools.

Finally, Figures 3.8(b) and 3.8(d) exhibit an interesting result: the maximum displacements generated by the peak loads of a 2-way/1-way series (pairs of odd then even loop number, as highlighted by the different colors in Figures 3.8(a) and 3.8(b) for example) is the same as that from the previous series. Consequently, at the end of a series, there is no significant accumulated deformation.

This observation bears out with the findings from LeBlanc *et al.* (2010b) where series of load reversals were found to neutralise the accumulated rotation from previous loading in the opposite direction. This was not investigated any further during the course of this project, but complementary experimental tests targeting this phenomenon for relevant offshore wind turbine load cases would be useful in

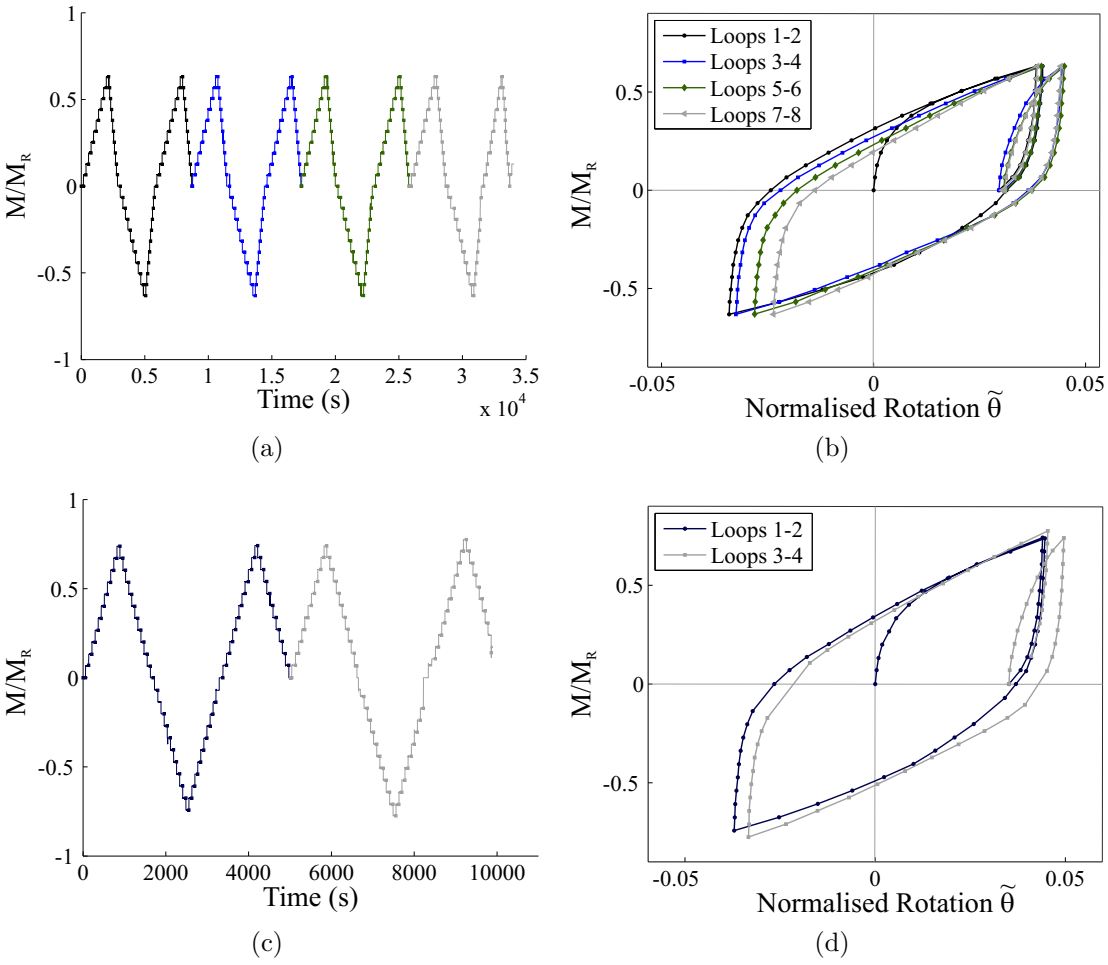

Figure 3.8: Alternated 2way/1way tests: (a) Load applied on the pile, (b) Moment-rotation curve of test HA1; (c) Load applied on the pile, (d) Moment-rotation curve of test HA2

the future, as this could mean that cyclic loading at certain load amplitude could "retard" the accumulation of rotation over the lifetime of the monopile.

For the final stage of this testing phase, the above tests were extended by applying 1-way loading at increasing magnitudes to the pile. The results are displayed in Figures 3.9(a) and 3.9(b). On these two graphs, the horizontal dotted lines mark the initial elastic threshold and the gray dotted lines indicate the initial elastic modulus estimated from the monotonic test MCo4 (Chapter 2, Section 2.5). Both graphs show that the elastic modulus and threshold remain unchanged with increasing load and cycle number and that the response progressively stiffens in order to rejoin the backbone curve.

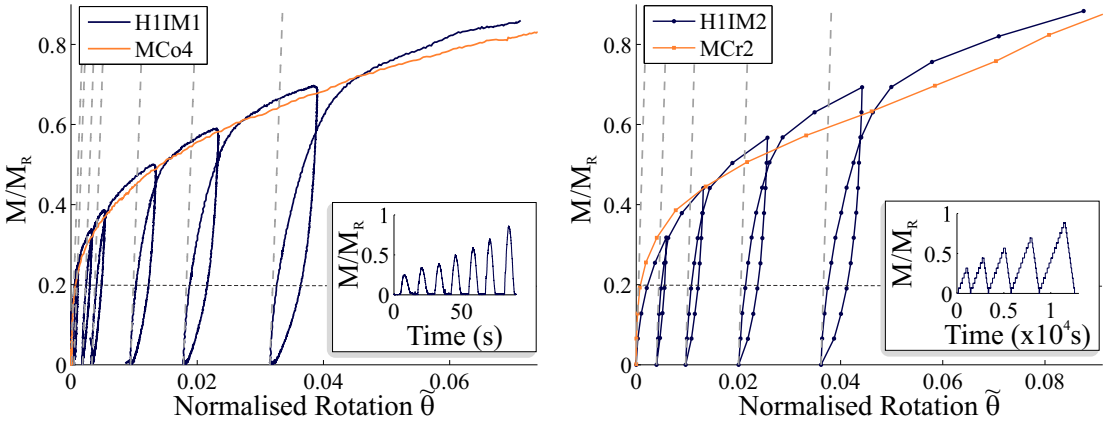

Figure 3.9: 1-way loading tests at increasing magnitude: (a) Test H1IM1, Comparison with monotonic test MCo4, (b) Test H1IM2, Comparison with test MCr2

In fact, the response displayed in these two graphs feature the key conclusions of this section:

1) First, the tangent modulus of each reloading curve is equal to the initial modulus, which accommodates Masing rule no.2
2) The reloading paths follow the backbone curve (orange lines) when exceeding the maximum historic load. This conforms to the extended Masing rules
3) Pile accumulates rotation when subjected to non-symmetric loading cases

The accumulation of deformation due to cyclic loading at non-zero mean load is detrimental to the long term performance such that there are serviceability limits, and therefore, the problem needs to be understood and designed against. The following section focuses on continuous long-term cyclic loading at non-zero mean load in order to propose a detailed analysis of the ratcheting behaviour of the pile.

3.3 Long-term continuous cyclic loading

Figure 3.10 displays the typical pile response to non-symmetric, continuous long-term cyclic loading. On this graph, selected cycles have been highlighted in gray to emphasize the evolution of the hysteresis loop shape and pile accumulated

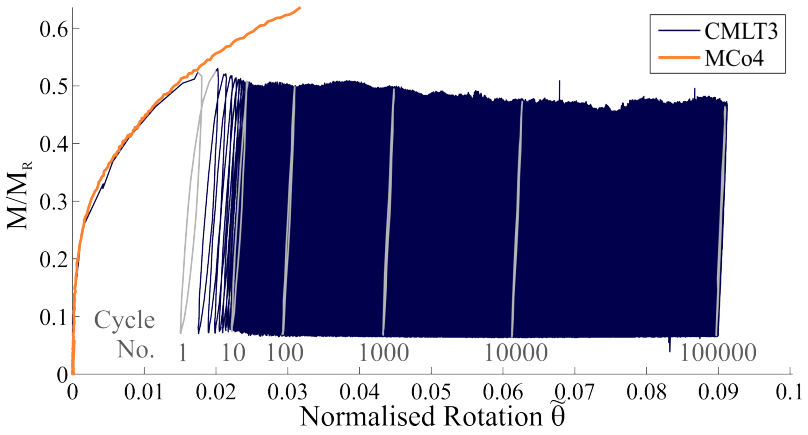

Figure 3.10: Typical moment-rotation curve from long-term cyclic test (CMLT3) super-imposed with data from monotonic test (MCo4)

deformation with cycle number. In order to model such behaviour in future designs, detailed description of the loop evolution with cycle number is required. This involves description of both the accumulated rotation and the loop shape.

As mentioned in Chapter 1, previously published literature has derived frameworks of response for the evolution of the pile rotation and secant stiffness to continuous cyclic loading. This section takes the analysis described in Section 1.4.2.1 (p. 30) one step further, first, by performing experiments with greater numbers of cycles, and second, by using more advanced data acquisition equipment that enables precision measurement of the pile response and its variations over time (compared with LeBlanc *et al.*, 2010a). The following therefore analyses data from the experimental tests listed in Table 2.7 (p. 66, tests CMLT1-3, CC1-7 and CCLB1-4). Results of pile deformation with cycle number are presented in three different ways and the advantages of each method are discussed. Evolution of the hysteresis loop shape is characterised by both the secant stiffness and the hysteresis loop area. In this section, the secant stiffness is analysed with regards to the constitutive modelling described in the following chapters. Finally, the evolution of the hysteresis loop area is also analysed. This parameter was found to provide interesting information for future modelling and also on the evolution of damping due to one-way cyclic loading.

In the following analysis, the evolution of parameters with cycle number will be

displayed using either solid lines or scattered plots, which represent two different data processing techniques. Solid lines represent the totality of the test data, i.e. one point per cycle. Since tests involved large number of cycles, the points end up very close to each other and it is much clearer representing the results with a single line. On the other hand, some parameters, such as the rate of increase, the secant stiffness or the loop area, involve operations on a very small fraction of the displacement and are subjected to more error and noise in the response. To smooth the resulting curve, a process is used where the data are logarithmically selected and averaged over the previous order of magnitude (e.g. for cycle number 500, $\tilde{k}_{500} = average(\tilde{k}_{495} \mapsto \tilde{k}_{505})$ and for cycle 5000, $\tilde{k}_{5000} = average(\tilde{k}_{4950} \mapsto \tilde{k}_{5050})$). In this section, the cyclic results obtained using this process are displayed using scattered plots. Finally, the results for large cycle number tests (tests CMLT1,2,3, N>100,000 cycles) are separated from shorter tests (tests CC1-7; CCLB1-4) in order to outline the long-term cyclic trends.

3.3.1 Cyclic deformation and ratcheting

There are three different ways of presenting the evolution of the pile deformation with cycle number: (i) accumulated rotation/displacement $\Delta\tilde{\theta} = \tilde{\theta}_N - \tilde{\theta}_0$ (see LeBlanc *et al.* (2010a) and Figure 2.7(a), Chapter 2, p. 63), (ii) rate of increase $\delta\tilde{\theta} = \tilde{\theta}_{N+1} - \tilde{\theta}_N$ and (iii) pile rotation/displacement at pile head $\tilde{\theta}_N$. Each method provides different information both for understanding the response and for modelling. In the following, the test results from Table 2.7 are interpreted using the three methodologies and the information derived from each of them and their contribution to the modelling developments are highlighted.

3.3.1.1 Accumulated rotation

As suggested by LeBlanc *et al.* (2010a), the most appropriate way of presenting the degradation caused by cyclic loading on pile deformation is in terms of accumulated rotation $\Delta\theta$. This is indeed the relevant value for designers when verifying the

induced displacement caused by a given fatigue load series. In LeBlanc *et al.* (2010a), the accumulated rotation $\Delta\theta$ is normalised according to the rotation that could occur in a static test when the load is equivalent to the maximum cyclic load, called θ_s. However, this makes comparison with design tolerances more difficult as it is quite complicated to accurately estimate θ_s for full-scale prototypes from the current design approaches (c.f. Chapter 1, Section 1.3.5, p. 23) . Consequently, it was decided to present the accumulated rotation results using the usual dimensionless form of the rotation $\tilde{\theta}$ (Table 2.1, p. 51). For a 30 m pile in dense sand, the maximum tolerated pile tilt due to operational condition is $\Delta\tilde{\theta}_{lim} = 0.25 \times \frac{\pi}{180}\sqrt{\frac{p_a}{L\gamma'}} = 0.0025$ (cf. Chapter 1, Section 1.2, p. 14).

The accumulated rotation observed for the cyclic tests in Table 2.7 are displayed in Figures 3.11(a) for long-term cyclic tests (N>100,000 cycles) and 3.11(b) for all the other tests. The data were fitted using the empirical law proposed by LeBlanc *et al.* (2010a) and reminded below:

$$\Delta\tilde{\theta} = \tilde{T}_b(\zeta_b, R_d) \cdot \tilde{T}_c(\zeta_c) \cdot N^{0.31} \tag{3.2}$$

The fitted curves are displayed using gray dashed lines and demonstrate that Equation 3.2 accurately captures the increase in pile deformation, at least for the first 10 000 cycles. However, passing this limit, the experimental data depart from the predictions. Figure 3.11(a) shows that Equation 3.2 over-estimates the pile displacement after 100,000 cycles and therefore is a conservative approach for predicting pile displacement to very large cycle number.

Figure 3.11(c) displays the values of $\tilde{T}_b\tilde{T}_c = \tilde{T}_{bc}$ as a function of the load magnitude ζ_b. Only some of the tests have been selected for this plot (CMLT1,2,3 and CC1,3,4,7) according to their load magnitude value ($0 \leq \zeta_c < 0.25$). According to LeBlanc *et al.* (2010a) (Figure 11.b of this paper, reported in Figure 3.11(d) here), for these values of ζ_c, T_c is sufficiently close to 1 so that $\tilde{T}_{bc} \sim \tilde{T}_b$. The results obtained here match with

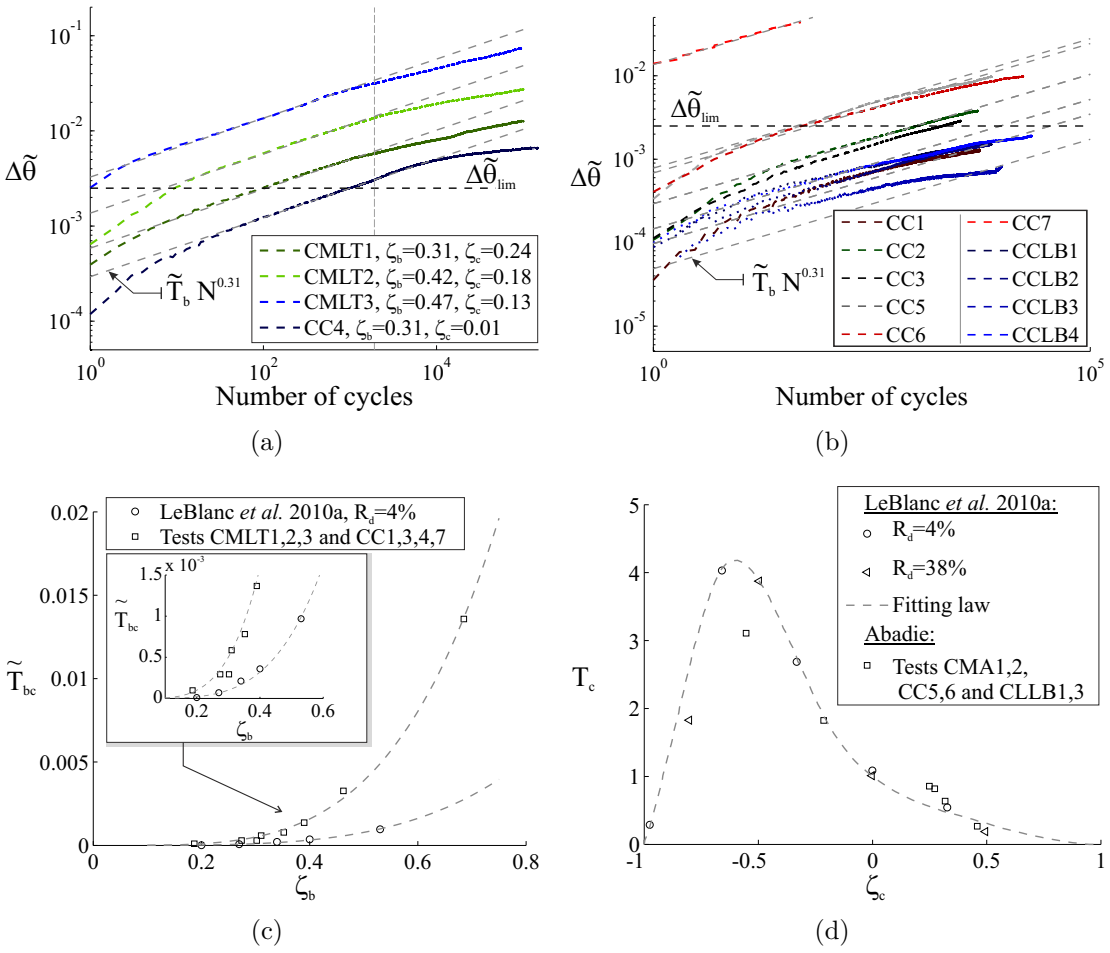

Figure 3.11: Pile accumulated rotation during (a) tests involving at least 100,000 cycles and (b) all the other tests in Table 2.7; (c) Function relating $\tilde{T}_b$ to load magnitude ζ_b for tests CMLT1,2,3 and CC1,3,4,7 and LeBlanc *et al.* (2010a) test results, dashed line = fitting power laws of exponent 4; (d) Function relating T_c to load amplitude ζ_c for tests CMA1,2, CC5,6 and CLLB1,3 and LeBlanc *et al.* (2010a) test results, dashed line = fitting power law proposed by LeBlanc *et al.* (2010a)

a power law with a power coefficient of 4 (dashed lines). As shown in Figure 3.11(c) this compares favourably with LeBlanc *et al.* (2010a) data, which also match with a power law of exponent 4. The minor differences observed for the numerical values arise from slight variations in the experimental set-up and small errors generated by the conversion of T_b into $\tilde{T}_b$ for LeBlanc *et al.*'s data. The variable $\tilde{T}_b$ plotted here does not indeed correspond to the variable T_b plotted by LeBlanc *et al.* (2010a). This is because it was chosen here to investigate $\Delta\tilde{\theta}$ and not $\Delta\theta/\theta_S$. However, it is fairly straightforward to convert the values of T_b into $\tilde{T}_b$ by multiplying by $\tilde{\theta}_S$.

According to the expression of $\tilde{\theta}_S$ given by LeBlanc *et al.* (2010a), this translates into $\tilde{T}_b = T_b \times 0.038\zeta_b^{2.33}$.

Similarly, Figure 3.11(d) reports the values of T_c obtained for the test results where $\zeta_c \in [-1, 0[\cup [0.25, 1]$. Note that, unlike $\tilde{T}_b$, T_c and $\tilde{T}_c$ are strictly the same and the normalisation is accounted for by the T_b function. The graph shows that most of the results from this test series are consistent with those from LeBlanc *et al.* (2010a). In addition, the data point located in the critical region, although not superimposed with Leblanc *et al.*'s prediction, confirms that the worse case scenario occurs for one and a half way loading.

Finally, plotted on Figures 3.11(a) and 3.11(b) is the maximum tolerance $\Delta\tilde{\theta}_{lim}$. This shows that, for the load cases studied here, the allowable limit is reached for a number of load cases. It is noteworthy that the minimum load magnitude applied here is 20% of the ultimate capacity (test CC1), which is close to the elastic limit estimated in Chapter 2, Section 2.5. It would be interesting to extend the testing described to smaller load magnitudes, within the elastic range, and see whether this would generate any accumulated rotation. This would be relevant to many operational loading on offshore wind monopiles, which are likely to be much less than 20% of the ultimate.

3.3.1.2 Rate of increase

As outlined in Figure 3.11(a), there is a clear decrease in the accumulated rotation rate after 10 000 cycles. It is legitimate to quantify this decrease and estimate whether the pile still accumulates deformation after large cycle number or reaches an asymptotic value. This is actually an important aspect for constitutive modelling as constant accumulation of permanent strain with cycle number, also called ratcheting, is difficult to model, while stabilisation after a given number of cycles, either accommodation or adaptation, can be captured using combined isotropic and kinematic hardening (see introduction of Chapter 4). The evolution

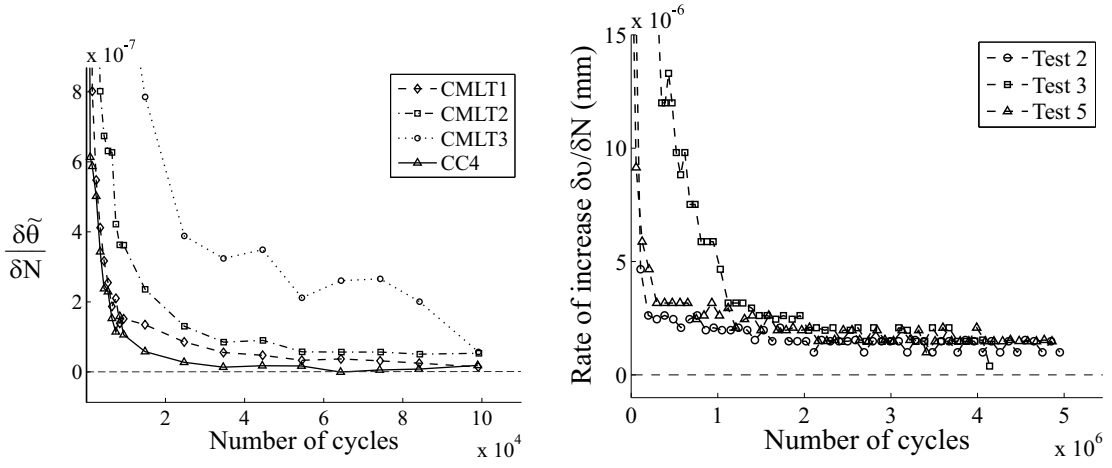

Figure 3.12: Rate of increase during long-term cyclic loading tests: (a) Tests in Table 2.7 (normalised rotation) (b) Test results from Cuéllar (2011) (ground-line pile displacement)

Table 3.1: Relevant properties of the cyclic tests selected from Cuéllar (2011) (Figure 4.9.a, p.156)

Test No.	L (m)	D (m)	Load eccentricity (m)	Relative density (%)	N	ζ_b	ζ_c
Test 2	0.3	0.075	0.2	93	5e6	0.13	-0.5
Test 3	0.3	0.075	0.2	93	5e6	0.2	-0.33
Test 5	0.3	0.075	0.2	93	5e6	0.2	0

of $\delta\tilde{\theta} = \tilde{\theta}_{N+1} - \tilde{\theta}_N$ with cycle number provides relevant information on the rate at which the pile deformation is accumulated. The results of the long-term cyclic tests are displayed in Figure 3.12(a).

The graph shows that the rate continues to decrease with cycle number. However, for the load cases studied here and the number of cycles involved, the rate never decays to zero as N increases. This proves that the pile experiences ratcheting with cyclic loading at non-zero mean load, at least for the first 100,000 cycles.

In order to extrapolate the above conclusion to much larger cycle number, test results from Cuéllar (2011) were used for comparison. The properties of the selected tests are provided in Table 3.1, showing that the pile geometry is very close to that of this research programme but the sand sample is much denser and the load magnitude

lower. Cuéllar (2011) performed five laboratory floor model tests on rigid model piles, applying more than one million cycles. Three of the data sets were digitised and the rate of increase was then deduced and plotted against cycle number. The results are displayed in Figure 3.12(b) and are consistent with the observations shown in Figure 3.12(a). Since the published results were plotted in terms of pile head displacement, the rate of increase plotted in Figure 3.12(b) is that of the displacement. However, given the aspect ratio chosen for Cuellar's tests, this relates linearly to the pile rotation. Although the quantity plotted is different here (rotation vs. displacement), the general trend appears to be similar.

3.3.1.3 Total deformation

Finally, in some cases, it is sensible to consider the total rotation instead of the accumulated rotation (or displacement instead of accumulated displacement). In particular, capturing the evolution of the cyclic rotation with a simple expression becomes essential when developing the *p-y* method for cyclic loading using the Degradation Stiffness Model (see following section). In published literature, the evolution of the rotation is usually fitted using either a power law or a logarithmic law (e.g. Lin and Liao, 1999; Verdure *et al.*, 2003; Peralta, 2010). However, the use of a power law allows straightforward development of the Degradation Stiffness Model and is therefore selected here for fitting the data according to the equation:

$$\tilde{\theta}_N = \tilde{\theta}_r N^{m_\theta} \tag{3.3}$$

Figure 3.13(a) and 3.13(b) display the results of the rotation as a function of the cycle number for the long-term and short-term cyclic tests respectively. The gray dotted lines plot the predictions using Equation 3.3. In this expression, $\tilde{\theta}_r$ is a dimensionless coefficient. In order to obtain the best data fitting, θ_r slightly differs from θ_0, though it is very close. m_θ is an empirical factor. Figures 3.13(a) and

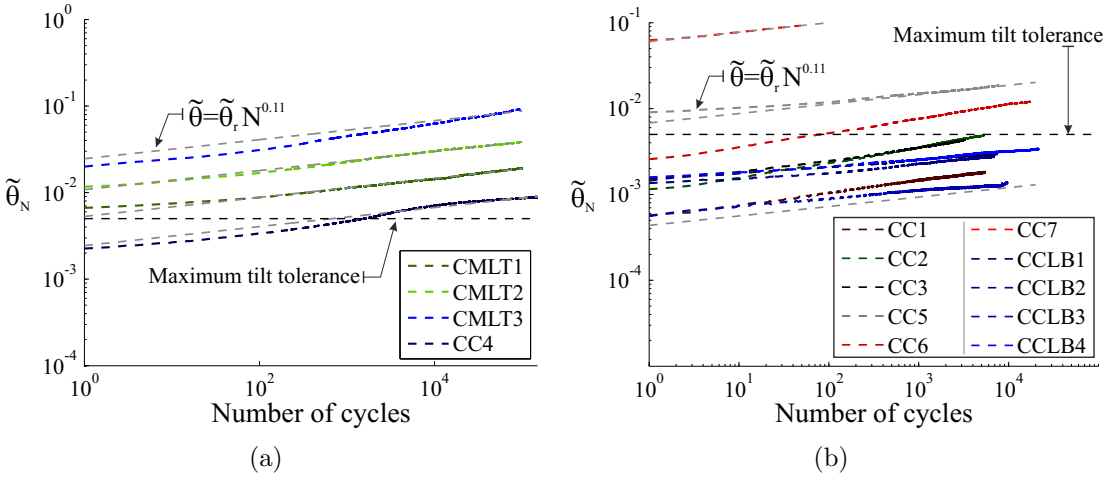

Figure 3.13: Pile rotation during (a) tests involving at least 100,000 cycles and (b) all the other tests in Table 2.7

3.13(b) show that very accurate predictions are provided using a power-law and the average value of the exponent m_θ obtained for these tests was 0.11. This compares favourably with the results from Peralta (2010) who obtained a value of 0.12 after fitting a range of experimental data.

Also plotted on this graph is the maximum tolerated deformation of the pile over its lifetime (0.5 degrees, cf. Chapter 1, Section 1.2, p. 14) and normalised $\tilde{\theta}_{lim} = 0.5 \times \frac{\pi}{180}\sqrt{\frac{p_a}{L\gamma'}} = 0.005$. The graphs show that the limit is here again exceeded in many load cases.

3.3.2 Degradation Stiffness Model

The principles of the Degradation Stiffness Model (DSM), and its use within the *p-y* method for cyclic loading applications, were previously presented in Chapter 1, Section 1.4.2.2, p. 33. It was then noted that this model had only been benchmarked against experimental data pertaining to flexible piles and small cycle numbers. However, in the case of rigid piles, the DSM can actually directly be derived from the equilibrium equations and experimental test results such as those presented in the previous paragraph. This section outlines the theoretical developments leading to Equations 1.17 and 1.18 (p. 33) and applies the resulting methodology to a range

of test results from this research programme and from published literature. The conclusions then enable to validate the methodology for use in modelling of rigid pile response to large cycle numbers. It is noted that the term *Stiffness* in the expression "Degradation Stiffness Model" refers to the *p-y* curve modulus E_{py} and not the experimental secant stiffness, studied in the next section.

3.3.2.1 Case of rigid piles

In the following demonstration, the pile is assumed to be perfectly rigid, and therefore, the relationship from Chapter 2, Section 2.6.1, p. 80 (Equation 2.19, reminded below) applies:

$$y(x) = tan(\theta)(\alpha L - x) \simeq \theta(\alpha L - x) \tag{3.4}$$

The equilibrium equation of a laterally loaded rigid pile, presented earlier in Chapter 2, Section 2.6.1, p. 80, is:

$$\int_0^L p_y(x,y)(x-L)\,\mathrm{d}x = M_t + H_t L \tag{3.5}$$

Combined with the general expression of the soil reaction $p(x,y) = E_{py}y$, this becomes:

$$\begin{cases} \int_0^L E_{py0} \cdot y_0 \cdot (x-L)\,\mathrm{d}x = M_t + H_t L \\ \int_0^L E_{pyN} \cdot y_N \cdot (x-L)\,\mathrm{d}x = M_t + H_t L \end{cases} \tag{3.6}$$

And therefore:

$$\int_0^L E_{pyN} \cdot y_N \cdot (x-L)\,\mathrm{d}x = \int_0^L E_{py0} \cdot y_0 \cdot (x-L)\,\mathrm{d}x \tag{3.7}$$

Now, using the rigid pile assumption (Equation 3.4) provides:

$$\theta_N \int_0^L E_{pyN} \cdot (\alpha L - x) \cdot (x - L)\,\mathrm{d}x = \theta_0 \int_0^L E_{py0} \cdot (\alpha L - x) \cdot (x - L)\,\mathrm{d}x \tag{3.8}$$

Assuming that the pile pivot point is located at 70% of the pile length from the ground surface, and remains unchanged regardless of the cycle number (Chapter 2, Section 2.5.4, Figure 2.13(b), p. 76), Equation 3.8 can be re-written as:

$$\int_0^L \left(E_{pyN} - E_{py0} \cdot N^{-m_\theta}\right) \cdot (\alpha L - x) \cdot (x - L)\,\mathrm{d}x = 0 \tag{3.9}$$

A trivial solution to the above is then:

$$E_{pyN} = E_{py0} \cdot N^{-m_\theta} \tag{3.10}$$

Which corresponds to Equation 1.18 (Chapter 1, Section 1.4.2.2, p. 33). Note, though, that since $(E_{pyN} - E_{py0} \cdot N^{-m_\theta}) \cdot (\alpha L - x) \cdot (x - L)$ is not a strictly positive function, Equation 3.10 might not be the only solution of Equation 3.9.

Finally, according to the above demonstration, the degradation coefficient m_θ deduced from the global pile response for rigid piles (Equation 3.3) and the one involved in the Degradation Stiffness Model δ (Chapter 1, Section 1.4.2.2, Equation 1.18) should be identical. This property will be verified in the following Section.

3.3.2.2 Application and validation

The above framework has been applied to a series of test results from this research programme (Tests CMLT1,2,3, Table 2.6, p. 65) and from the literature (Klinkvort, 2012; Verdure *et al.*, 2003). The selected tests relate to the experiments chosen for validation of the *p-y* method for monotonic loading in Figures 2.19(a)-(d) (Chapter 2, Section 2.6, p. 86). Consequently, the data from Table 2.6, and Klinkvort (2012) correspond to rigid piles and those from Verdure *et al.* (2003) correspond to a flexible

Test No.	L/D	Load eccentricity (h_e/L)	Relative density (%)	N	ζ_b	ζ_c
Klinkvort (2012)						
55	6	2.5	84	500	0.18	-0.46-0.32
56	6	2.5	84	500	0.29	-0.46-0.32
57	6	2.5	84	500	0.36	-0.46-0.32
Verdure et al. *(2003)*						
C2-20	16.7	0.13	95	50	1	0.8
C1-60	16.7	0.13	95	16	1	0.4
C2-80	16.7	0.13	95	50	1	0.2

Table 3.2: Relevant properties of the cyclic tests selected from Klinkvort (2012) and Verdure *et al.* (2003)

pile. The properties of the tests extracted from the literature are summarised in Table 3.2.

For each case, the soil reaction is predicted using Equations 2.20 (Chapter 2, Section 2.6, p. 82) and the base shear is obtained from the equilibrium of the forces (Equation 2.23, p. 83). Parameter y_c is optimized in order to get a close match of the initial pile displacement. Then, δ is optimized based on the cyclic results and compared with m_θ from direct data fitting in the case of rigid piles.

The results of this procedure are displayed in Figures 3.14(a) - (c) and illustrate that the pile deflection predicted by the Degradation Stiffness Model shows good agreement over increasing cycles. Furthermore, the values of δ obtained in the case of the test results presented in Table 2.6, and Klinkvort (2012) matches with the corresponding values of m_θ obtained via data fitting. The values of m_θ obtained for the rigid piles (Tests CMLT1,2,3; Klinkvort (2012)) are between 0.078 and 0.89 with an average and median values of 0.23 and 0.11, respectively. The investigation of m_θ (and δ) has not been considered any further here. This parameter is likely to be quite difficult to assess and even more complex to scale-up appropriately.

Finally, the results from Figure 3.14(c) show that the Degradation Stiffness Model also applies fairly well to predictions of cyclic displacement of flexible piles. However,

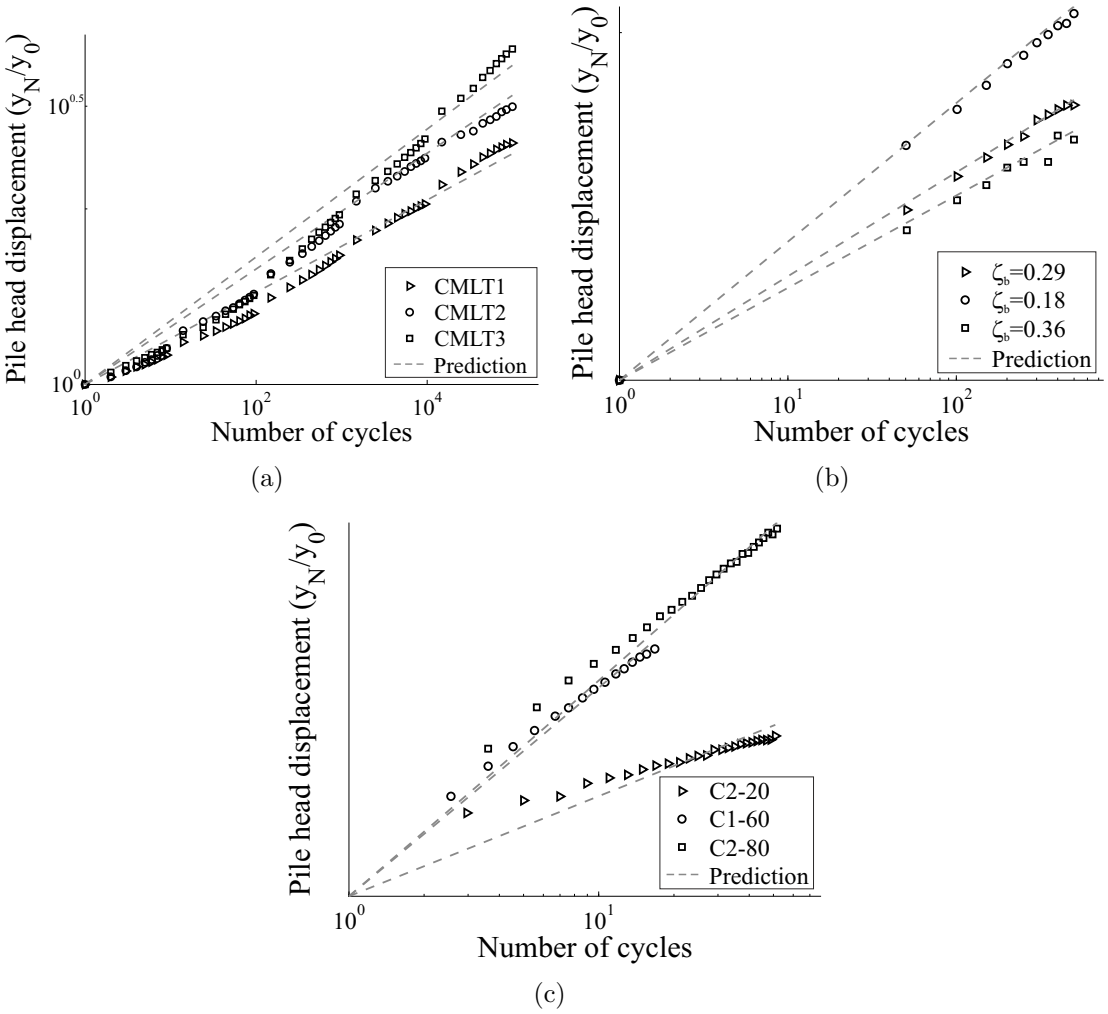

Figure 3.14: Comparison between experimental results (scattered plots) and predictions using the Degradation Stiffness Model (dashed lines) for a range of relevant tests from (a) Table 2.6, (b) Klinkvort (2012) and (c) Verdure *et al.* (2003)

in this case, the values obtained for m_θ (Equation 3.3; 0.035,0.087,0.102 for Tests no. C2-20,C1-60 and C2-80 respectively) differ from the values obtained for δ (Equation 1.18; 0.140,0.290,0.300 for Tests no. C2-20,C1-60 and C2-80 respectively). More work on flexible piles would be required to investigate the values of m_θ and δ further.

3.3.3 Secant stiffness

As illustrated previously in Figure 3.10 (p. 102), there is a progressive change in loop shape as cycles develop. One way to quantify this change is to analyse the evolution of the secant stiffness with cycle number. Also, this is relevant for

fatigue design as the first tower bending mode is a function of the foundation stiffness (Chapter 1, Section 1.2.3, p. 12).

LeBlanc *et al.* (2010a) and Klinkvort (2012) both demonstrate that the secant stiffness increases with cycle number. The published results involved tests on dry and saturated sand with relative densities of 4%, 38% (LeBlanc *et al.*, 2010a) and 80%-97% (Klinkvort, 2012). The results obtained during this research project (Figure 3.15(a) and 3.15(b)) are consistent with this argument. The empirical evolution law proposed by LeBlanc *et al.* (2010a) is outlined below and has been used to fit the experimental data:

$$\tilde{k}_N = \tilde{k}_0 + 8.02 \cdot ln(N) \tag{3.11}$$

The results displayed in Figures 3.15(a) and 3.15(b) show that Equation 3.11 closely matches the test results for cycle number greater than 50. However, for small cycle numbers (< 50), the secant stiffness departs from the predicting trend and exhibits a much steeper slope, and therefore a larger logarithmic coefficient, that appears to depend on the loading conditions (see for example the differences in initial logarithmic slopes between the four tests of Figure 3.15(a)). The tests presented here are not adapted for investigating the initial portion of the curve any further. However, future work might want to consider exploring the evolution of the early cycles secant stiffness with regards to load magnitude and amplitude and proposing an empirical law for design.

Figure 3.15(c) displays a comparison of the values obtained for $\tilde{k}_0$ for selected tests in Table 2.7 compared with the data obtained by LeBlanc *et al.* (2010a). There is a very favourable comparison, with the minor differences attributable to slight variations in the experimental set-up.

Finally, the initial elastic modulus E_{S0}, as calculated in Section 2.5.1.2 and normalised in the same way as $\tilde{k}$, has been plotted on Figure 3.15(a) and (b) for

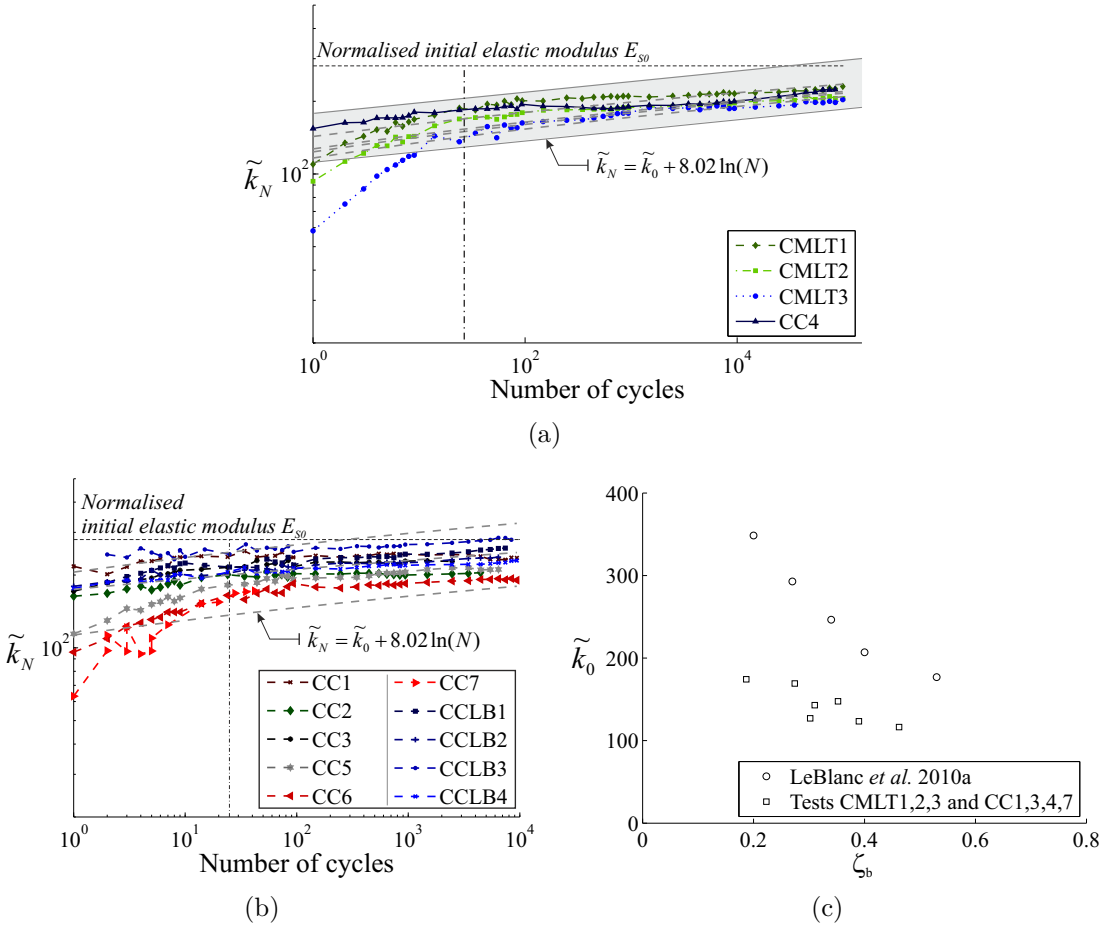

Figure 3.15: Evolution of the cyclic secant stiffness for tests in Table 2.7: (a) Tests that involve at least 100,000 cycles (b) All other cyclic tests mentioned in last part of table. (c) Comparison of k_0 values for tests CMLT1,2,3 and CC1,3,4,7 and tests from LeBlanc *et al.* (2010a)

comparison. It is noteworthy that the initial elastic stiffness is always greater than the cyclic secant stiffness, which tends towards this value as cycles develop.

Another way to illustrate the above phenomena is to plot the loading paths of selected cycle number for long-term cyclic tests (here, CMLT1-3). In order to compare them all, the displacement induced by the number of cycles is discarded (i.e. the cycles are rezeroed), and the results are plotted along with the initial elastic modulus slope E_{S0} for comparison. The results are displayed in the upper part of Figures 3.16(a) to 3.16(c), where the progressive stiffening of the response can be clearly seen. Also, cycles number 1 and 10 always stand out from the other loading curves, which is consistent with previous observations from Figures 3.15(a) and

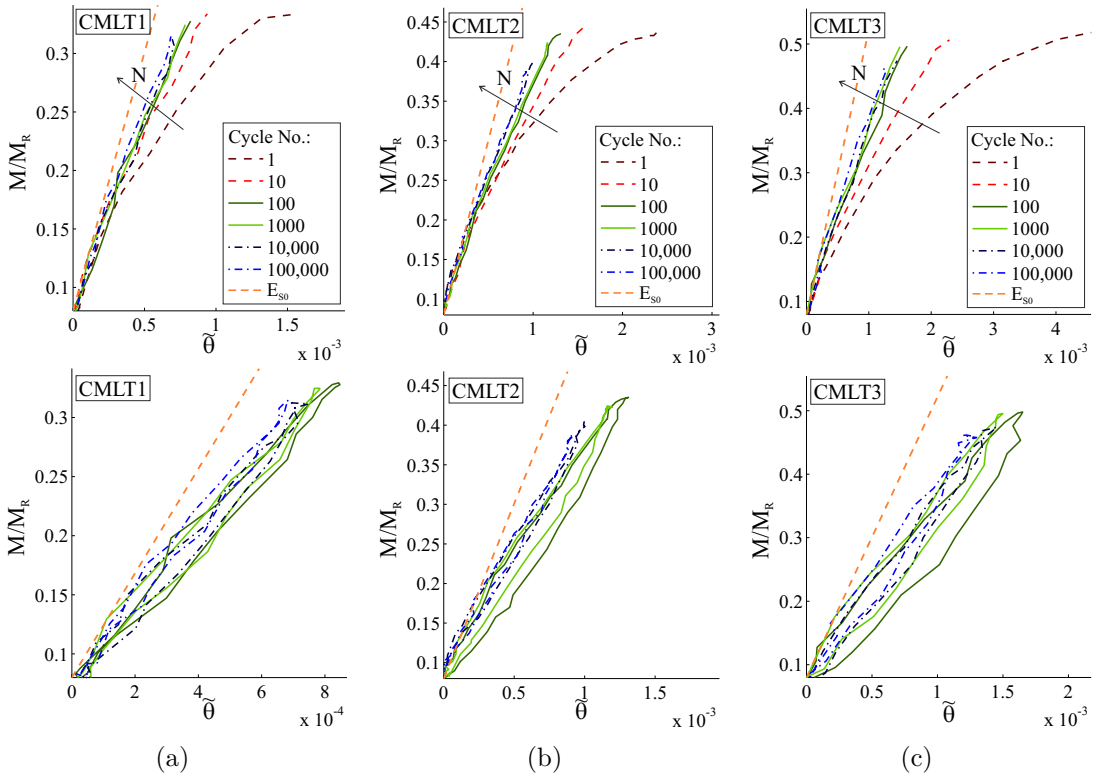

Figure 3.16: Evolution of the loading curve portion to maximum cyclic load magnitude (top) and entire cyclic loop (zoom at bottom) at different cycle number for tests (a) CMLT1, ($\zeta_b = 0.33,\ \zeta_c = 0.21$) (b) CMLT2, ($\zeta_b = 0.44,\ \zeta_c = 0.18$) (c) CMLT3, ($\zeta_b = 0.48,\ \zeta_c = 0.14$)

3.15(b). Small fatigue-type loads are likely to involve large number of cycles, however, large storm-type loads will probably only occur for few cycle numbers. Consequently, it is important to capture this transition in secant stiffness response in future design methods.

The lower part of graphs 3.16(a), 3.16(b) and 3.16(c) shows a zoom on the entire cycle loop for the same cycle numbers and the same tests as the upper part. On these plots, cycles 1 and 10 have been removed to improve clarity. An interesting feature outlined here is that, despite being very close to a straight line, the cycle loop never close, which means that the response to large cycle number is not purely elastic. This conclusion would obviously need to be extended to larger cycle number.

3.3.4 Hysteresis loop area

Another way to describe the evolution of the loop shape in Figure 3.10 (p. 102) is to consider the hysteresis loop area, which is also a relevant parameter for fatigue design.

Before considering the evolution of damping, the results of the normalised loop area are analysed. According to the framework exposed in Chapter 2, Section 2.2, p. 51, the dimensional expression for A is:

$$\tilde{A} = \frac{A}{D}\sqrt{\frac{p_a}{L^7\gamma'^3}} \tag{3.12}$$

The evolution of the normalised loop area for the cyclic tests in Table 2.6, are displayed in Figures 3.17(a) and 3.17(b). First of all, deriving the loop area from the experimental data requires extreme precision in both set-up and data acquisition and it is probably the parameter that is most subject to experimental errors and noise. Test CC4 is one of the early tests from this experimental campaign and the precision and confidence regarding the loop area results on this test was poor. Therefore, the results from this particular test have been omitted from Figure 3.17(a).

The results from Figure 3.17(a) and 3.17(b) clearly show a tightening of the loop shape with cycle number that follows the pattern of an exponential decay. The data fitting, shown with the gray dotted lines, correspond to the empirical law:

$$\tilde{A} = \tilde{A}_r N^{-m_A} \tag{3.13}$$

Where $\tilde{A}_r$ is a dimensionless function of the load magnitude (Figure 3.17(c)) and m_A is a power coefficient equal to 0.15. Finally, it is interesting to investigate the relationship between the loop area and the secant stiffness as these parameters are likely to be linked. Figure 3.17(d) shows that, as a first approximation, the evolution of the loop area can be considered as a linear function of the secant flexibility $1/\tilde{k}$

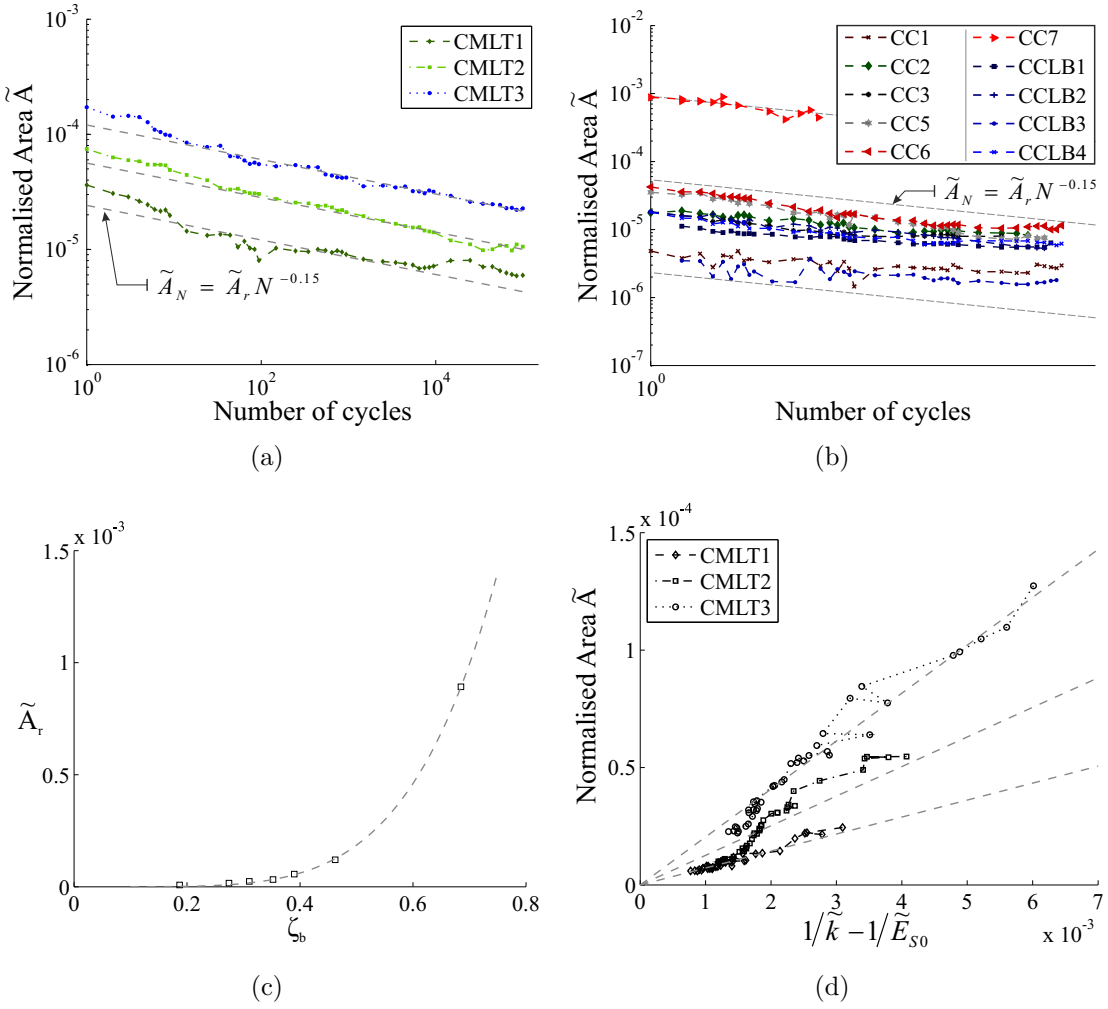

Figure 3.17: Evolution of the normalised hysteresis loop area $\tilde{A}_N$ with cycle number for (a) long-term cyclic loading tests CMLT1,2,3 (b) continuous cyclic loading tests CC1,2,3,5,6,7 (c) Function relating $\tilde{A}_0$ to the load magnitude ζ_b for tests CMLT1,2,3 and CC1,3,4,7; (d) Relationship between hysteresis loop area and secant stiffness

minus the initial flexibility $1/\tilde{E}_{S0}$. This can be justified more rigorously and will be addressed in the theoretical developments presented in Chapter 5 (Section 5.3, p. 197). In conclusion, for theoretical developments, the above observation means that accurate modelling of the change in hysteresis loop shape will require both an increase in secant stiffness and decrease in energy dissipation with cycle number.

Finally, the measurements of the evolution of the hysteresis loop area can be used to provide an indicator of the evolution of the soil damping during cyclic loading. The definition of the damping ratio is not usually applied to 1-way loading, especially

when deformation of the hysteresis loop occurs due to ratcheting. Consequently, the definitions of the expended and stored elastic energy are more complicated. First, the energy dissipated during one reload-unload loop A_{hys} can be considered as the sum of the energy expended due to hysteretic behaviour plus the energy expended due to ratcheting. For any cyclic loop, this is best approximated by the area enclosed by the reload-unload loop as illustrated by the gray surface in Figure 3.18(a). Secondly, as the loop does not close due to ratcheting, the definition of the stored elastic energy is imprecise. Ignoring ratcheting first, the stored elastic energy of a theoretical 1-way loading closed loop is estimated by the upper triangle from the mean to maximum applied load, characterised by the line connecting the tips of the moment-rotation loop (e.g. Taborda *et al.*, 2016). Based on this definition and in order to account for stored internal energy due to ratcheting on both loading and unloading, it was chosen to define the secant stiffness as the median secant stiffness, that is to say the line passing from the median minimum displacement between cycle N and $N+1$ and the summit of the cyclic loop (see Figure 3.18(a)). Accordingly, the maximum stored elastic energy A_{el} is then defined by the upper triangle from the mean load amplitude to maximum load (hatched surface, Figure 3.18(a)). With these definitions for A_{hys} and A_{el}, the cyclic damping ratio D_{a1N} is deduced using Equation 3.1.

The results for the continuous cyclic tests are plotted in Figures 3.18(b) and 3.18(c). The graph shows that the damping ratio decreases with cycle number and its evolution is well estimated using a power-law:

$$D_{a1N} = \tau D_{a0} N^{-m_d} \tag{3.14}$$

where $D_{a0} = 0.28$ is the damping ratio measured from the symmetric loading test (test H0, Section 3.2.1, p. 93) and τ, an empirical cyclic reduction coefficient. The data were found to be well approximated using the exponent value $m_d = 0.31$ (see Figures 3.18(b) and 3.18(c)). It is noteworthy that the value of the power exponent

is the same as that for the evolution of the accumulated rotation (Equation 3.2). Both $\Delta\theta$ and D_{1aN} quantify how much non-linearity there is in a cyclic loop, or in other words, measure the irrecoverable process occurring during any one cyclic loop. It is therefore consistent to find that these two parameters develop in a similar fashion. Finally, Figure 3.18(d) shows the evolution of the cyclic damping coefficient $\tau = D_{a1,N=1}/D_{a0}$ as a function of the load magnitude. First, apart for the two early points that correspond to small load magnitude, and therefore, are subjected to larger experimental errors, the coefficient τ linearly increases with load magnitude. Finally, the graph shows that the cyclic damping ratio is about 50 times smaller than

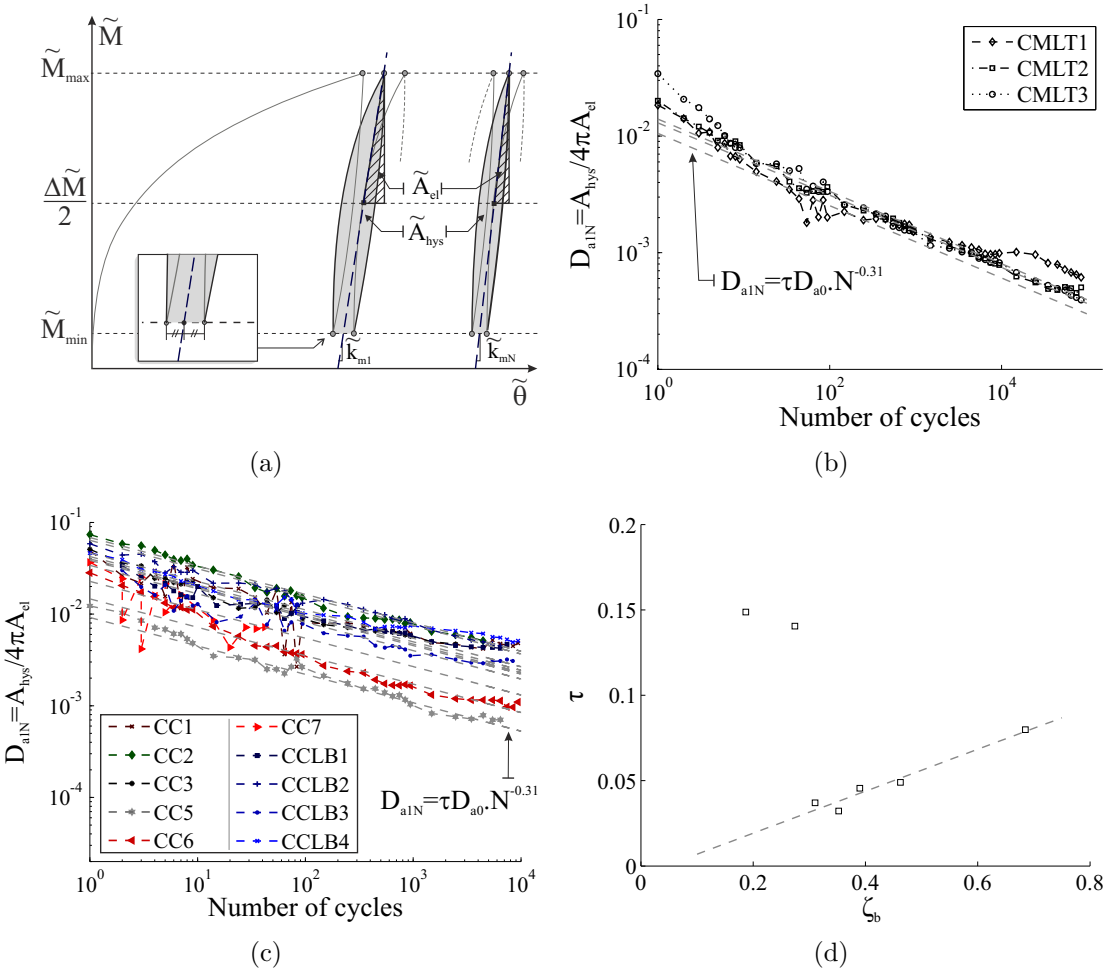

Figure 3.18: (a) Definition of the cyclic damping ratio; Evolution of the cyclic damping ratio for (b) long-term cyclic tests CMLT1,2,3 (c) continuous cyclic tests CC1,2,3,5,6,7; (d) Function relating D_r to the load magnitude ζ_b for tests CMLT1,2,3 and CC1,3,4,7

D_{a0} for comparable load magnitudes. At this stage, it is difficult to say whether this arises from the definition of the damping ratio for 1-way loading, or occurs due to change in hysteretic behaviour during cyclic loading. As shown in the next section, with the shape of the reloading curves after cyclic loading, the later is quite likely. However, complementary tests, considering cyclic loading, followed by a symmetric loading test, would enable to complete this study.

3.4 Effect of cyclic loading on monotonic response

3.4.1 Overview

The results from Section 3.3 suggest a progressive hardening of the pile response with cyclic loading. However, the load cases investigated so far were always continuous, i.e. never exceeded the maximum cyclic load. The next step before investigating multi-amplitude loading, is therefore to analyse how the monotonic response is influenced by cyclic loading, and how it compares to the backbone curve. The results from Section 3.2.1 indeed showed the relevance of accurate prediction of the initial loading curve (backbone curve) for the determination of the subsequent response. Consequently, it is of interest to determine whether the initial backbone curve develops with long-term cyclic loading and whether the response still conforms to the extended Masing rules after many cycles.

This section therefore analyses the results of static reloading tests performed immediately after cyclic loading and is concerned with the evolution of the loading curve with respect to the ratcheting and stiffening phenomenon outlined in the previous section. The tests are listed in Table 2.7 and noted "-M" in the *Test method* cell. In the following, the effect of cycle number (tests CMC1-7, CMLT2,3), load magnitude (CMLT1-3, CMM1-4) and amplitude (CMA1-2) are investigated. A typical moment-rotation curve for a long and short-term cyclic test is displayed in Figures 3.19(a) and 3.19(b) respectively.

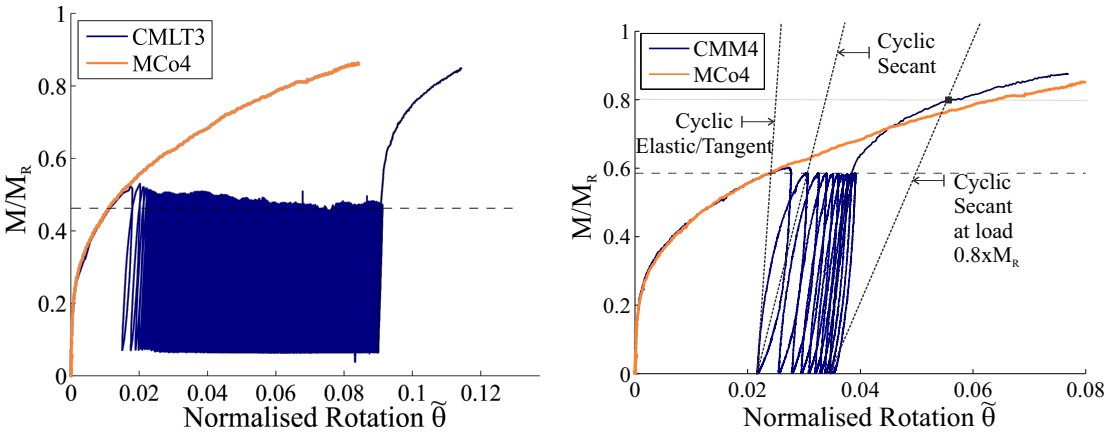

Figure 3.19: Typical results obtained during continuous cyclic loading tests immediately followed by a monotonic test (a) Test CMLT3, 100,000 cycles; (b) Test CMM4, 10 cycles

In the following analysis, only the reloading monotonic response is of interest. Consequently, the cyclic load history will not be displayed on the plots (light blue lines of small amplitude on Figures 3.19(a) and (b)), and solely mentioned through (i) a dashed horizontal line indicating the maximum cyclic load magnitude and (ii) the origin of the reloading curve, plotted from the final cyclic rotation at minimum peak load. In the legends, the past cyclic loads are characterised by their cycle numbers, load magnitudes and amplitudes. The influence of each of these on the monotonic response is investigated in separate sections.

3.4.2 Effect of cycle number

The influence of cycle number is first explored by performing tests with the same load amplitude and magnitude, but increasing cycle numbers. Two series of tests have been performed, one at 42% of the ultimate capacity and the second at 47%. The results are displayed in Figures 3.20(a)-(c). On Figures 3.20(a) and 3.20(c), the gray dotted lines show the initial elastic modulus and the oblique black dotted lines represent the initial tangent modulus as found in Chapter 2, Section 2.5 (p. 68).

First of all, Figures 3.20(a) and 3.20(c) indicate that neither the elastic nor the

tangent modulus are altered by cyclic loading. When exceeding the maximum cyclic load, the reloading curve tends towards the backbone curve, which conforms to the extended Masing rules. Figure 3.20(b) shows a zoom on the initial portion of each monotonic curve, plotted from the origin. In a similar fashion to Figures 3.16(a)-(c), this graph outlines the progressive stiffening of the initial portion of the curve (below the maximum cyclic load) towards the initial elastic modulus. Also, it illustrates a very sharp increase in secant stiffness from the first cyclic load and then a second change between cycle 10 and 100. This is consistent with the findings from Figures 3.15(a) and 3.15(b) (p. 115), where a change in the rate of increase of stiffness was

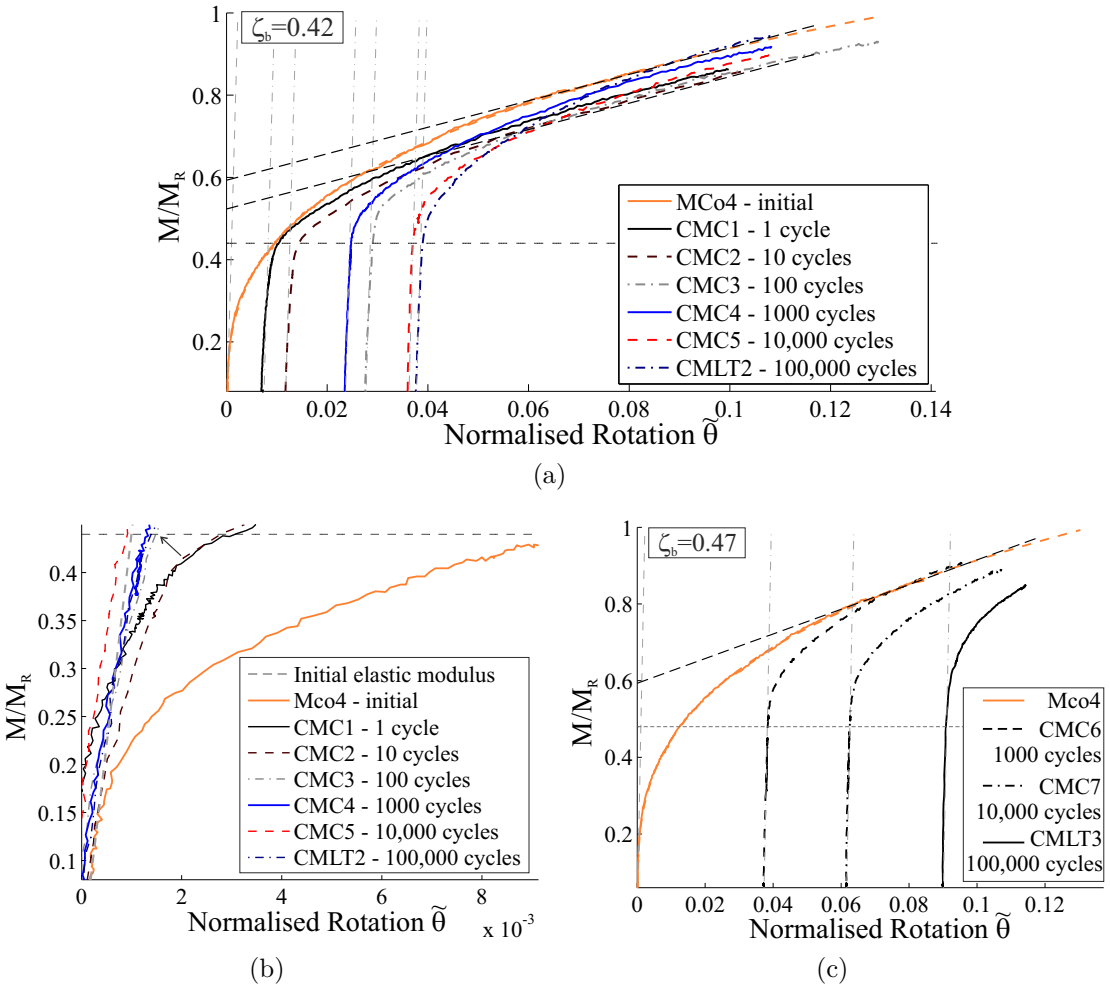

Figure 3.20: Influence of cycle number on monotonic response: (a) Test series with ($\zeta_b = 0.44,\ \zeta_c = 0.18$) (b) Zoom on the initial portion of each curve of Figure 3.20(a) and comparison with initial elastic modulus (c) Test series with ($\zeta_b = 0.48,\ \zeta_c = 0.14$)

observed at around 50 cycles. From a modelling point of view, this means that a hardening mechanism, such as isotropic hardening, will need to be implemented, but in a small proportion and as a progressive and controlled function of the load history.

The accumulation of ratcheting deformation takes the reloading curve away from the backbone curve while the stiffening phenomenon actually brings it closer. This is illustrated in Figure 3.20(c), where the final reloading curve tends to rejoin the backbone curve but actually never reaches it, probably because the reloading monotonic test was not taken to a sufficiently large load. This shows that there is a competition between (i) Masing behaviour, (ii) ratcheting and (iii) progressive stiffening of the response.

3.4.3 Effect of load magnitude and amplitude

To complete the above framework, three load series investigate the effect of the cyclic load magnitude and amplitude on the subsequent monotonic response. First, tests CMM1,2,3,4 investigate the influence of cyclic loads at 4 different load magnitudes and after 10 cycles, while tests CMLT1,2,3 focus on three load magnitudes at 100,000 cycles. The results are displayed in Figures 3.21(a) and 3.21(b) and exhibit the same type of trends as outlined in Figures 3.20(a) and 3.20(c). The figures show that the initial and tangent moduli are unchanged by cyclic loads and that the reloading curves rejoin the backbone curve. Both figures also illustrate the competition between the Masing behaviour, ratcheting and stiffening of the response.

An interesting outcome from these graphs is that the amplitude of the stiffening region (portion of the curve close to the elastic modulus), is proportional, or perhaps equal, to the maximum cyclic load (matching color dotted lines). This re-enforces the conclusions from Figure 3.15(c), showing that the evolution of the secant stiffness depends on the cyclic load magnitude.

The above findings raise the question of what would happen if the cyclic load magnitude was within the elastic region. It would be interesting to find out whether

accumulated deformation would be experienced, but also, whether the stiffness of the response would develop and to what extent the following monotonic response would resemble the backbone curve. If the reloading curve closely followed the backbone curve, this would mean that cyclic loading at small amplitude could be discarded in design. However, the loading rig used for the testing was not configured in such a way as to allow such small amplitude loading to be applied, but future modifications of the testing equipment should take this remark into account.

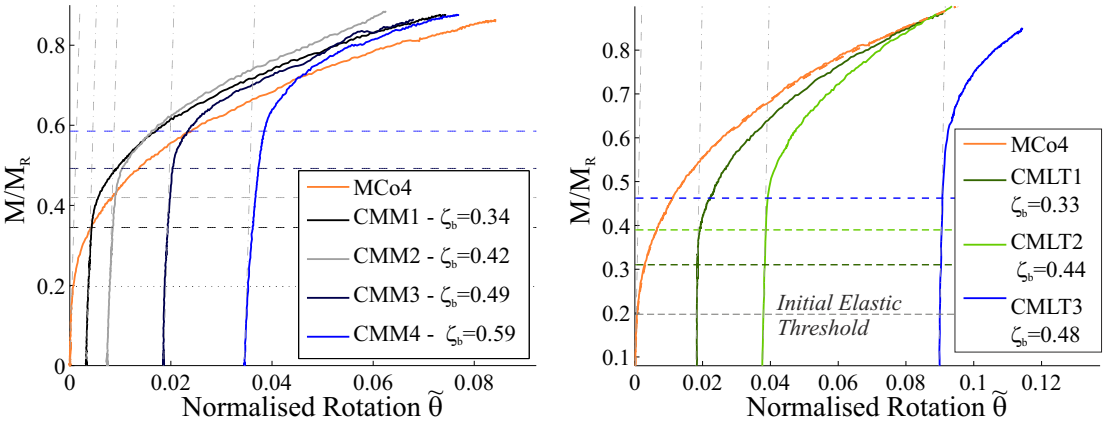

Figure 3.21: Influence of maximum cyclic load magnitude on monotonic response: (a) 10 cycles test series (b) 100,000 cycles test series

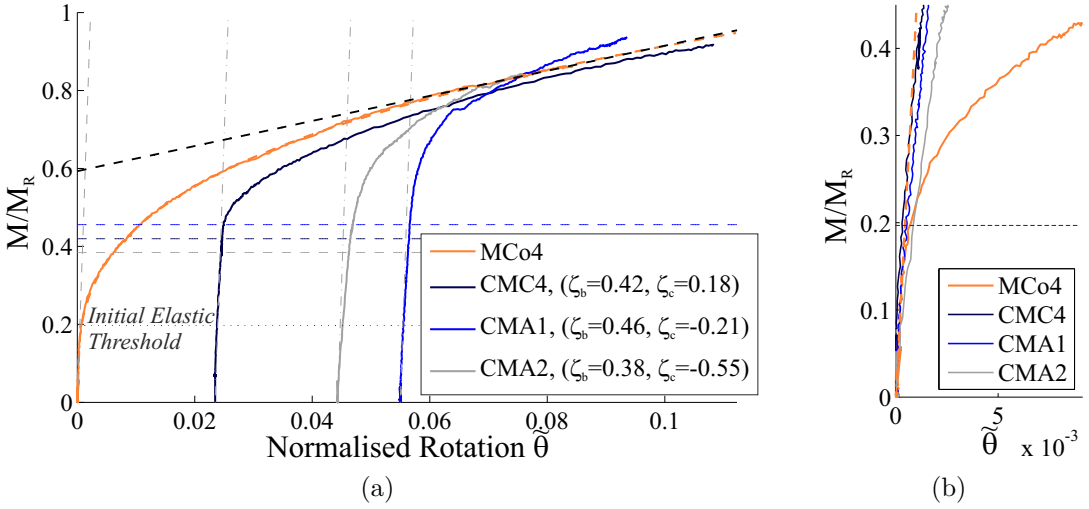

Figure 3.22: (a) Influence of load amplitude on monotonic response 10 cycles test series (b) Zoom on the initial portion of each curve of Figure 3.22(a)

Finally, it is legitimate to envisage that cyclic loading amplitude might also have an influence on the reloading monotonic curve. To investigate this further, three tests of 1000 cycles, involving various values of $\zeta_c = M_{min}/M_{max}$ have been conducted. The results of the tests are plotted in Figure 3.22(a) and 3.22(b). Once more, the trends are very similar to that of Figures 3.20(a)-(c) and no distinct additional conclusion arise from these test results.

3.5 Multi-amplitude cyclic loading

The logical development of the work presented above is to study the pile response to multi-amplitude cyclic loading. Chapter 1, Section 1.4.3 (p. 35) described the current knowledge on this topic through the findings of two published research studies (results from LeBlanc *et al.*, 2010b; Peralta, 2010). The key conclusion was that the loading history has an influence on the pile response. In addition, a model proposed by LeBlanc *et al.* (2010b) for the prediction of the response to load series of variable amplitudes was presented. It is based on Miner's linear cumulative damage rule (Miner, 1945) and was proven to reasonably predict the sequences investigated.

These studies are the first steps towards a better understanding of the pile response to multi amplitude cyclic loading, but they only involve very limited data sets, with the loading featuring 1,000 cycles per load sequence. Hence, they are not completely representative of offshore loading conditions, and in particular, do not address what the pile response could be during and after a storm period. Leblanc *et al.*'s model has so far been applied to only two test results (one published in LeBlanc *et al.* (2010b) and one published in Abadie *et al.* (2015)). Consequently, this model requires validation against a larger data base.

The following section presents a series of test results that address these issues, and in particular, analyses the effect of load history in more details. First of all, this paragraph explores the results of test H1IM1 (see Table 2.6, p. 65). This test

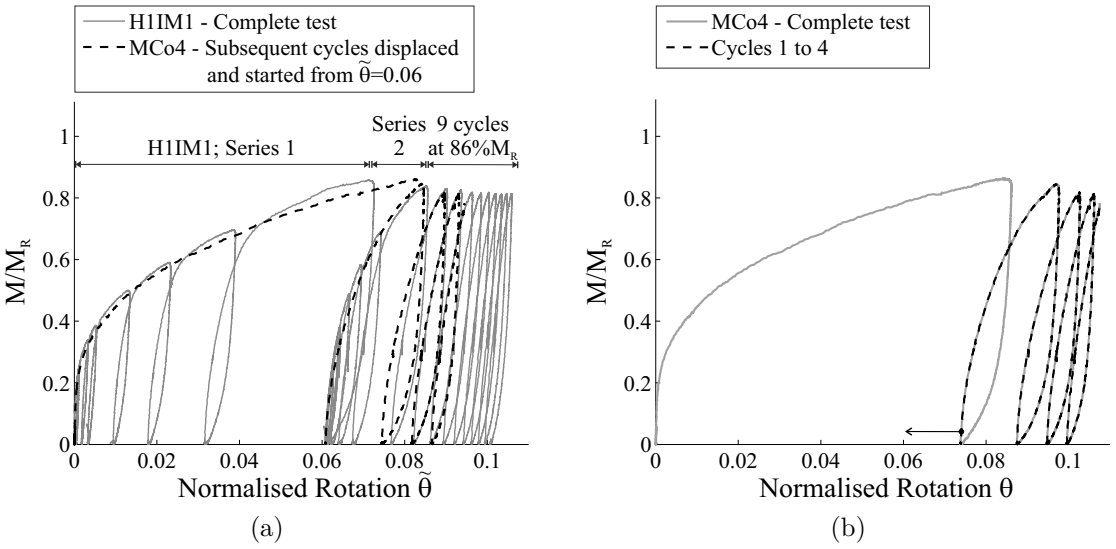

Figure 3.23: (a) Complete response measured during test H1IM1 compared with cycles 1 to 4 of test MCo4; (b) Complete response measured during test MCo4

involved a second series of increasing load cycles identical to the first series, followed by 9 cycles at 86% ultimate capacity. Similarly, test MCo4 actually included more cycles (about 5, until the LVDTs reached maximum stroke capacity). Figure 3.23(a) shows the second load series response of test H1IM1, along with cycles 1 and onwards (cycle no. 0 is discarded) of test MCo4, which is displaced and re-origin from the same origin as the second portion of test H1IM1 for comparison. For complementary information, Figure 3.23(b) displays the total response obtained from test MCo4, showing the initial origin of cycle no. 1, around 0.074. Section 3.2.1 demonstrated that the first load series of test H1IM1 followed the backbone curve of test MCo4 (see Figure 3.9(a), p. 101). Figure 3.23(a) shows that the load series no. 2 of test H1IM1 closely follows the response of cycle no. 1 of test MCo4, which conforms to the extended Masing rules. The graph shows that the response of test H1IM1 to the cyclic loads at 86% ultimate capacity closely follow that of test MCo4, regardless of the previous smaller load history. This raises the questions of (i) whether the load history can be discarded in some cases, and when and (ii) what the effect of the load history on Masing behaviour, ratcheting and hysteresis loop shape is. These are the key points behind the work presented in the following paragraphs.

The test campaign presented in the following is that of Table 2.8 (p. 67), with the load series (Table 2.9, p. 67) carefully chosen based on realistic design loads for ultimate (ULS), accidental (ALS), serviceability (SLS) and fatigue (FLS) limit states as described in Table 1.3 (Chapter 1, p. 8). The work proposed here is limited to one-way loading only. Tests MALL1 to 3 investigate the influence of large load history on the final pile displacement and hysteresis loop shape. Tests MALL4,5 and 6 then explore the effect of cycle number and load magnitude of ULS/ALS load types on the subsequent response to SLS cyclic loads. Tests MASL1 to 5 examine the effect of load history when storm and long-term FLS loading are alternatively applied to the top of the pile. Finally, test MASL6 mimics the application of two storms on a continuous FLS cyclic load and test MASL7 was designed to better understand the influence of increasing load events on the pile response during continuous cyclic FLS loading.

3.5.1 Large load history

The first three tests studied in this section involve three load series (100 cycles of C, 10 of D and 1 of E; see Table 2.9) tested in different orders and compared with each other. Figures 3.24(a)-(c) display the moment-rotation curves of the three tests compared with the backbone curve of test MCo4. The three figures clearly show that, when exceeding the maximum previously applied load, the reloading curve follows that of the backbone curve, which conforms to the extended Masing rules. Therefore, this shows that the Masing behaviour is not altered by the load history which compares favourably with the test results of the previous section.

Figure 3.24(d) displays the normalised rotation of the three tests. The light gray lines represent the total rotation evolution (minimum to maximum) while the darker lines highlight the maximum rotation of each test. This graph first shows that the final displacement of each test do not match, proving that the load history is significant. Also, the order in test results is MALL2>MALL3>MALL1. Analysing

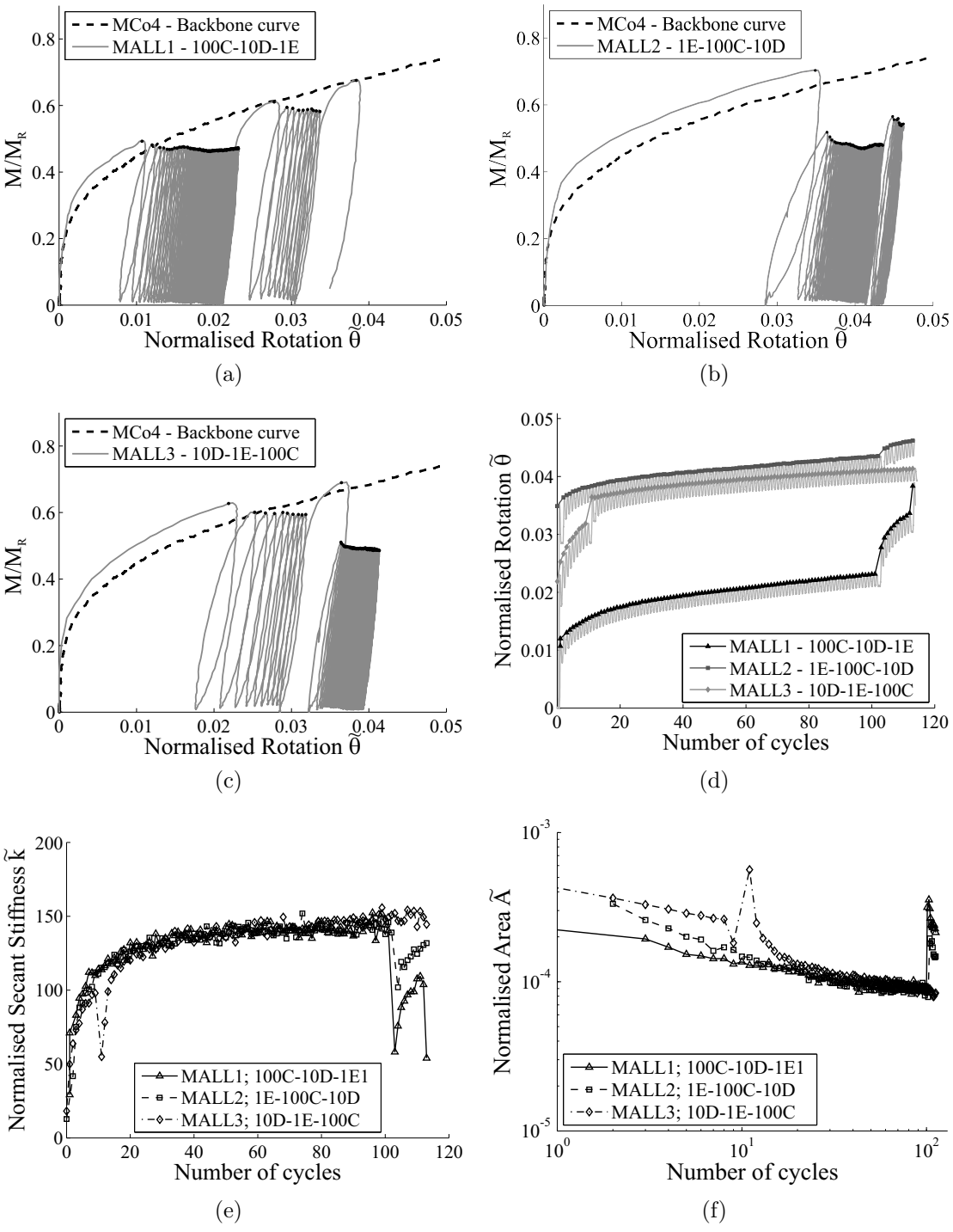

Figure 3.24: Moment-rotation curve for tests (a) MALL1, (b) MALL2 and (c) MALL3; Evolution of (d) the pile rotation, (e) the secant stiffness and (f) the hysteresis loop area for tests MALL1-3

Figures 3.24(a)-(c), this order can be explained by the fact that, in general, the largest load is responsible for the largest contribution to the pile deformation. This is due to the shape of the backbone curve, with a softer response towards higher load. However, the *larger* the load history before the extreme event, the stiffer the subsequent response to the extreme load event, and therefore, the less the induced ratcheting. Therefore, the test where the extreme event occurs last is the one that induces the least deformation, and accordingly, the test where the largest load appears first produces the largest pile rotation. It remains to define what the term "larger" highlighted in italics means, i.e. whether it is in terms of cycle number, load magnitude or both, and also, whether there are thresholds after which the response remains unchanged.

Finally, the rotation induced by the last two series 100C-10D of test MALL2 are responsible for 25% of the final displacement, showing that the smaller loads following the extreme load event cannot be discarded in design.

Figure 3.24(e) shows the evolution of the secant stiffness for the three tests. Interestingly, the curves from the three tests super-impose for the same load magnitude and cycle number. This means that, for the load sequences investigated here, the secant stiffness depends on the load magnitude and cycle number only but is insensitive to the load magnitude history. Similarly, Figure 3.24(f) shows the evolution of the loop area for the three tests and the conclusion for this graph is the same as for the secant stiffness. This demonstrates that, for the load sequences studied above, only the accumulated rotation depends on the load history, but the hysteresis loop shape solely depends on the current load magnitude and the number of cycles the pile has already experienced, regardless of their load magnitudes. This observation could explain the results from Figure 3.23(a) (p. 127) and why the loop shapes are similar.

Clearly, the accumulated rotation induced by the 100C series for the three tests is very different. Just as for the rotation induced by the largest load, this depends on the previous load history. This was investigated in more detail with tests MALL4, 5

and 6. First, tests MALL1,2,4 and 5 investigate the influence of the cycle number of a cyclic load at 59% of ultimate capacity on the load series 100C ($49\%M_R$). Figure 3.25(a) displays the rotation of the 100C load series, plotted from the origin (previous load history discarded) and Figure 3.25(b) shows the loading portion of the second cycle of this load series also plotted from the origin for each test. Figure 3.25(a) illustrates the intuitive conclusion that the number of previous load cycles reduces the ratcheting induced by the subsequent cyclic load. In addition, it shows that something happens between 10 and 100 cycles that has a significant effect on the

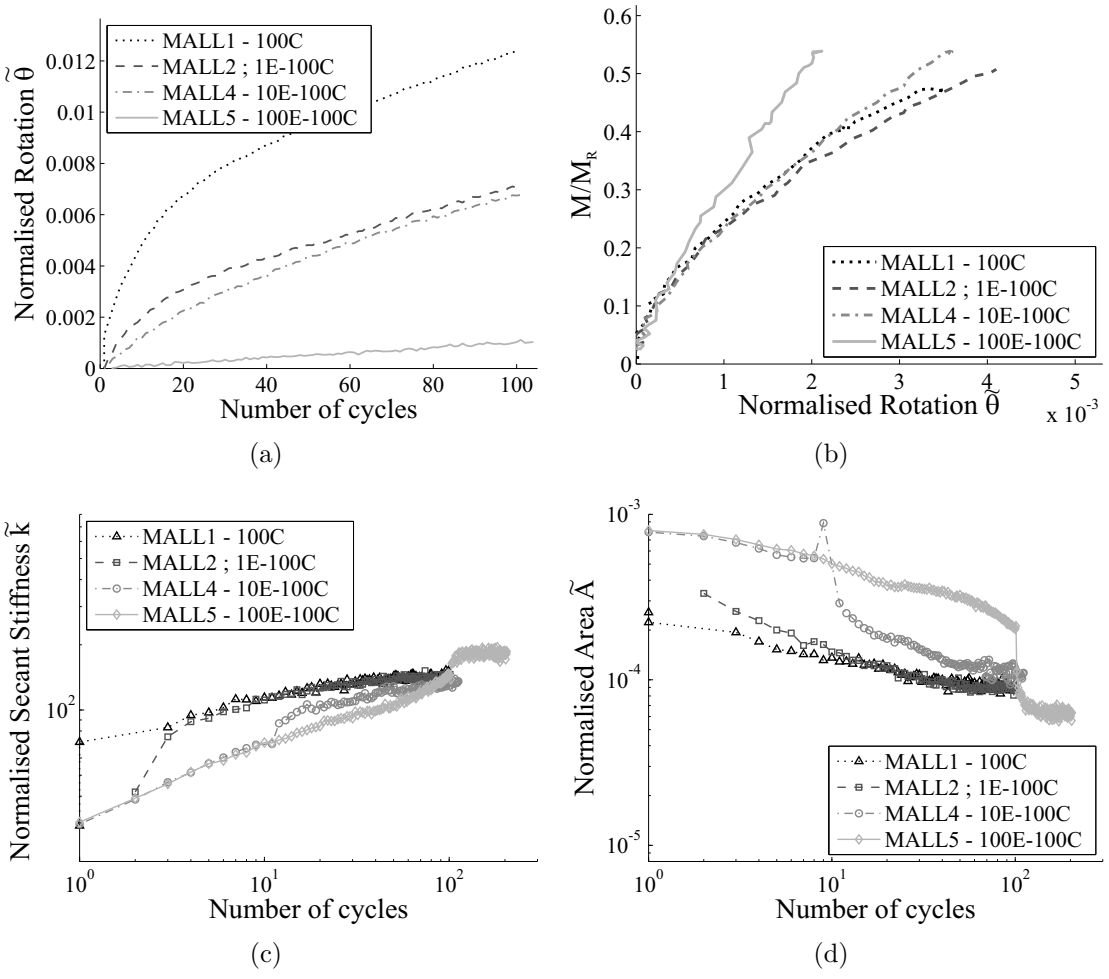

Figure 3.25: (a) Comparison of the rotation evolution during the 100C series only for four multi-amplitude tests involving different loading histories; (b) Comparison of the moment-rotation curve for cycle no.2 of the 100C series; Evolution of the (c) secant stiffness and (d) hysteresis loop area for the complete load sequences for tests MALL1,2,4 and 5

accumulated rotation and drastically reduces it. In comparison, the differences between the responses after 1 cycle of E and 10 cycles of E are negligible. Finally, Figures 3.25(c) and 3.25(d) show the evolution of the secant stiffness and loop area respectively for the complete tests. The graphs shows that the curve of test MALL5 departs from the other tests and that the general trend is modified by the application of the 100E load sequence.

This agrees with the results on the secant stiffness from Section 3.3.3 (Figures 3.15(a), 3.15(b), p. 115 and Figures 3.16(a)-(c), p. 116) and the conclusions from Section 3.4.2 (Figure 3.20(b), p. 123) where a change in rate of increase of stiffness was clearly observed after about 50 cycles. This demonstrates that the response greatly stiffens between cycle number 1 and 50 and that this phenomenon significantly retards the ratcheting of the pile response for subsequent load cycles at smaller load magnitude. Of course, one limitation of this conclusion is the low relative density of the tests and it would be useful in future to extend this work to denser sand samples.

Moreover, this justifies why the stiffness and loop area evolutions of Figures 3.24(e) and 3.24(f) (p. 129) respectively were super-imposed; because the number of cycles of the extreme load events ($10D + 1E$) were below the cycle number threshold after which a clear change in stiffness is observed.

Finally, tests MALL1,4 and 6 investigate the influence of previous load magnitude on the 100C load series response for the same number of cycles. Here, the influence of 10 cycles at 69% (E) and 83% (F) ultimate capacity are tested and the results are reported in Figures 3.26(a) and 3.26(b). First, Fzxigure 3.26(a) displays the evolution of the rotation for the 100C series only and shows that ratcheting is decreased by larger previous load magnitude, but that the differences are not as significant as between cycles 10 and 100 in Figure 3.25(a). Figure 3.26(b) presents the moment-rotation of cycle no.2 of each 100C series and demonstrates that the reloading curve is unaltered by the previous load sequences. Similarly, Figures 3.26(c) and 3.26(d) capture the evolution of the secant stiffness and hysteresis loop area and suggest that

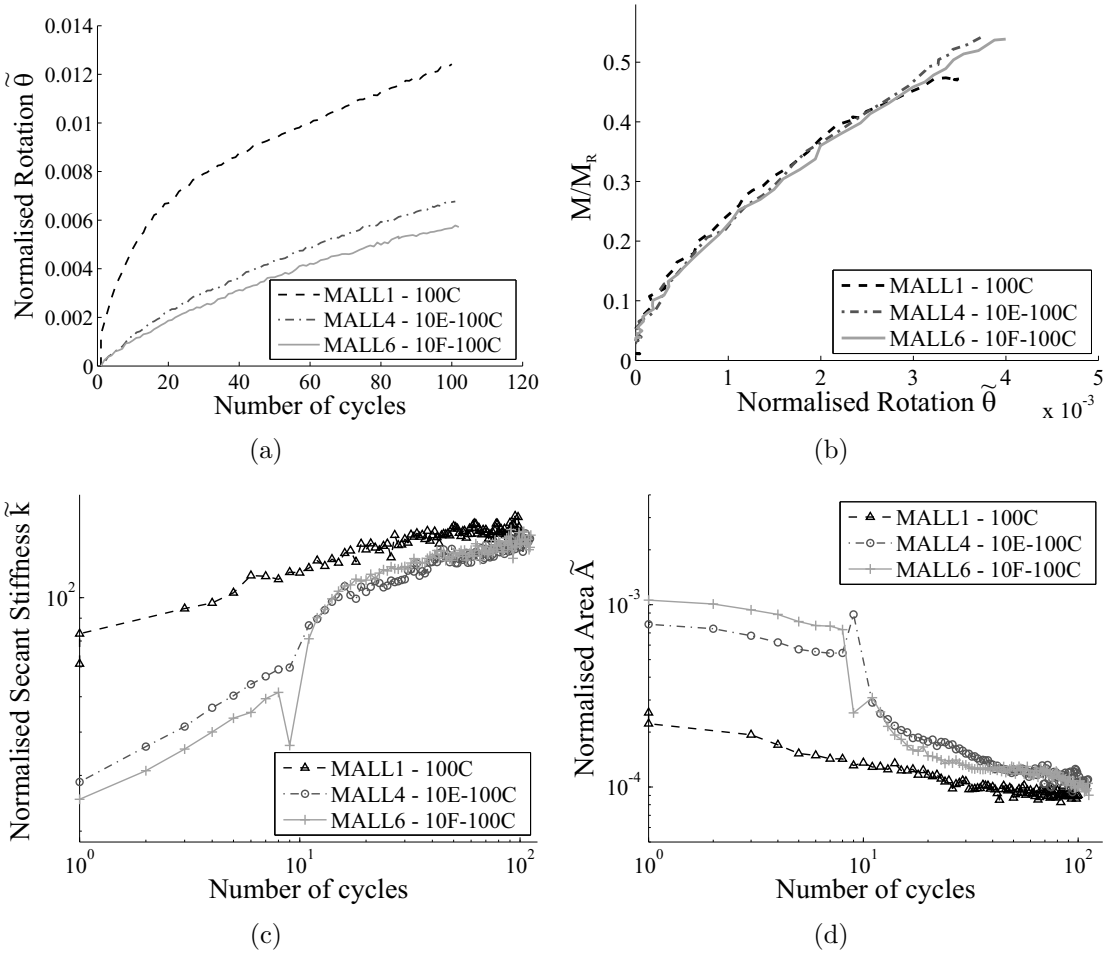

Figure 3.26: (a) Comparison of the rotation evolution during the 100C series only for three multi-amplitude tests involving different loading magnitude histories; (b) Comparison of the moment-rotation curve for cycle no.2 of the 100C series; Evolution of the (c) secant stiffness and (d) hysteresis loop area for the complete load sequences for tests MALL1,4 and 6

the hysteresis loop shape is mildly affected by the load history. This is consistent with the previous conclusions (Figures 3.23(a), 3.24(e), 3.24(f), 3.25(c) and 3.25(d)). This shows that the load magnitude is not the primary mechanism that reduces the ratcheting rate and that the number of cycles of previous larger load is more significant for design.

If the above conclusions are taken one step further, large number of cycles of large load events could possibly cancel accumulated rotation from any subsequent cyclic load at small magnitude. This is a very interesting point for design as it indicates

that pre-loading of the pile, prior to installation of the turbine, could be beneficial for the foundation lifetime, and also, that extreme load events (both monotonic and cyclic) are the primary concern in design. This is investigated further in the next paragraphs of this section.

3.5.2 Alternating operational and storm type loads

Tests MASL1 to 5 were specially designed to study the influence of alternating long-term FLS, short-term SLS and single ALS load events on the pile response. First, tests MASL1,2 and 3 investigate the influence of the sequence order 1000A, 100C and 1E. The results are displayed in Figure 3.27 where the light gray lines represent the total displacement (minimum to maximum) and the darker lines represent the maximum displacement of each test. The ultimate maximum pile displacement has been highlighted with a dot for the three tests. The graph shows that the final displacement of the three tests is very close. One possible explanation of this result is that the small load history does not affect the pile response much and that the final deformation is mostly due to the large load series (mostly 1E, and to a smaller extent, 100C).

This statement could be verified by (a) increasing the number of cycles of the small load series and (b) changing the small load magnitude to a different value. In

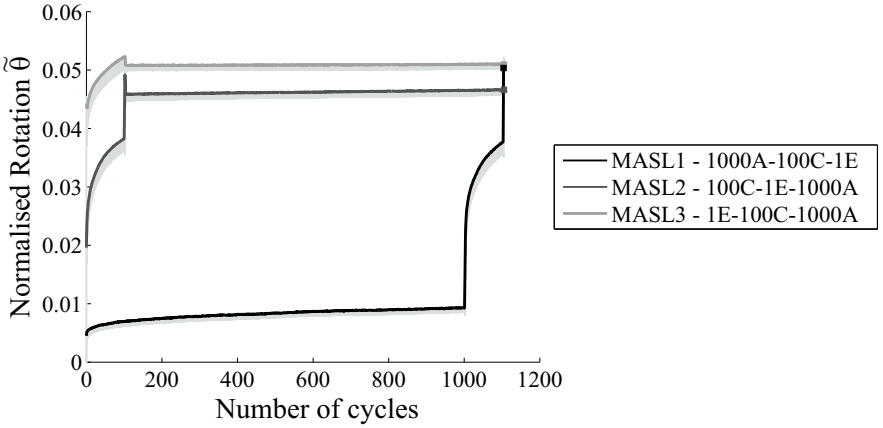

Figure 3.27: Evolution of the pile rotation with cycle number for tests MASL1,2,3,5

both cases, this should not alter the final pile deformation. This was demonstrated with tests MASL4 and 5 respectively. The results are displayed in Figure 3.28(a) and show that, in both cases, the final displacement remains the same. This demonstrates that, in some cases where the difference in load magnitudes is sufficiently large, the load history can be ignored.

Figures 3.28(b) and 3.28(c) display the evolution of the secant stiffness and hysteresis loop area for the 5 first MASL tests. The graphs show that the hysteresis loop shape is mildly altered by the load history, probably because the most extreme load event only involves a single cycle.

Finally, Figure 3.29(a)-(d) display the results of tests MASL6 and 7. The moment-

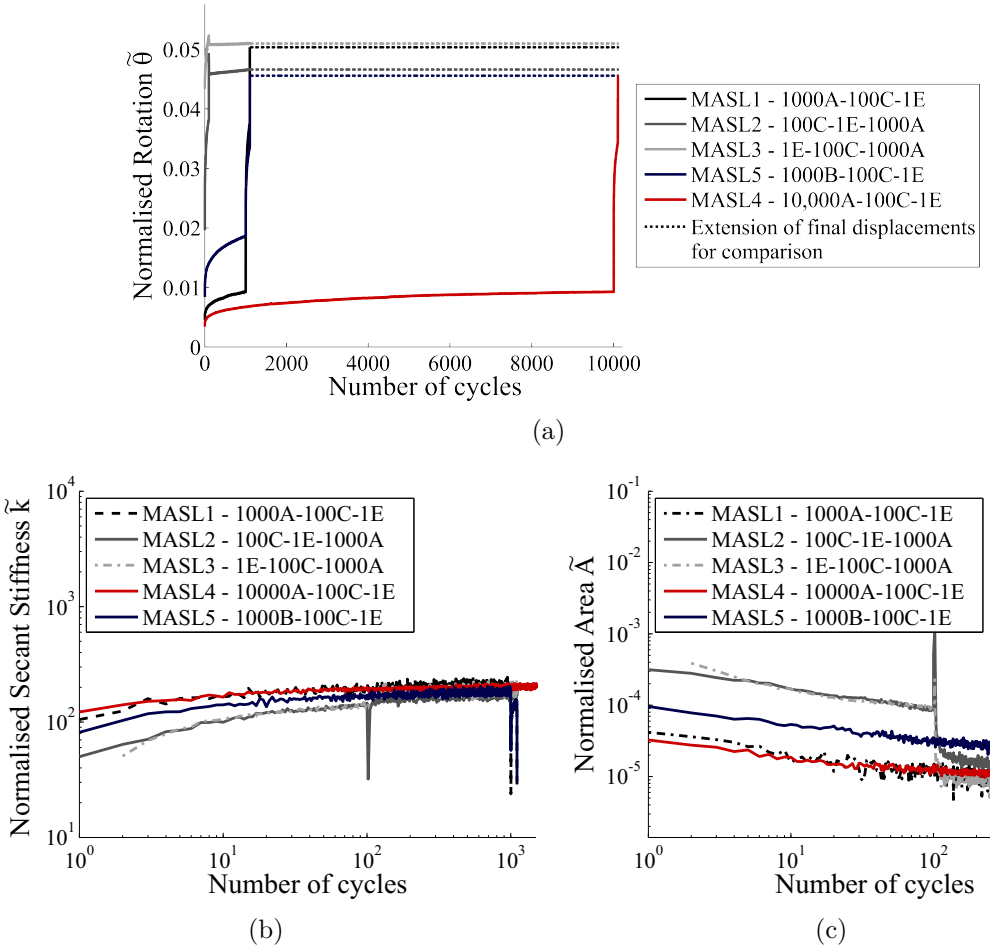

Figure 3.28: Evolution of (a) the pile rotation, (b) the secant stiffness and (c) the hysteresis loop area tests MASL1-5

rotation curves for the two tests are shown on the upper part of the figure. It is observed that for both tests the rotation tends to a limiting value once the pile has undergone the first series of storm type loads (e.g. 100xC2-1xE2-100xC2 for MASL6 in Table 2.8, p. 67).

This phenomenon is demonstrated on Figures 3.29(a) and 3.29(b) where the pile rotation is plotted against cycle number for both tests. An interesting outcome of test MASL7 is that the increase in rotation due to cyclic load amplitude A2 reduces to approximately zero following the fourth peak load event ($\zeta_b = 0.54$, corresponding to a load magnitude of the SLS). Similar tests with larger cycle number would be helpful to assess the above statement for larger cycle numbers (10^7), though it would require a higher cyclic frequency for tests to run in a reasonable time frame.

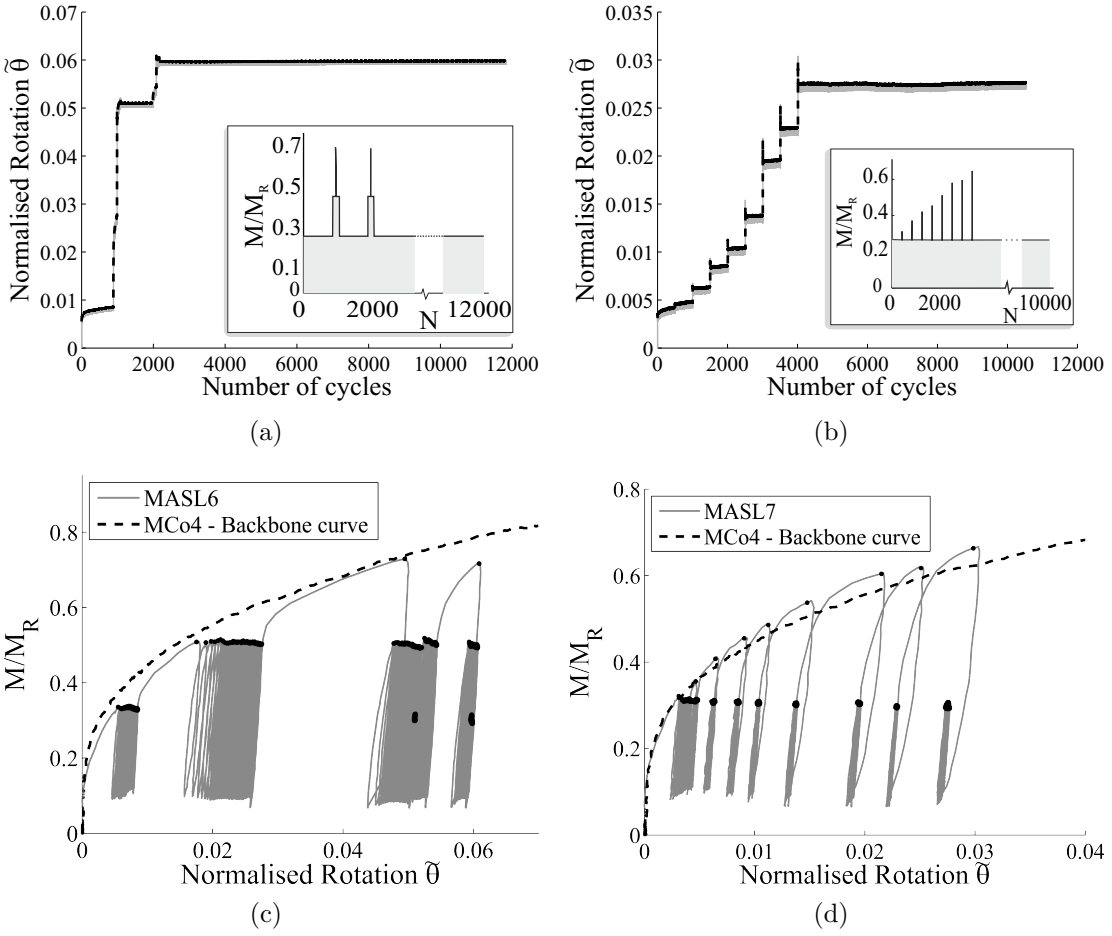

Figure 3.29: Evolution of the pile rotation for tests (a) MASL6 and (b) MALS7 - Moment rotation curves for tests (c) MASL6 and (d) MASL7

Finally, the above test results indicate that the pile displacement response, following a change in load, depends on whether there is an increase in load or decrease. Figure 3.30 demonstrates this by plotting the difference in pile head rotation against difference in load, when a change in load amplitude occurs for tests MASL6 and 7. Decreases in load magnitude are displayed on the left, and increases on the right. It also shows that the order in which loads occur matters, by highlighting a sharper increase in pile rotation during the first storm events (top right ellipse) compared with the subsequent events (bottom right ellipse). Given the findings from Sections 3.2.1 and 3.5.1, the results and retardation phenomenon highlighted in this plot are not surprising and are explained by the Masing behaviour of the response and hence, the shape of the unloading-reloading curve after large load events (see Figures 3.29(c) and 3.29(d)). It is also due to the fact that no more ratcheting rotation is accumulated at this point, and that therefore, the final displacement is dictated by the kinematic response. This aspect cannot be captured using the linear cumulative model proposed by LeBlanc *et al.* (2010b) as it does not take Masing behaviour into account.

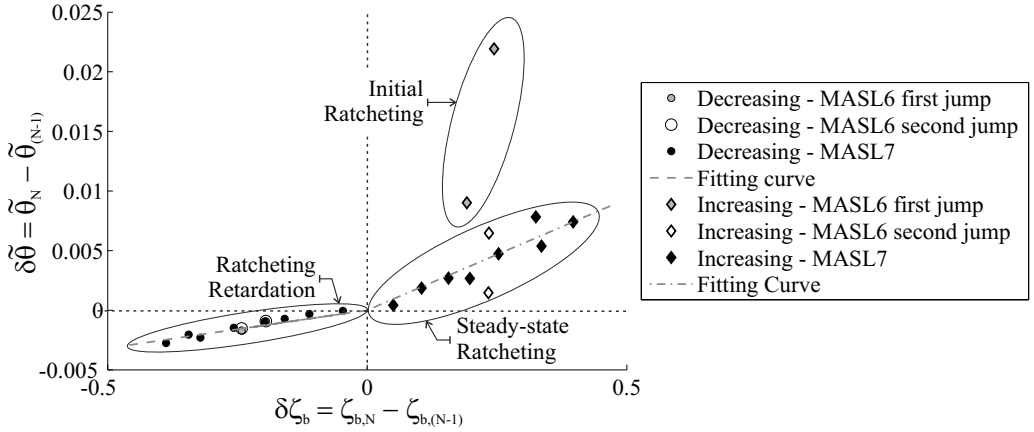

Figure 3.30: Analysis of the change in rotation during the loading sequence changing phases of tests MASL6 and 7

3.5.3 Linear cumulation model

In this final paragraph, the linear cumulative model initially proposed by LeBlanc *et al.* (2010b) and presented in Chapter 1, Section 1.4.3, p. 35 is applied to selected test results from this research campaign. The values of the parameters adopted in the model, i.e. the rotation that could occur in a static test when the load is equivalent to the maximum cyclic load θ_S, the initial maximum rotation θ_0 and T_{bc} for each load series, are provided in Table 3.3. The results are displayed in Figures 3.31(a)-(c), with the predictions plotted with black dotted lines. The results show that the model always over-estimate the final pile displacement and provides a satisfactory first approximation of the results, demonstrating that this model is a useful tool for

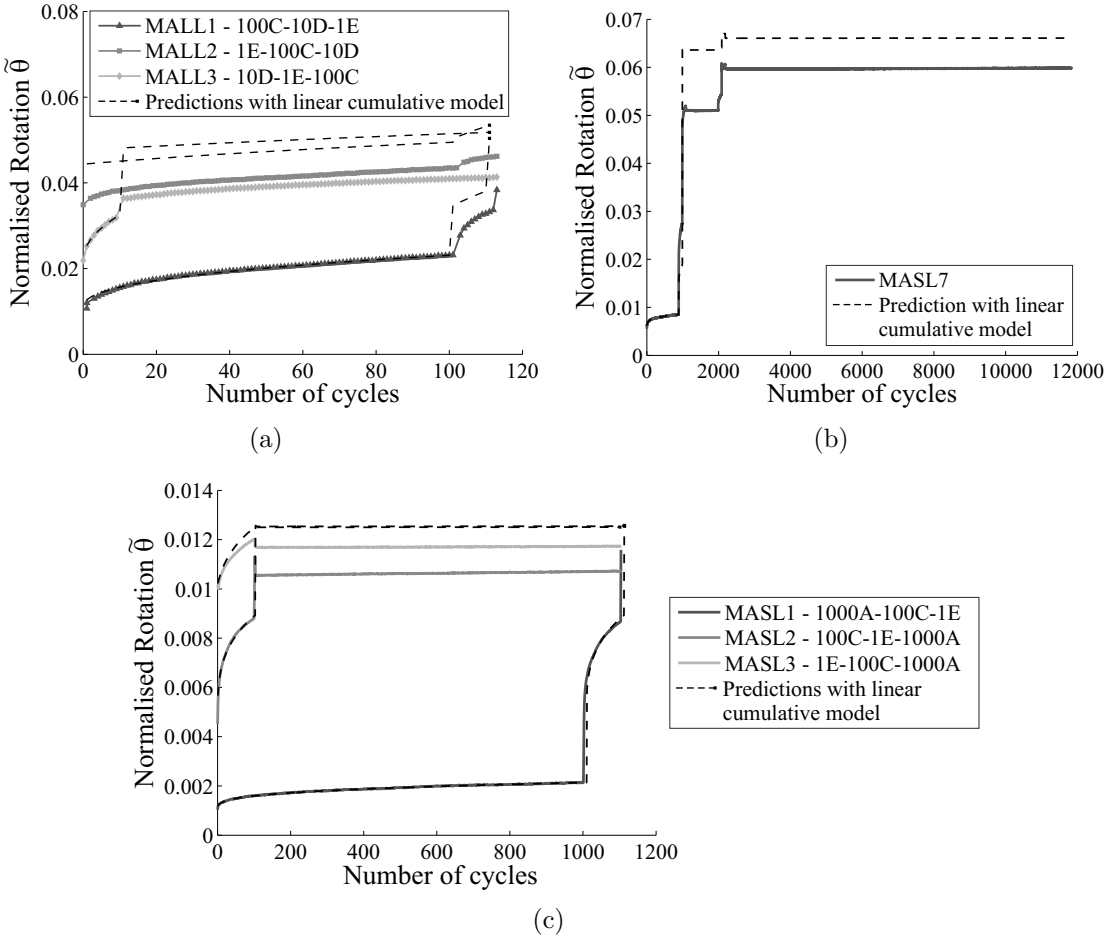

Figure 3.31: Prediction using linear cumulation rule for tests (a) MALL1,2,3 (b) MASL7 and (c) MASL1,2,3

Table 3.3: Characteristics of the load types A,C,D,E and A2,C2 and E2

Load case	ζ_b	ζ_c	T_{bc}	θ_S $(rad.)$	θ_0 $(rad.)$
A	0.30	0.11	0.22	0.0007	0.001
C	0.49	0.00	0.14	0.0032	0.0025
D	0.59	0.03	0.11	0.0071	0.005
E	0.69	0.00	0.22	0.0099	0.008
A2	0.31	0.29	0.17	0.0009	0.0013
C2	0.51	0.15	0.12	0.0035	0.0029
E2	0.72	0.10	0.30	0.0113	0.0112

earlier stage of the design process.

3.6 Concluding comments

3.6.1 Key findings

The results presented in this chapter have indicated that the lateral loading response of a rigid monopile is mostly driven by:

(1) Masing behaviour, even after long-term cyclic load series of variable load magnitudes

(2) Increase in accumulated ratcheting deformation due to cyclic loadings at non-zero mean stress, with the rate of ratcheting decreasing with cycle number but never decaying to zero

(3) Change in hysteresis loop shape, including an increase in secant stiffness and reduction of the hysteresis loop area, mostly during the first 50 cycles of a given load magnitude

(4) The evolution of the latest 2 phenomenon greatly depend on the cyclic load magnitude

The above points are the key mechanisms driving the pile response that need to be accounted for in the detailed modelling. These mechanisms occur all at once and compete with each other, leading the pile response to depart or not from the initial

backbone curve. There is still a question to be explored of how the response observed with the model scale tests relates to that at full scale. Future work on large-scale model piles in the field would be extremely useful to confirm the major conclusions of this chapter and correlate the numerical values to that at full scale.

This chapter has also highlighted many more interesting behaviours and Table 3.4 provides an extensive summary of the primary findings. In this table, the major contributions have been highlighted in bold.

Finally, this chapter has outlined an experimental method that can be used when identifying key mechanisms for the development of constitutive model. The next step is now to thoroughly interpret the results within an appropriate theoretical framework. This will be expanded upon in Chapters 4 and 5. Mostly, point (2) will require careful consideration as this effect is quite difficult to model rigorously.

3.6.2 Implications for design

Finally, the work presented in this Chapter has outlined interesting points that have a direct impact on the design to cyclic lateral loading of monopiles:

- The pile response exhibits an hysteretic response that corresponds to energy loss when the pile pushes and deforms the soil. So far, this is not accounted for by the *p-y* method but needs to be addressed to estimate soil damping.
- Cyclic loading can induce significant accumulation of pile deformation with time. The use of empirical laws such as that proposed by LeBlanc *et al.* (2010a), or empirical methods added to current design procedures (e.g. Equation 3.3 and Degradation Stiffness Model included in the *p-y* method) can provide a first approximation of the final pile displacement in design.
- The initial modulus of the foundation is unaltered by cyclic loading and can therefore be used in design to cyclic loads when relevant.
- Cyclic loading generates a change in hysteresis loop shape that involves (a) an increase in secant stiffness that could infer a change in the first bending mode

of the structure and (b) decrease in hysteresis loop area, which also involves a decrease in soil damping.

- Large load history can induce a reduction of accumulated rotation from the subsequent cyclic loads at smaller magnitude. This means that, if full-scale wind turbines were monitored, it would be possible to re-assess the predicted foundation performance after extreme load events, and possibly extend their service life.
- Repeated cyclic loads at small magnitude reduces the impact of extreme load events on the pile deformation. This could signify that the time between installation of the foundation and the rest of the turbine could be very beneficial for the lifetime of the turbine. The above two points also raises the question of pre-loading of the pile and it would be very useful in future to investigate this further.
- A satisfactory and conservative first approximation of the pile deformation to load sequences of variable amplitude can be obtained with the simple model proposed by LeBlanc *et al.* (2010b) and based on Miner's linear cumulative method. This does not provide any information on the secant stiffness nor on the evolution of soil damping though.

Table 3.4: Summary of experimental results and conclusions, Chapter 3

Conclusions	Test No.	Figure No.
Hysteresis behaviour		
1) A very good approximation of the pile response to symmetric load reversal can be obtained with pure kinematic hardening	H0	3.2(a)-(b)
2) Pile response conforms to extended Masing rules	HIM, H1IM1, H1IM2	3.5(b), 3.9(a)-(b)
3) Isotropic hardening is a plausible mechanism to capture the differences in pile response compared with pure kinematic hardening (both 2-way and 1-way)	HC, H1IM1, H1IM2	3.7(b), 3.9(a)-(b)
4) Pure symmetrical loading does not generate maximum accumulated displacement with cycle number	HC	3.7(b)
5) Pile response experiences ratcheting when subjected to non-symmetrical load cycles	HA1, HA2, H1IM1, H1IM2	3.8(b), 3.8(d), 3.9(a)-(b)
6) symmetric loading cancels the accumulated displacement experienced during 1-way loading	HA1, HA2	3.8(b), 3.8(d)
Accumulated rotation and ratcheting		
7) When subjected to constant amplitude cyclic loads, even for very large cycle number (over 1 million), the pile experience ratcheting	CMLT1-3, CC4 + test results from Cuéllar (2011)	3.12(a)-(b)
8) The empirical law proposed by LeBlanc *et al.* (2010a) (Equation 3.2) is a conservative approach for prediction of the pile accumulated rotation over cycle number	CMLT1-3, CC1-7, CCLB1-4	3.11(a), 3.11(b)
9) The evolution of total pile rotation can be captured with a power law (Equation 3.3), which enables application of the Degradation Stiffness Model within the *p-y* method for applications to cyclic loading	CMLT1-3, CC1-7, CCLB1-4 + selected tests from published literature	3.13(a)-(b); 3.14(a)-(c)

Continued on next page

Conclusions	Test No.	Figure No.
Evolution of stiffness and damping		
10) The secant stiffness increases with cycle number: it sharply develops over the first 50 cycles, then reaches an asymptotic increasing trend that can be captured using a logarithmic law	CMLT1-3, CC1-7, CMC1-5	3.15(a), 3.15(b), 3.16(a)-(c), 3.20(b)
11) The hysteresis loop area, and therefore, the soil damping, decreases with cycle number and its trend can be captured using a power-law	CMLT1-3, CC1,2,3,5,6,7	3.17(a)-(c), 3.18(b)-(d)
12) There is a relationship between the evolution of the secant stiffness and hysteresis loop area	CMLT1-3	3.17(d)
Effect of cyclic loading on monotonic response		
13) The elastic and tangent moduli remain unchanged with cyclic loading	CMC1-7, CMLT1-3, CC4, CC6, CMM1-4	3.15(a), 3.15(b), 3.16(a)-(c), 3.20(a)-(c), 3.21(a)-(b)
14) The reloading curves rejoins the backbone curve when exceeding the maximum cyclic load (Extended Masing rules)	CMC1-7, CMLT1-3, CC4, CC6, CMM1-4	3.15(a)-(b), 3.16(a)-(c), 3.20(a)-(c), 3.21(a)-(b)
15) The load domain for which the pile experiences a stiffer response progressively grows for the first 50 cycles and is proportional to the cyclic load magnitude	CMC1-7, CMLT1-3, CC4, CC6, CMM1-4	3.15(a)-(b), 3.16(a)-(c), 3.20(a), 3.20(c), 3.21(a)-(b)
Multi-amplitude cyclic loading		
16) The largest the FLS and SLS load history before an extreme load event, the more limited the induced displacement from this event	MALL1,2,3	3.24(a)-(d)
17) The response greatly stiffens between cycle number 1 and 50 and this phenomenon significantly retards the ratcheting of the pile response for subsequent load cycles at smaller load magnitude. On the contrary, large cyclic loads of small cycle number (≥ 10) have no influence on the hysteresis loop shape (both secant stiffness and loop area)	H1IM1, MALL1-6	3.23(a), 3.24(e), 3.24(f), 3.25(a)-(d), 3.26(a)-(d)

Continued on next page

Conclusions	**Test No.**	**Figure No.**
18) In some cases where the differences in load magnitudes are sufficiently large, the load history can be ignored	MASL1-5	3.28(a)-(c)
19) When experiencing extreme load events, the pile does not accumulate any more rotation during the subsequent operational loads, even at very large cycle number.	MASL6,7	3.29(a)-(d)
20) The linear cumulative model such as proposed by LeBlanc *et al.* (2010b) proposes a reasonable first approximation of the pile response to loads of variable amplitudes that is usually conservative.	MALL1,2,3, MASL1,2,3,7	3.31(a)-(c)

Chapter 4

Constitutive Modelling for Ratcheting (HARM)

4.1 Introduction

The previous chapter has demonstrated the appropriateness of empirical laws and a linear cumulative model when used within common design methodologies for the determination of the pile response due to cyclic loading (i.e. Equations 3.2, p. 104; 3.11, p. 114 and 3.12, p. 117; Equation 3.3 p. 108 and Degradation Stiffness Model; linear accumulation model from Chapter 1, p. 35). These types of approaches are appropriate for obtaining a rapid first approximation of the pile response to cyclic loading in the early stages of the design process, especially for series of loads of variable amplitude. However, this type of methodology relies on small scale model test results and is naturally empirical. Consequently, there is the issue of accuracy and scaling when it comes to the design of full scale turbine monopiles. It was shown that the predictions obtained for the pile deformation, whether continuous or multi-amplitude cyclic loading are considered, are over-conservative. Finally, these models do not address the evolution of the secant stiffness or hysteresis loop area, and therefore cannot be used for estimating the structural natural frequency and soil damping for fatigue and serviceability limit state design.

The purpose of the next two chapters is therefore to present a more rigorous

approach, the theoretical constitutive model HARM ("Houlsby Abadie Ratcheting Model"), that is capable of capturing the key mechanisms highlighted in the conclusions of Chapter 3, Section 3.6.1 (p. 139). The advantage of developing a constitutive model for the response of the pile is that it can be used as a macro-element for the representation of the global foundation response. This will allow it to be directly integrated in structural analyses, without considering the distributed load down the pile. As the macro-response is very likely to represent the integrated soil reaction distribution along the pile shaft, further work could also allow the model to be integrated within the *p-y* method, or used as a basis for the development of a constitutive model for the soil in FE calculations that would then be adapted for cyclic behaviour.

The modelling of soil response with constitutive models has been of great interest over the last 30 years. Complex aspects of granular media behaviour, such as hysteresis, small strain non-linearity, frictional behaviour and creep, have successfully been described using standard plasticity techniques originally developed for continuous media. More recently, an approach called *Continuous Hyperplasticity* (Houlsby and Puzrin, 2006) has been introduced in order to capture non-linear behaviour of soils within a rigorous mathematical framework that, compared with standard plasticity techniques, enforces the model to be thermodynamically acceptable. Also, the methodology is remarkably concise and methodical which guarantees a certain rigour of the model outputs. The hyperplasticity approach has since been successfully applied to model foundation responses, such as shallow foundations (Houlsby *et al.*, 2005) and suction caissons (Byrne, 2000; Byrne and Houlsby, 2004; Villalobos, 2006; Nguyen-Sy, 2006). However, this has not yet been extended to laterally loaded piles.

Chapter 3 has reported four core mechanisms characterising rigid pile response to cyclic lateral loading (Section 3.6.1, p. 139). The two first mechanisms describe ratcheting behaviour that is actually quite often observed for both continuous and granular media. The third and fourth mechanisms more specifically describe the cyclic ratcheting behaviour of the laterally loaded pile. For generality, this chapter is

therefore only concerned with the two first points: (i) the pile response is non-linear and conforms approximately to the Masing rules and (ii) during any one unload-reload loop, and if the mean effective load is not zero, the hysteresis loop does not exactly close and an accumulated ratcheting deformation develops, even at large cycle number. Chapter 5 will then go into the details of the modelling of ratcheting behaviour and accommodate the last two points. The idea behind this organisation is to present a general model that can be used to capture ratcheting while conforming approximately to Masing rules, and then outline a methodology for accommodating the generic model to specific aspects of cyclic response.

When it comes to modelling cyclic loading response, capturing ratcheting while conforming to the extended Masing rules is a challenge. The combination of standard kinematic and isotropic hardening mechanisms are capable only of modelling adapted or accommodated behaviour where a stabilized loop is clearly identified after a few cycles (Figure 4.1). Ratcheting, or cyclic creep on the other hand, has received less attention and remains difficult to model rigorously. In particular, the author is not aware of any published work examining models that would be cast within the continuous hyperplasticity framework and would be appropriate for modelling ratcheting of soils.

This chapter proposes to address this particular issue. The first two sections

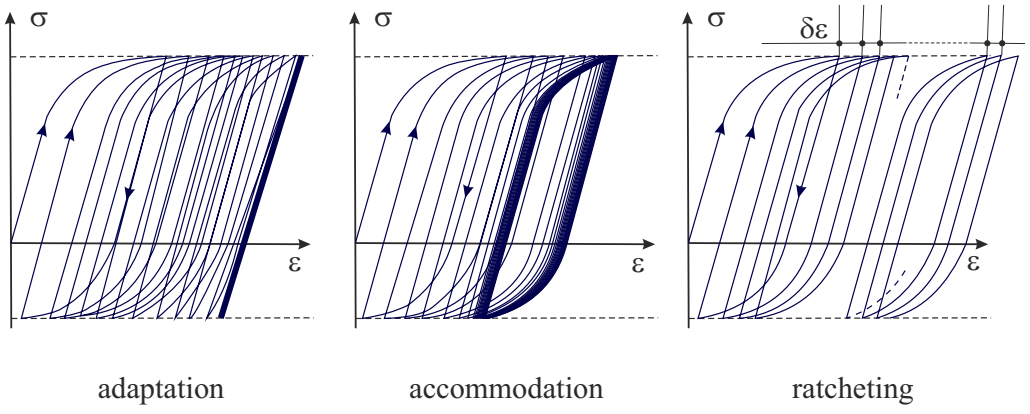

Figure 4.1: Schematic representation of fatigue behaviours in loading at non-zero mean stress (after François, 2010)

present work from published literature that was used in the early stage of the development of HARM. This involves, first, a summary of the most common standard plasticity models used for capturing ratcheting, described together with the primary reasons why these models have not been pursued for this particular application. Secondly, the basics of kinematic hardening hyperplasticity as described by Puzrin and Houlsby (2001a) and Puzrin and Houlsby (2003) are outlined. The new model HARM directly builds on this particular model, and therefore its understanding is essential for the following developments.

The following three sections then present the fundamentals of HARM. First, a hierarchy of kinematic hardening and ratcheting models are presented, along with the necessary fundamental equations and theoretical developments. One of the main issues when modelling high-cycle fatigue problems is that the computational time becomes prohibitive. One of the powerful features of the HARM model is that it can be adapted to accelerate the effects of cyclic loading of thousands or even millions of cycles within the computation of only few cycles. The principles of this approach are developed in the penultimate section of this chapter before finally extending the model to multi-directional loading.

Although the model is applied here to the description of laterally loaded piles, it is in principle applicable to any other one-dimensional loading problem. In order to emphasise this generality, the model is presented here using the terminology of "stress" (σ) and "strain" (ϵ). However, in this particular application the "stress" stands for the lateral load on the pile and "strain" for the displacement at the point of load application. Of course, careful attention needs to be applied to the appropriate dimensions for all variables, and in particular for the stiffness and loop area.

4.2 Context and motivation

4.2.1 Conventional methods for modelling ratcheting

In standard plasticity theories, the strains of an inelastic body are determined by the stresses and a number of internal variables that contain information on the effects of the stress or strain history on the response (e.g. elastic strain ϵ_e, or accumulation of plastic strain p (Equation 4.1)). One common approach consists in assuming a partition between the elastic and plastic strains ($\epsilon = \epsilon^e + \epsilon^p$) and using two functions to describe the constitutive behaviour: the *limit function* F, that defines the admissible states ($F \leq 0$), and the *yield function* f, that delineates the elastic domain ($f < 0$). For each time step in the calculation, the yield criterion is recalculated according to the current value of plastic strain and the updated values of stress and the limit function allows the computation of the induced strain values.

The yield surface can be expressed following the generic formulation of Equation 4.2, where X is the kinematic hardening parameter that drives the translation of the centre of the elastic domain and R is the isotropic hardening parameter that describes the elastic domain growth with stress history (Figure 3.1, Chapter 3, Section 3.2.1, p. 91). In most models, X is linear with ϵ_p and extra care is required when making this term non-linear. R is a function of the accumulation of plastic strain p (Equation 4.1) and can either be linear or non-linear.

$$\dot{p} = |\dot{\epsilon}_p| \quad \Rightarrow \quad p = \int_0^t |\dot{\epsilon}^p(t)| \mathrm{d}t \tag{4.1}$$

$$\begin{cases} f = |\sigma - X| - R - k \\ X = H \cdot \epsilon^p, \ \dot{X} = H \cdot \dot{\epsilon}_p \\ R = R(p); \ \dot{R} = h(p) \cdot \dot{p} \end{cases} \tag{4.2}$$

Modelling ratcheting behaviour of alloys is commonly introduced by accommodating the kinematic hardening feature of the standard plasticity approach while discarding isotropic hardening for the simplest models. The most popular method is the Armstrong-Frederick model (Armstrong and Frederick, 1966). It has seen a significant amount of research over the final quarter of the 20th century and has been implemented in commercial FE codes such as ABAQUS or ANSYS.

The principle of the Armstrong-Frederick model is to modify the expression for $\dot{X}$ (Equation 4.2) by introducing a new term that plays the role of an evanescent memory of the loading history. This new term, called the *recovery term*, essentially makes kinematic hardening non-linear as shown in Equation 4.3. In this formulation, κ and C are characteristic constant variables that depend on the material properties. The recovery term, $\kappa \cdot X \cdot \dot{p}$, depends on the incremental cumulative plastic strain $\dot{p} \geq 0$ and is proportional to X. This allows for an accumulation of plastic strain cycle by cycle in the direction of non-zero mean stress.

$$\dot{X} = C \cdot \dot{\epsilon}^p - \kappa \cdot X \cdot \dot{p} \tag{4.3}$$

If the Armstrong-Frederick model allows the accumulation of plastic strain at each cycle, the increment of ratcheting strain can only be constant and the initial cyclic load response does not conform to the Masing rules (see Figure 4.2(a)). Chaboche (1986) and Chaboche and Nouailhas (1989) proposed to accommodate the rate of ratcheting by super-imposing a small number of Armstrong-Frederick surfaces. This approach is similar to that proposed by Mroz (Mróz, 1967) for continuous kinematic hardening. 2 to 5 surfaces are usually used, with three recommended in most models (e.g. Lemaitre and Chaboche, 2010, ABAQUS). A linear surface is also suggested if ratcheting at decreasing rate is to be captured (Lemaitre and Chaboche, 2010). A typical stress-strain curve obtained with 2 surfaces, one of which is linear, is displayed in Figure 4.2(b).

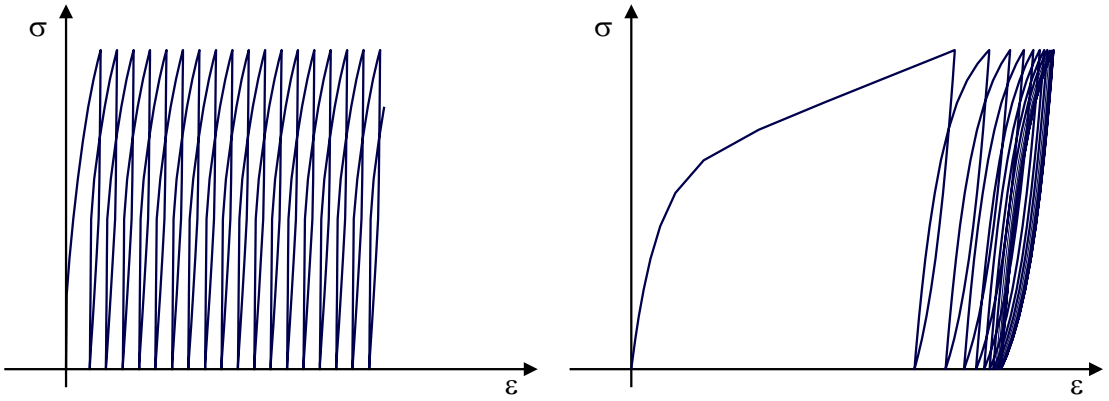

(a) (b)

Figure 4.2: Typical reaction curve obtained with (a) the Armstrong-Frederick model and (b) the Chaboche extension

4.2.2 Limitations

The Armstrong-Frederick model presented above has been used for modelling the ratcheting behaviour of alloys. However, the accumulated ratcheting strain, using this particular model is usually highly over-predicted (Lemaitre and Chaboche, 2010; Ohno and Wang, 1995). The superposition of several non-linear kinematic hardening surfaces with one linear kinematic hardening surface provides an improved prediction. However, the calibrated model usually exhibits a stabilised asymptotic response where ratcheting stops (Lemaitre and Chaboche, 2010, Figure 4.2(b)) and the transient accumulated ratcheting strain is often over-predicted (Bari and Hassan, 2000; Lemaitre and Chaboche, 2010). As a result, a number of modifications have been proposed to improve these models (e.g. Ohno and Wang, 1995; Chaboche, 1991).

Nevertheless, the determination of the model parameters requires an extensive data base that includes tensile curves, cyclic curves, stabilised strain-stress loop curves and ratcheting tests with increasing mean load. A detailed step-by-step procedure for the determination of the parameters of the multi-surface model is presented in Chaboche (1991). However, since the micro and meso-phenomena in alloys and soils are very different, the fundamentals of the Armstrong-Frederick approach for applications in geotechnics are questionable, especially with regard to parameter

identification. A robust parameter determination for laterally loaded monopiles would require a thorough investigation of the soil mechanisms with advanced soil element testing, and an understanding of how these translate to the soil-pile interaction problem, with no guarantee that this would succeed. In addition, when applied to laboratory model tests on piles, a very detailed analysis of the dimensional framework would be required in order to be able to use these results for industrial applications.

Besides, the specific monopile ratcheting behaviour highlighted in Chapter 3 would be quite difficult to address using the Armstrong-Frederick framework, and therefore, this direction was not pursued any further during the course of this research project. It was decided instead, to develop a new model that directly and conceptually describes the phenomena and mechanisms observed in the laboratory for laterally loaded piles. The following section describes the theoretical background and principles of this new model, called HARM.

4.3 Preliminary modelling (Houlsby and Puzrin, 2006)

4.3.1 Summary of rate-dependent hyperplastic formulation

Hyperplasticity is an approach to plasticity theory introduced by Ziegler (1977,1983); Houlsby (1981) and Collins and Houlsby (1997) and further developed for the description of non-linear behaviour of soils by Houlsby and Puzrin (2000) and Houlsby and Puzrin (2002). The primary benefits of using this technique, rather than standard plasticity is that (i) it guarantees that the model cannot generate thermodynamically unreasonable results, (ii) the entire constitutive behaviour is described using only two scalar functions, with the response then derived using rigorous and standardised procedures, and consequently (iii) the model is concise and uses a single and methodical framework that can be used to create subsequent developments or new

models that are consistent with each other.

The following section presents a very brief summary of the key elements of the hyperplasticity theory that will be useful for the development of the HARM model presented in this chapter. Yet, the author invites the interested reader to refer to Houlsby and Puzrin (2000) and Puzrin and Houlsby (2001a) for a complete presentation of the framework for rate-independent behaviour, to Houlsby and Puzrin (2002) and Puzrin and Houlsby (2003) for rate-dependent and finally to Houlsby and Puzrin (2006) for a comprehensive description of the whole framework and examples of applications.

The hyperplasticity method describes the state of a material in terms of stresses (or strains) and a set of internal variables usually noted with the Greek letter α. These variables contain the information on the effect of the loading history and, in the particular case of the HARM model, will be interpreted as the plastic and ratcheting strains. As mentioned above, the description of the material behaviour is achieved through the definition and derivation of two scalar functions: one defining the energy stored in the system and one defining the rate of dissipation.

The energy function can either be the internal energy u, the Helmholtz free energy f, the enthalpy h or the Gibbs free energy g. All of these functions are related by Legendre-Fenchel transforms, which means that the models developed with any of the energy functions are equivalent (see Houlsby and Puzrin (2006) for details). For rate-independent behaviour, the dissipative potential can either be the dissipative potential d or the canonical yield function $\bar{y}$. These two potentials are also related and the expression of only one of them is sufficient for the model development. Unless stated otherwise, the following analysis will mostly use the Helmholtz free energy f. In the framework presented by Houlsby and Puzrin (2000), the constitutive behaviour is then derived from the following equations:

$$\sigma = \frac{\partial f}{\partial \epsilon} \tag{4.4}$$

$$\overline{\chi} = -\frac{\partial f}{\partial \alpha} \tag{4.5}$$

$$\chi = \frac{\partial d}{\partial \dot{\alpha}} \tag{4.6}$$

For $\bar{y}$, Equation 4.6 is replaced by:

$$\dot{\alpha} = \bar{\lambda}\frac{\partial \bar{y}}{\partial \chi} \tag{4.7}$$

where $\bar{\lambda}$ is an arbitrary positive multiplier. In the above equations, $\overline{\chi}$ is the generalised stress and χ the dissipative generalised stress. The second law of thermodynamics implies that $(\overline{\chi} - \chi)\dot{\alpha} = 0$. The hyperplasticity framework presented by Houlsby and Puzrin (2006) makes use of a stronger assumption:

$$\overline{\chi} = \chi \tag{4.8}$$

This statement, also known as the Ziegler's orthogonality principle (Ziegler, 1977,1983), enforces the dissipation to be maximal and is more restrictive than the second law of thermodynamics. It is therefore usually considered as a classifying hypothesis. However, this assumption applies to a remarkably wide range of materials and behaviours, and using this principle, the entire constitutive response can be derived without any further assumptions being necessary. Consequently, the following work is developed with the use of Equation 4.8.

The above framework describes rate-independent materials and needs to be modified to account for rate effects. Houlsby and Puzrin (2002) demonstrate that, in this case, the role of the energy function remains unchanged, while the dissipation and yield functions no longer serve as potentials for χ and need to be replaced. This is then achieved by introducing the force potential z and the flow potential w, which are related to the dissipation function according to $z + w = d$ and are linked by a

Legendre-Fenchel transform. The theoretical justification and advantages of this function choice is not explained here and the author invites the interested reader to refer to Houlsby and Puzrin (2002) and Puzrin and Houlsby (2003) for more detail. Using f and z or f and w, the constitutive behaviour is then deduced from Equations 4.4 and 4.5 and Equations 4.6 and 4.7 are replaced by Equations 4.9 and 4.10 respectively:

$$\chi = \frac{\partial z}{\partial \dot{\alpha}} \tag{4.9}$$

$$\dot{\alpha} = \frac{\partial w}{\partial \chi} \tag{4.10}$$

As described above, the hyperplasticity framework can be developed for rate-independent or rate-dependent behaviours. However, even for rate-independent materials, it is often beneficial to formulate the model as rate-dependent and then artificially set the "viscosity" to a very small value. The implementation of the rate-dependent behaviour then becomes straightforward, as a direct relationship between the incremental strain and stress is obtained through derivation (e.g. see later Equations 4.22 p. 159 and 4.41 p. 167). Also, despite the fact that the laboratory pile response appears to be rate-independent, this may not be the case for large-scale prototypes. Consequently, for generality, the HARM model will be developed using the rate-dependent formulation.

4.3.2 Hierarchy of kinematic plasticity models

The starting point for the development of the HARM model is a hierarchy of plasticity models that captures pure kinematic hardening, They are presented in detail by Puzrin and Houlsby (2001a) (rate-independent) and Puzrin and Houlsby (2003) (rate-dependent). The following provides a short summary of these models.

Single-yield surface model

The simplest model of kinematic hardening consists of an elastic element E in series with a kinematic hardening unit made of a spring H in parallel with a slider k. This model was originally proposed by Prager (1955). When considering rate-dependent behaviour, the parallel components are supplemented with a damper μ. A conceptual representation of the rate-independent and rate-dependent models are given in Figure 4.3(a). In the top schematic of Figure 4.3(a), the slider only moves when the absolute value of the stress within the slider reaches the threshold $k > 0$, after which the system response is a combination of both springs. The energy of this system is thus the sum of the energies from both springs:

$$f(\epsilon, \alpha) = \frac{E}{2}(\epsilon - \alpha)^2 + \frac{H}{2}\alpha^2 \tag{4.11}$$

The dissipation function is equal to zero until the slider is mobilised and then is equal to the power dissipated by the slider:

$$d(\dot{\alpha}) = k|\dot{\alpha}| \geq 0 \tag{4.12}$$

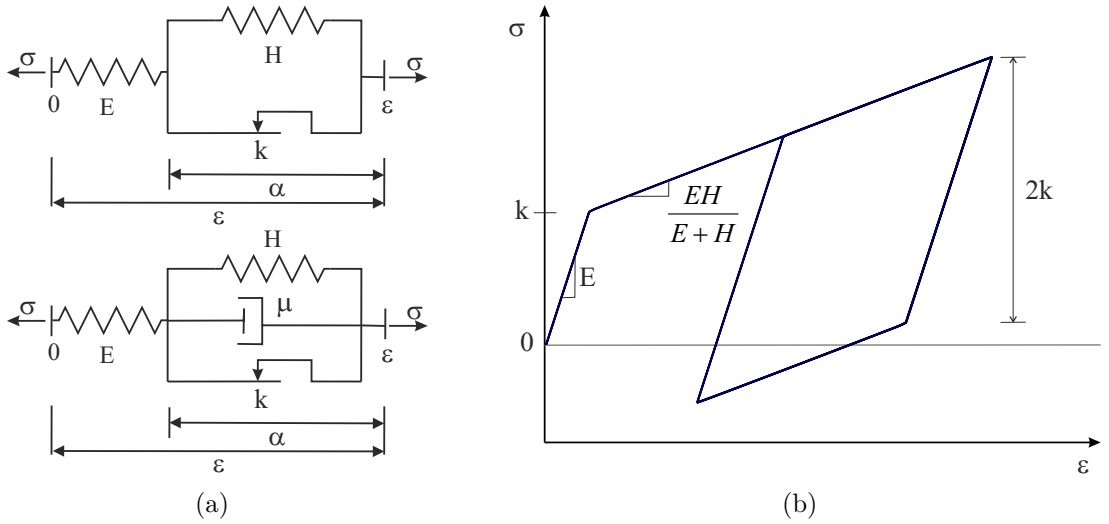

Figure 4.3: (a) Schematic representation of rate-independent (top) and rate-dependent (bottom) single-surface kinematic hardening model and (b) typical response

For the rate-dependent case, the flow potential is deduced from the dissipation potential simply by considering the additional dissipation from the damper:

$$z(\dot{\alpha}) = k|\dot{\alpha}| + \frac{\mu}{2}\dot{\alpha}^2 \geq 0 \tag{4.13}$$

Then using Equations 4.4, 4.5 and 4.9 and the Ziegler's orthogonality principle, it follows that:

$$\sigma - H\alpha = kS(\dot{\alpha}) + \mu\dot{\alpha} \tag{4.14}$$

Where $S(.)$ is the modified signum function (see Nomenclature, p. xiii). First, if $\dot{\alpha} \neq 0$, Equation 4.14 can be re-arranged into:

$$\sigma - H\alpha = S(\dot{\alpha})\left(k + \mu|\dot{\alpha}|\right) \tag{4.15}$$

Since $\mu|\dot{\alpha}| \geq 0$, this means that, if $\dot{\alpha} \neq 0$ then $\sigma - H\alpha \geq k$. The contraposition is that, if $\sigma - H\alpha < k$, then $\dot{\alpha} = 0$. It also follows that for $\dot{\alpha} \neq 0$, $S(\dot{\alpha}) = S(\sigma - H\alpha)$. Consequently, Equation 4.14 gives:

$$\alpha = \frac{\mathrm{d}t}{\mu} S(\sigma - H\alpha)\left\langle \sigma - H\alpha \right\rangle \tag{4.16}$$

where $\langle . \rangle$ are Macaulay brackets; $\langle x \rangle = 0,\ x < 0$ and $\langle x \rangle = x,\ x \geq 0$ (see Nomenclature, p. xiii). It follows that the incremental behaviour is then completely defined from the above equation and:

$$\mathrm{d}\epsilon = \frac{\mathrm{d}\sigma}{E} + \mathrm{d}\alpha \tag{4.17}$$

From Equation 4.17, it is straightforward to deduce the tangent modulus:

$$E_t = \frac{EH}{E + H} \tag{4.18}$$

Equation 4.16 could have been obtained in a more concise way by simply deriving the flow potential w instead of z. w is obtained using the Legendre transform $w = d - z = \mu\frac{\dot{\alpha}^2}{2}$ and the fact that $\chi = \sigma$:

$$w(\chi) = \frac{\langle|\chi| - k\rangle^2}{2\mu} \tag{4.19}$$

Multi-surface formulation

The simple model above is able to capture pure bi-linear kinematic hardening. However, to capture most kinematic behaviour, it is necessary to simulate a smooth elastic-plastic transition. This can be achieved by simply adding a number of kinematic hardening unit in series with each other. This concept is represented in Figures 4.4(a) and 4.4(b) for rate-independent and rate-dependent behaviour respectively. Here, each spring-slider unit provides pure kinematic hardening, resulting in a multi-linear stress-strain response (see Figure 4.4(c)). Therefore, when the number of units - or surfaces - is sufficiently large, the loading curve response is smoother (Figure 4.4(d)). This approach, also called the nested method, was originally suggested by Mróz (1967) and Iwan (1967).

For each surface, there is an internal variable $\alpha_1, \alpha_2, \cdots, \alpha_{N_S}$ (Figure 4.4(a)) and the energy and flow potentials of the assembly are now the sum of the individual contribution from each surface according to:

$$f = \frac{E}{2}\left(\epsilon - \sum_{n=1}^{N_S}\alpha_n\right)^2 + \sum_{n=1}^{N_S}\frac{H_n}{2}\alpha_n^2 \tag{4.20}$$

$$w = \sum_{n=1}^{N_S}\frac{1}{2\mu_n}\langle|\chi_n| - k_n\rangle^2 \tag{4.21}$$

As rate-dependency of the final behaviour will not be investigated any further, the above equation is simplified by equating the viscosity parameters ($\mu_1 = \mu_2 = \cdots = \mu_{N_S} = \mu$). The dampers $\mu_n,\ n \in [1, N_S]$ are solely responsible for rate-dependency.

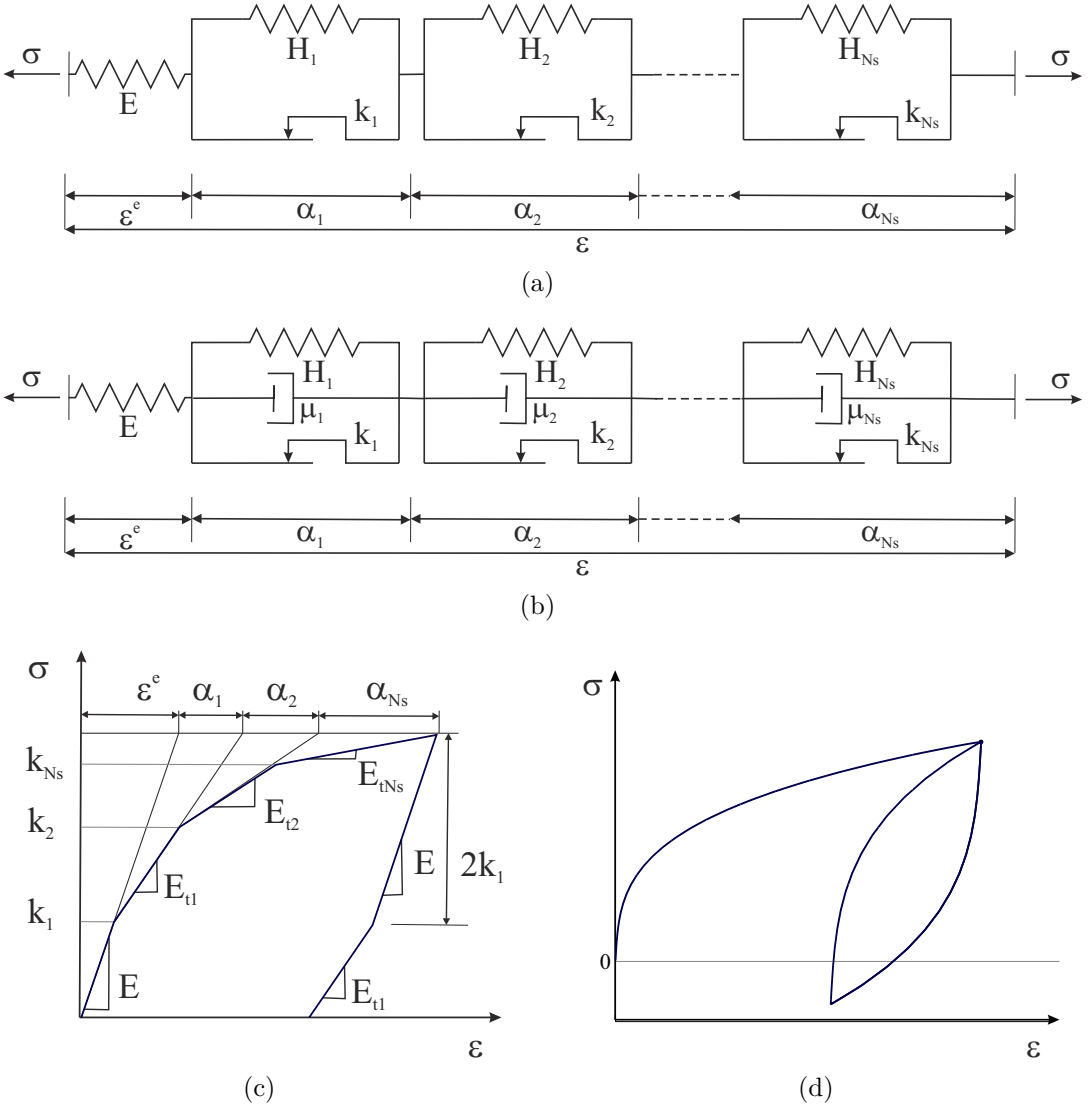

Figure 4.4: Schematic representation of (a) rate-independent and (b) rate-dependent multi-surface kinematic hardening model. (c) Schematic representation of the response obtained with 3 kinematic hardening surfaces (after Houlsby and Puzrin (2006)). (d) Typical non-symmetric loading rate-dependent smooth response

In order to simplify the conceptual representations of HARM, the dampers will not be displayed in the following schematics. However, they will always be accounted for in the framework and equations using the methodology described in this paragraph.

Now, using Equations 4.9, 4.4 and 4.10 together with the Ziegler's principle, it follows that:

$$\mathrm{d}\epsilon = \frac{\mathrm{d}\sigma}{E} + \mathrm{dt}\sum_{n=1}^{N_S}\frac{\langle|\sigma - H_n\alpha_n| - k_n\rangle}{\mu}S(\sigma - H_n\alpha_n) \tag{4.22}$$

And the tangent modulus of each linear portion is:

$$E_{tN^*} = \frac{1}{\frac{1}{E} + \sum_{n=1}^{N^*} \frac{1}{H_n}} \tag{4.23}$$

where N^* signifies the last N^{th} sliding element of which the slider is mobilised.

Infinite number of surfaces

As mentioned above and illustrated in Figure 4.4(d), a perfectly smooth elastic-plastic transition can be obtained by using an infinitely large number of kinematic hardening surfaces. Houlsby and Puzrin (2006) therefore take the above mathematical development one step further and describe the case of a continuous field of yield surface. For that purpose, they introduce an internal coordinate η that replaces the index n and substitute the internal variables $\alpha_1, \alpha_2, ..., \alpha_{N_S}$ by an internal function $\widehat{\alpha}(\eta)$. The notation "$\widehat{\ }$" is then used in order to identify any variable that depends on the internal coordinate η. The Helmholtz free energy f and the flow potential w are now called functionals and are expressed according to:

$$f = \frac{E}{2}\left(\epsilon - \int_0^{N_S} \widehat{\alpha} \mathrm{d}\eta\right)^2 + \int_0^{N_S} \widehat{H}\frac{\widehat{\alpha}^2}{2}\mathrm{d}\eta \tag{4.24}$$

$$w = \frac{1}{2\mu}\int_0^{N_S} \left\langle |\widehat{\chi}| - \widehat{k} \right\rangle^2 \mathrm{d}\eta \tag{4.25}$$

And therefore:

$$\mathrm{d}\epsilon = \frac{\mathrm{d}\sigma}{E} + \mathrm{d}t \int_0^{N_S} \frac{\left\langle |\sigma - \widehat{H}\widehat{\alpha}| - \widehat{k} \right\rangle}{\mu} S(\sigma - \widehat{H}\widehat{\alpha})\mathrm{d}\eta \tag{4.26}$$

As displayed in Figure 4.4(d), on unloading and reloading, hysteresis occurs and it can be shown that it conforms to the Masing rules. The above model therefore captures the initial loading response observed from laboratory results, except for the

accumulation of ratcheting strain. The following section describes a methodology for supplementing the above with an additional feature that captures ratcheting.

4.4 Theoretical development of HARM

4.4.1 Single-surface model

As for the Armstrong-Frederick model, the objective is to work towards a formulation that accounts for an additional accumulation of strain during each cycle in the direction of loading. However, the idea developed here departs from the dependence on non-linearity of the kinematic hardening variable as the key element in introducing ratcheting. Instead, the kinematic hardening model described in Section 4.3.2 (Figure 4.3(a), p. 156) is complemented by an additional element that accounts for a slight accumulation of plastic strain along with kinematic hardening plastic strain. This new element is characterised by a dimensionless ratcheting parameter R that controls the ratcheting rate. A representation of the ratcheting concept within the single-surface kinematic model is given in Figure 4.5(a).

The ratcheting element is activated each time that the kinematic unit is mobilised, but R is *a-priori* independent from the kinematic hardening variables (H and k). In Figure 4.5(a), it is represented by a slider, emphasizing the fact that the hysteresis loop "slips" with accumulated plastic strains (See Figure 4.5(a)). However, provided an appropriate value of k has been chosen, the dissipation from the ratcheting slider can be discarded in the theoretical developments.

The additional strain, or ratcheting strain caused by the ratcheting element is noted α_r. This new internal variable is intended to be defined as a fraction of the accumulation of plastic strain in the direction of loading, according to the constraint function:

$$c_r = \dot{\alpha}_r - S(\sigma)R|\dot{\alpha}| = 0 \;\; ; \quad R \geq 0 \tag{4.27}$$

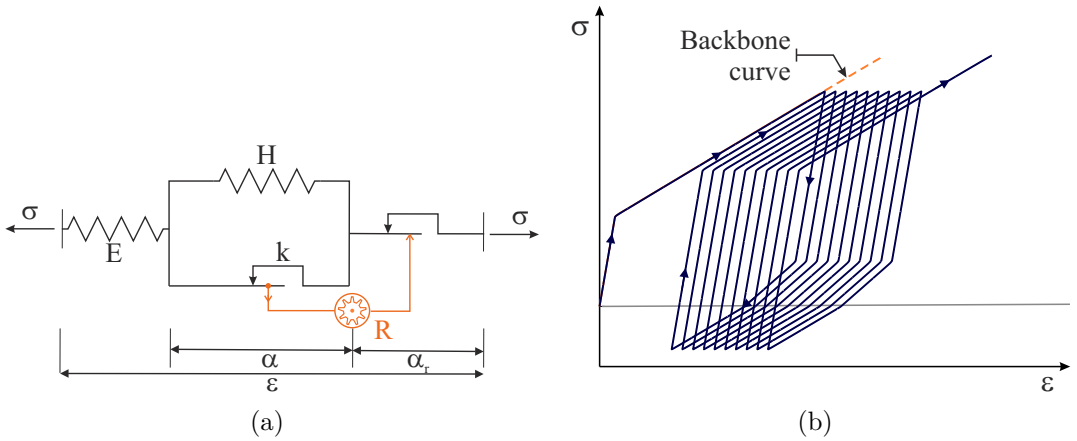

Figure 4.5: (a) Schematic representation of single-yield surface HARM model and (b) typical response ($R = 0.4$)

R is then a small fraction of unity that directly controls the amount of ratcheting strain. For the time being, this factor will be considered constant. Further developments of the parameter R will be discussed later in Chapter 5, Section 5.1 (p. 181) in order to accommodate the ratcheting behaviour. The direction of loading is accounted for by $S(\sigma)$, which results in an increment of ratcheting strain $\dot{\alpha}_r$ of the same sign as σ.

Based on this framework, the accumulation of ratcheting strain α_h is defined according to another constraint function, following the same principles as for the definition of the accumulation of plastic strain $\dot{p}$ (e.g. Equation 4.1, p. 149):

$$c_h = \dot{\alpha}_h - |\dot{\alpha}_r| = 0 \tag{4.28}$$

The usefulness of this variable might not yet be apparent. However, this internal variable is essential for the future work described in Chapter 5, Section 5.1, where the key expressions will be functions of the accumulated ratcheting strain. Each new variable α_r and α_h is conjugate to a generalised stress χ_r and χ_h.

In the following, the theoretical development of the model will be outlined using the energy and flow potentials. The reasons for this choice is that, in addition to allowing for a more direct access to the incremental strain, the flow potential also allows a simpler treatment of constraints, such as those expressed in Equations 4.27

and 4.28. Hence, according to the above description of ratcheting and the schematic of Figure 4.5(a), the energy and flow potentials from Equations 4.11 and 4.13 now become:

$$f(\epsilon, \alpha) = \frac{E}{2}(\epsilon - \alpha - \alpha_r)^2 + \frac{H}{2}\alpha^2 \tag{4.29}$$

$$w(\chi) = \frac{\langle |\chi| + R(|\chi_r| + \chi_h) - k \rangle^2}{2\mu} \tag{4.30}$$

Derivation according to Equations 4.4, 4.5 and 4.10 now gives:

$$\sigma = \frac{\partial f}{\partial \epsilon} = E(\epsilon - \alpha - \alpha_r) \tag{4.31}$$

$$\overline{\chi} = -\frac{\partial f}{\partial \alpha} = \sigma - H\alpha \;\; ; \qquad \dot{\alpha} = \frac{\partial w}{\partial \chi} = \frac{S(\chi)}{\mu} \langle |\chi| + R(|\chi_r| + \chi_h) - k \rangle \tag{4.32}$$

$$\overline{\chi}_r = -\frac{\partial f}{\partial \alpha_r} = \sigma \;\; ; \qquad \dot{\alpha_r} = \frac{\partial w}{\partial \chi_r} = \frac{S(\chi_r)}{\mu} R \langle |\chi| + R(|\chi_r| + \chi_h) - k \rangle \tag{4.33}$$

$$\overline{\chi}_h = -\frac{\partial f}{\partial \alpha_h} = 0 \;\; ; \qquad \dot{\alpha_h} = \frac{\partial w}{\partial \chi_h} = \frac{R}{\mu} \langle |\chi| + R(|\chi_r| + \chi_h) - k \rangle \tag{4.34}$$

According to Ziegler's orthogonality principle, Equation 4.33, directly provides constraint 4.27, together with $S(\chi_r) = S(\sigma) = S(\dot{\alpha_r})$. Equation 4.34, leads to constraint 4.28. Finally, Equation 4.32 gives:

$$\mathrm{d}\alpha = \frac{\mathrm{d}t}{\mu} \langle |\sigma - H\alpha| + R|\sigma| - k \rangle \, S(\sigma - H\alpha) \tag{4.35}$$

And from there, the incremental behaviour is defined according to:

$$\begin{cases} \mathrm{d}\alpha_r = S(\sigma) R \mathrm{d}\alpha \\ \mathrm{d}\alpha_h = |\mathrm{d}\alpha_r| \\ \mathrm{d}\epsilon = \dfrac{\mathrm{d}\sigma}{E} + \mathrm{d}\alpha + \mathrm{d}\alpha_r \end{cases} \tag{4.36}$$

Considering that $|\sigma - H\alpha| + R|\sigma| - k \geq 0$ and that the material is yielding, there is the issue of when $\mathrm{d}\alpha \to 0$. Four cases are to be addressed depending on both the sign of $\mathrm{d}\alpha$ and σ:

$$\dot{\alpha} \to 0^+, \qquad \sigma > 0, \qquad \alpha = \frac{\sigma(1+R) - k}{H} \qquad (1)$$

$$\sigma > 0, \qquad \alpha = \frac{\sigma(1-R) - k}{H} \qquad (2)$$

$$\dot{\alpha} \to 0^-, \qquad \sigma > 0, \qquad \alpha = \frac{\sigma(1-R) + k}{H} \qquad (3)$$

$$\sigma > 0, \qquad \alpha = \frac{\sigma(1+R) + k}{H} \qquad (4)$$

This provides the equation of four boundary lines that define the yield surface, which are shown in Figure 4.6. As long as α and σ are located away from the external top and bottom corner, the yield surface is unequivocally defined and so is the incremental behaviour. However, when reaching the corners, there is a region where both $\dot{\alpha} > 0$ and $\dot{\alpha} < 0$ are satisfied and α is undefined. Therefore, if implemented in this way, Equation 4.35 produces numerical instabilities when σ reaches the upper value k/R. One pragmatic option to deal with this mathematical issue is to ensure that the maximum value of $|\sigma|$ in the analysis remains below k/R. It would be useful

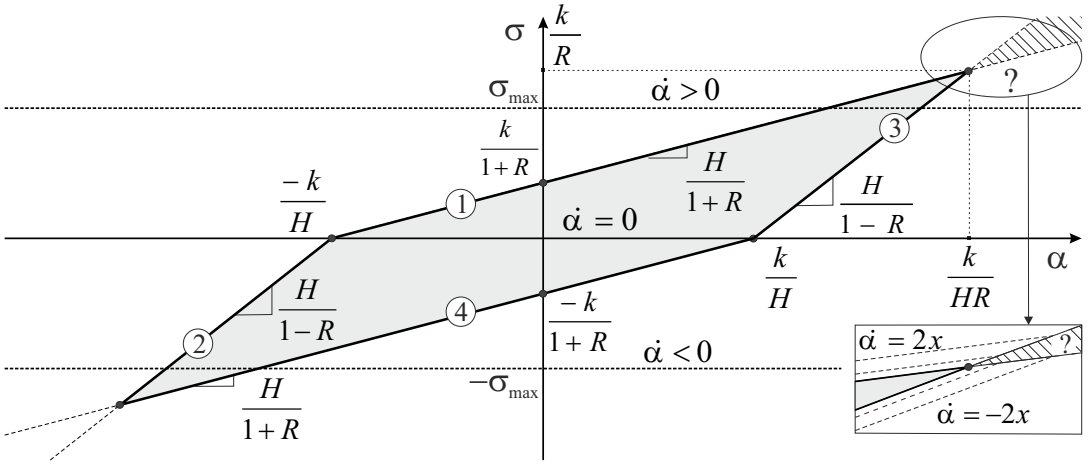

Figure 4.6: Schematic representation of HARM yield surface (single surface)

in future though to develop this mathematical framework further and rigorously establish the expression of α beyond the top and bottom corners. However, due to time constraints, this has not been developed during this research programme and therefore, in the following, R, k and σ will always satisfy:

$$\forall t, \quad |\sigma(t)| < \frac{k}{R} \tag{4.37}$$

Comparing Equation 4.35 with Equation 4.16, it is clear that the expression of the incremental strain is similar to that of pure kinematic hardening, only altered by a small fraction of the plastic strain that depends both on the direction of loading and yielding. As a result, a small ratcheting strain is accumulated each time plastic strains are generated, resulting in the loading curve presented in Figure 4.5(b). The graph shows that, on reloading and exceeding the maximum cyclic load, the model now simulates a competition between (i) Masing behaviour and (ii) ratcheting, for bi-linear plastic materials.

4.4.2 Multi-surface formulation

As for the kinematic model presented earlier, the above framework is extended to a multi-surface model, in order to obtain a smooth elastic-plastic transition. The ratcheting element is now triggered each time that at least one of the kinematic hardening surfaces is active and each surface is characterised by a ratcheting parameter R_n. These are currently independent from the kinematic hardening variables (H_n and k_n) and a conceptual representation of the model is given in Figure 4.7(a). At this stage it can be chosen either to have a single ratcheting parameter, in which case $R_n = R_0, \forall n \in [1, N_S]$ or independent parameters where $R_n = R(n)$. This point will be discussed in further detail later in this section and in Chapter 5, Section 5.1 (p. 181). For generality, it is proposed that the R_n can differ from one surface to another in the following work. The total ratcheting strain is now defined as the sum

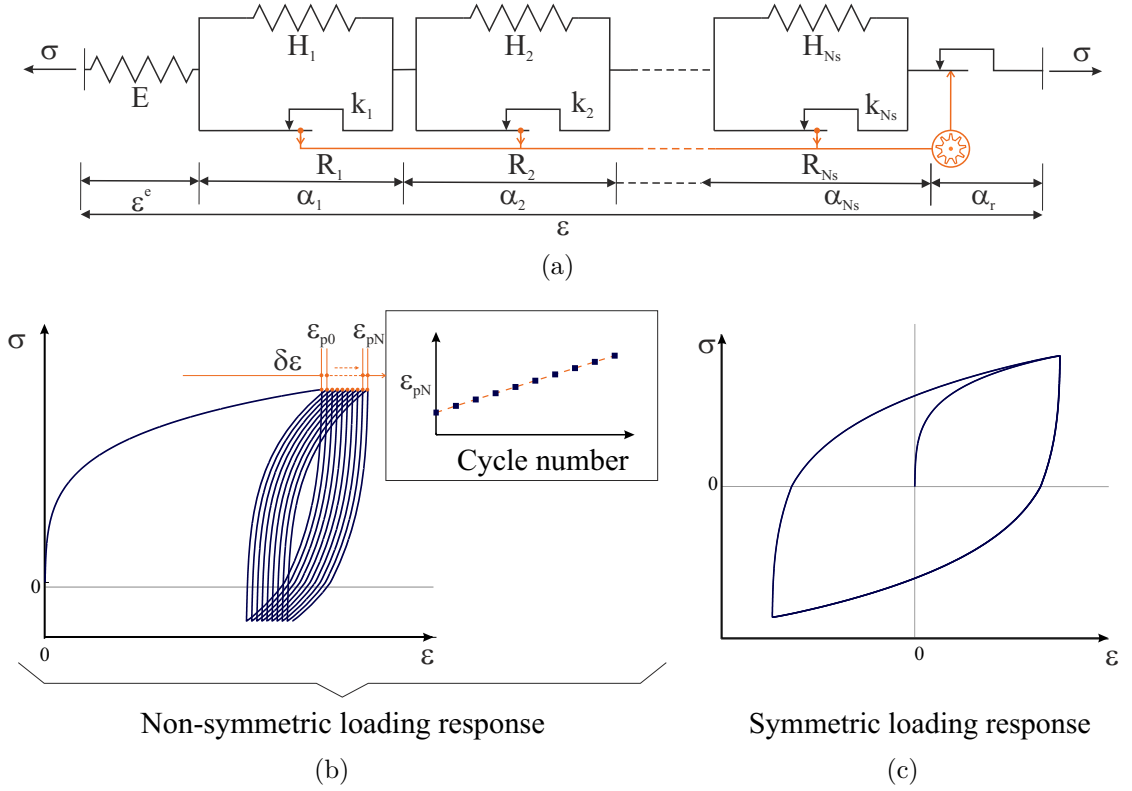

Figure 4.7: (a) Schematic representation of multi-surface HARM model. Typical response for (b) non-symmetric and (c) symmetric (2-way) loading with a ratcheting element characterised by $R_0 = 0.4$

of the contributions of each fraction of plastic strain from each surface according to:

$$c_n = \dot{\alpha}_r - S(\sigma) \sum_{n=1}^{N_S} R_n |\dot{\alpha}_n| = 0 \; ; \quad \forall n \in [1, N_S] \tag{4.38}$$

Hence, the energy and flow potentials from Equations 4.20 and 4.21 are now expressed according to:

$$f = \frac{E}{2} \left(\epsilon - \sum_{n=1}^{N_S} \alpha_n - \alpha_r \right)^2 + \sum_{n=1}^{N_S} \frac{H_n}{2} \alpha_n^2 \tag{4.39}$$

$$w = \sum_{n=1}^{N_S} \frac{1}{2\mu} \langle |\chi_n| + R_n(|\chi_r| + \chi_h) - k_n \rangle^2 \tag{4.40}$$

And on derivation, it follows that:

$$\begin{cases} \mathrm{d}\epsilon &= \dfrac{\mathrm{d}\sigma}{E} + \displaystyle\sum_{n=1}^{N_S} \mathrm{d}\alpha_n + d\alpha_r \\ \mathrm{d}\alpha_n &= S(\sigma - H_n\alpha_n)\dfrac{\langle|\sigma - H_n\alpha_n| + R_n|\sigma| - k_n\rangle}{\mu}\mathrm{d}t \\ \mathrm{d}\alpha_r &= S(\sigma)\displaystyle\sum_{n=1}^{N_S} R_n|\mathrm{d}\alpha_n| \end{cases} \tag{4.41}$$

It is interesting to note that Equations 4.38, 4.39 and 4.40 describe dependent yield surfaces that ratchet at a different rate, but at the same time. There is the choice to consider completely independent surfaces instead where $\forall n \in [1, N_S]\,, \dot{\alpha}_{r,n} = S(\sigma)R_n\dot{\alpha}_n$. However, in the case where the $R_n,\ n \in [1, N_S]$ are a function of n only, both models are strictly equivalent, so it is unnecessary to introduce multiple ratcheting variables.

As for the single yield surface, there is an issue when the value of the stress magnitude increases (and $\dot{\alpha_n} \to 0$) and the restriction of Figure 4.6 and Equation 4.37 now applies to each individual surface (i.e. each set of $\{k_n, H_n, R_n; \alpha_n, \dot{\alpha}_n\}$). Consequently, in the following work, Equation 4.42 will be enforced:

$$\forall t, \forall n \in [1, N_S], \quad |\sigma(t)| < \frac{k_n}{R_n} \tag{4.42}$$

There are several options for obeying Equation 4.42. Since the k_n increase with n, it is straightforward to consider R_n as a function of k_n (or n). For Figures 4.7(c) and 4.7(b), the following expression of R_n was selected:

$$R_n = R_0\left(\frac{k_n}{k_{U0}}\right) \tag{4.43}$$

where R_0 is the initial rate of ratcheting and k_{U0} is the upper limit stress. Using this expression of R_n, Equation 4.42 simply becomes $k_{U0}/R_0 > \sigma_{max} \Rightarrow\ R_0 < 1$ which sets the upper limit for R_0.

As for the single yield surface model, the expression for the incremental behaviour is very similar to that of Equation 4.22, but now accounts for a small accumulation of plastic strain that creates ratcheting. This procedure therefore allows the simulation of what is observed experimentally, i.e. a behaviour that is dominated by kinematic hardening and conforms to extended Masing rules, but, slightly altered by a small accumulation of strain in the direction of loading (Figure 4.7(b)). This will become crucial when modelling multi-amplitude loading where the response will need to rejoin the backbone curve on exceeding maximum cyclic load (see Chapter 3). Also, note that, when performing perfect two-way loading with the model described above, the loop closes as if no ratcheting had occurred (see Figure 4.7(a)).

4.4.3 Infinite number of surfaces

As for the pure kinematic hardening model, the above framework is extended to the extreme case of an infinite number of yield surfaces. The procedure is identical to that described in Section 4.3.2 and therefore the energy and flow potentials are:

$$f = \frac{E}{2}\left(\epsilon - \int_0^{N_S} \widehat{\alpha}\mathrm{d}\eta - \widehat{\alpha_r}\right)^2 + \int_0^{N_S} \widehat{H}\frac{\widehat{\alpha}^2}{2}\mathrm{d}\eta \tag{4.44}$$

$$w = \frac{1}{2\mu}\int_0^{N_S} \left\langle |\widehat{\chi}| + \widehat{R}(|\chi_r| + \chi_h) - \widehat{k}\right\rangle^2 \mathrm{d}\eta \tag{4.45}$$

And the incremental response is now expressed according to:

$$\begin{cases} \mathrm{d}\epsilon = \dfrac{\mathrm{d}\sigma}{E} + \displaystyle\int_0^{N_S} \mathrm{d}\widehat{\alpha}\mathrm{d}\eta + \mathrm{d}\alpha_r \\ \mathrm{d}\widehat{\alpha} = S(\sigma - \widehat{H}\widehat{\alpha})\dfrac{\left\langle \left|\sigma - \widehat{H}\widehat{\alpha}\right| + \widehat{R}|\sigma| - \widehat{k}\right\rangle}{\mu}\mathrm{d}t \\ \mathrm{d}\alpha_r = S(\sigma)\displaystyle\int_0^{N_S} \widehat{R}\widehat{\alpha}\mathrm{d}\eta \\ \mathrm{d}\alpha_h = |\mathrm{d}\alpha_r| \end{cases} \tag{4.46}$$

Numerically speaking, it is complicated to implement the continuous formulation described above, and therefore, a large but finite number of variables is usually employed instead. For this reason, the following developments will be pursued using the finite multi-surface approach.

4.4.4 Parallel form

The multisurface kinematic hardening curve as displayed in Figure 4.4(d) can be obtained using either the series approach described in Section 4.3.2 or a parallel form. This is detailed in Houlsby and Puzrin (2006), where it is noted that the model and internal variables then have slightly different meanings. However, the final response is identical given an appropriate choice in parameters. Similarly, this is also true for the ratcheting model.

In some cases, it can be beneficial to consider a parallel formulation rather than a series, mostly because the stresses then become additive rather than the plastic strains. Consequently, it is more convenient to use such an approach when considering strain-controlled cases, and this can be more advantageous in FEM analyses.

Accordingly, the basics of the parallel version of the HARM model are presented in this section, as this could be useful for future applications. The schematic representation is given in Figure 4.8. Here, the spring stiffnesses, slider strengths and also internal variables are named differently in order to underline the fact that they have slightly different meanings compared with the series model (see Houlsby and Puzrin (2006); Einav (2004)).

According to this conceptual representation, the flow potential remains unchanged, apart from the notation, and the energy function is now expressed according to:

$$f = \frac{E}{2} \cdot (\epsilon - \beta_r)^2 + \sum_{n=1}^{N_S} \frac{G_n}{2} (\epsilon - \beta_n)^2 \tag{4.47}$$

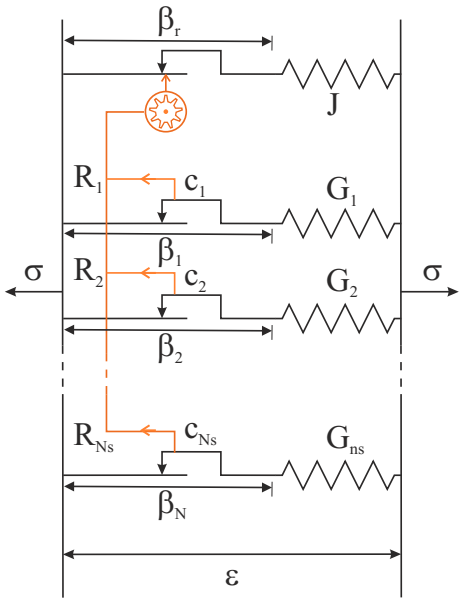

Figure 4.8: Schematic representation of parallel form of HARM model.

$$w = \sum_{n=1}^{N_S} \frac{1}{2\mu} \langle |\chi_n| + R_n(|\chi_r| + \chi_h) - c_n \rangle^2 \tag{4.48}$$

This theory has not been developed any further as the case studied here is load controlled. However, the interested reader should now have all the elements for developing this further if required.

4.4.5 Discussion

As mentioned earlier and outlined in Section 4.3.2, a conjugate force potential exists for each flow potential expressed above. These would be expressed based upon the respective kinematic hardening force potentials and are augmented by the constraints defining the ratcheting strain and the accumulated ratcheting strain (i.e. Equations 4.27 and 4.28). However, the force potential is a function of the state variables, internal variables and change of internal variables and not the variations of state. Consequently, since both constraints involve the sign of σ, these cannot be integrated into the force potential as such. Further mathematical investigation of

the Legendre-Fenchel transforms of the flow potentials would be useful in future in order to complete the model with the force potential form of the model.

The Gibbs free energy g on the other hand, is very easy to obtain. Table 4.1 summarizes the different formulations of HARM developed above and gives the equivalent Gibbs energy for each form of the model. For completeness, the table also provides the rate-independent forms (i.e. yield function $\bar{y}$) that have not been developed in this thesis but are fairly straightforward to deduce from the rate-dependent flow potentials. For the same reason as for the force potential, the rate-independent dissipation potential d is omitted in this Table.

Table 4.1: Hierarchy of ratcheting plasticity models HARM

Single-surface kinematic and ratcheting plasticity (series)		
Energy	$f = \frac{E}{2} \cdot (\epsilon - \alpha - \alpha_r)^2 + \frac{H}{2}\alpha^2$	$g = -\frac{\sigma^2}{2E} - \sigma \cdot (\alpha + \alpha_r) + \frac{H}{2}\alpha^2$
Dissipation	$\bar{y} = \left(\frac{\lvert\chi\rvert + R(\lvert\chi_r\rvert + \chi_h)}{k}\right) - 1$	$w = \frac{\langle \lvert\chi\rvert + R(\lvert\chi_r\rvert + \chi_h) - k\rangle^2}{\mu}$
Multi-surface kinematic and ratcheting plasticity (series)		
Energy	$f = \frac{E}{2} \cdot \left(\epsilon - \sum_{n=1}^{N_S} \alpha_n - \alpha_r\right)^2 + \sum_{n=1}^{N_S} \frac{H_n}{2}\alpha_n^2$	$g = -\frac{\sigma^2}{2E} - \sigma \cdot \left(\sum_{n=1}^{N_S} \alpha_n + \alpha_r\right) + \sum_{n=1}^{N_S} \frac{H_n}{2}\alpha_n^2$
Dissipation	$\bar{y} = \sup_n \left(\frac{\lvert\chi_n\rvert + R_n(\lvert\chi_r\rvert + \chi_h)}{k_n}\right) - 1$	$w = \sum_{n=1}^{N_S} \frac{\langle \lvert\chi_n\rvert + R_n(\lvert\chi_r\rvert + \chi_h) - k_n\rangle^2}{\mu}$
Continuous kinematic and ratcheting plasticity (series)		
Energy	$f = \frac{E}{2} \cdot \left(\epsilon - \int_0^{N_S} \widehat{\alpha}\mathrm{d}\eta - \widehat{\alpha_r}\right)^2 + \int_0^{N_S} \widehat{H}\frac{\widehat{\alpha}^2}{2}\mathrm{d}\eta$	$g = -\frac{\sigma^2}{2E} - \sigma \cdot \left(\int_0^{N_S} \widehat{\alpha}\mathrm{d}\eta + \alpha_r\right) + \int_0^{N_S} \widehat{H}\frac{\widehat{\alpha}^2}{2}\mathrm{d}\eta$
Dissipation	$\bar{y} = \sup_\eta \left(\frac{\lvert\widehat{\chi}\rvert + \widehat{R}(\lvert\chi_r\rvert + \chi_h)}{\widehat{k}}\right) - 1$	$w = \int_0^{N_S} \frac{\left\langle \lvert\widehat{\chi}\rvert + \widehat{R}(\lvert\chi_r\rvert + \chi_h) - \widehat{k}\right\rangle^2}{\mu}$
Multi-surface kinematic and ratcheting plasticity (parallel)		
Energy	$f = \frac{E}{2} \cdot (\epsilon - \beta_r)^2 + \sum_{n=1}^{N_S} \frac{G_n}{2} (\epsilon - \beta_n)^2$	$g = -\frac{(\sigma + J\beta_r)^2 + \sum_{n=1}^{N_S} (\sigma + G_n\beta_n)^2}{2\left(J + \sum_{n=1}^{N_S} G_n\right)} + \frac{J}{2}\beta_r^2 + \sum_{n=1}^{N_S} \frac{G_n}{2}\beta_n^2$
Dissipation	$\bar{y} = \sup_n \left(\frac{\lvert\chi_n\rvert + R_n(\lvert\chi_r\rvert + \chi_h)}{k_n}\right) - 1$	$w = \sum_{n=1}^{N_S} \frac{\langle \lvert\chi_n\rvert + R_n(\lvert\chi_r\rvert + \chi_h) - k_n\rangle^2}{\mu}$

4.5 Accelerated modelling

One of the key issues with constitutive modelling of large cycle behaviours is the computation time. Most numerical strategies consist of modelling every single cycle incrementally and the computation times quickly become prohibitive. For example, the calculation provided in Section 4.4.2, Figure 4.7(b) (p. 166) was optimised to the largest acceptable time step and the selected implementation took 16s with 8 Intel(R) Core(TM) i7 CPU processors (Q 840 1.87GHz). Therefore, 1 million cycles would take 18 days. Also, incremental solving requires thorough implementation in order to clear the memory while saving relevant strain-stress response history.

A powerful aspect of the HARM model is that it can be adapted to "accelerate" the effect of the ratcheting behaviour in a very simple manner, while rigorously capturing the response that would have been obtained with the incremental method. This is achieved by directly multiplying the initial ratcheting rate R_0 by a factor R_{fac} that corresponds to the number of cycles that are to be "skipped". With regards to the mathematical work described above, this implies that line 3 of Equation 4.41 now becomes:

$$\mathrm{d}\alpha_r = R_{fac} \cdot \left(S(\sigma) \cdot \sum_{n=1}^{N_S} R_n |\dot{\alpha}_n| \right) \tag{4.49}$$

Note that *only* this particular equation is altered by R_{fac}. Equation 4.27 (p. 161) and the expression of the incremental plastic strain (line 2, Equation 4.41, p. 167) remain unchanged, as it would otherwise change the size of the yield surface and therefore, the mathematical framework described in Section 4.4, Subsection 4.4.2 (p. 165).

Based on this, an infinite number of "skipping cycle" programmes can be considered. The method is illustrated using the programme summarized in Table 4.2. This particular series allows the evolution of the response every 10^{nth} cycles to be observed.

The calculation with the accelerated approach took 153s. vs. 26 min. (1000 cycles) with the standard incremental procedure.

A comparison of the results obtained with the accelerated and the incremental approaches is displayed in Figures 4.9(a)-(c). Figure 4.9(b) first shows the complete stress-strain response that would be obtained using the accelerated approach and comparison with Figure 4.9(a) shows that the targeted cycles are modelled accurately. The intermediate accelerated cycles (see Table 4.2) should be discarded when plotting the final results, as illustrated in Figure 4.9(c). The graphs show that the accelerated

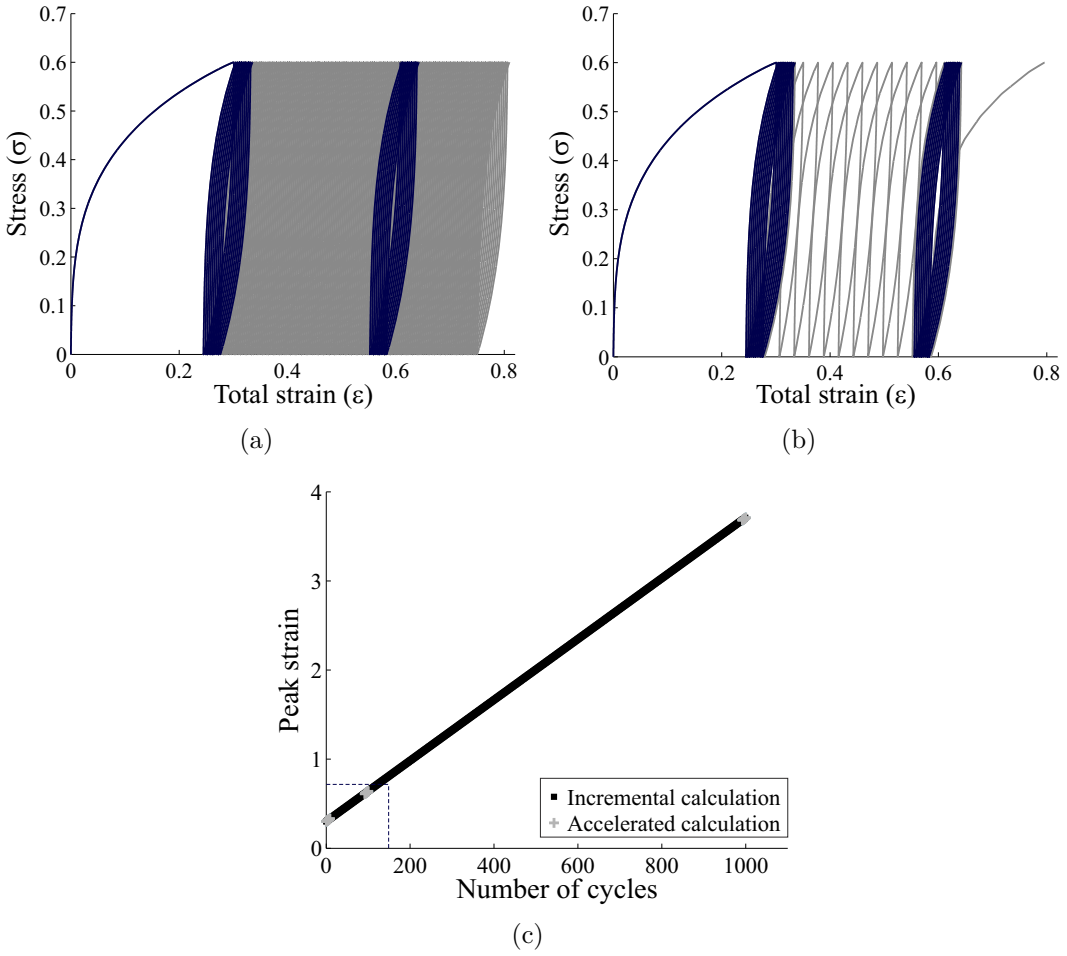

Figure 4.9: Comparison between the stress-strain curves obtained using (a) the standard incremental and (b) the accelerated solving method for HARM for $R_0 = 0.2$ (Zoom on first 150 cycles; cycles 1-10 and 90-100 highlighted in dark); (c) Comparison of peak strain at maximum cyclic load calculated with the incremental (black) and accelerated (grey) modelling

Table 4.2: Example of cyclic loading programme for incremental and accelerated approaches of HARM

	Incremental approach		**Accelerated approach**	
	Cycle No.	R_{fac}	Cycle No.	R_{fac}
Normal:	10	1	10	1
Intermediate:	80	1	10	8
Normal:	10	1	10	1
Intermediate:	890	1	10	89
Normal:	10	1	10	1
Total	1,000	-	50	-

method allows the accurate prediction of what would have been obtained with the standard incremental calculation in a much reduced computation time.

4.6 Two-dimensional model

As mentioned in Chapter 1, Section 1.4.4 (p. 37), the loading on a wind turbine foundation is likely to be multi-directional. For a pile in cross-anisotropic soil (i.e. with the same properties in all horizontal directions) the response to loading in any direction should be the same. Assuming this, the 1-D version of the HARM model is here extended to a two-dimensional case.

Unfortunately, due to time constraints, the scope of the experimental work proposed in this thesis did not include multi-directional loading tests. In addition, limited data is available in published literature on this topic and consequently, the following developments will not be benchmarked against experimental results. However, this generalisation should be applicable to a number of loading problems and hopefully, will be validated against experimental or field-test data in the near future.

The principles of the extension to two-dimensional loading is very similar to that previously described in Houlsby and Puzrin (2006) for the Drucker-Prager Model. The two principal directions are noted "1" and "2", where direction "2" is

perpendicular to direction "1" and stresses and strains are projected along these directions. Ratcheting strain is accumulated in each direction according to the total accumulation of plastic strain (in directions 1 and 2) and in the direction of the stress in that particular direction. Consequently, the increment of ratcheting strain in the direction $i \in 1,2$ is now expressed according to:

$$c_{ir} = \dot{\alpha}_{ir} - \frac{\sigma_i}{\sqrt{\sigma_1^2 + \sigma_2^2}} \sum_{n=1}^{N_S} R_n \sqrt{\dot{\alpha}_{1n}^2 + \dot{\alpha}_{2n}^2} = 0 \quad ; \qquad i \in 1,2 \tag{4.50}$$

However, the accumulated ratcheting strain is now defined as the norm of the ratcheting strains in the two directions and therefore:

$$c_h = \dot{\alpha}_h - \sqrt{\dot{\alpha}_{1r}^2 + \dot{\alpha}_{2r}^2} = 0 \tag{4.51}$$

The energy function is now the sum of the energies in both directions, as is the dissipation:

$$\begin{aligned} f = \frac{E}{2} \cdot \left[\left(\epsilon_1 - \sum_{n=1}^{N_S} \alpha_{1n} - \alpha_{1r} \right)^2 + \left(\epsilon_2 - \sum_{n=1}^{N_S} \alpha_{2n} - \alpha_{2r} \right)^2 \right] \\ + \sum_{n=1}^{N_S} \frac{H_n}{2} \left[\alpha_{1n}^2 + \alpha_{2n}^2 \right] \end{aligned} \tag{4.52}$$

$$w = \sum_{n=1}^{N_S} \frac{1}{2\mu_n} \left\langle \sqrt{\chi_{1n}^2 + \chi_{2n}^2} + R_n(|\chi_{1r}| + |\chi_{2r}| + \chi_h) - k_n \right\rangle^2 \tag{4.53}$$

It is clear from the above equations that, when either $\sigma_1 = 0$ or $\sigma_2 = 0$, this reduces to the 1-dimensional formulation outlined in Section 4.4.

4.7 Conclusions

This chapter has presented a novel hyperplasticity model, HARM ("Houlsby Abadie Ratcheting Model"), that is capable of reproducing a behaviour that is dominated by kinematic hardening while accumulating a small fraction of plastic strain, also called ratcheting strain, at each load increment. The model is concise and simple yet rigorous and is constructed so that the increment of ratcheting strain depends on the direction of loading and yielding. The fundamentals of the 1-D multi-surface formulation of the HARM model are summarized in Table 4.3. This chapter has also demonstrated how to accelerate artificially the ratcheting effect of a large number of cycles within the computation of only few cycles. This is a very powerful aspect of the HARM framework, as it will allow considerable computational time saving. Finally, an extension of the model to multi-directional load cases for isotropic soil conditions was presented.

Because the model builds on the hyperplastic kinematic hardening model, it adheres to the extended Masing rules and the response to cyclic loading at non-zero mean load exhibits a competition between (1) Masing behaviour (2) ratcheting. This corresponds to the primary mechanisms observed experimentally for the model monopile (Chapter 3, Section 3.6.1, p. 139). This model is likely to apply to many more applications than laterally loaded piles. For example, ratcheting was also observed for cyclically loaded caissons (e.g. Zhu *et al.*, 2014), upheaval buckling of pipelines (e.g. Williams, 2014) or generally speaking, cyclically loaded soils (e.g. Achmus *et al.*, 2011). Ratcheting also occurs for a large range of cyclically loaded continuous media. The above framework can therefore be adapted to a wide range of applications, but will need to be accommodated to each case individually and based on experimental test results. The following chapter demonstrates how the above framework is modified and adapted to capture the characteristic ratcheting behaviour observed experimentally for cyclically loaded rigid monopiles.

Table 4.3: Fundamentals of the 1-D multi-surface kinematic hardening and ratcheting hyperplasticity model HARM

Variables	ϵ, σ	Strain, stress
	n	Yield surface index
	α_n, α_r, α_h	Plastic, Ratcheting and accumulated ratcheting strains
	χ_n, χ_r, χ_h	Corresponding generalised stresses
Constants	E	Initial stiffness
	N_S	Number of surfaces
	k_n, H_n	Hardening strengths and stiffness
	R_0	Initial rate of ratcheting
Energy	$f = \frac{E}{2} \cdot \left(\epsilon - \sum_{n=1}^{N_S} \alpha_n - \alpha_r \right)^2 + \sum_{n=1}^{N_S} \frac{H_n}{2} \alpha_n^2$	$\begin{cases} \sigma = \frac{\partial f}{\partial \epsilon} = E(\epsilon - \sum_{n=1}^{N_S} \alpha_n - \alpha_r) \\ \forall n, \quad \overline{\chi}_n = -\frac{\partial f}{\partial \alpha_n} = \sigma - H_n \cdot \alpha_n \\ \overline{\chi}_r = -\frac{\partial f}{\partial \alpha_r} = \sigma \\ \overline{\chi}_h = -\frac{\partial f}{\partial \alpha_h} = 0 \end{cases}$
Flow	$w = \sum_{n=1}^{N_S} \frac{1}{2\mu} \langle \lvert\chi_n\rvert + R_n(\lvert\chi_r\rvert + \chi_h) - k_n \rangle^2$	$\begin{cases} \forall n, \quad \dot{\alpha}_n = \frac{\partial w}{\partial \chi_n} = \frac{S(\chi_n)}{\mu} \langle \lvert\chi_n\rvert + R_n(\lvert\chi_r\rvert + \chi_h) - k_n \rangle \\ \dot{\alpha_r} = \frac{\partial w}{\partial \chi_r} = S(\chi_r) \lvert\dot{\alpha}_n\rvert \\ \dot{\alpha_h} = \frac{\partial w}{\partial \chi_h} = \lvert\dot{\alpha}_r\rvert \end{cases}$
Accelerated	$\mathrm{d}\alpha_r = R_{fac} \cdot \left(S(\sigma) \cdot \sum_{n=1}^{N_S} R_n \lvert\dot{\alpha}_n\rvert \right)$	

Chapter 5

Calibration against Experimental Data

5.1 Introduction

The previous chapter has introduced a novel constitutive model that is capable of capturing the primary features of the experimental test results: development of ratcheting strain within Masing behaviour. This chapter demonstrates how to accommodate this framework in order to describe more complex aspects of ratcheting and predict the experimental test results presented in Chapter 3.

More specifically, the first section describes a framework, called HARM+, that captures the following key properties outlined in Chapter 3 and summarised in Section 3.6.1, p. 139:

(i) The rate of accumulated displacement gradually reduces as the number of cycles increases

(ii) The shape of the hysteresis loop changes, with less hysteresis and an increase in secant stiffness after many cycles

(iii) The rate of accumulated ratcheting displacement strongly depends on the loading conditions, and in particular, on the cyclic load magnitude

The identification of parameters associated with a selected plasticity model is a critical issue for future use in industrial simulations. The second section of this

chapter therefore presents a short calibration methodology based on four selected test results: one monotonic (MCo4) and three long-term continuous cyclic (CMLT1,2,3). The procedure details how to identify the model parameters that specifically describe the backbone curve and ratcheting behaviour. A short section also outlines how to determine the modelling parameters, i.e. the parameters that have been introduced for numerical purposes but whose values should not modify the underlying response.The final section then shows the results of the calibrated model for the three selected continuous cyclic tests and for a range of key tests listed in Table 2.6 (p. 65).

In contrast with Chapter 3, the test results will be expressed here in terms of lateral force vs. lateral displacement at the level of the applied load. It is more appropriate here to use the displacement at the pile top in order to accommodate the work from both the moment and lateral force at ground surface level and to bypass the need for a two-variable macro-element to capture both rotation and displacement at ground level. Since the laboratory pile can be approximated as perfectly rigid, the relationship between the pile displacements at the load application point or at ground level and the rotation is linear, and therefore changing the parameter space does not make a difference to the results described in Chapters 2 and 3. In particular, for the power-law expressions obtained in Chapter 2, Section 2.5 (p. 68) and Chapter 3, Section 3.3 (p. 101), the power exponents remain unchanged.

In the following analysis, the lateral force and the pile top displacement are both normalised using the corresponding values at ultimate capacity (denoted H_R and y_{tR}). For the copper pile in loose Yellow Leighton Buzzard sand, the values at pile top (430 mm above ground level) are $H_{tR} = M_R/h_e = 78N$ and $y_{tR} = 0.25 \times D$. Hence, for this application, the "stress" and "strain" from Chapter 4 correspond to:

$$\sigma = \frac{H_t}{H_R} \tag{5.1}$$

$$\epsilon = \frac{y_t}{y_{tR}} \tag{5.2}$$

With this definition of σ, at peak load, $\sigma_p \equiv \zeta_b$. As the parameters depend on the soil properties and pile geometry, they need to be properly scaled in a rigorous way for application to piles of different size and in different ground conditions. This was addressed in Chapter 2, Section 2.2.

Finally, rate-dependency will not be investigated in the following analysis as this phenomenon was found to be irrelevant to the laboratory test case. Consequently, the "viscosity" will artificially be set to a very small value ($\mu \to 0$) and this parameter will therefore be considered as a modelling parameter.

5.2 Accommodating the ratcheting behaviour (HARM+)

As displayed in Figure 4.7(b) (p. 166), the HARM model as described in the previous chapter only captures a constant ratcheting rate, with no change in hysteresis loop shape. In this section, this framework is extended in order to accommodate the three points outlined in the introduction. Each of the three sections below target one of these aspects, starting with point number (ii).

5.2.1 Change in hysteresis loop shape

An efficient option for capturing the change in hysteresis loop shape is to make all of the surface strengths k_n increase by a small amount with the accumulation of hardening strain. This will gradually stiffen the overall response on each unload-reload loop and therefore both tighten the hysteresis loop shape and increase the secant stiffness. This is thus in agreement with the experimental conclusions from Chapter 3, Sections 3.3.3 and 3.3.4 (p. 113 and 117 respectively).

It is noteworthy that the idea developed here is to modify the strengths and not the stiffnesses, which at first glance could have appeared to be more straightforward for changing the secant stiffness. However, if the H_n were made functions of the state

variables (ϵ, α_n, α_r or α_h), this would directly affect the differential form of Equation 4.39 and therefore modify the mathematical framework described in Section 4.4.2 (p. 165). However, making the k_n (or accordingly, the R_n) functions of internal variables will not affect the theoretical work described in Section 4.4. This technique corresponds to that used when combining isotropic and kinematic hardening (see Houlsby and Puzrin, 2006).

As the accumulated ratcheting strain is defined as a small fraction of the accumulation of plastic strain, it is straightforward to make the k_n a function of α_h. As most of the experimental cyclic key parameters are well fitted using power-laws (Chapter 3), it was chosen to express the k_n using a power law:

$$k_n = k_{0n} \cdot \left(\frac{\alpha_h}{\alpha_{h0}} \right)^{m_k}, \quad n \in [1, N_S] \tag{5.3}$$

Here, the $k_{0n},\ n \in [1, N_S]$ are the initial kinematic hardening strengths obtained by fitting the backbone curve (see Section 5.3.1, p. 190). α_{h0} is the initial value of hardening parameter, and consequently α_h has to be initialised at this particular value (it is also a possible option for initialisation of α_r, though, not necessary). m_k is the exponent that defines the rate at which the hysteresis loop closes with hardening parameter. If $m_k = 0$, this effect is disabled and therefore the shape of the hysteresis loop remains unchanged. Otherwise, m_k is expected to be a positive fraction of unity. The relationship between the experimental results and model parameters are not discussed here but will be outlined later in Section 5.3 (p. 190).

Figures 5.1(a) and 5.1(c) - (e) (squared dotted lines) display the typical response obtained with the HARM model supplemented with Equation 5.3. Here, the same model as that for Figure 4.7(b) (p. 166) is used (i.e. $R_0 = 0.4$) and in addition, $m_k = 0.15$ and $\alpha_{h0} = 0.02$. Figure 5.1(a) highlights the change in loop shape induced by Equation 5.3. For completeness, the change in secant stiffness and loop area are displayed in Figures 5.1(d) and 5.1(e) respectively.

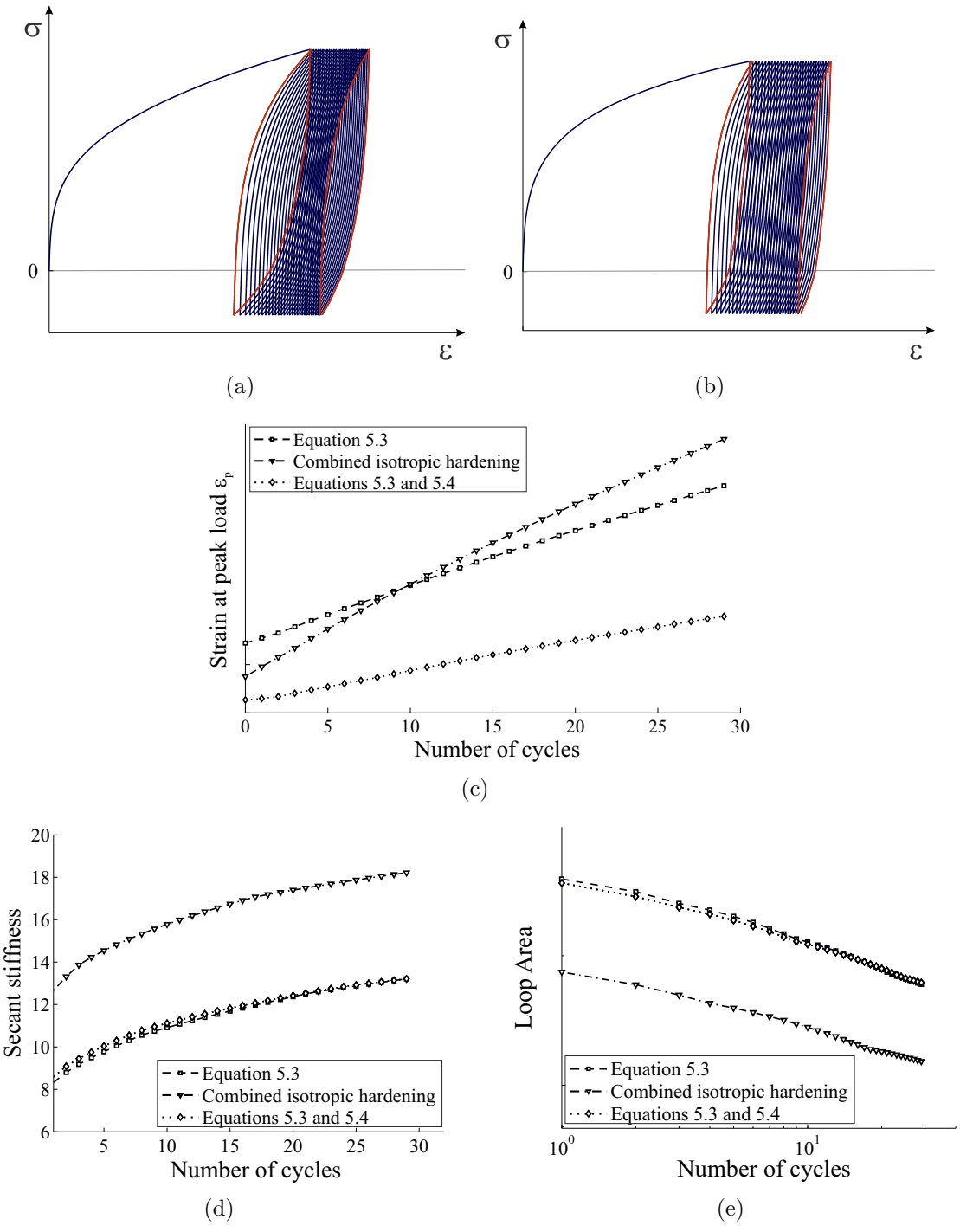

Figure 5.1: Illustration of the effect of Equations 5.3 ($m_k = 0.15$, $\alpha_{h0} = 0.02$) (squared lines) and compared with combined isotropic hardening ($k_n = k_{0n}\left(1 + 0.95\beta^{0.15}\right)$, $R_0 = 1.2$) (triangled lines): (a) stress-strain curve (Equation 5.3); (b) stress-strain curve (combined isotropic hardening); evolution of (c) strains at peak load, (d) stiffness and (e) hysteresis loop area with cycle number - diamond curves illustrate the effect of Equation 5.4 with $m_r = 0.3$

Equation 5.3 is one of the many options that can be used to trigger the change in loop shape, and the one that appeared to be the most straightforward. Similar results could be obtained using combined isotropic hardening for each individual surface. This is illustrated in Figures 5.1(b)-(e) (triangled lines). From a mathematical point of view, introducing isotropic hardening requires the introduction of a new internal variable, β, to the model described in Subsection 4.4.2, which accounts for the accumulation of plastic strain and is equivalent to the variable p used within the conventional plasticity approach (Chapter 4, Section 4.2, Equation 4.1, p. 149). Instead of Equation 5.3, the k_n parameters are then a function of β that is tuned to match the experimental trends. For the application illustrated in Figures 5.1(b) to 5.1(e), $k_n = k_{0n}\left(1 + Q\beta^{1/m_y}\right),\ Q = 0.95,\ m_y = 1/0.15$.

The procedure that employs Equation 5.3 is similar to that of isotropic hardening. The accumulated plastic strain β is replaced by the accumulated ratcheting strain α_h, which is similar to the accumulated plastic strain, only modified by coefficients R_n. However, introducing isotropic hardening would require the introduction of an additional internal variable which can be avoided by using the available accumulated ratcheting strain. Consequently, this direction has not been developed any further during the course of this research programme.

5.2.2 Decrease of ratcheting rate

The introduction of Equation 5.3 within the model has an effect on the rate of ratcheting, which is no longer constant (see Figure 5.1(c)). However, the effect obtained via this method is usually small and it is unlikely that the rate of ratcheting will properly be captured using only this method.

It is possible though to accommodate the ratcheting rate by making the ratcheting parameter R itself a function of the accumulated ratcheting strain. For the same reasons as for Equation 5.3, a power-law was here chosen for accommodating the

ratcheting rate as a function of α_h:

$$R_n(\alpha_h) = R_0 \left(\frac{k_{0n}}{k_{U0}}\right) \left(\frac{\alpha_h}{\alpha_{h0}}\right)^{-m_r} \tag{5.4}$$

where R_0 is the initial rate of ratcheting parameter. Note that if $R_0 = 0$ then all ratcheting effects are disabled. m_r is the exponent that defines the dependence of the ratcheting rate on the hardening parameter. If $m_r = 0$, the rate of ratcheting is triggered solely by Equation 5.3 and if both $m_k = 0$ and $m_r = 0$, the ratcheting rate remains constant. The above equation is responsible for reducing the increment of ratcheting strain with accumulated ratcheting strain - or ratcheting history - and therefore allows the reduction of the rate of accumulation of ratcheting strain with time/cycle number.

The effect of Equation 5.4 compared with Equation 5.3 is illustrated in Figure 5.1(c) for $m_r = 0$ and $m_r = 0.3$. Figures 5.1(d) and 5.1(e) demonstrate that, as expected, this change in R_n has negligible effect on the evolution of the hysteresis loop shape (stiffness and loop area).

5.2.3 Dependence on load magnitude

The first and obvious option available to capture the effect of load magnitude on ratcheting behaviour is to make the ratcheting parameters R_n a function of the stress magnitude σ. However, as the R_n are already expressed as a function of the initial strengths k_{0n} (see Equation 4.43, p. 167) and the k_{0n} directly depend on the load magnitude, a more convenient and direct option is to simply modify the original expression of Equation 4.43 (p. 167) and 5.4 (p. 185) for the k_{0n}. For the same reasons as in the previous two paragraphs, a power-law is selected:

$$R_n(\alpha_h, k_{0n}) = R_0 \cdot \left(\frac{\alpha_h}{\alpha_{h0}}\right)^{-m_r} \cdot \left(\frac{k_{0n}}{k_{U0}}\right)^{m_s} \tag{5.5}$$

where the exponent m_s defines the dependence of the ratcheting rate on the stress.

Figures 5.2(a) - (d) demonstrate the effect of Equation 5.5 ($m_s = 2$) compared with Equation 5.4 ($m_s = 1$) and displays typical results obtained using the HARM model plus Equations 5.3 and 5.5 for a multi-amplitude load series of $\{20\ cycles \times (\sigma_{max} = 0.25) \rightarrow\ 20\ cycles \times (\sigma_{max} = 0.45) \rightarrow\ 20\ cycles \times (\sigma_{max} = 0.60)\}$. As the introduction of term $\left(\frac{k_{0n}}{k_{U0}}\right)^{m_s}$ significantly reduces the ratcheting rate (for $\sigma < 1$), it was necessary to modify the value of R_0 accordingly. In Figures 5.2(a) - (d), the squared lines were obtained with $m_s = 2$ and $R_0 = 1.9$. Figure 5.2(b) clearly shows that the introduction of this new term increases the accumulation of ratcheting strain with load magnitude while trends for stiffness and loop area are not significantly modified (Figure 5.2(c) and 5.2(d)). Figure 5.2(a) displays the computed backbone curve for comparison. The graph demonstrates that there is a competition between (a) Extended Masing rules, (b) progressive stiffening of the response and (c) ratcheting, which is the key behaviour that was targeted. Consequently, on reloading, the curve does not perfectly rejoin the backbone curve but tends towards it.

When calibrating Equation 5.5, one has to be very careful about satisfying the criterion $|\sigma(t)| < \frac{k_n}{R_n}$ (Equation 4.42, p. 167) at all time. Substituting in Equations 5.3 and 5.5, this becomes:

$$\forall t, \forall n \in [1, N_S], \quad \frac{k_{U0}}{R_0} \left(\frac{\alpha_h}{\alpha_{h0}}\right)^{m_k+m_r} \left(\frac{k_{0n}}{k_{U0}}\right)^{1-m_s} > |\sigma(t)| \tag{5.6}$$

Since $\frac{\alpha_h}{\alpha_{h0}} \geq 1$ and $m_k + m_r \geq 0$, $min\left(\left(\frac{\alpha_h}{\alpha_{h0}}\right)^{m_k+m_r}\right) = 1$. And therefore Equation 5.6 becomes:

$$\forall t, \forall n \in [1, N_S], \quad \frac{k_{U0}}{R_0} \left(\frac{k_{0n}}{k_{U0}}\right)^{1-m_s} > |\sigma(t)| \tag{5.7}$$

This provides an upper bound value for R_0 for a given value of m_s and was used during the calibration procedure.

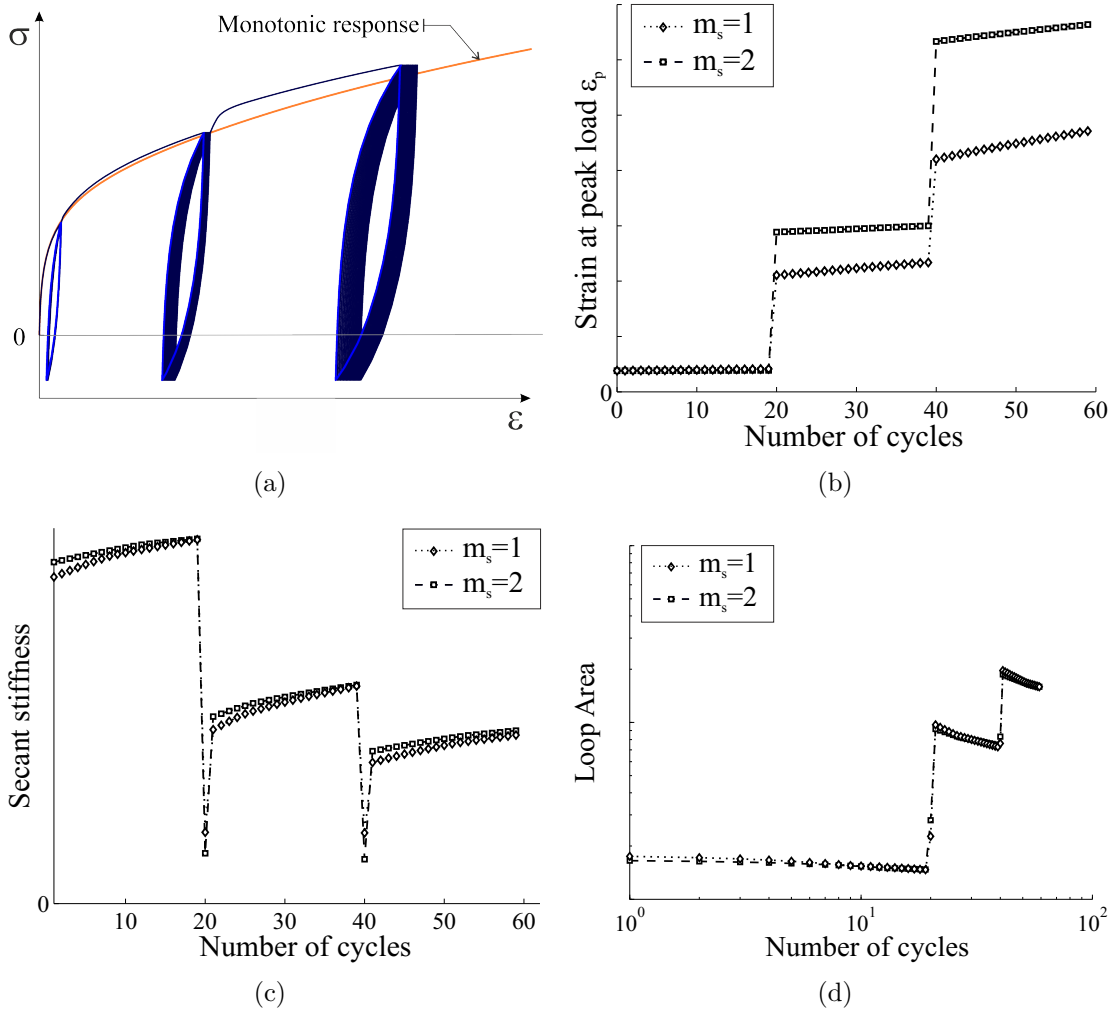

Figure 5.2: Typical response obtained with final HARM+ model(HARM plus Equations 5.3 and Equations 5.5) and $\{m_k = 0.15,\ m_r = 0.3,\ m_s = 2,\ \alpha_{h0} = 0.02,\ R_0 = 1.9\}$ (squared lines): (a) stress-strain curve; Evolutions of (b) strains at peak load, (c) stiffness and (d) hysteresis loop area with cycle number - Illustration of the influence of m_s by comparison with $\{m_k = 0.15,\ m_r = 0.3,\ m_s = 1,\ \alpha_{h0} = 0.02,\ R_0 = 0.4\}$ (diamond lines)

5.2.4 Additional remarks

5.2.4.1 Hysteretic response

The HARM model described in Chapter 4 supplemented with Equations 5.3 and 5.5 is called HARM+ and is intended to capture the key mechanisms observed experimentally for the laterally loaded rigid pile response (Chapter 3, Section 3.6.1, p. 139)).

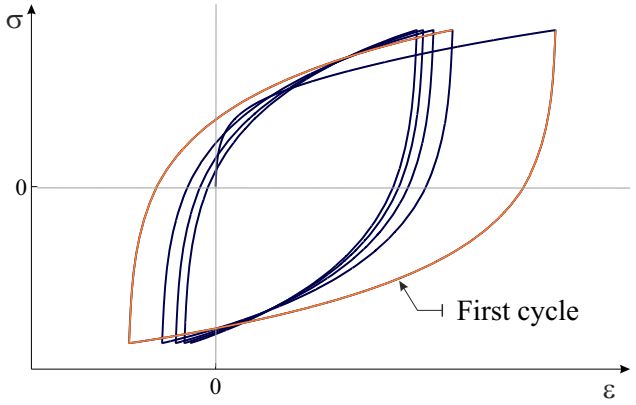

Figure 5.3: Typical 2-way cyclic loading response obtained with HARM+ model

Equations 5.3 and 5.5 are now responsible for a permanent modification of the model parameters with ratcheting history and in particular, the k_n parameters. Consequently, when simulating symmetric load tests (2-way loading), the hysteresis loop no longer closes exactly (as opposed to that shown in Figure 4.7(c)). This is illustrated in Figure 5.3. Given the equations chosen for the evolution of the strength and ratcheting rate, it is expected that the largest modification of the kinematic hardening response due to ratcheting will occur during initial loading. This implies significant changes in k_n and R_n parameters values over the initial loop and therefore explains the differences in loop shape between first and subsequent cycles.

5.2.4.2 Aspects of modelling

As mentioned earlier in Chapter 4, Section 4.4.2, there is a debate on whether to choose linked or independent ratcheting surfaces (i.e. $\forall n \in [1, N_S], \dot{\alpha}_r = S(\sigma) \sum_{n=1}^{N_S} R_n |\dot{\alpha}_n|$ or $\forall n \in [1, N_S], \dot{\alpha}_{r,n} = S(\sigma) R_n \dot{\alpha}_n$ respectively). It was previously indicated that the HARM model with none of the modifications described here, was insensitive to one or the other option. However, with the introduction of Equations 5.3 and 5.5, this is no longer true and the two approaches provide different results. This is a similar phenomenon to modelling isotropic hardening (see Houlsby and Puzrin, 2006). Due to time constraints, this point has not been developed any further and only the linked surface case was considered here.

5.2.4.3 Accelerated formulation

Finally, it is noteworthy that none of the modifications outlined in this section alter the framework described for the accelerated modelling (Chapter 4, Section 4.5, p. 173). Figures 5.4(a)-(d) compare the response obtained using the incremental and accelerated methods, showing that the same response is obtained with both, and emphasising that this also holds true for the prediction of the secant stiffness and hysteresis loop area. Also, the above modifications do not change the framework of the two-dimensional model (Chapter 4, Section 4.6, p. 175).

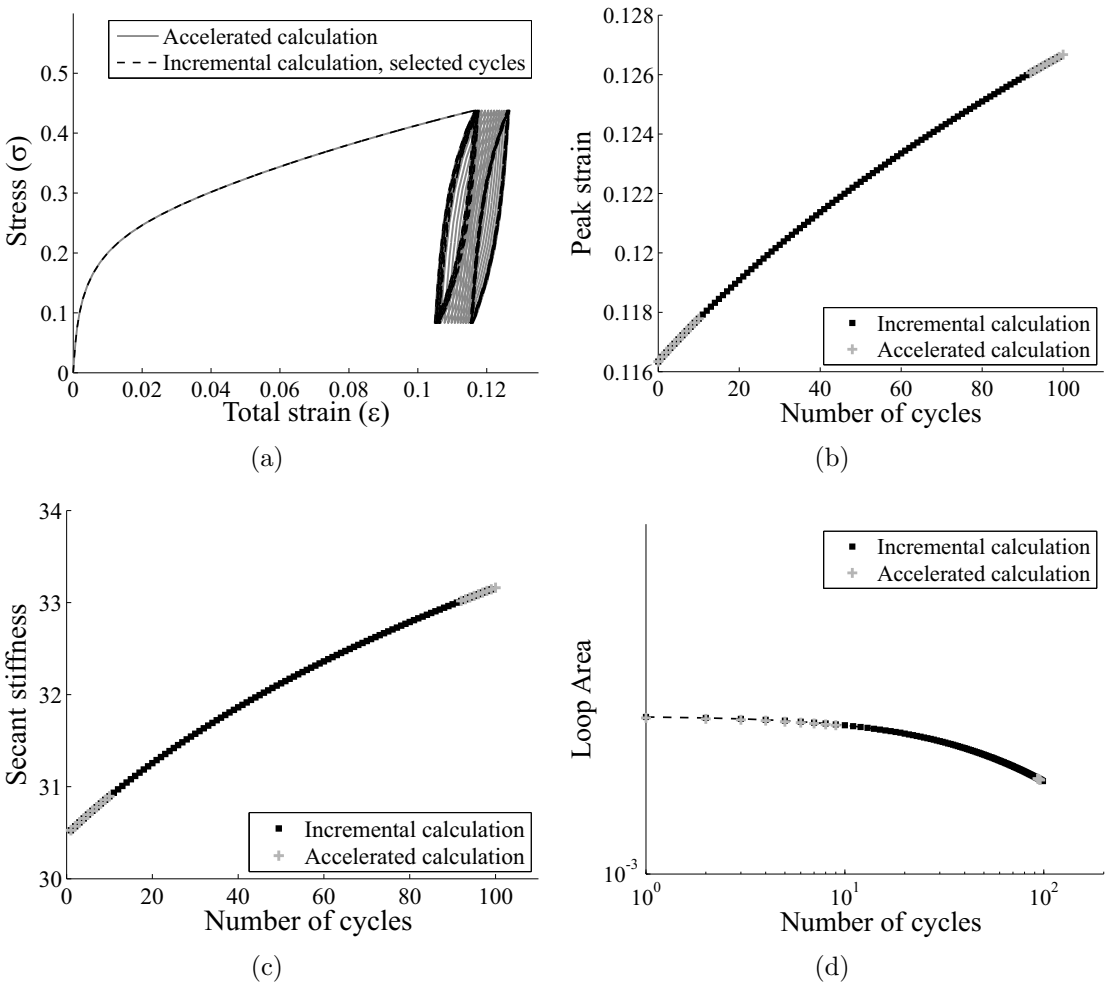

Figure 5.4: Comparison between the standard incremental (black) and the accelerated (gray) solving method for HARM+: (a) stress-strain curve; cycles 1-10 and 90-100 highlighted in black; (b) peak strain at maximum cyclic load(c) secant stiffness and (d) hysteresis loop area

5.3 Calibration

The parameters introduced in the HARM+ model can be classified in three categories: (a) model parameters that describe the backbone curve, (b) model parameters that describe the ratcheting behaviour and (c) modelling parameters. The latter are artificial values that are introduced for numerical purposes, and therefore are unrelated to the underlying model response. The following three sections explain how the model parameters relate to experimental test results and provide a methodology on how to identify each model and modelling parameter. Calibration against experimental results is performed based on one continuous monotonic test (MCo4) and three long-term cyclic loading tests (CMLT1,2 and 3) (Table 2.6 and 2.7, p. 65).

5.3.1 Backbone curve

The backbone curve is defined according to the values of the H_n and k_{0n} parameters. For the time being, ratcheting is disabled ($R_0 = 0 \Rightarrow \forall t,\ \mathrm{d}\alpha_r = \mathrm{d}\alpha_h = 0$) and the monotonic test MCo4 (Table 2.6) is used for calibration of the backbone curve. Figure 2.11 (Chapter 2, Section 2.5, p. 73) illustrated that the monotonic test results were well fitted using a power law (Equation 2.15, p. 73). This ignored the initial elastic portion and the ultimate lateral resistance of the pile. In order to address this, Equation 2.15 can be re-arranged to fit the experimental monotonic curve with three sections: an initial elastic portion, a power-law curve and a constant stress cut-off (see Figure 5.5(a)). The expression is also inverted so that the displacement

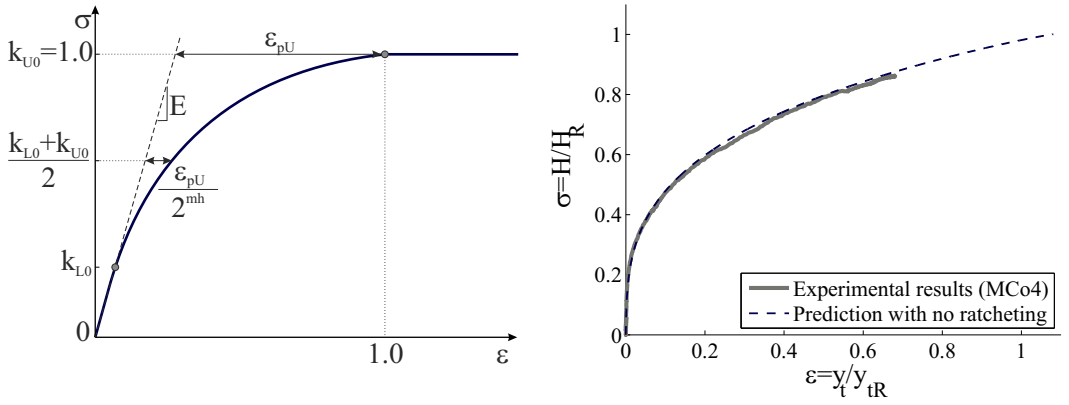

Figure 5.5: (a) Determination of HARM parameters to fit the normalised backbone curve (b) Comparison of experimental monotonic data with prediction (ratcheting disabled ($R_0 = 0$))

is expressed as a function of the load:

$$\begin{cases} 0 < \sigma < k_{L0}, & \epsilon = \dfrac{\sigma}{E} \\ k_{L0} < \sigma < k_{U0}, & \epsilon = \dfrac{\sigma}{E} + \epsilon_{pU} \left(\dfrac{\sigma - k_{L0}}{k_{U0} - k_{L0}} \right)^{m_h} \\ \sigma = k_{U0}, & \epsilon \in \left[\dfrac{k_{U0}}{E} + \epsilon_{pU}, \infty \right] \end{cases} \tag{5.8}$$

Here, k_{L0} is the stress at which first yield occurs and k_{U0} is the ultimate stress. E is the initial elastic modulus. ϵ_{pU} is the ultimate monotonic plastic strain and m_h the monotonic exponent. They both define the shape of the non-linear section of the loading curve according to Figure 5.5(a).

First, E is determined according to the procedure described in Figure 2.9, Chapter 2, Section 2.5 (p. 70) and is then fixed as constant according to the results of Chapter 3, Section 3.4 (p. 121). Then, the strengths of the sliders are uniformly spread from the elastic limit k_{L0}, up to the ultimate strength k_{U0} that is to be modelled. And therefore:

$$k_{0,n} = k_{L0} + (k_{U0} - k_{L0}) \frac{n-1}{N_s - 1} \tag{5.9}$$

The tangent moduli can be expressed as:

$$\begin{cases} n = 1, & \dfrac{1}{E_{t1}} = \dfrac{\epsilon(k_{0,2}) - \epsilon(k_{L0})}{k_{0,2} - k_{L0}} \\ 1 < n < N_S, & \dfrac{1}{E_{tn}} = \dfrac{\epsilon(k_{0,n+1}) - \epsilon(k_{0,n})}{k_{0,n+1} - k_{0,n}} \\ n = N_S, & E_{tN_S} = 0 \end{cases} \tag{5.10}$$

Considering Equation 4.23 (Chapter 4, Section 4.4), it follows that:

$$\begin{cases} n = 1, & \dfrac{1}{E_{t1}} = \dfrac{1}{E} + \dfrac{1}{H_1} \\ n \in [2, N_S - 1], & \dfrac{1}{E_{tn}} = \dfrac{1}{E_{tn-1}} + \dfrac{1}{H_n} \\ n = N_S, & E_{tN_S} = 0 \end{cases} \tag{5.11}$$

And therefore:

$$\begin{cases} n = 1, & \dfrac{1}{H_1} = (N_S - 1)^{1-m_h} \cdot \left(\dfrac{\epsilon_{pU}}{k_{U0} - k_{L0}} \right) \\ n \in [2, N_S - 1], & \dfrac{1}{H_n} = \left(\dfrac{\epsilon(k_{0,n+1}) - \epsilon(k_{0,n})}{k_{0,n+1} - k_{0,n}} \right) - \left(\dfrac{\epsilon(k_{0,n}) - \epsilon(k_{0,n-1})}{k_{0,n} - k_{0,n-1}} \right) \\ & \qquad = \dfrac{N_S - 1}{k_{U0} - k_{L0}} \cdot (\epsilon(k_{0,n+1}) - 2\epsilon(k_{0,n}) + \epsilon(k_{0,n-1})) \\ n = N_S, & H_{N_S} = 0 \end{cases} \tag{5.12}$$

Finally, using Equation 5.8, it can be shown that:

$$\begin{cases} H_1 = \dfrac{k_{U0} - k_{L0}}{\epsilon_{pU}} \cdot (N - 1)^{(m_h - 1)} \\ H_n = \dfrac{H_1}{n^{m_h} - 2(n-1)^{m_h} + (n-2)^{m_h}}, \quad n \in [2, N_S - 1] \\ H_{N_s} = 0 \end{cases} \tag{5.13}$$

On this basis, the backbone curve is defined by **5 model parameters**: E, k_{L0}, k_{U0}, ϵ_{pU} and m_h. These can be estimated based on experimental data and Equation 5.8 using a least-squares curve fitting. In the case where no purely elastic region is observed, then $k_{L0} = 0$. Also, the value of m_h can be determined from the intercept at $(k_{L0} + k_{U0})/2$, when the plastic strain is $\epsilon_{pU}/2^{m_h}$ (see Figure 5.5(a)).

The application of the method described above to the laboratory pile test MCo4 provides the following values of the parameters:

i- $E = 85$. Note that this constant is now dimensionless as both σ and ϵ have been normalised (Equations 5.1 and 5.2).

ii- $k_{L0} = 0$ and $k_{U0} = 1$. The lower bound was not taken equal to the elastic limit estimated in Chapter 2, Section 2.5 (Figure 2.9) because this limit varies from one cyclic test to the other. This is due to larger experimental errors at small displacement. The upper bound was taken equal to the ultimate capacity.

iii- Both ϵ_{pU} and m_h have been fitted to experimental data using Equation 5.8, resulting in $\epsilon_{pU} = 1.07$ and $m_h = 3.2 = 1/0.31$.

Note that in theory, $\epsilon_{pU} \leq 1$ (see Figure 5.5(a)). However, the range of the LVDTs used for test MCo4 did not allow the measurement of the backbone curve up to the ultimate capacity and therefore, the curve had to be extrapolated to k_{U0}. This results in small errors that explain why, when fitting and with the value selected for y_{tR}, the value of ϵ_{pU} obtained for this application is slightly greater than 1.

The prediction of the backbone curve using the above values with ratcheting effects disabled is displayed in Figure 5.5(b) and compared with experimental data, showing a good correlation. However, when adding ratcheting, this prediction is slightly modified due to the accumulation of ratcheting strain on loading. Nevertheless, the modifications due to ratcheting on initial loading should be sufficiently small for it not to distort the backbone curve displayed in Figure 5.5(b) significantly (see later Figures 5.14(a)-(c), p. 210 for example).

5.3.2 Ratcheting behaviour

The effect of the ratcheting behaviour is achieved using Equations 5.3 and 5.5 (Section 5.1, p. 182). Accordingly, there are **5 model parameters** yet undetermined:

- The initial rate of ratcheting R_0 (Equation 5.5)
- The initial value of hardening parameter α_{h0} (Equations 5.3 and 5.5)
- The exponent m_k that defines the rate of change in hysteresis loop shape with hardening parameter (Equation 5.3)
- The exponent m_r that defines the rate of change of ratcheting parameter (Equation 5.5)
- The exponent m_s that defines the effect of stress on ratcheting (Equation 5.5)

The following paragraphs describe a procedure to determine each parameter. The application to the laboratory pile case uses tests CMLT1,2,3 (Table 2.7, p. 66).

5.3.2.1 Preliminary remarks

Notations and definitions

In the following work, special attention must be paid to notation and definitions of strain quantities. Figure 5.6 displays the conventions used in the paragraphs below, that correspond to the notation previously applied in Chapters 2 and 3 (Figure 2.7(a), p. 63). In particular, the initial load-unload loop is indexed "0" to indicate that this cycle actually corresponds to the backbone curve. Subsripts "p" and "m" are used to indicate **p**eak and **m**inimum cyclic points respectively. Finally, the schematic also provides a definition of the ratcheting strain at initial peak load with regard to the initial hardening parameter α_{h0}.

It is obvious from Equations 5.3 and 5.5 that the accumulated ratcheting strain α_h and increment of ratcheting strain $\mathrm{d}\alpha_h$ are critical variables here. According to

Figure 5.6, these relate to the following experimental quantities at peak load:

$$\alpha_{hpN} - \alpha_{hp0} = \epsilon_{pN} - \epsilon_{p0} \tag{5.14}$$

$$d\alpha_{hpN} = \alpha_{hpN} - \alpha_{hpN-1} = \epsilon_{pN} - \epsilon_{pN-1} \tag{5.15}$$

Also, it is important not to confuse the number of cycles, which is denoted N, with the model number of surfaces, denoted N_S and indexed n.

Working hypotheses

In the following, a series of working hypotheses are used and allow the problem to be simplified. These are listed below.

Working hypothesis #1 - As the origin of α_h, and therefore the value of α_{hp0} (Figure 5.6), is *a-priori* unknown, it is impossible to calculate directly the quantity α_{hpN} from experimental results. However, supposing that, for large cycle number, $\alpha_{hp0} \ll \alpha_{hpN}$, it can be shown that:

$$\alpha_{hpN} \approx \epsilon_{pN} - \epsilon_{p0} \tag{5.16}$$

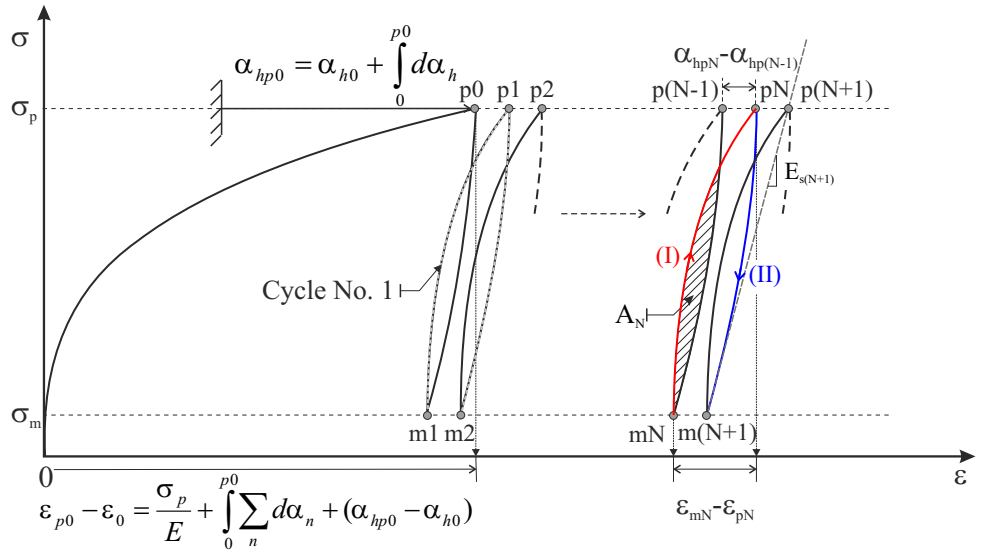

Figure 5.6: Schematic of notations for calibration of the HARM+ model and illustration of hardening parameter

For many of the following applications, a plot of $log(\alpha_{hpN})$ as a function of some logarithmic quantity is necessary to calculate the values of exponents. As a first approximation, it is assumed that $log(\alpha_{hpN}) \approx log(\alpha_{hpN} - \alpha_{hp0})$ for large cycle number and therefore, that the logarithmic increase in ratcheting strain can directly be deduced from experimental data according to $log(\alpha_{hpN}) \approx log(\epsilon_{pN} - \epsilon_{p0})$. This assumption is used in all figures where the experimental quantity $log(\alpha_{hpN})$ is displayed. This hypothesis must be validated at the end of the calibration process by checking that α_{hp0} is small compared with the accumulated displacement for large cycle number.

Working hypothesis #2 - Most of the demonstrations proposed below are developed under the assumption that for large cycle numbers the change of the hardening parameter α_h is small during any one unload-reload loop. This implies that the change in ratcheting strain and behaviour during the loop itself can be discarded as a first approximation. This means that the k_n and α_h can be considered constants during one loop, and this greatly facilitates integrations over the unload-reload loop.

Working hypothesis #3 - The tests used for calibration in the following analysis are all one-way loading tests, and therefore, $\forall t, \sigma \geq 0$. This implies that $\alpha_r = \alpha_h \geq 0$.

Expression of unload-reload curve

According to working hypothesis #2, for large cycle numbers, the change in accumulated ratcheting strain over any single and independent reload-unload loop is negligible compared to the plastic strain. Therefore, the equation of the curve can be approximated using Equation 5.8, updated at cycle N, doubled in both dimensions for both unloading and reloading (Masing rule). With $k_{L0} = 0$ the expression of the loading curve (I) (Figure 5.6) then becomes:

$$\frac{\epsilon_N^{(I)} - \epsilon_{mN}}{2} = \frac{\frac{\sigma - \sigma_{mN}}{2}}{E} + \epsilon_{pU} \left(\frac{\frac{\sigma - \sigma_{mN}}{2} - k_{LN}}{k_{UN} - k_{LN}} \right)^{m_h} \tag{5.17}$$

Since $k_{L0} = 0$, then $k_{LN} = 0$. According to Equation 5.3, $k_{UN} = k_{U0}\left(\frac{\alpha_{hN}}{\alpha_{h0}}\right)^{m_k}$. Therefore, Equation 5.17 simplifies into:

$$\epsilon_N^{(I)} = \epsilon_{mN} + \frac{\sigma}{E} - \frac{\sigma_{mN}}{E} + 2\epsilon_{pU}\left(\frac{\sigma - \sigma_{mN}}{2k_{U0}}\right)^{m_h}\left(\frac{\alpha_{hN}}{\alpha_{h0}}\right)^{-m_k m_h} \tag{5.18}$$

Under working hypothesis #2, α_{hN} can be considered constant, and therefore, on differentiation it follows that:

$$\mathrm{d}\epsilon_N^{(I)} = \frac{\mathrm{d}\sigma}{E} + \frac{m_h \epsilon_{pU}}{k_{U0}}\left(\frac{\alpha_{hN}}{\alpha_{h0}}\right)^{-m_k m_h}\left(\frac{\sigma - \sigma_{mN}}{2k_{U0}}\right)^{m_h - 1}\mathrm{d}\sigma \tag{5.19}$$

The second term of this equation is the increment of plastic strain on reloading (I) $\int_{\sigma_{mN}}^{\sigma_{pN}}\left(\sum_{n=1}^{N_S}\mathrm{d}\alpha_n\right)\mathrm{d}\sigma$. Similarly, on unloading (II) the increment of strain is:

$$\epsilon_N^{(II)} = \epsilon_{pN} + \frac{\sigma}{E} - \frac{\sigma_{pN}}{E} + 2\epsilon_{pU}\left(\frac{\sigma_{pN} - \sigma}{2k_{U0}}\right)^{m_h}\left(\frac{\alpha_{hN}}{\alpha_{h0}}\right)^{-m_k m_h} \tag{5.20}$$

$$\mathrm{d}\epsilon_N^{(II)} = \frac{\mathrm{d}\sigma}{E} + \frac{m_h \epsilon_{pU}}{k_{U0}}\left(\frac{\alpha_{hN}}{\alpha_{h0}}\right)^{-m_k m_h}\left(\frac{\sigma_{pN} - \sigma}{2k_{U0}}\right)^{m_h - 1}\mathrm{d}\sigma \tag{5.21}$$

5.3.2.2 Hysteresis loop closing with ratcheting parameter (m_k)

Demonstration 1

Firstly, the hysteresis loop area during any one loop, providing that the change in accumulated ratcheting strain α_h is small, can be approximated by the formula:

$$A_N = 4k_{U0}\epsilon_{pU}\frac{m_h - 1}{m_h + 1}\left(\frac{\alpha_{hN}}{\alpha_{h0}}\right)^{-m_k m_h}\left(\frac{\sigma_p - \sigma_m}{2k_{U0}}\right)^{m_h + 1} \tag{5.22}$$

According to this Equation, the slope of $log\,(A)$ vs. $log\,(\alpha_h)$ will be $-m_A = -m_k m_h$. Knowing m_h, it is then straightforward to deduce m_k.

The results of the evolution of the loop area with accumulated ratcheting strain as defined in Equation 5.16 for tests CMLT1,2 and 3 have been plotted in Figure

5.7(a). The graph shows that the experimental data are well fitted using a power coefficient of $-m_A = -0.5$. Using the value of $m_h = 3.2$ obtained in Section 5.3.1, it follows that $m_k = 0.15$.

Demonstration 2

An alternative approach is to consider the expression of the secant flexibility between extrema of the hysteresis loop. Equations 5.18 and 5.21 give:

$$\frac{1}{E_{S0}} = \frac{\epsilon_{pN} - \epsilon_{mN}}{\sigma_p - \sigma_m} = \frac{1}{E} + \frac{\epsilon_{pU}}{k_{U0}} \left(\frac{\alpha_{hN}}{\alpha_{h0}}\right)^{-m_h m_k} \left(\frac{\sigma_p - \sigma_m}{2k_{U0}}\right)^{m_h - 1} \tag{5.23}$$

According to the above expression, the slope of $log(\frac{1}{E_{S0}} - \frac{1}{E})$ vs. $log(\alpha_h)$ is also $-m_h m_k$ allowing an alternative way for determining m_k. The application of this to experimental results is shown in Figure 5.7(b). The graph confirms the value of $m_k = 0.15$ obtained above. This also demonstrates the relationship between the secant stiffness and the hysteresis loop area mentioned previously in Chapter 3, Section 3.3.4, Figure 3.17(d) (p. 118). Note that, compared with Chapter 3, the secant stiffness is here noted E_s instead of k because the notation "k" is reserved to the slider strengths of the model.

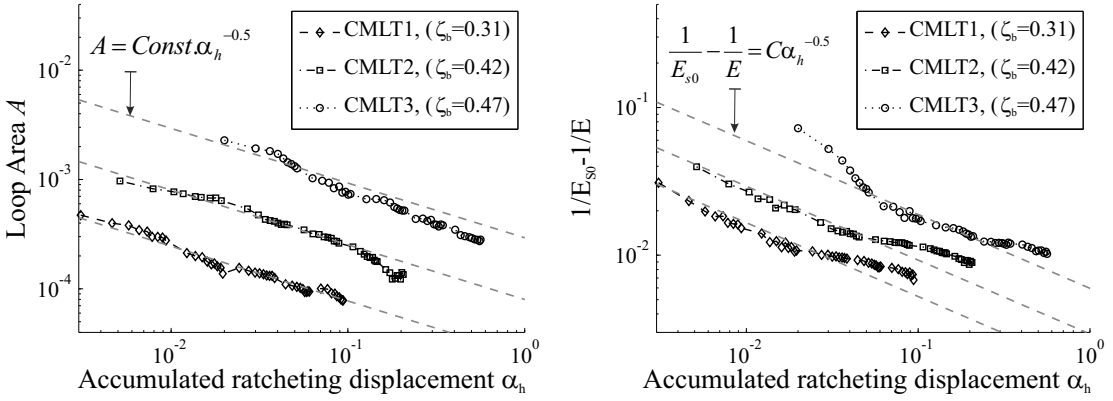

(a) (b)

Figure 5.7: Evolution of (a) the hysteresis loop area and (b) relative secant flexibility $\frac{1}{E_s} - \frac{1}{E}$ as a function of the accumulated ratcheting displacement for tests CMLT1,2 and 3. Data fitted using a power-law with power coefficient equal to -0.5 (dotted lines) on both graphs

5.3.2.3 Initial hardening parameter (α_{h0})

α_{h0} is a conceptual artefact introduced to ensure the existence of the k_n and the R_n parameters when α_h tends to its initial value (Equations 5.3 and 5.4). Consequently, this parameter is difficult to calculate directly from experimental results. However, considering Equation 5.18 at peak load, it can be shown that:

$$(\epsilon_{pN} - \epsilon_{mN}) - \left(\frac{\sigma_{pN} - \sigma_{mN}}{E}\right) = 2\epsilon_{pU} \left(\frac{\sigma_{pN} - \sigma_{mN}}{2k_{U0}}\right)^{m_h} \left(\frac{\alpha_{hpN}}{\alpha_{h0}}\right)^{-m_k m_h} \tag{5.24}$$

According to Chapter 3, Section 3.3 (p. 101), the accumulated rotation increases with cycle number according to a power law. Obviously, this is also the case of the accumulated ratcheting displacement and therefore, for α_h as defined by Equations 5.2 and 5.16. This is illustrated in Figure 5.8(a) and therefore:

$$\alpha_{hN} = T_{bc} N^{m_\alpha} \tag{5.25}$$

where $m_\alpha = 0.31$. Substituting Equation 5.25 into Equation 5.24 gives:

$$\begin{aligned} \delta_{PlasN} = \frac{\alpha_{hpN}}{\alpha_{h0}} \left(\frac{\sigma_{pN} - \sigma_{mN}}{2k_{U0}}\right)^{-\frac{1}{m_k}} &= \left[\frac{1}{2\epsilon_{pU}} \left((\epsilon_{pN} - \epsilon_{mN})\right.\right. \\ \left.\left. - \left(\frac{\sigma_{pN} - \sigma_{mN}}{E}\right)\right)\right]^{\frac{-1}{m_k m_h}} &= \left(\frac{\sigma_{pN} - \sigma_{mN}}{2k_{U0}}\right)^{-\frac{1}{m_k}} \left(\frac{T_{bc} N^{m_\alpha}}{\alpha_{h0}}\right) \end{aligned} \tag{5.26}$$

According to Equation 5.26, the slope of δ_{PlasN} vs. N^{m_α} allows the determination of α_{h0}. The relevant values that lead to the value of α_{h0} for tests CMLT1,2 and 3 are displayed in Figure 5.8(b) and Table 5.26 and give $\alpha_{h0} \sim 0.02$.

Table 5.1: Relevant parameter values for determination of α_{h0}

Test No.	CMLT1	CMLT2	CMLT3
T_{bc}	0.0046	0.0106	0.0250
$a/\ \delta_{PlasN} = a.N^{m_\alpha}$	1.1E5	4.0E4	1.8E4
α_{h0}	0.022	0.020	0.029

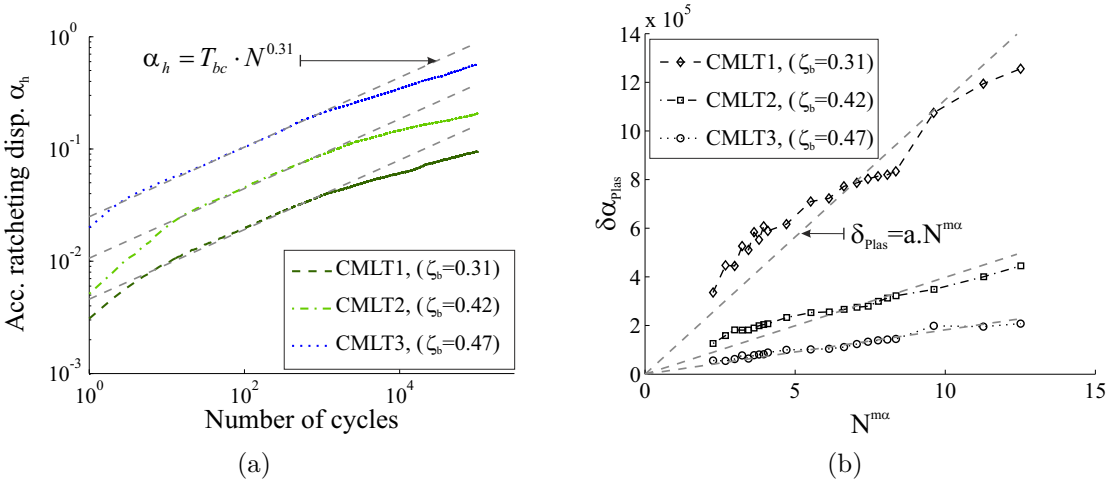

(a) (b)

Figure 5.8: (a) Evolution of accumulated ratcheting displacement as a function of the number of cycles. Data fitted according to a power-law with power coefficient of 0.31 (dotted lines) as suggested by LeBlanc *et al.* (2010a) (b) Evolution of δ_{Plas} with N^{m_α} for determination of α_{h0} (Equation 5.26)

Finally, according to working hypothesis #2, there should be $\alpha_{h0} \ll \epsilon_{pN} - \epsilon_{p0}$. Figure 5.8(a) shows that this is an acceptable assumption for test CMLT3 but not quite for tests CMLT1 and 2. For more accuracy, the ratcheting parameter calculation procedure should be reiterated taking into account the first estimate of α_{h0}, $\alpha_h = \epsilon_{pN} - \epsilon_{p0} + \alpha_{h0,current}$, $\alpha_{h0,current} = 0.02$ and iterated until the change of α_{h0} is negligible, compared with experimental accumulated ratcheting displacement. For the particular application presented here, this has not been judged useful, as the predictions obtained with the first set of parameters were satisfactory.

5.3.2.4 Dependence of rate of ratcheting on hardening parameter (m_r)

The determination of parameters m_r, m_s and R_0 is derived from the increase in ratcheting strain over a cycle $\delta\alpha_h/\delta N = \delta\alpha_r/\delta N$, where $\delta N = 1$. This corresponds to:

$$\frac{\delta\alpha_h}{\delta N} = \int_{\sigma_{mN}}^{\sigma_{pN}} \left(\sum_{n=1}^{N_S} R_n |\mathrm{d}\alpha_n| \right) \mathrm{d}\sigma + \int_{\sigma_{pN}}^{\sigma_{mN+1}} \left(\sum_{n=1}^{N_S} R_n |\mathrm{d}\alpha_n| \right) \mathrm{d}\sigma \tag{5.27}$$

Unfortunately, because the R_n parameters depend on the k_{0n} parameters, and therefore, on n, a satisfactory way of extracting the R_n from the sum and integral has not yet be found, but could be achieved with appropriate simplifications. Solving Equation 5.27 would then require thorough mathematical developments that were not pursued during this thesis. However, discarding the dependence on load amplitude ($m_s = 0$ in Equation 5.5), Equation 5.27 is straightforward to integrate. For the determination of m_r, it is therefore assumed that the dependence on load amplitude is decoupled from the dependence of ratcheting rate on ratcheting strain and $m_s = 0$ for the time being. It can then be shown that:

$$\frac{\delta\alpha_h}{\delta N} = R_0 \left(\frac{\alpha_h}{\alpha_{h0}}\right)^{-m_r} \left(\int_{\sigma_{mN}}^{\sigma_{pN}} \left(\sum_{n=1}^{N_S} |\mathrm{d}\alpha_n| \right) \mathrm{d}\sigma + \int_{\sigma_{pN}}^{\sigma_{mN+1}} \left(\sum_{n=1}^{N_S} |\mathrm{d}\alpha_n| \right) \mathrm{d}\sigma \right) \tag{5.28}$$

Using Equations 5.19 and 5.21, this becomes:

$$\begin{aligned} \frac{\delta\alpha_{hN}}{\delta N} = \quad & R_0 \frac{m_h \epsilon_{pU}}{k_{U0}} \left(\frac{\alpha_{hN}}{\alpha_{h0}}\right)^{-(m_r + m_k m_h)} \int_{\sigma_m}^{\sigma_p} \left[\left(\frac{\sigma - \sigma_{mN}}{2k_{U0}} \right)^{m_h - 1} \right. \\ & \left. + \left(\frac{\sigma_{pN} - \sigma}{2k_{U0}} \right)^{m_h - 1} \right] \mathrm{d}\sigma \end{aligned} \tag{5.29}$$

Noting $M_r = m_r + m_k m_h$, on integration over cycle number (minimum and peak loads do not vary), this yields:

$$\left(\frac{\alpha_{hN}}{\alpha_{h0}}\right)^{M_r+1} = \left(\frac{\alpha_{hp0}}{\alpha_{h0}}\right)^{M_r+1} + \frac{m_h (M_r + 1) R_0 \epsilon_{pU}}{\alpha_{h0}} N \mathscr{F}(\dots) \tag{5.30}$$

where the dimensionless function $\mathscr{F}$ is defined according to:

$$\begin{aligned} \mathscr{F}\left(\frac{\sigma_{mN}}{k_{U0}}, \frac{\sigma_{pN}}{k_{U0}}, m_h, m_s\right) = \quad & \frac{1}{k_{U0}} \int_{\sigma_{mN}}^{\sigma_{pN}} \left[\left(\frac{\sigma - \sigma_{mN}}{2k_{U0}} \right)^{m_h - 1} \right. \\ & \left. + \left(\frac{\sigma_{pN} - \sigma}{2k_{U0}} \right)^{m_h - 1} \right] \mathrm{d}\sigma \end{aligned} \tag{5.31}$$

For large cycle number the term $\left(\frac{\alpha_{hp0}}{\alpha_{h0}}\right)^{M_r+1}$ becomes negligible compared with the second term and therefore, the slope of $log\,(\alpha_h)$ vs. $log(N)$ is $m_\alpha = 1/(M_r + 1)$,

allowing the determination of m_r. Figure 5.8(a) then gives $m_r = 1.73$. The above development might need to be revisited in future with rigorous integration of Equation 5.27. However, for the time being, it provides a reasonable estimation for m_r.

5.3.2.5 Undetermined parameters

According to the above work, m_k and α_{h0} have been identified rigorously, m_r is determined under the condition that it can be decoupled from m_s and so far, m_s and R_0 remain unidentified. The key for the determination of both parameters lies in solving Equation 5.27.

The chosen approach consists of testing increasing values of m_s for which R_0 is optimised to match the ratcheting rate while satisfying condition 5.7. Note that for $m_s = 0$, an analytical expression for R_0 can be derived from Equation 5.30. For each value of m_s, a series of continuous cyclic loading cases at different load amplitude are considered and the ratio of ratcheting strain between tests and predictions are compared. Unfortunately, for values of $m_s \geq 2$, the initial rate of ratcheting R_0 was capped at a value that did not allow the calculation of the appropriate ratcheting rate. Consequently, the analysis was stopped at $m_s = 2$ and the results are provided in Figure 5.9. It is expected that further investigation will allow the identification of more appropriate values for both m_s and R_0. For the time being, $m_s = 2$ has been

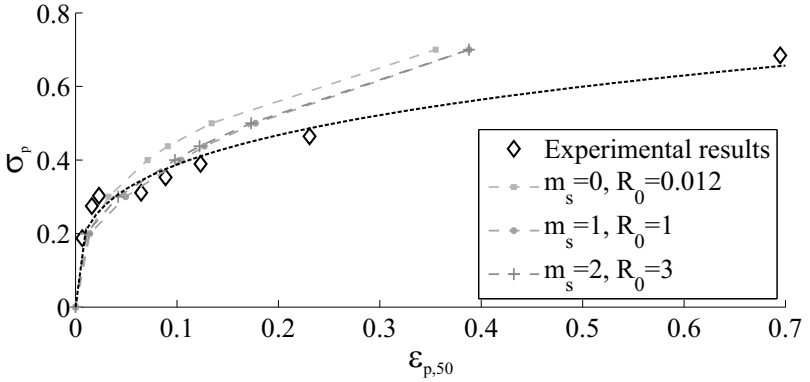

Figure 5.9: Evolution of peak load vs. peak strain at cycle number 50 for experimental test results CMLT1,2,3 and CC1,3,4,5,7 and predictions using $(m_s = 0, R_0 = 0.012)$, $(m_s = 1, R_0 = 1)$ and $(m_s = 2, R_0 = 3)$

selected for analysis and $R_0 = 3$ was found to match the ratcheting rate sufficiently while satisfying $k_n/R_n > \sigma$ at all time.

5.3.3 Modelling parameters

As mentioned in Chapter 4, the viscosity is calibrated as a small value, so that results approach rate-independent behaviour within a suitable tolerance. In addition, μ is also bounded by a lower value that ensures the stability of the numerical calculation with regards to the time step value. The ratio between the time step multiplied by the highest value of the stiffness in the problem, divided by the viscosity $\left(\frac{\mathrm{d}t \cdot max(E_t)}{\mu}\right)$ must be greater than a critical value, below which the calculation becomes unstable. This value is directly related to the number of surfaces selected for simulation, and therefore, the smaller this number, the bigger the range of possibilities for both μ and $\mathrm{d}t$. Ideally, in order to save computational time, $\mathrm{d}t$ has to be the smallest value for which there is a tolerable value of μ that enables capture of rate-dependent behaviour.

Consequently, there are **4 modelling parameters**: the "viscosity" μ, the time step $\mathrm{d}t$, the number of kinematic surfaces N_S and the cyclic load frequency f_r. For each set of model parameters, a parametric study is conducted in order to select appropriate values and ensure that they have no effect on the underlying model response.

Figures 5.10(a) - 205 display the results of the parametric study based on the displacement at peak load and stiffness at cycle number 5, obtained for a perfectly one-way cyclic load characterised by $\sigma_{max} = 0.7; \sigma_{min} = 0.0$. All these figures exhibit a plateau where the response is stable against each parameter and the selected value, located on the plateau, is highlighted with a red arrow. Figures 5.10(c) and 5.10(d) show that $N_S = 40$ was selected. With this number of surfaces, it was found that $\left(\frac{\mathrm{d}t \cdot max(E_t)}{\mu}\right) = \frac{\mathrm{d}t \cdot E}{\mu}$ had to be greater than 19.4, below which the calculations become unstable (see Figures 5.10(a), 5.10(b)). Graphs 5.10(a) and 5.10(b) then

show that $\mu = 0.5$ and $\mathrm{d}t = 2 \times 10^{-4}$ is the smallest combination possible before the model response is altered by viscosity effects.

The frequency would ideally be fixed to the same loading frequency as in the laboratory, i.e. $f_r = 0.1$. Figures 5.10(e) and 5.10(f) show that, with the set of parameters chosen, this value does not affect the numerical response.

Finally, it is noteworthy that the parametrisation might slightly differ depending on whether the incremental or accelerated approach is used and it is strongly advised to retake this short study when switching to the accelerated model. In this particular case, the same set was found to be suitable.

In conclusion, according to the above three sections, the HARM+ model involves **10 model** and **4 modelling** parameters in total. A list of the parameters together with the values selected for this application is provided at the end of this Chapter in Table 5.2 (p. 215).

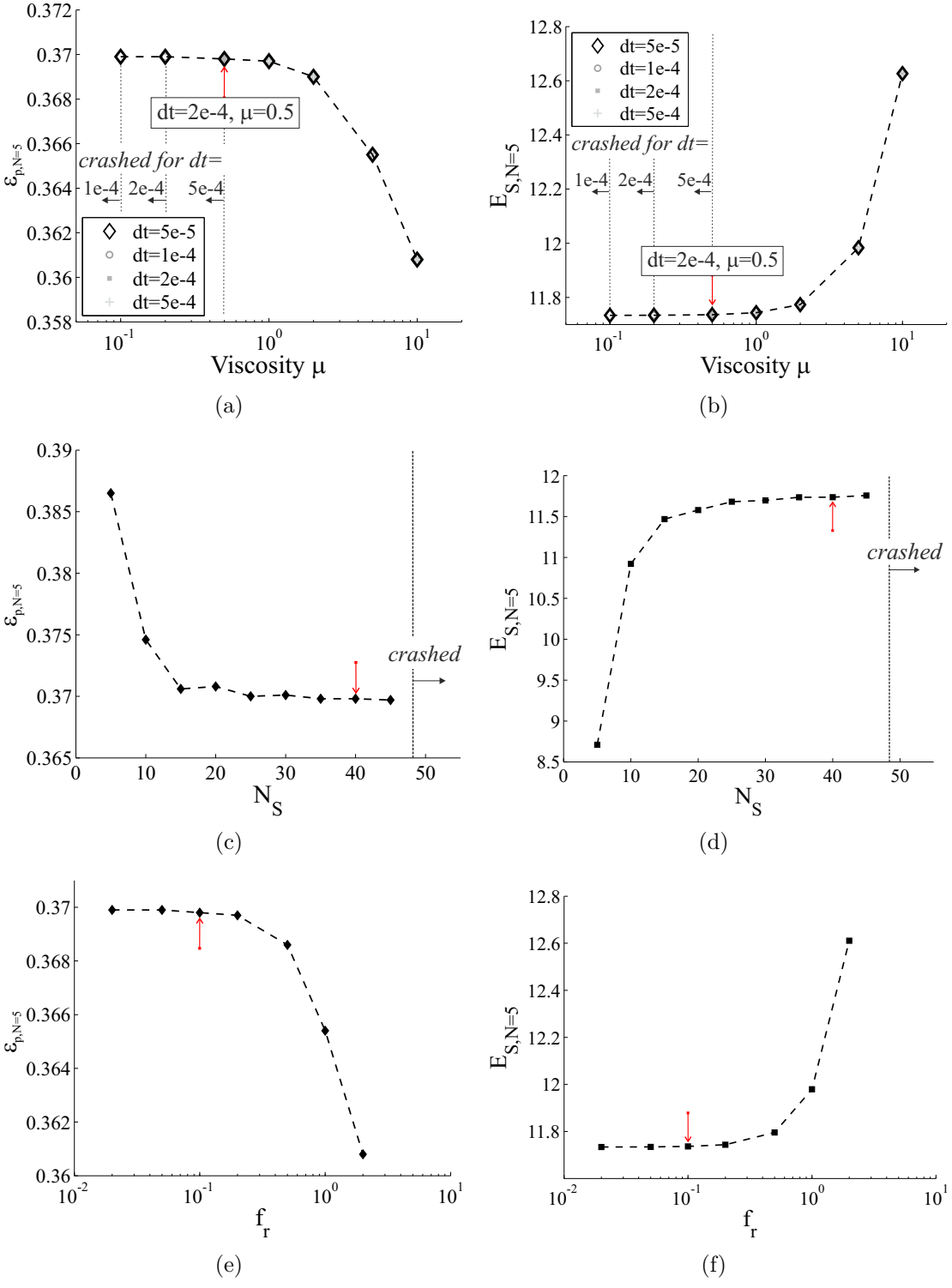

Figure 5.10: Parametrisation of (a), (b) the viscosity and time step, (c), (d) the number of kinematic surfaces and (e), (f) the loading frequency

5.4 Prediction of experimental results

5.4.1 Continuous cyclic loading

In this final section, the calibrated model described above is used for simulating key cyclic test results from Chapter 3. This first subsection starts by presenting the results obtained for the three continuous cyclic tests used for calibration.

The results are presented in Figures 5.11(a)-(b) and 5.12(a)-(f) as pairs of figures where experimental test results are provided on the left hand figure and predictions obtained with the calibrated HARM+ model on the right hand figure. For these simulations, the accelerated form of HARM+ has been used and 100,000 cycles have been simulated. Consequently, the results of the predictions are plotted for selected cycles only according to the programme of Table 4.2 (p. 175).

All four sets of Figures show that, for large cycle number, the predictions capture the experimental trends reasonably well, even though the absolute values of the predictions are not accurately matching the experimental data. However, for the first few cycles, the rates of ratcheting, stiffness and loop area are underestimated compared with experimental observations (Figures 5.12(a)-(f)). This phenomenon

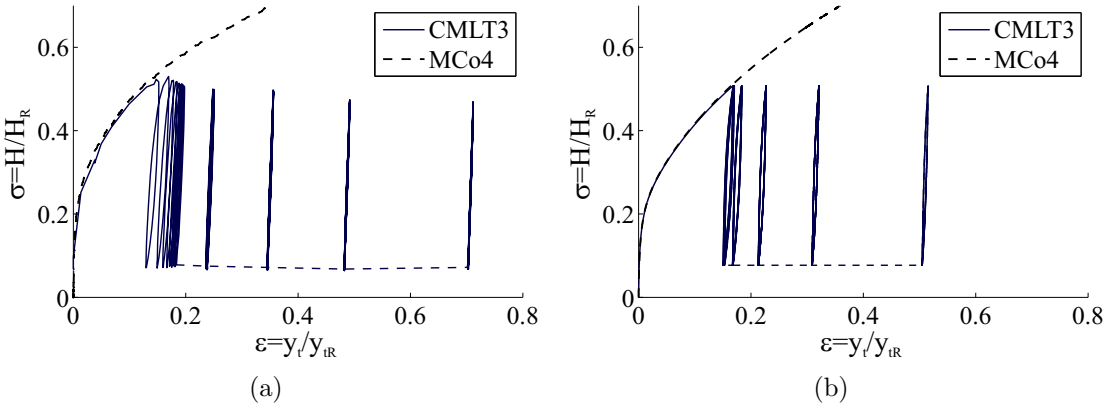

Figure 5.11: Example of comparison between (a) Experimental (b) and predicted load-displacement curves for monotonic test MCo4 and continuous cyclic test CMLT3 at selected cycles (1-10;91-100;991-1000;9991-10000;99991-1000000)

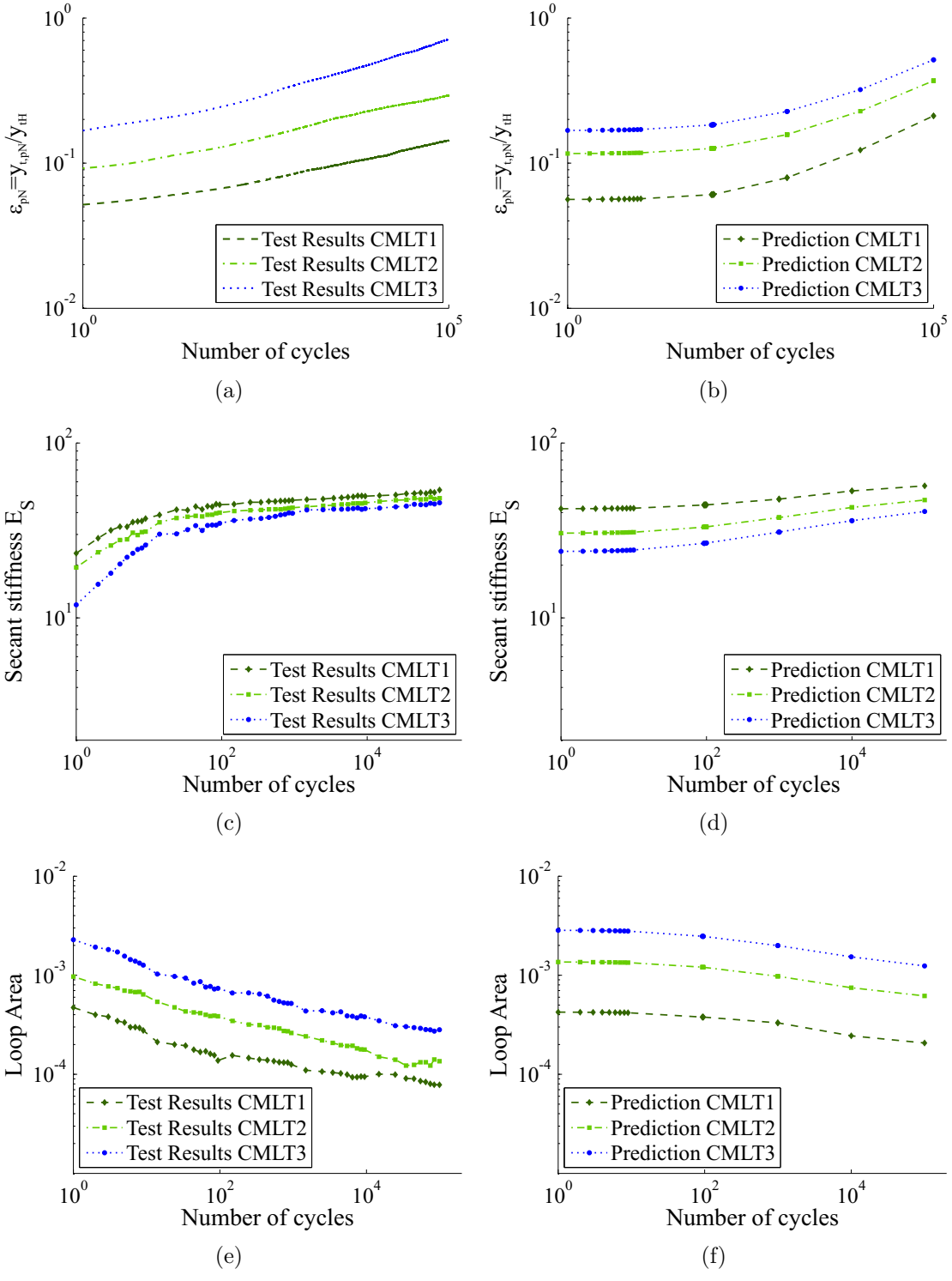

Figure 5.12: Experimental results (left) and Predictions (right) for tests CMLT1,2 and 3: (a), (b) Pile displacement at peak load (c), (d) Secant stiffness (e), (f) Hysteresis loop area

is not surprising given that the calibration has been undertaken under working hypothesis #2 (p. 196), which is only valid for large cycle numbers. Further work will be needed in future to improve both the accommodation framework and calibration to capture better the response at small cycle numbers.

The results displayed in Figures 5.11(a)-(f) give confidence that the model is well adapted for capturing continuous cyclic loading response and that the calibration procedure is satisfactory. In the following, this model is used to predict relevant load cases selected from the test series presented in Tables 2.6, 2.7 and 2.8 (p. 65-67). This also verifies that the model captures all the key mechanisms identified in Chapter 3.

5.4.2 Monotonic reloading response

Tests CMC1-5 and CMLT2, followed by a monotonic reload have been simulated in order to reproduce the evolution of the monotonic curves displayed earlier in Figure 3.20(a) (Chapter 3). The results of this simulation together with the experimental results plotted in the $\sigma - \epsilon$ parameter space are displayed in Figures 5.13(a) and 5.13(b). The graphs display similar trends, where a competition between (a) Masing behaviour (b) ratcheting and (c) stiffening of the response is observed.

There is a small discrepancy between both trends with regards to the location of the reloading curves compared with the backbone curve. However, since the reloading portions are close to the backbone curve, this is likely to be due to experimental variations. The position compared with the backbone curve differs from one experimental test to another (compare for example with Figure 3.21(a), Chapter 3, p. 125). Consequently, the author recommends not to draw any conclusions related to the position of the reloading curves and therefore, concerning the softening or hardening of the behaviour. In addition, given the results obtained for the evolution of the secant stiffness and loop area (Figures 5.12(d) and 5.12(f)), it is likely that the hardening process chosen for Equation 5.3 is well adapted for application to model tests. Finally, the predicted and experimental locations of each reloading curve origin

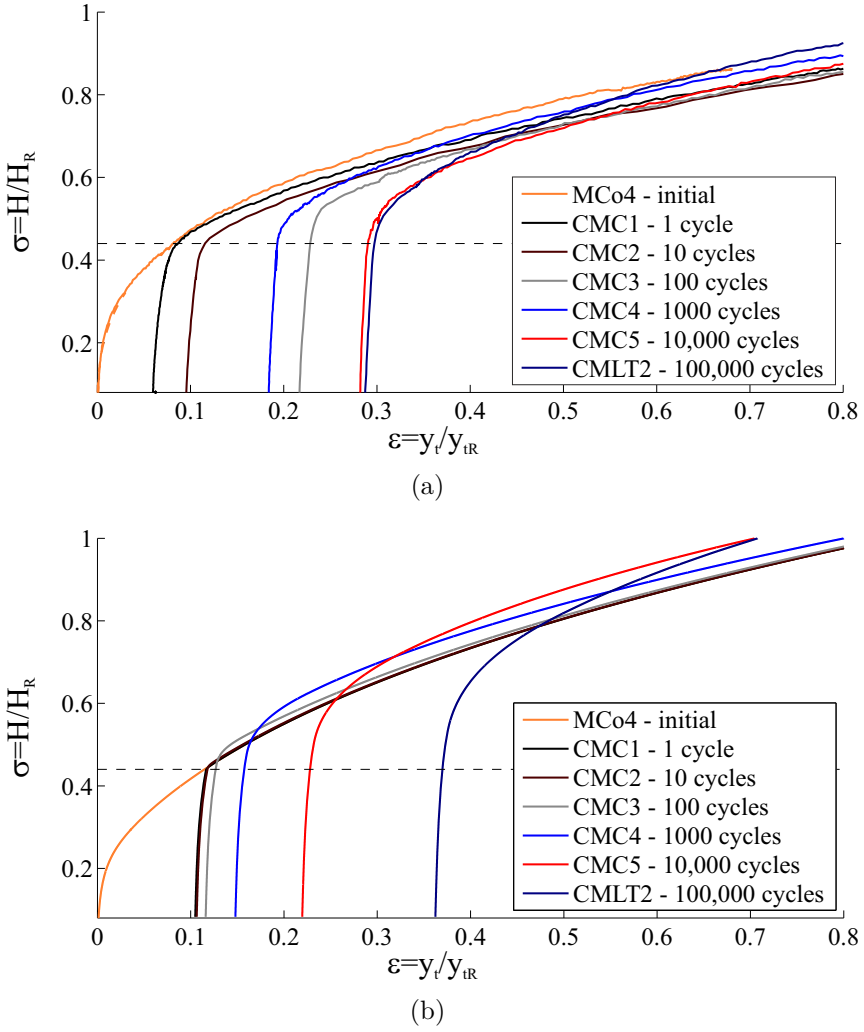

Figure 5.13: (a) Experimental results and (b) Predictions for monotonic tests following continuous cyclic tests CMC1-5 and CMLT2 (N.B.: results relating to 1 and 10 cycles almost super-impose)

differ, which is partly explained by experimental variations and also, means that further work on calibration is needed.

5.4.3 Multi-amplitude cyclic loading

The above framework is now applied to model six of the multi-amplitude cyclic tests: three addressing the effect of large load history (MALL1-3) and three addressing combined large and small load series (MASL1-3). Chapter 3, Section 3.5.3 demonstrated that the linear cumulative method, based on empirical laws for the

accumulation of ratcheting strain, did not accurately predict the evolution of the pile response involving large non-linearities. This was demonstrated based on the test results MALL1-3.

Figures 5.14(a)-(b) and 5.15(a)-(c) display the predictions obtained for tests MALL1-3 compared with experimental results. First, the load-displacement curves 5.14(a)-(b) show that the trends for each tests are correct. First, the response tends to rejoin the backbone curve on reloading, and the response exhibits the competition between Masing behaviour, ratcheting and stiffening discussed earlier. Also, when cyclic load magnitude decreases, the displacement also decreases, in line with the

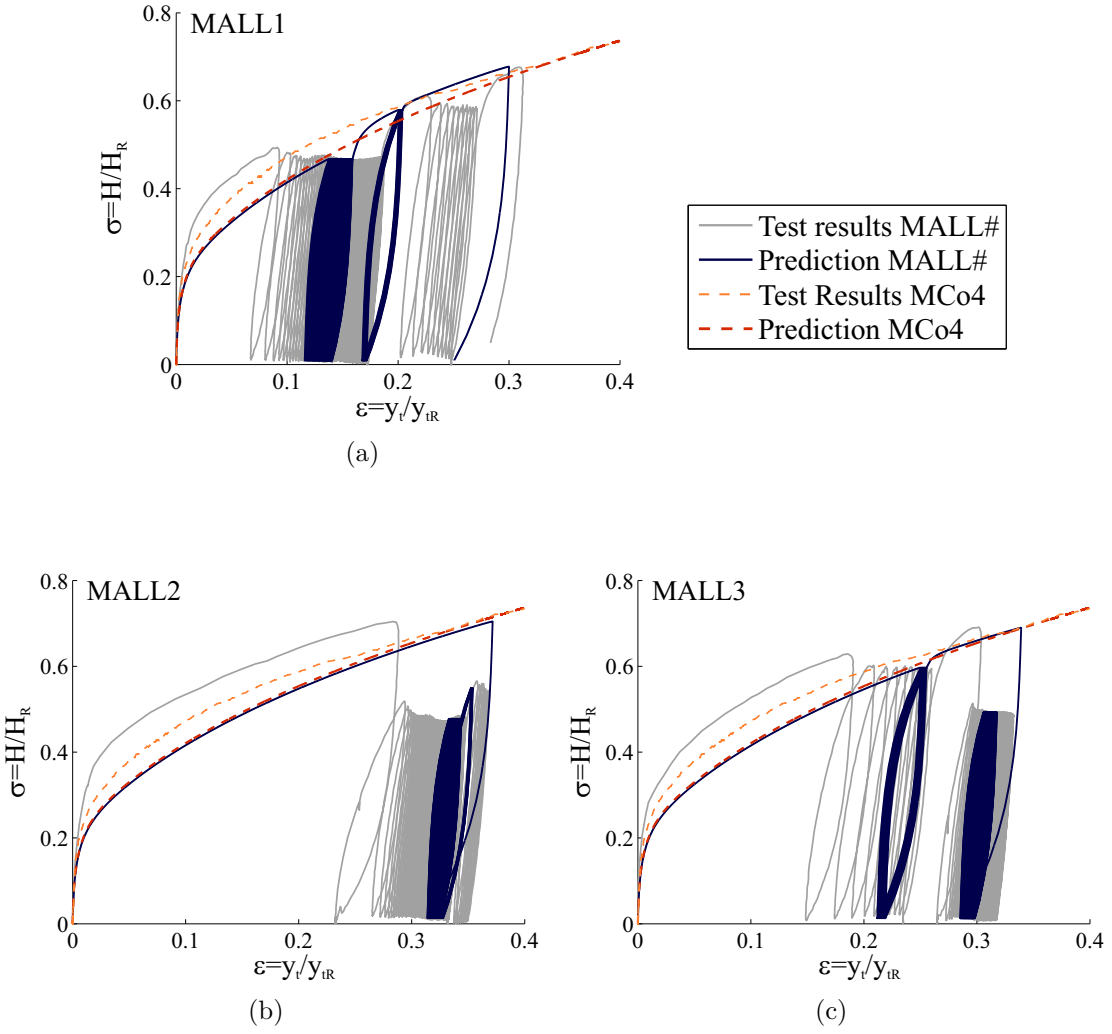

Figure 5.14: Comparison of experimental and predicted load-displacement curves for multi-amplitude cyclcic tests (a) MALL1 (b) MALL2 and (c) MALL3

Masing rule. This aspect is presently missing from the linear cumulative approach and allows the response to be modelled more precisely.

Figure 5.15(a) shows the evolution of the displacement at peak strain with cycle number. The graph shows that the trends and difference in displacement magnitude at load change are well captured. Also, the fact that the load scenario of test MALL2 generates larger deformation than that of MALL3 then MALL1 is captured by the model. This shows that the HARM+ model, and in particular, Equation 5.5, is well adapted for modelling the response to series of loads of variable amplitude.

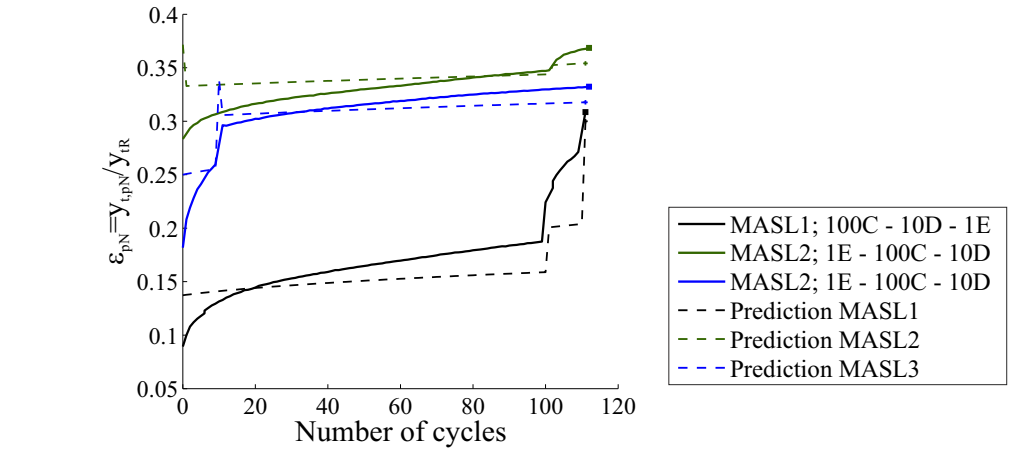

(a)

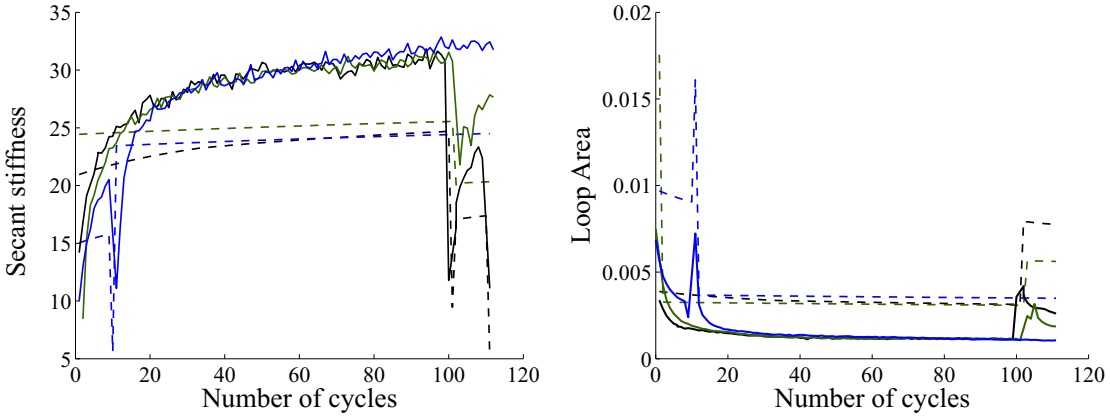

(b) (c)

Figure 5.15: Comparison of experimental and predicted test results (tests MALL1,2,3) evolutions of (a) displacement (b) secant stiffness and (c) hysteresis loop area with cycle number

Finally, one of the advantage of this approach is that it also provides the evolution of the stiffness and loop area fairly accurately (see Figures 5.15(b) and 5.15(c)). This aspect is not addressed by the current design approaches but could be useful for dynamic analyses in future.

The results presented above show that the model is well adapted for predicting the response of the foundation during storm-type events. For completeness, the model was also tested on series of loads where long-term cyclic loading of small amplitude are involved (tests MASL1-3). The predictions for the evolution of the displacement,

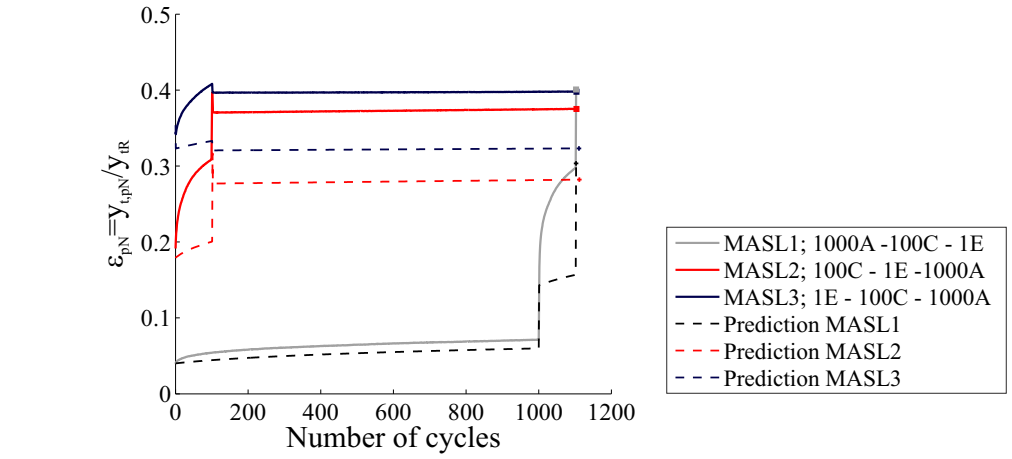

(a)

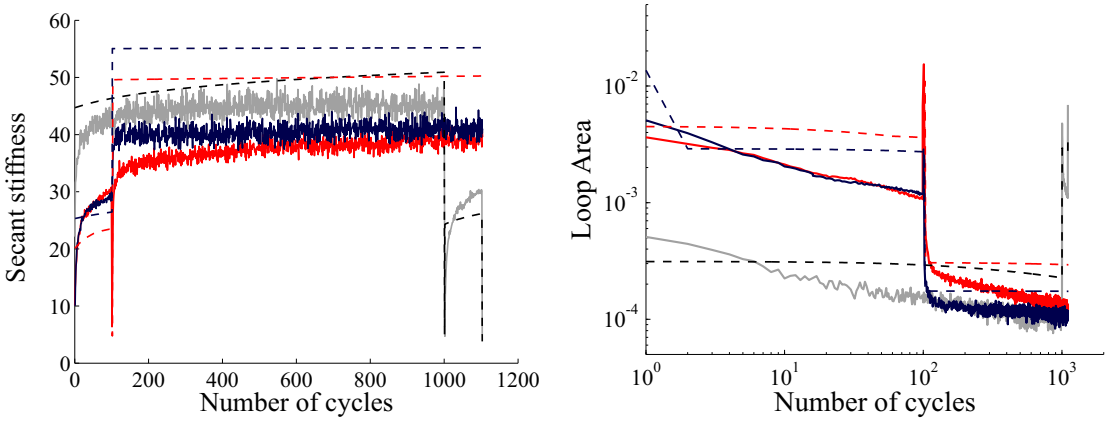

(b) (c)

Figure 5.16: Comparison of experimental and predicted test results (tests MASL1,2,3) evolutions of (a) displacement (b) secant stiffness and (c) hysteresis loop area with cycle number

secant stiffness and hysteresis loop area are displayed in Figures 5.16(a)-(c) and compared with experimental results. The graphs show that the trends for these tests are also well captured.

5.4.4 Hysteresis load

Finally, the model was used to simulate two of the hysteresis tests: Tests H0 and HIM (Table 2.6). The predictions are displayed in Figure 5.17(b) and compared with experimental results (5.17(a)). First, the model captures the hysteresis loop shape observed experimentally. The model prediction also exhibits a decrease in secant stiffness with load magnitude. However, the hysteresis loop does not close up, as seen in the experimental test results. These differences can be explained by both shortcomings in modelling and experimental errors. As underlined earlier in this thesis, performing perfectly symmetric load tests is a challenge and it is recommended to retake some of the 2-way loading tests in future, with more precise loading equipment, in order to capture more detailed aspects of the hysteresis curves, and in particular, whether the loop closes or not.

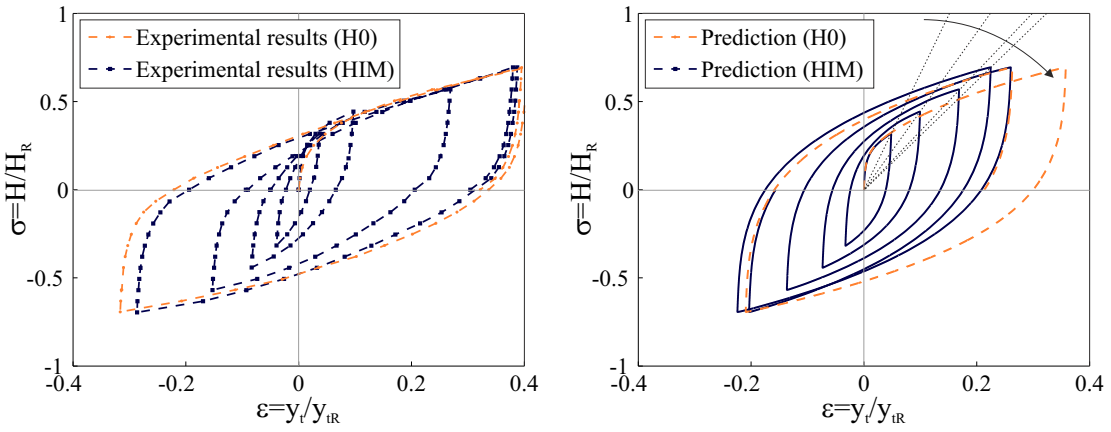

(a) (b)

Figure 5.17: Comparison of (a) experimental and (b) predicted load-displacement curves for hysteresis test HIM

5.5 Concluding comments

5.5.1 Key findings

This section has introduced two key Equations (5.3 and 5.5) that allow the HARM model to predict specific aspects of the ratcheting behaviour. The results show that the model now successfully captures: (i) a decrease of the ratcheting rate with cycle number (ii) a change in hysteresis loop shape with both an increase of the secant stiffness and decrease in loop area and (iii) a dependence of the ratcheting rate on load magnitude; which were the key mechanisms identified experimentally for the response of laterally loaded piles (Chapter 3, Section 3.6.1, p. 139). Consequently, the model accurately predicts the response to series of loads of variable amplitude, and in particular, captures the competition between Masing behaviour, ratcheting and stiffening of the response observed on reloading and exceeding the maximum cyclic load (Chapter 3, Sections 3.4 and 3.5, pp. 121 and 126).

The HARM+ model involves **10 model** and **4 modelling** parameters in total. A methodology for the identification of these parameters has been outlined and illustrated based on three long-term cyclic test results. A list of the parameters together with their meaning, the key Equation numbers for identification and the values for application to laboratory laterally loaded pile are provided in Table 5.2.

Based on this analysis, the calibrated model has then been applied to a short series of continuous cyclic tests, multi-amplitude cyclic tests and hysteresis tests. The results of the prediction capture the experimental trends with good accuracy and demonstrate the appropriateness of the HARM methodology for applications to offshore wind foundations.

Key Equations for accommodation of ratcheting behaviour

$$k_n(\alpha_h, k_{0n}) = k_{0n} \cdot \left(\frac{\alpha_h}{\alpha_{h0}}\right)^{m_k}, \quad n \in [1, N_S]$$

$$R_n(\alpha_h, k_{0n}) = R_0 \cdot \left(\frac{\alpha_h}{\alpha_{h0}}\right)^{-m_r} \cdot \left(\frac{k_{0n}}{k_{U0}}\right)^{m_s}, \quad n \in [1, N_S]$$

Table 5.2: List of HARM+ model and modelling parameters and values for application to laboratory test pile

Symbol	**Definition**	**Equations No.**	**Value**
Model Parameters			
1- Backbone curve (5)			
E	Initial stiffness		$E = 84.9$
k_{U0}, k_{L0}	Lower and upper bounds to the non-linear portion of the backbone curve	5.8, 5.9, 5.13	$k_{L0} = 0$ $k_{U0} = 1$
ϵ_{pU},m_h	Ultimate monotonic plastic strain and monotonic exponent defining the shape of the non-linear section of the loading curve		$\epsilon_{pU} = 1.07$ $m_h = 3.2$
2- Ratcheting behaviour (5)			
α_{h0}	Initial value of hardening parameter	5.26	$\alpha_{h0} = 0.02$
R_0	Initial rate of ratcheting parameter (If $R_0 = 0$ all ratcheting effects are disabled)	5.27	$R_0 = 3$
m_k	Exponent that defines the rate at which the hysteresis loop closes with hardening parameter (If $m_k = 0$ the shape of the hysteresis loop remains unchanged)	5.22	$m_k = 0.15$
m_s	Exponent that defines the dependence of the rate of ratcheting on the stress	5.27	$m_s = 2$
m_r	Exponent that defines the dependence of the rate of ratcheting on the hardening parameter (If $m_r = 0$ and $m_k = 0$ the rate of ratcheting remains constant rather than decreasing with cycle number)	5.27, 5.30	$m_r = 1.73$
Modelling Parameters (4)			
μ	Viscosity		$\mu = 0.5$
dt	Time step		d$t = 2e-4$
N_S	Number of yield surface		$N_S = 40$
fr	Loading frequency		$fr = 0.1$

5.5.2 Limitations

The constitutive model presented above captures the key aspects observed for the macro-behaviour of a small-scale rigid monopile in laboratory conditions subjected to lateral cyclic loading. However, before this is used for applications to full-scale prototypes, some aspects still need to be addressed.

First, further work is required to refine the trends for small cycle number, maybe by considering different equations for the evolution of the k_n and R_n. A more rigorous procedure for the determination of coefficients m_s and R_0 would also be useful for future use in design.

The real response of a laterally loaded monopile is likely to involve few additional features that have not been investigated in the above chapter. For instance, this model does not describe the formation of a gap between the soil and the pile, the influence of set-up, time-effect due to consolidation or anisotropy of the soil. All these effects would need to be investigated in detail before developing the theoretical framework and introducing them within the HARM model. Further developments, determined by experiment or large-scale field test, will therefore be required in future.

Finally, this model only describes the macro-behaviour of the foundation. However, the macro-response of the foundation actually reflects the integrated distribution of the soil reaction down the pile. This means that the model presented above could be integrated within current foundation design model, such as the p-y method. The next step of this work would then be to investigate how to integrate the HARM model within current design practice. In particular, work will be required to thoroughly scale the model parameters and accurately describe the backbone curve.

Chapter 6

Conclusions

This thesis presents a detailed analysis of the response of rigid monopiles to cyclic lateral loading in cohesionless soil for offshore wind applications. It primarily aims to provide new insights for future designs with respect to fatigue and serviceability limit state, as well as guidance for the development of design methods specifically adapted to cyclic loading. The work is based on a comprehensive laboratory testing programme that includes series of monotonic tests, symmetric reversed loading tests, long-term continuous and multi-amplitude cyclic tests. The key experimental findings provide the fundamental knowledge for the development of a constitutive model that accurately captures the pile behaviour in a rigorous manner while being computationally efficient. The key contributions from the two main research areas explored in this thesis are summarised below, together with implications for offshore wind turbine foundation design. The final section discusses possible future directions for research following this work.

6.1 Contributions

6.1.1 Key experimental results

The experimental work presented in this thesis involves a series of detailed laboratory floor model tests exploring the pile response to a range of load cases. The testing programme was performed using 1g experimental equipment including a rigid

monopile, scaled to reflect full-scale prototype behaviour. The main conclusions from the testing campaigns, and contributions to the knowledge gaps outlined in Table 1.7 (p. 42), are listed below.

1) **Rate effect** - The laboratory pile response is not affected by rate effects for the load frequencies investigated. However, rate dependency might become significant for faster loading rates and different soil properties, in particular when considering partially-drained or undrained loading.
2) **Hysteretic response** - The pile response to symmetric reversed load exhibits a hysteresis loop that corresponds to dissipated energy due to the plastic behaviour of the foundation. The response conforms to the extended Masing rules and can hence be approximated using pure kinematic hardening.
3) **Accumulated displacement** - The pile accumulates irreversible deformation when subjected to cyclic loading at non-zero mean load (ratcheting). The ratcheting rate progressively decreases with cycle number, but never decays to zero, at least during the first million cycles. The evolution of the accumulated rotation with cycle number strongly depends on the cyclic load magnitude and can be fitted using a power-law, which is conservative for large cycle numbers ($> 10,000$). The prediction of the pile response to cyclic loading using common design approaches, such as the p-y method, can be achieved using experimental results (Equation 3.3) and the Degradation Stiffness Model. This requires a thorough consideration of the loads acting on the pile and of the p-y curves expression to model the monotonic loading response prior to the analysis of cyclic loading. A power-law expression for the p-y curves (Equation 2.20) could be a possible option for future investigation of an adapted p-y method.
4) **Secant stiffness at ground level** - The secant stiffness of the foundation increases with cycle number. There is a sharp development in secant stiffness over the first 50 cycles, after which the secant stiffness rate of increase reaches a steady trend that can be approximated by a logarithmic law.

5) **Hysteresis loop area** - The hysteretic damping of the foundation decreases with cycle number and can be described with a power law. Additionally, the hysteresis loop area and secant stiffness are linked parameters that both describe the tightening of the hysteresis loop shape with cycle number.

6) **Multi-amplitude loading** - The response of the pile to monotonic reloading following cyclic loading exhibits an interaction between: (a) Masing behaviour (b) ratcheting (c) progressive stiffening of the response. If the number of load cycles before reloading is not too large, the reloading curve rejoins the backbone curve when exceeding the maximum cyclic load. The response of the pile to multi-amplitude cyclic loading conforms to the above statement. Additionally, the effect of extreme storm events can be limited provided a large number of FLS and SLS loads have been experienced beforehand. Accordingly, when experiencing extreme load events, the pile might not accumulate any more deformation under FLS loading. Finally, a conservative estimation of the pile response to multi-amplitude cyclic loading can be obtained using a linear cumulative approach.

6.1.2 Theoretical and numerical modelling

Chapters 4 and 5 present a novel constitutive model that captures the key findings outlined experimentally and listed above. The model is framed within the hyperplasticity framework presented by Houlsby and Puzrin (2006), which guarantees that the model is thermodynamically consistent and also provides a rigorous and concise development framework. The key aspects of the model are summarised below.

7) **Constitutive modelling of ratcheting** - The HARM model is developed based on the fundamentals of kinematic hardening hyperplasticity, and enables the generation of incremental ratcheting strain along with kinematic hardening plastic strain in the direction of loading. The ratcheting strain is then defined as a small fraction R of the kinematic hardening strain. The ratcheting coefficient

R characterises the ratcheting behaviour and controls the ratcheting rate. The model can be formulated using many kinematic hardening surfaces in order to simulate a smooth elastic-plastic transition. This particular formulation of the model allows for the response to conform to the extended Masing rules, while accumulating permanent deformation with cyclic loading at non-zero mean-stress, which is the primary mechanism identified experimentally.

8) **Accelerated modelling** - One of the great advantages of the HARM model is that it can easily be accelerated in order to simulate the response to very large cycle numbers within the computation of only a few cycles. This corresponds to modifying the definition of the ratcheting strain by multiplying the ratcheting coefficient R by a factor that corresponds to the number of cycles that the user wants to skip.

9) **Accumulated rotation** - The fundamentals of the HARM model as described above only enables a constant ratcheting rate and fixed hysteresis loop shape along with cycle number. It is then possible to adapt the basic model to capture specific aspects of the ratcheting behaviour for a given application. In the case of the rigid monopile, the ratcheting rate is decreased with cycle number by modifying the ratcheting coefficient R along with the accumulation of ratcheting strain. The influence of the cyclic load magnitude can then be incorporated within the model by making R a function of the initial strengths (which are directly a function of the stress).

10) **Secant stiffness and damping** - The change in hysteresis loop shape with cycle number, i.e. increase of secant stiffness and decrease in hysteresis loop area, is then captured by accommodating the kinematic hardening strengths according to the accumulation of ratcheting strain, using a similar technique as for isotropic hardening.

11) **Multi-amplitude loading** - The model that results from the above developments enables the key trends observed during multi-amplitude cyclic loading

tests to be captured. In particular, the resulting behaviour features the competition between (a) Masing behaviour (b) ratcheting and (c) progressive stiffening of the response.

12) Calibration - The final model is characterised by 10 model and 4 modelling parameters in total. A calibration procedure based on a number of continuous tests and a monotonic test enables seven of the model parameters to be determined and the final three approximated. A short parametric study then enables the modelling parameter values to be set. The final model then accurately captures the experimental test results, for both long-term continuous and multi-amplitude cyclic loading.

6.1.3 Further implications for design

The above sections have outlined key aspects of the pile response to cyclic lateral loading that have a direct implication for design. The following section develops the interpretation of some of the conclusions further with regards to current practice in the offshore wind industry.

- **Hysteretic response**: One of the great limitations of the *p-y* method is that, on unloading, the response reverses along the exact same curve as during loading. Firstly, the test results from this research clearly show that this practice does not represent the soil behaviour properly. In particular, this neglects the hysteretic response of the soil, and therefore prevents the estimation of the soil damping of the foundation.
- **Design tolerances for cyclic loading**: The cyclic load cases investigated during this research programme demonstrated that the design tolerance for cyclic loading, in terms of pile deformation, can be breached and need to be considered thoroughly.
- **Prediction of pile deformation**: The pile deformation with cycle number can be predicted using empirical frameworks such as that proposed by LeBlanc *et al.*

(2010a) or the Degradation Stiffness Model. This can then be extended one step further to multi-amplitude cyclic loading, using a linear cumulative model as in LeBlanc *et al.* (2010b). These frameworks were found to provide a conservative approach for the prediction of the pile response that could be very well suited for the early stages of the design process. However, these do not provide any information on the secant stiffness or evolution of the damping ratio with cycle number. This means that this type of approach is not appropriate for precise design to fatigue lifetime.

- **Effect of pile pre-loading**: The test results on multi-amplitude loading have shown that extreme load events could strongly diminish the induced pile deformation by subsequent cyclic load at smaller magnitude. This suggests that pre-loading of the pile, such as temporary exposure of the turbine to a particular wind direction prior to operation, and also the time window between installation of the foundation and mounting of the turbine, might be beneficial for the fatigue life of the turbine.
- **Relevance of full-scale monitoring**: The above also suggests the importance of turbine monitoring for assessment and extension of the turbine lifetime. As far as the foundation is concerned, establishing the real-time loading on the turbine might enable current pile tilting, natural frequency and damping of the structure to be established and assess the impact of future operational load on subsequent pile deformation.

6.2 Future directions

According to the findings in this thesis, this section proposes further directions for future research.

6.2.1 Suggestions for future experimental work

- **Soil conditions** - One of the primary limitations of the experimental work presented in this thesis relates to the restricted soil conditions tested.
  - First of all, some of the original contributions of this thesis (e.g. hysteresis response, evolution of monotonic reloading response) would need to be extended to denser samples.
  - Some of the loading cases experienced offshore might also involve partially-drained or undrained response of the soil in some locations along the pile. This is likely to affect the pile response and investigation of this topic would greatly contribute to design improvements.
  - The investigations presented in this thesis did not involve the formation of a gap between the pile and the soil. Experimental work to investigate the conditions for gapping and its influence on the pile response would be very useful for future modelling.
  - This research focused on pile response in cohesionless soils, which is a clear limitation for many sites in the European waters. The framework would need to be broadened to include piles in clay. Also, the response to piles in chalk or limestone is critical for many sites in Europe (see for example Figure 1.5, p. 10) and very little information is currently available in published literature on this topic.
  - A logical extension of the above is to analyse the influence of soil layering on the response. This is particularly relevant for sites closer to shore and could provide information on how the p-y springs should be related to each other.
- **Small magnitude cyclic loads** - The load cases investigated during this research programme were limited to a minimum load magnitude, after which the test results were subject to large experimental errors. It would be very interesting in future to design experimental equipment in order to investigate the pile response

to smaller load amplitude, located within the elastic range, in order to assess whether the pile still accumulates deformation and changes in hysteresis loop shape.

- **Retardation of degradation** - Some of the tests presented in this thesis suggest that cyclic loading at specific amplitude could retard the accumulation of deformation. This is an interesting aspect for design that should be investigated further.
- **Pre-loading** - The previous section outlined that pre-loading of the pile could be beneficial for its fatigue lifetime. This would need to be investigated in more detail in order to provide guidelines for pre-loading.
- **Installation effects** - This research has only considered the pile deformation due to the fatigue lifetime of the turbine. However, installation is likely to have an effect on the results and also contribute to an initial angle of the monopile.
- **Scour protection** - One of the key features of the cyclic loading response is the change in secant stiffness. However, many offshore wind farms make use of scour protections and, as suggested by Kallehave *et al.* (2015b), this affects the stiffness of the foundation. Further work would enable quantification of this effect and its evolution with cycle number.
- **Multi-directional loading** - As outlined in Chapter 1, further investigation is needed to extend the current state of knowledge on monopile response to multi-directional loading.
- **Scaling** - Finally, when considering small scale model testing, there is always the issue of scaling and how the results relate to full-scale prototype behaviour, especially when it comes to numerical values. It would be of great interest to investigate the dimensionless framework by providing a comparison of test results at different scales.

6.2.2 Modelling of offshore wind monopile foundations

Modelling of offshore wind monopile foundations under operational and fatigue loads could be reasonably achieved using a *p-y* based method, providing further work is carried out in future, for the design regarding both monotonic and cyclic loads. Using the developments presented in this thesis, a robust method could be developed that would accurately capture the real pile response. The possible developments and combination of the HARM model within the *p-y* approach are detailed below.

Firstly, regarding monotonic loading design, it has recently been outlined that the conventional *p-y* curves method leaves some of the soil reaction components out (Byrne *et al.*, 2015a). Chapter 2, Section 2.6 (p. 78) has mentioned the case of the shear base, but Byrne *et al.* (2015a) also state that design methods should take into account distributed moment curves down the pile length, accounting for vertical shear stress acting on the pile shaft as well as base moment (see Figure 6.1). Consequently, it is a priority for future research to extract appropriate expressions for each of these reaction components through specific testing and numerical modelling.

As mentioned in Section 6.1.3 (p. 221), another major issue from the current *p-y* approach is that the soil reaction curve follows the same line on loading and unloading (see left-hand side of Figure 6.1). However, a correct loading-unloading response of the soil down the pile should account for hysteresis (see Figure 6.1, right-hand side). Hence, further work would be needed to assess how the damping in the soil affects the damping of the pile response, and this should be included within the *p-y* method.

Finally, the next step would then be to accommodate cyclic behaviour. The Degradation Stiffness Model could potentially allow for the prediction of the pile deformation with cycle number. It would need to be modified for multi-amplitude load cases using, for example, a linear cumulation approach such as that proposed by LeBlanc *et al.* (2010b) (see Chapter 1, Section 1.4.3, p. 35). However, the DSM is presently unable to predict the evolution of the secant stiffness and hysteretic

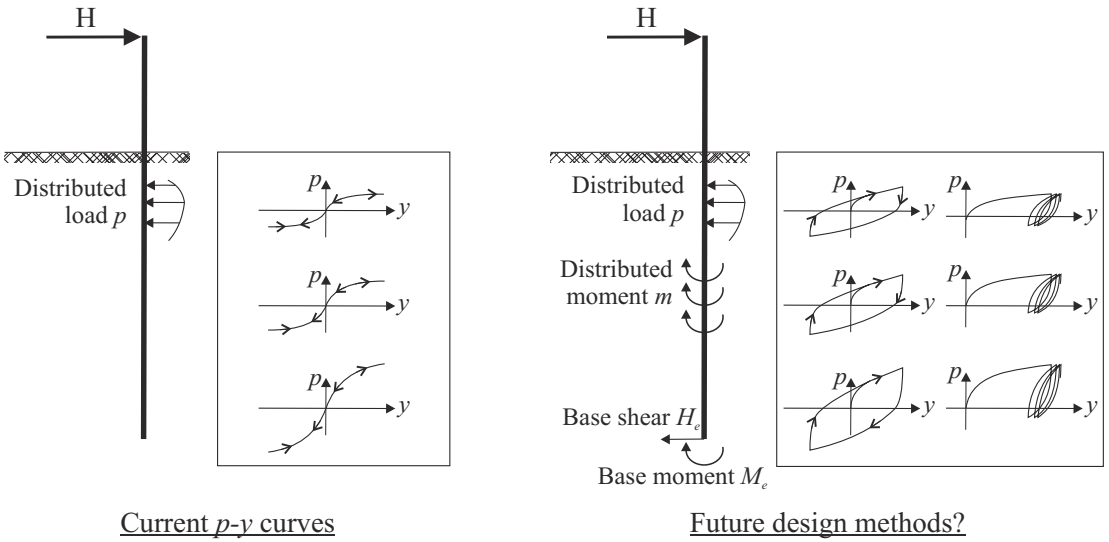

Figure 6.1: Suggestion for future design approaches

behaviour. As highlighted previously, this is a major issue for fatigue design that might actually invalidate this type of methodology.

A more accurate and robust alternative is therefore to consider approaches such as the HARM model, but discretised down the pile. Obviously, much more work is needed to integrate this type of approach within design, and to select the appropriate procedure for determination of the model parameters and calibration. However, it would enable very accurate prediction of the pile response to monotonic and cyclic loading of large cycle number and of variable amplitude, within a reasonable time frame. This would be a major improvement for assessment of the fatigue lifetime. The final model could also easily be integrated within structural analysis design codes. Finally, it would then be possible to expand modelling to more complex soil behaviours, such as gapping, time-effect due to consolidation or soil anisotropy.

References

Abadie, C. N. and Byrne, B. W. (2014), Cyclic loading response of monopile foundations in cohesionless soils, *in* 'Proceedings of the 8th International Conference on Physical Modelling in Geotechnics (ICPMG)', Vol. 2, pp. 779–784.

Abadie, C. N., Byrne, B. W. and Levy-Paing, S. (2015), Cyclic loading response of monopile foundations in cohesionless soils, *in* 'Proceedings of the 3rd International Symposium on Frontiers in Offshore Geotechnics (ISFOG), Oslo, Norway', Vol. 1, pp. 681–686.

Achmus, M., Albiker, J. and Abdel-Rahman, K. (2011), Investigations on the behavior of large diameter piles under cyclic lateral loading, *in* 'Proceedings of the 2nd International Symposium on Frontiers in Offshore Geotechnics (ISFOG)', pp. 471–476.

Achmus, M., Kuo, Y.-S. and Abdel-Rahman, K. (2009), 'Behavior of monopile foundations under cyclic lateral load', *Computers and Geotechnics* **36**(5), 725–735.

API (2010), *Recommended Practice for Planning, Designing and Constructing Fixed Offshore Platforms, RP2A-WSD, Washington*, American Petroleum Institute.

Armstrong, P. J. and Frederick, C. O. (1966), *A mathematical representation of the multiaxial Bauschinger effect*, Cegb Report No. Rd/B/N 731.

Bari, S. and Hassan, T. (2000), 'Anatomy of coupled constitutive models for ratcheting simulation', *International journal of plasticity* **16**(3), 381–409.

Bhattacharya, S. and Adhikari, S. (2011), 'Experimental validation of soil-structure interaction of offshore wind turbines', *Soil Dynamics and Earthquake Engineering* **31**(5-6), 805–816.

Billiam, J. (1972), 'Some aspects of the behaviour of granular materials at high pressures', *Stress-Strain behaviour of soils; Proceeding of the Roscoe Memorial Symposium, Cambridge University* pp. 69–80.

Bishop, A. W. (1972), 'Shear strength parameters for undisturbed and remoulded soils specimens', *Stress-Strain behaviour of soils; Proceeding of the Roscoe Memorial Symposium, Cambridge University* pp. 3–58.

Bolton, M. D. (1986), 'Strength and dilatancy of sands', *Géotechnique* **36**(1), 65–78.

Bourgeois, E., Rakotonindriana, M., Le Kouby, A., Mestat, P. and Serratrice, J. (2010), 'Three-dimensional numerical modelling of the behaviour of a pile subjected to cyclic lateral loading', *Computers and Geotechnics* **37**(7-8), 999–1007.

Broms, B. B. (1964), 'Lateral resistance of piles in cohesionless soils', *Journal of the Soil Mechanics and Foundations Division* **90**(3), 123–156.

Buckingham, E. (1914), 'On physically similar systems; illustrations of the use of dimensional equations', *Physical Review* **4**(4), 345–376.

Byrne, B. W. (2000), Investigations of Suction Caissons in Dense Sand, PhD thesis, University of Oxford.

Byrne, B. W. (2011), 'Foundation design for offshore wind turbines'. Géotechnique lecture 2011. Available at http://www.eng.ox.ac.uk/civil/pdf/Geotechnique_Lecture_BWB_2011_Web.pdf (accessed September 2015).

Byrne, B. W. and Houlsby, G. T. (2003), 'Foundations for offshore wind turbines', *Philosophical Transactions of the Royal Society of London A: Mathematical, Physical and Engineering Sciences* **361**(1813), 2909–2930.

Byrne, B. W. and Houlsby, G. T. (2004), 'Experimental investigations of the response of suction caissons to transient combined loading', *Journal of Geotechnical and Geoenvironmental Engineering* **130**(3), 240–253.

Byrne, B. W. and Houlsby, G. T. (2015), 'Helical piles: an innovative foundation design option for offshore wind turbines', *Philosophical Transactions of the Royal Society A: Mathematical, Physical and Engineering Sciences* **373**(20140081).

Byrne, B. W., McAdam, R., Burd, H. J., Houlsby, G. T., Martin, C. M., Gavin, K., Doherty, P., Igoe, D., Zdravković, L., Taborda, D. M. G., Potts, D. M., Jardine, R. J., Sideri, M., Schroeder, F. C., Muir Wood, A., Kallehave, D. and Skov Gretlund, J. (2015b), Field testing of large diameter piles under lateral loading for offshore wind applications, *in* 'Proceedings of the Fifteenth European Conference on Soil Mechanics and Geotechnical Engineering (ECSMGE), Edinburgh'.

Byrne, B. W., McAdam, R., Burd, H. J., Houlsby, G. T., Martin, C. M., Zdravković, L., Taborda, D. M. G., Potts, D. M., Jardine, R. J., Sideri, M., Schroeder, F. C., Gavin, K., Doherty, P., Igoe, D., Muir Wood, A., Kallehave, D. and Skov Gretlund, J. (2015a), New design methods for large diameter piles under lateral loading for offshore wind applications, *in* 'Proceedings of the 3rd International Symposium on Frontiers in Offshore Geotechnics (ISFOG), Oslo, Norway', pp. 759–764.

Chaboche, J. L. (1986), 'Time-independent constitutive theories for cyclic plasticity', *International Journal of Plasticity* **2**(2), 149–188.

Chaboche, J. L. (1991), 'On some modifications of kinematic hardening to improve the description of ratchetting effects', *International Journal of Plasticity* **7**(7), 661–678.

Chaboche, J. L. and Nouailhas, D. (1989), 'Constitutive modeling of ratchetting effects. part ii. possibilities of some additional kinematic rules', *Journal of Engineering Materials and Technology, Transactions of the ASME* **111**(4), 409–416.

Collins, I. F. and Houlsby, G. T. (1997), Application of thermomechanical principles to the modelling of geotechnical materials, *in* 'Proceedings of the Royal Society A: Mathematical, Physical and Engineering Sciences', Vol. 453, pp. 1975–2001.

Cook, M. F. and Vandiver, J. K. (1982), Measured and predicted dynamic response of a single pile platform to random wave excitation, *in* 'Proceedings of the 14th annual offshore technology conference, Houston, Texas', pp. 637–643.

COP 21 (2015), 'United nations climate change conference'. 21st yearly session of the Conference of the Parties (COP) to the 1992 United Nations Framework Convention on Climate Change (UNFCCC). http://www.cop21paris.org/.

Cox, W. R., Reese, L. C. and Grubbs, B. R. (1974), Field testing of laterally loaded piles in sand, *in* 'Proceedings of the Sixth Annual Offshore Technology Conference, Houston, Texas'.

Cuéllar, P. (2011), Pile Foundations for Offshore Wind Turbines: Numerical and Experimental Investigations on the Behaviour under Short-Term and Long-Term Cyclic Loading, PhD thesis, BAM, Bundesanstalt für Materialforschung undprüfung (Federal Institute for Materials Research and Testing), Berlin.

Cuéllar, P., Baeßler, M. and Rücker, W. (2009), 'Ratcheting convective cells of sand grains around offshore piles under cyclic lateral loads', *Granular Matter* **11**(6), 379–390.

DECC (2013), 'Electricity generation costs - 2013'. Department of Energy and Climate Change. Available at https://www.gov.uk (accessed September 2015).

DECC (2015), 'Uk energy statistics, q2 2015'. Department of Energy and Climate Change. Available at https://www.gov.uk/government/uploads/system/uploads/attachment_data/file/463016/Press_Notice_September_2015.pdf (accessed December 2015).

Devriendt, C., Magalhães, F., El Kafafy, M., De Sitter, G., Cunha, A. and Guillaume, P. (2013), Long-term dynamic monitoring of an offshore wind turbine, *in* 'Topics in Dynamics of Civil Structures - Proceedings of the 31st IMAC', pp. 253–267.

Dietrich, T. (1982), Incremental parabolic hardening of psammic material; application to laterally loaded piles in sand, *in* 'IUATAM Conference on Deformation and Failure of Granular Materials, Delft', pp. 13–22.

DNV (2004), *Offshore Standard DNV-OS-J101, Design of offshore wind turbine structures (first edition).*

DNV (2014), *Offshore Standard DNV-OS-J101, Design of offshore wind turbine structures (last edition).*

DONG Energy (2013), 'Scope of work: Academic work group for carbon trust owa - pisa project'. Muir Wood A., Kallehave D., Scharling Holm J. and Skov Gretlund J.; Doc. no. 1290891. Available at http://www.carbontrust.com/media/262212/2013-04-owa-pisa-scope-of-work.pdf (accessed September 2015).

Einav, I. (2004), 'Thermomechanical relations between stress-space and strain-space models', *Géotechnique* **54**(5), 315–318.

European Commission (2010), 'Europe 2020: A european strategy for smart, sustainable and inclusive growth'. Communication from the commission COM(2010) 2020, Brussels. Available at http://ec.europa.eu/eu2020/pdf (accessed September 2015).

Eurostat (2015), 'Energy from renewable sources'. Available at http://ec.europa.eu/eurostat/statisticsexplained/index.php/Energy_from_renewable_sources (accessed December 2015).

EWEA (2009), 'The economics of wind energy'. European Wind Energy Association. Available at http://www.ewea.org/fileadmin/files/library/ publications/reports/Economics_of_Wind_Energy.pdf (accessed September 2015).

EWEA (2013), 'Deep water: The next step for offshore wind energy'. European Wind Energy Association. Available at http://www.ewea.org/fileadmin /files/library/publications/reports/Deep_Water.pdf (accessed September 2015).

EWEA (2015*a*), 'The european offshore wind industry - key trends and statistics 1st half 2015'. European Wind Energy Association. Available at http://www.ewea.org/fileadmin/files/library/publications/statistics/EWEA-European-Offshore-Statistics-H1-2015.pdf (accessed September 2015).

EWEA (2015*b*), 'The european offshore wind industry - key trends and statistics 2014'. European Wind Energy Association. Available at http://www.ewea.org/fileadmin/files/library/publications/statistics/EWEA-European-Offshore-Statistics-2014.pdf (accessed September 2015).

François, D. (2010), *Structural Components: Mechanical Tests and Behavioral Laws*, ISTE Ltd.

Germanischer Lloyd (2005), 'Overall damping for piled offshore support structures'. Guideline for the Certification of OffshoreWind Turbines, WindEnergie, Edition 2005. Available at http://www.gl-group.com/pdf/1.d._Overall_Damping_for_Piled_Offshore_Support_Structures.pdf (accessed September 2015).

Golightly, C. (2014), 'Tilting of monopiles - long, heavy and stiff; pushed beyond their limits', *Ground Engineering* pp. (January) 20–23.

Gotschol, A. (2002), 'Veränderlich elastisches und plastisches verhalten nichtbindiger böden und schotter unter zyklisch-dynamischer beanspruchung'. Schriftenreihe Geotechnik, Universität Gh Kassel, Heft 12.

Hald, T., Morch, C., Jensen, L., LeBlanc, C. and Ahle, K. (2009), Revisiting monopile design using p-y curves. results from full scale measurements on horns rev, *in* 'Proceedings of European Offshore Wind'.

Hoadley, P., Barton, Y. and Parry, R. (1981), Cyclic lateral load on model pile in a centrifuge., *in* 'Proceedings of the International Conference on Soil Mechanics and Foundation Engineering', Vol. 1, pp. 621–625.

Houlsby, G. T. (1981), A Study of Plasticity Theories and their Applicability to Soils, PhD thesis, University of Cambridge.

Houlsby, G. T., Cassidy, M. J. and Einav, I. (2005), 'A generalised winkler model for the behaviour of shallow foundations', *Géotechnique* **55**(6), 449–460.

Houlsby, G. T. and Puzrin, A. M. (2000), 'Thermomechanical framework for constitutive models for rate-independent dissipative materials', *International journal of plasticity* **16**(9), 1017–1047.

Houlsby, G. T. and Puzrin, A. M. (2002), 'Rate-dependent plasticity models derived from potential functions', *Journal of Rheology* **46**(1), 113–126.

Houlsby, G. T. and Puzrin, A. M. (2006), *Principles of hyperplasticity: An approach to plasticity theory based on thermodynamic principles*, Springer.

Iwan, D. W. (1967), 'On a class of models for the yielding behaviour of continuous and composite systems', *Journal of Applied Mechanics, ASME* **34**, 612–617.

Kallehave, D., Byrne, B. W., LeBlanc Thilsted, C. and Mikkelsen, K. K. (2015a), 'Optimization of monopiles for offshore wind turbines', *Philosophical Transactions of the Royal Society A: Mathematical, Physical and Engineering Sciences* **373**(20140100).

Kallehave, D., LeBlanc-Thilsted, C. and Liingaard, M. A. (2012), Modification of the api formulation of initial stiffness of sand, *in* 'Proceedings of the 7th International Conference on Offshore Site Investigation and Geotechnics (OSIG), London, UK', pp. 465–472.

Kallehave, D., LeBlanc Thilsted, C. and Troya, A. (2015b), Observed variations of monopile foundation stiffness, *in* 'Proceedings of the 3rd International Symposium on Frontiers in Offshore Geotechnics (ISFOG), Oslo, Norway', Vol. 1, pp. 717–722.

Kelly, R. B., Houlsby, G. T. and Byrne, B. W. (2006), 'A comparison of field and laboratory tests of caisson foundations in sand and clay', *Géotechnique* **56**(9), 617–626.

Klinkvort, R. T. (2012), Centrifuge modelling of drained lateral pile-soil response, PhD thesis, DTU.

LeBlanc, C. (2009), Design of Offshore Wind Turbine Support Structures: Selected topics in the field of geotechnical engineering, PhD thesis, Aalborg University.

LeBlanc, C., Byrne, B. W. and Houlsby, G. T. (2010b), 'Response of stiff piles to random two-way lateral loading', *Géotechnique* **60**(9), 715–721.

LeBlanc, C., Houlsby, G. T. and Byrne, B. W. (2010a), 'Response of stiff piles in sand to long-term cyclic lateral loading', *Géotechnique* **60**(2), 79–90.

LeBlanc Thilsted, C. and Tarp-Johansen, N. (2011), 'Monopiles in sand - stiffness and damping'. Presentation at the EWEA conference, Brussels.

Lemaitre, J. and Chaboche, J.-L. (2010), *Mécanique des matériaux solides, 3rd edition*, DUNOD - (1st edition translated in English (Cambridge University Press): Mechanics of solid materials, 1994).

Lesny, K. and Wiemann, J. (2005), Design aspects of monopiles in german offshore wind farms, *in* 'Proceedings of the 1st International Symposium on Frontiers in Offshore Geotechnics (ISFOG)', pp. 383–389.

Lin, S.-S. and Liao, J.-C. (1999), 'Permanent strains of piles in sand due to cyclic lateral loads', *Journal of Geotechnical and Geoenvironmental Engineering* **125**(9), 798–802.

Little, R. and Briaud, J.-L. (1988), 'Cyclic horizontal load tests on six piles in sands at houston ship channel'. Research report 5640 to USAE Waterways Experiment Station, Miscellanous paper GL-88-27.

Lombardi, D., Bhattacharya, S. and Muir Wood, D. (2013), 'Dynamic soil-structure interaction of monopile supported wind turbines in cohesive soil', *Soil Dynamics and Earthquake Engineering* **49**, 165–180.

Long, J. H. and Vanneste, G. (1994), 'Effects of cyclic lateral loads on piles in sand', *Journal of Geotechnical Engineering* **120**(1), 225–244.

Malhotra, S. (2011), *Chapter 10 - Selection, Design and construction of Offshore Wind Turbine Foundations*, Dr. Ibrahim Al-Bahadly (Ed.).

Maltock, H. (1970), Correlations for design of laterally loaded piles in soft clay, Vol. 1, pp. 577–594.

Mansur, C. I. and Hunter, A. H. (1970), 'Pile tests - arkansas river project', *Journal of the Soil Mechanics and Foundations Division* **96**(5), 1545–1582.

Masing, G. (1926), Eiganspannungen und verfestigung beim messing, *in* 'Proceedings for the 2nd International Congress of Applied Mechanics'.

Meyer, B. J. (1979), Analysis of single piles under lateral loading, PhD thesis, University of Texas, Austin.

Miner, M. A. (1945), 'Cumulative damage in fatigue', *Journal of applied mechanics* pp. 159–165.

Mróz, Z. (1967), 'On the description of anisotropic workhardening', *Journal of the Mechanics and Physics of Solids* **15**(3), 163–175.

Muir Wood, A. (2014), 'Future monopile design'. Presentation at the Danish Geotechnical Society Seminar. Available at http://www.danskgeotekniskforening.dk/sites/default/files/pdf/pdf2014 (accessed September 2015).

Nguyen-Sy, L. (2006), The theoretical modelling of circular shallow foundations for offshore wind turbines, PhD thesis, University of Oxford.

Ohno, N. and Wang, J. (1995), 'On modelling of kinematic hardening for ratcheting behaviour', *Nuclear Engineering and Design* **153**(2-3), 205–212.

O'Neill, M. and Murchison, J. (1983), 'An evaluation of p-y relationships in cohesionless soils'. Research Report No. GT-DF02-83. Departement of Civil Engineering, University of Houston, TX.

Palmgren, A. G. (1924), 'Die lebensdauer von kugellagern (life length of roller bearings, in german)', *Zeitschrift des Vereines Deutscher Ingenieure (VDI Zeitschrift), ISSN* **68**(14), 339–341.

Peralta, P. (2010), Investigations on the Behavior of Large Diameter Piles under Long-Term Lateral Cyclic Loading in Cohesionless Soil, PhD thesis, University of Hannover.

Peralta, P. and Achmus, M. (2010), An experimental investigation of piles in sand subjected to lateral cyclic loads, *in* 'Proceedings of the 7th International Conference on Physical Modelling in Geotechnics (ICPMG)', Vol. 2, pp. 985–990.

Poulos, H. G. (1982), 'Single pile response to cyclic lateral load.', *Journal of the Geotechnical Engineering Division* **108**(GT3), 355–375.

Poulos, H. G. and Hull, T. S. (1989), 'Role of analytical geomechanics in foundation engineering', *Foundation Engineering, Current Principals and Practices, ASCE 2* pp. 1578–1606.

Prager, W. (1955), The theory of plasticity: A survey of recent achievements, *in* 'Proceedings of the Institution of Mechanical Engineers, London', Vol. 169, pp. 41–57.

Prevost, J.-H. (1977), 'Mathematical modelling of monotonic and cyclic undrained clay behavior', *International Journal for Numerical and Analytical Methods in Geomechanics* **1**(2), 195–216.

Puzrin, A. M. and Houlsby, G. T. (2001a), 'Fundamentals of kinematic hardening hyperplasticity', *International Journal of Solids and Structures* **38**(21), 3771–3794.

Puzrin, A. M. and Houlsby, G. T. (2003), 'Rate-dependent hyperplasticity with internal functions', *Journal of Engineering Mechanics* **129**(3), 252–263.

Pyke, R. M. (1979), 'Nonlinear soil models for irregular cyclic loadings.', *Journal Geotechnical Engineering Division, ASCE* **105**(GT6, Proc Paper, 14642), 715–726.

Rayleigh, J. W. S. B. (1877), *The Theory of Sound*, Macmillan.

Reese, L. C., Cox, W. R. and Koop, F. D. (1974), Analysis of laterrally loaded piles in sand.

Reese, L. C. and Van-Impe, W. F. (2011), *Single piles and pile groups under lateral loading - 2nd Edition*, CRC Press.

Reese, L. C. and Welch, R. C. (1975), 'Lateral loading of deep foundations in stiff clay', *Journal of the Geotechnical Engineering Division* **101**(7), 633–649.

Reese, L. and Wang, S.-T. (2006), 'Verification of computer program lpile as a valid tool for design of a single pile under lateral loading'. LPILE verification notes.

Remaud, D., Garnier, J. and Frank, R. (1998), Pieux sous charges latérales: étude de l'effet de groupe, *in* 'Journées Nationales Génie Civil et Génie Cotier, Toulon'.

RenewableUK (2014), 'Come 2020 onshore wind will be the cheapest electricity source we have. that's worth political backing, yes?'. RenewableUK blog, Maf Smith, Deputy Chief Executive of RenewableUK. Available at http://www.renewableuk.com/en/blog/index.cfm/id/C9915402-D43E-4B34-8585416EC1783B4F (accessed December 2015).

Rovere, M. (2004), Cyclic loading test machine for caisson suction foundations, Master's thesis, Centrale Lille and Politechnico di Milano.

Rowe, P. W. (1962), The stress-dilatancy relation for static equilibrium of an assembly of particles in contact, *in* 'Proceedings of the Royal Society of London A: Mathematical, Physical and Engineering Sciences', Vol. 269, pp. 500–527.

Rudolph, C., Grabe, J. and Bienen, B. (2014), 'Effect of variation of the loading direction on the displacement accumulation of large-diameter piles under cyclic lateral loading in sand', *Canadian Geotechnical Journal* **51**(10), 1196–1206.

Rychlik, I. (1987), 'A new definition of the rainflow cycle counting method', *International Journal of Fatigue* **9**(2), 119–121.

Sandford, R. J. (2012), Lateral buckling of high pressure/high temperature on-bottom pipelines, PhD thesis, University of Oxford.

Schanz, T. and Vermeer, P. A. (1998), 'On the stiffness of sands', *Géotechnique* **48**, Pre–failure Deformation Behaviour of Geomaterials:383–387.

Schnaid, F. (1990), A study of the cone-pressuremeter test in sand, PhD thesis, University of Oxford.

Schneider, J. A. and Senders, M. (2010), 'Foundation design: A comparison of oil and gas platforms with offshore wind turbines', *Marine Technology Society Journal* **44**(1), 32–51.

Schroeder, F. C., Merritt, A. S., Sørensen, K. W., Muir Wood, A., LeBlanc Thilsted, C. and Potts, D. M. (2015), Predicting monopile behaviour for the godewind offshore wind farm, *in* 'Proceedings of the 3rd International Symposium on Frontiers in Offshore Geotechnics (ISFOG), Oslo, Norway', pp. 735–740.

Schupp, J. (2009), Upheaval buckling and flotation of buried offshore pipelines, PhD thesis, University of Oxford.

Smart Wind Limited (2013), 'Hornsea offshore wind farm; project one - environemental statement'. Report by Wallingford, H. R.; Annex 5.1.2., Wave modelling. Available at http://infrastructure.planningportal.gov.uk (accessed September 2015).

Smith, T. D. (1987), 'Pile horizontal soil modulus values', *Journal of Geotechnical Engineering* **113**(9), 1040–1044.

Stewart, H. E. (1986), 'Permanent strains from cyclic variable-amplitude loadings', *Journal of Geotechnical Engineering* **112**(6), 646–660.

Suryasentana, S. K. and Lehane, B. M. (2014), 'Numerical derivation of cpt-based p-y curves for piles in sand', *Géotechnique* **64**(3), 186–194.

Taborda, D. M. G., Potts, D. M. and Zdravković, L. (2016), 'On the assessment of energy dissipated through hysteresis in finite element analysis', *Computers and Geotechnics* **71**, 180–194.

Tarp-Johansen, N. J., Andersen, L., Christensen, E. D., Mørch, C., Kallesøe, B. and Frandsen, S. (2009), Comparing sources of damping of cross-wind motion, *in* 'Proceedings of the European Offshore Wind, Stockholm, Sweden'.

The Crown Estate (2012), 'Offshore wind cost reduction - pathways study'. The Crown Estate. Available at http://www.thecrownestate.co.uk/media/5493/ei-offshore-wind-cost-reduction-pathways-study.pdf (accessed September 2015).

The Crown Estate (2014), 'UK offshore wind: Opportunities for trade and investment'. Available at https://www.gov.uk/government/uploads/system/uploads/attachment_data/file/437077/Offshore_Wind.pdf (accessed September 2015).

Tjelta, T. I. (2014), 'Installation of suction caissons for offshore wind turbines'. Presentation at the Danish Geotechnical Society Seminar.

Verdure, L., Garnier, J. and Levacher, D. (2003), 'Lateral cyclic loading of single piles in sand', *International Journal of Physical Modelling in Geotechnics* **3**, 17–28.

Vermeer, P. A. and de Borst, R. (1984), *NON-ASSOCIATED PLASTICITY FOR SOILS, CONCRETE AND ROCK*, Heron.

Vesic, A. S. and Clough, G. W. (1968), 'Behaviour of granular materials under high stresses', *Journal of the Soil Mechanics and Foundations Division. American Society of Civil Engineers* **SM3**(94), 661–688.

Villalobos, F. A. (2006), Model testing of foundations for offshore wind turbines, PhD thesis, University of Oxford.

Vucetic, M. (1990), 'Normalized behavior of clay under irregular cyclic loading', *Canadian Geotechnical Journal* **27**(1), 29–46.

Vucetic, M. and Dobry, R. (1991), 'Effect of soil plasticity on cyclic response', *Journal of Geotechnical Engineering* **117**(1), 89–107.

Williams, E. S. (2014), Upheaval buckling of offshore pipelines buried in loose and liquefiable soils, PhD thesis, University of Oxford.

Winkler, E. (1867), *Die Lehre von der Elasticität und Festigkeit*, (in German) 1st Edition, H. Dominicus, Prague.

Wroth, C. P. and Houlsby, G. T. (1985), Soil mechanics - property characterization and analysis procedures., *in* 'Proceedings of the 11th international conference on soil mechanics and foundation engineering, San Francisco, August 1985. (Balkema)', Vol. 1, pp. 1–55.

Zdravković, L., Taborda, D. M. G., Potts, D. M., Jardine, R. J., Sideri, M., Schroeder, F. C., Byrne, B. W., McAdam, R., Burd, H. J., Houlsby, G. T., Martin, C. M., Gavin, K., Doherty, P., Igoe, D., Muir Wood, A., Kallehave, D. and Skov Gretlund, J. (2015), Numerical modelling of large diameter piles under lateral loading for offshore wind applications, *in* 'Proceedings of the 3rd International Symposium on Frontiers in Offshore Geotechnics (ISFOG), Oslo, Norway', pp. 705–710.

Zhu, B., Sun, Y., Chen, R. and Chen, Y.-M. (2014), Model tests on offshore monopile subjected to lateral monotonic and cyclic loading, *in* 'Proceedings of the 8th International Conference on Physical Modelling in Geotechnics (ICPMG)', Vol. 1, pp. 553–559.

Ziegler, H. (1977,1983), *An Introduction of Thermomechanics, 1st and 2nd editions*, Amsterdam, Holland.